



Friedrich-Alexander-Universität
Naturwissenschaftliche Fakultät

MASTER'S THESIS
IN PHYSICS

SPATIALLY-RESOLVED SPECTROSCOPY OF
AN EXTRAGALACTIC MASSIVE YOUNG
STELLAR OBJECT WITH JWST

JURK KATHARINA

SUPERVISOR: PROF. DR. MANAMI SASAKI

DR.KARL-REMEIS-STERNWARTE

ERLANGEN CENTRE FOR ASTROPARTICLE PHYSICS

SUBMISSION DATE: APRIL 2, 2025

SPATIALLY-RESOLVED SPECTROSCOPY OF AN EXTRAGALACTIC MASSIVE YOUNG STELLAR OBJECT WITH JWST

ABSTRACT

Aims. Star formation is the fundamental driver in galaxy evolution. By introducing turbulence, shocks and mixing in the ISM, high-mass stars ultimately determine the course of star formation. They constantly interact with their surroundings through various types of radiative feedback and mass loss during their entire evolution. Starting from protostellar outflows and disk winds in pre-stellar phases over UV radiation, stellar winds and expanding photoionised (H II) regions through their stellar evolution to, finally, core-collapse supernova explosions ending their life. As such they both disrupt ongoing star formation as well as trigger the formation of new stars. Nevertheless, the processes which govern their formation remain unclear. Various theoretical models and their simulations predicting a range of properties of massive young stellar objects (MYSOs) across different evolutionary stages require observations constrains.

Methods. We analyse high spatial and spectral resolution integral field observations of a $\sim 15\text{--}20 M_{\odot}$ MYSO S7A located in the vicinity of R136 in 30 Doradus in the Large Magellanic Cloud using NIRSpec and MIRI/MRS on JWST. We focus on the identification of the emission lines in the available $0.9\text{--}27.5 \mu\text{m}$ wavelength range and create continuum-subtracted line-emission maps revealing the emission morphology for each transition. We estimate flux densities of the identified transitions with the automated fitting package ALFA. Line flux ratios are employed to estimate extinction towards the MYSO. The H I Br γ line is utilised to estimate the accretion luminosity as well as the mass accretion rate of S7A.

Results. S7A presents itself as a MYSO with several extended structures in the most active star-forming region in the Local Group. We identify S7A as a MYSO externally-illuminated by the young massive star cluster R136 producing a C-shaped shell at ~ 35 kAU. The detection of CO bandhead emission together with H₂O and CO₂ ice absorption hints towards the presence of an accretion disk. Broad H I and He I recombination lines within ~ 0.02 pc of the MYSO suggest photoionising radiation escaping from S7A. An hyper-compact H II region or a disk wind is the likely explanation of the observed transitions. H₂ and [Fe II] emission from a knot oriented towards the south-west at $\sim 5\text{--}8$ kAU away from the MYSO traces an protostellar outflow. Extinction-corrected H₂ and [Fe II] line ratios confirm the presence of shocks. The low mass accretion rate $\dot{M} \lesssim 10^{-7} M_{\odot} \text{yr}^{-1}$ indicates S7A is an evolved MYSO which has commenced Hydrogen fusion within its core. Nevertheless, S7A remains embedded within a colder H₂ and dust structure with a complex morphology. Towards the north-east an additional YSO emerges from a condensation within the same structure.

Eigenständigkeitserklärung

Hiermit versichere ich, Jurk Katharina, dass ich diese Arbeit selbstständig und nur mit den im Literaturverzeichnis angegebenen Quellen angefertigt habe. Alle wörtlichen Zitate oder sinngemäß übernommenen Aussagen wurden als solche gekennzeichnet. Ich erkläre weiterhin, dass diese Arbeit bisher nicht Gegenstand eines anderen Prüfungsverfahrens gewesen ist und nicht bereits veröffentlicht wurde.

April 2, 2025

Jurk Katharina

Contents

1	Introduction	6
1.1	Definitions	7
1.2	Difficulties in observing young massive stars	8
1.3	Star formation	8
1.3.1	Low-mass stars	11
1.3.2	Massive stars	12
1.4	Observations of Massive Young Stellar Objects	17
1.4.1	Radiative feedback – compact H II regions and disk winds	19
1.4.2	Outflows	20
2	Photometry	23
2.1	Luminosity, flux density and magnitude	23
2.2	Interstellar extinction	24
3	Spectroscopy	26
3.1	Basic principles of astronomical spectrographs	27
3.2	Integral field spectroscopy	29
4	Origin of spectral lines	32
4.1	Schroedinger equation and quantisation of energy levels	32
4.2	Energy spectrum of Hydrogen	34
4.3	Multi-electron systems	35
4.4	Transitions	36
4.4.1	Transition probabilities	36
4.4.2	Electric dipole transitions	38
4.4.3	Forbidden lines	38
4.5	Quadrupole transitions in molecular hydrogen H ₂	38
5	Infrared Photodetectors	41
5.1	Intrinsic and extrinsic semiconductors	42
5.2	IR Detector arrays	43
5.2.1	HgCdTe Photodiodes	43
5.2.2	Impurity band conduction detectors	44
6	JWST	46
6.1	Diffraction limited resolution	47
6.2	Instruments	48
6.2.1	NIRCam	48
6.2.2	NIRSpec	48
6.2.3	MIRI	51
6.3	Infrared Background	54
6.4	Dithering	54
6.5	Detector readout patterns and exposure time	54

7	Data overview	59
	NIRCam	59
	MIRI	59
	IFU	59
8	Data Reduction	61
8.1	NIRCam and MIRI Imaging	61
	Image2	63
	1/ <i>f</i> noise correction	63
	Image3	63
	<i>Gaia</i> DR3 alignment	64
8.2	Near- and Mid-infrared IFS	64
	Spec2	64
	Spec3	65
	MIRI/MRS Fringing	66
9	IFU emission line spectrum of massive YSO S7A	67
9.1	Previous studies	67
9.2	NIRCam and MIRI view	71
9.3	NIRSpec and MIRI/MRS IFU spectra – Methods	73
	9.3.1 Spectral Extraction	73
	9.3.2 Contamination by other point sources and possible multiplicity	74
	9.3.3 Identification and Continuum-subtracted Line Emission Maps	76
	9.3.4 Line Flux	82
9.4	General spectral features	83
9.5	NIRSpec and MIRI/MRS IFU spectra – Spectral Lines	84
	9.5.1 Transitions tracing the MYSO and the shell	85
	Recombination lines	85
	Forbidden Transitions	87
	9.5.2 Molecular Hydrogen Lines	89
	9.5.3 O I transitions	89
	9.5.4 Unidentified transitions	92
9.6	Disk tracers – CO bandhead emission and fluorescent Fe II	93
	9.6.1 Comparison to the NIR X-shooter spectrum	93
	CO emission	93
	Fluorescent Fe II	96
	9.6.2 Comparison of S7A and S9 spectra	97
	CO absorption	97
9.7	HI lines as accretion tracers	99
	9.7.1 Extinction Correction	99
	9.7.2 Accretion luminosity	102
	9.7.3 Stellar parameters from SED fitting	102
	9.7.4 Mass accretion rate	106
9.8	Knot emission – a protostellar outflow	108
	9.8.1 Line Profiles	109

9.8.2 Shock- or photo-excitation?	111
10 Summarised Conclusions	116
References	119
A Spectra	125
A.1 Parameters of ds9 spectral extraction regions	125
A.2 S7A spectrum	126
A.3 YSO+Outflow Spectrum	127
A.4 Shell spectrum	128
A.5 SED of pointsource C1	129
B Identified emission lines	130
C Continuum-subtracted Line Emission Maps	138
C.1 Fluorescent Fe II transitions	138
C.2 NIR [Fe II] and O I knot-tracing lines	139
C.3 Electric-dipole forbidden transitions	140
C.4 Unidentified transitions	143
D Ionisation potentials of observed atoms	144
E Line Flux Densities	145
E.1 Fit results	145
E.2 ALFA fitted spectra	155

1 Introduction

Massive stars are fundamental drivers of star formation, galaxy evolution and ultimately the evolution of the Universe. They present the source of radiation detected from galaxies at high redshift. Firstly, massive stars are crafters of heavy elements. They fuse elements up to Iron during their lifetime. Through their death in type II supernovae (SNe), they enrich the interstellar medium (ISM) with heavier elements. Neutron stars (NS) as (one type of) compact remnants of type II SNe, introduce even heavier elements through NS-NS mergers. Secondly, they constantly interact with their surroundings through various types of radiative feedback and mass loss: their UV radiation, stellar winds and outflows, expanding H II regions and SNe. As such they are able both to disrupt ongoing star formation as well as trigger it. Several generations of stars form over the course of billions of years. By introducing turbulence, shocks and mixing in the ISM, high-mass stars ultimately determine the evolution of the galaxy. Nevertheless, the processes which govern their formation remain unclear.

The Large Magellanic Cloud (LMC) is the largest and closest satellite galaxy of the Milky Way at $49.59 \pm 0.54 \pm 0.09$ kpc (Pietrzyński et al. 2019). The face-on view with a low inclination angle towards the line of sight ($25\text{--}40^\circ$, van der Marel & Kallivayalil 2014) make the LMC an ideal target for studies of the galactic matter cycle. In addition, the LMC's position at -33° galactic latitude implies a much lower foreground absorption ($N_{\text{H}} < 10^{21} \text{ cm}^{-2}$, e.g. Bekhti et al. 2016) than towards the Galactic plane ($N_{\text{H}} > 10^{22} \text{ cm}^{-2}$, e.g. Bekhti et al. 2016) enabling multiwavelength studies of various populations from young stellar objects (YSOs) to supernova remnants. The most active star-forming region in the Local Group is the 30 Doradus H II region also referred to as the Tarantula Nebula located in the LMC. Its centre hosts NGC 2070 powered by the ultraviolet radiation and winds from the young star cluster R136 consisting of the most massive known OB stars. Past infrared (IR) and optical surveys have established 30 Doradus as a complex region with extended gas filaments, dense clumps and dust pillars hosting multiple generations of stars including thousands of YSOs (e.g., Fahrion & De Marchi 2023).

YSOs exhibit envelopes from which they accrete matter onto a circumstellar disk. These envelopes absorb the radiation from the central protostar and re-emit it at mid- and far-IR wavelengths. The accreted material can be reprocessed by the protostar (initially embedded in the dense envelope) and ejected into the ISM through protostellar outflows. These outflows are discussed to consist of a fast collimated jet and a slower wide-angle disk wind (Arce et al. 2007). Throughout their evolution, the envelope becomes increasingly optically thin, revealing the pre-main sequence star and its disk where possibly planet formation will occur.

JWST with its 6.5 m diameter primary mirror is ideal for studying YSOs with high spatial and spectral resolution not only in our own Galaxy, but also in an extragalactic context. JWST's increased point-source sensitivity especially in the MIR enables the detection of the youngest YSOs towards the lower-mass range as well as deeply embedded massive YSOs. The instruments relevant for this work are discussed in detail in chapter 6. The detection principles of infrared radiation which are useful to grasp the meaning behind observation techniques are outlined in chapter 5. The data set which provides the basis for this thesis is described in chapter 7. The data reduction pipeline follows in chapter 8.

The introduction continues by summarising the main challenges in understanding massive

star formation and the current promising theories. More details can be found in [Beuther et al. \(2007\)](#); [Arce et al. \(2007\)](#); [Zinnecker & Yorke \(2007\)](#) and in the respective sections of [McKee & Ostriker \(2007\)](#); [Schulz \(2012\)](#). Further, several PhD thesis have provided guidance through this complex field ([Maud 2013](#); [Ward 2017](#); [Purser 2017](#); [Pomohaci et al. 2017](#)).

1.1 Definitions

In astrophysical terms a star is defined as a self-gravitating sphere of gas mainly consisting of hydrogen and helium whose core temperature is high enough to produce energy through thermonuclear fusion preventing its gravitational collapse. A star is defined through the following two conditions:

1. *Hydrostatic Equilibrium*: the internal pressure, i.e., the internal thermal motion, of the gas cloud and the gravity are in balance. There is no macroscopic contraction or expansion of the cloud. The equation of momentum conservation

$$\rho \frac{\partial \mathbf{v}}{\partial t} + \rho \mathbf{v} \cdot \nabla \mathbf{v} = -\nabla P + \mathbf{F}_{\text{grav}} \quad (1.1)$$

yields the virial theorem – the internal energy is half the gravitational energy.

2. *Thermal Equilibrium*: the energy radiated away by the star is made up for by the nuclear fusion in the star’s core.

A *protostar* or *protostellar object* is a sphere of gas in hydrostatic equilibrium which does not yet fuse Hydrogen. Once the burning starts, the protostar is referred to as a zero-age main sequence (ZAMS) star and as long as Hydrogen burning continues in its centre it remains a main-sequence star ([Zinnecker & Yorke 2007](#)). A *protostellar system* describes the entire system of protostar, infalling envelope and accretion disk. In general, it may also include companions and describe binary systems or those with higher multiplicity ([Schulz 2012](#)). After the envelope accretion significantly drops and once the central protostar becomes optically visible, it crosses the stellar birthline in the Hertzsprung-Russel diagram ([Schulz 2012](#), Fig. 6.7). The nomenclature changes to *pre-main sequence* (PMS) star and the protostar begins contracting towards the main sequence along its evolutionary track. In parallel to the case of a protostar and protostellar system, a PMS system includes the accretion disk which might eventually become the place for planet formation and therefore in the literature often named as the protoplanetary disk. A *young stellar object* (YSO) is somewhat more general, it can refer to the entire pre-stellar system across all its evolutionary stages ([Schulz 2012](#)).

A massive or high-mass star is a star of type OB with sufficient mass to fuse elements heavier than Carbon in their core. Eventually a type II supernova ends their red supergiant phase. For a solar metallicity environment, the mass should exceed about $8 M_{\odot}$. The term of a high-mass protostar with $M \gtrsim 8 M_{\odot}$ in hydrostatic equilibrium will exist only shortly between an intermediate-mass accreting *protostar* and a massive accreting *star*. Observationally, it cannot be distinguished once an accreting protostar begins Hydrogen burning and becomes by definition a star ([Zinnecker & Yorke 2007](#)). As we shall see in section 1.3.2, this is the case in massive star formation. Instead, massive young stellar objects can be defined by

the presence of regions of ionised Hydrogen (H II regions) around them during more evolved stages (Purser 2017, see Sect. 1.3.2). Further nomenclature encountered in the literature and particular to the evolutionary stages of massive stars will be introduced in section 1.3.2. Throughout this work, I prefer the term *massive young stellar object* (MYSO) to describe the central source (possibly together with its disk and remaining envelope) for our source of investigation.

1.2 Difficulties in observing young massive stars

The early evolutionary stages of massive stars are difficult to observe:

1. Massive stars are rare. Galactic initial mass functions (IMFs) are described with powerlaws $dN/d\log M \sim M^{-\alpha}$ with negative slopes. The higher the masses of stars, the less of them there are. For 30 Dor, $\alpha = 1.35$ and only $\sim 2\%$ have masses between $8 M_{\odot}$ and $128 M_{\odot}$ (Zinnecker & Yorke 2007, Tab. 2 and references therein).
2. More massive YSOs evolve more quickly than lower-mass YSOs – $\sim 10^5$ yr vs $\sim 10^7$ yr. Crucial pre-stellar evolutionary stages are short. The probability of finding a YSO that is, firstly, massive and, secondly, in an early evolutionary phase crucial for the understanding of their evolution is low.
3. MYSOs remain obscured in optically thick dusty envelopes through most of the pre-stellar phases. Optical extinction can be as high as $A_V \lesssim 200$ mag (Purser 2017, Sect. 2.2). Their higher luminosity compared to the lower-mass counterparts is helpful only to a limiting extent. Only mm and radio observations can reveal the youngest MYSOs.
4. MYSOs form in loosely bound OB associations or gravitationally bound clusters (such as R136 in 30 Dor) and almost never in isolation (Zinnecker & Yorke 2007, Sect. 2.3.3). Runaway or field OB stars found away from clusters and associations originated in clusters/associations, but were ejected. Other massive stars or MYSOs and their feedback and gravitational interactions will influence the high-mass (pre-) stellar evolution. Additionally, they are found at larger distances than low-mass YSOs. The closest known MYSOs are located at about 2 kpc (McKee & Ostriker 2007). Resolving individual objects within groups can be challenging.

We see that building a consistent theory of massive star formation is extremely difficult. Theoretical models remain controversial without observational evidence. And without a clear theoretical model, we lack fundamental understanding of not only high-mass star evolution, but also the processes and conditions within the ISM leading to their formation.

1.3 Star formation

Stars form in *giant molecular clouds* (GMCs). GMCs make up the coldest part in the five-phase galactic ISM with mean temperatures of 15–20 K. Although they occupy only about 1% of the galactic ISM volume, their Hydrogen number densities n_{H} are so high that

they contribute $\sim 30\text{--}60\%$ to the total ISM mass (Dopita & Sutherland 2003; Ryden & Pogge 2021).

GMCs mostly consist of molecular hydrogen H_2 . However, the distribution and properties of GMCs are mainly studied through the rotational transitions of the second most abundant molecule CO ($N_{\text{H}_2}/N_{\text{CO}} \sim 2 \times 10^{-4}$; Ryden & Pogge 2021) as H_2 is difficult to observe at the low temperatures of GMCs (see Sect. 4.5). Its most prominent rotational transition at 2.6 mm originates from the change in rotational quantum number J from 1 to 0 (see Sect. 4.5). It was found that the mass in GMCs is not distributed uniformly, but in clumps. It is turbulence together with self-gravity that creates a distribution of different gas densities of various size and mass (McKee & Ostriker 2007). Clumps are the entities where OB clusters or associations will eventually form. These clumps are further fragmented into dense cores which eventually form singular or binary stellar system or those with even higher multiplicity. Depending on the state of evolution of the protostellar system and the amount of heating introduced either by the embedded YSO(s) or by external sources (the ionising radiation from massive stars), *cold* (*starless*) and *hot* molecular cores can be distinguished (Purser 2017). Table 1.1 compares key characteristics such as mass M , Hydrogen density n_{H} , size D and temperature T of the different cloud types mentioned.

Thermal and magnetic pressure together with turbulences introduced mainly through outflows from low-mass young stellar objects are sufficient to stabilise these clouds against gravitational collapse (virial equilibrium; Dopita & Sutherland 2003, Ch. 14.2.1). A GMC remains in equilibrium until perturbations through, e.g., shocks, are introduced. In the 1920's James Jeans calculated the limiting mass for a static cloud with a temperature T and a density n to gravitationally contract in the simplified case of overcoming solely the thermal gas pressure. In this case, GMCs can be described by the virial theorem relating the total kinetic energy K of a system to its potential energy U : $2K + U = 0$. In reality, additionally to the gas pressure, gravity must exceed magnetic forces, turbulence, and rotation to eventually form stars (Zinnecker & Yorke 2007).

$$M_{\text{Jeans}} = \left(\frac{5kT}{G\mu m_{\text{H}}} \right)^{3/2} \left(\frac{3}{4\pi\rho_0} \right)^{1/2} \approx 0.32 M_{\odot} \left(\frac{T}{10\text{ K}} \right)^{3/2} \left(\frac{m_{\text{H}}}{\mu} \right)^{3/2} \left(\frac{10^6\text{ cm}^{-3}}{n_{\text{H}}} \right)^{1/2}, \quad (1.2)$$

where k and G are the Boltzmann and gravitational constant, respectively, m_{H} is the Hydrogen mass, T the temperature, μ the mean molecular mass, and n_{H} the Hydrogen density in the cloud (Draine 2011). Strictly speaking, M_{J} is unphysical as the assumption on the gravitational potential, $\nabla\phi_0 = 0$, imply a vacuum ($\nabla^2\phi_0 = 0$ and therefore $\rho_0 = 0$) (e.g., Draine 2011). However, more rigorous analysis (including external gas pressure, although still neglecting magnetic and turbulent effects, the Bonnor-Ebert mass) have yielded masses similar to M_{J} and is therefore nevertheless useful for order-of-magnitude estimations (Draine 2011).

A major difference in low- and high-mass star formation lies in the point in their evolution when Hydrogen burning starts. The relevant timescales are the free-fall (or dynamical) and the Kelvin-Helmholtz (or contraction or thermal) timescale. One can ask the question how long it would take the core to re-establish hydrostatic equilibrium after the collapse was initiated. Or, equivalently, the time it requires for the core to collapse under its own gravity. The answer is given by the free-fall (or dynamical) timescale. It is derived by solving the

equation of momentum conservation (1.1) under assumption of gravity as the only external force (Schulz 2012)

$$t_{\text{ff}} = \left(\frac{3\pi}{32G\bar{\rho}_0} \right)^{1/2} \sim 2.1 \times 10^3 (\bar{\rho}_0)^{-1/2} \text{ s}, \quad (1.3)$$

where $\bar{\rho}_0$ is the initial mean matter density in the cloud in cgs units (g cm^{-3}) and G the gravitational constant. Note that the free-fall timescale depends only on the density and not on the initial size or mass of the cloud. The densest parts collapse the fastest. Therefore, if a density gradient exists within a condensation of gas increasing towards its centre, t_{ff} is higher for material near the centre than for material farther away. Such collapse is said to proceed ‘inside-out’ and is believed to happen in low-mass star formation (Shu et al. 1987). As the density and opacity of the collapsing cloud increases – it is said to be optically thick – the internal pressure is high enough to slow down the collapse. Free-fall conditions no longer apply and the timescale of the evolution changes. The Kelvin-Helmholtz (contraction or thermal) timescale describes how long it would take for all potential gravitational energy to be radiated away and therefore to cool down the optically thick object. It therefore governs the contraction of the protostar until the temperature is high enough to ignite nuclear fusion (at which point the evolution is determined by the nuclear timescale – the time it takes for the Hydrogen fuel to be exhausted under constant burning rate. This determines the lifetime of the main sequence phase and depends on the mass of the star.). It is defined by the ratio of gravitational energy and the protostellar core’s luminosity (Schulz 2012).

$$t_{\text{KH}} = \frac{GM^2}{RL}, \quad (1.4)$$

where M and R are the protostellar core mass and radius, T the temperature at the surface. For low-mass stars, $t_{\text{KH}} > t_{\text{ff}}$. The protostar stops accreting material well before it arrives at the main sequence. For massive stars, on the other hand, $t_{\text{KH}} < t_{\text{ff}}$. Nuclear burning commences while they are still embedded within their dust envelopes and are still be accreting material. This introduces radiation pressure and photoionising radiation into the evolution of MYSOs which are not relevant for low-mass stellar evolution (McKee & Ostriker 2007). This is further elaborated in section 1.3.2. However, observations show that evolved MYSOs with photoionised regions around them still show signs of accretion. It must therefore be possible for Hydrogen burning massive stars to continue accretion (see, e.g., Klaassen et al. 2011).

TABLE 1.1 – Comparison of physical properties of giant molecular clouds, clumps, and cores in which stellar systems form as well as ultra- and hyper-compact H II regions produced by evolved MYSOs.

Type	$n_{\text{H}(2)}$ [cm^{-3}]	D [pc]	T [K]	M [M_{\odot}]
Giant Molecular Clouds (GMCs)	$>10^2$	~ 50	15–20	10^4 – 10^6
Individual dark clouds/Clumps	10^3	2	10	30
Dense Cores	10^4	0.1 – 1	10	0.3 – 10
Cold (starless) Molecular Cores (CMCs)	$>10^5$	0.2–0.3	<20	10^2 – 10^3
Hot Molecular Cores (HMCs)	$\sim 10^7$	~ 0.1	$\gtrsim 10^2$	$<10^2$
Ultra-compact H II regions (UCH IIs)	$\gtrsim 10^4$	$\lesssim 0.1$	$\sim 10^4$	$\sim 10^{-2,a}$
Hyper-compact H II regions (HCH IIs)	$\gtrsim 10^6$	$\lesssim 0.03$		$\sim 10^{-3,a}$

REFERENCES. Data adapted from [Tielens \(2021\)](#); [Dopita & Sutherland \(2003\)](#); [Ryden & Pogge \(2021\)](#) for GMCs and clumps, from [Purser \(2017, Tab. 1.1 and references therein\)](#) for CMCs and HMCs as well as from [Maud \(2013\)](#); [Kurtz \(2005, Tab. 3\)](#) for HCH IIs and UCH IIs regions. Further and slightly varying definitions are given in [Beuther et al. \(2007\)](#) and [Hoare et al. \(2007\)](#).

NOTES. ^(a) The stated mass corresponds to the ionised mass fraction ([Kurtz 2005](#)).

1.3.1 Low-mass stars

Low-mass protostars are ubiquitously found in our Galaxy and the LMC and SMC. They are exceptionally well studied. Several sub-type classifications from low-mass T Tauri and intermediate-mass Herbig Ae/Be stars over Herbig-Haro objects to FU Orionis objects with outbursts exist partially reflecting different evolutionary stages (see, e.g., [Schulz 2012, Fig. 6.1](#)). The same does not apply to massive YSOs and the theoretical understanding of their evolution. In the following, I, firstly, summarise the formation of low-mass stars and the initial assumptions that – as has been shown through simulations – can reproduce low-mass stars. In the next section, I highlight the conceptual differences between low- and high-mass star formation and the main argument that prevents the formation of higher-mass stars assuming the same initial conditions as for low-mass stars, namely, radiation pressure.

The formation of low-mass stars can be described in four steps ([Shu et al. 1987](#)). The process is illustrated in [Fig. 1.1](#). Detailed reviews of the individual steps can be found in [Shu et al. \(1987\)](#) or [McKee & Ostriker \(2007\)](#).

1. GMCs fragment into smaller entities such as clumps and dense cores once magnetic and turbulent pressure cannot prevent gravitational collapse.
2. A protostar forms by gravitational ‘inside-out’ collapse of the optically thick core. It remains embedded within an envelope made up of molecules and dust (see [Sect. 9.5.2](#)). The envelopes have temperatures of a few 100 K or 1000 K ([Karttunen et al. 2007](#)). According to Wien’s displacement law the corresponding wavelength range at maximum emission for the stated temperatures is 3–30 μm which falls into the infrared regime of the electromagnetic spectrum. As material continues to fall onto the protostar, an accretion disk develops.

3. Bipolar jets and outflows in the polar directions create Herbig-Haro objects and carve cavities into envelope. It is suggested that jets are associated with the presence of magnetic fields.
4. Matter infall from the envelope onto the accretion disk drops significantly. The material in the envelope was dissipated through the outflows. The pre-main sequence star becomes optically visible. Once the temperature within the pre-main sequence star is high enough ($\sim 10^7$ K), Hydrogen fusion starts. Thermal equilibrium is achieved. A low-mass main sequence star is born.

The radiation from the protostar escapes from the optically thick envelope by being re-processed by dust and re-radiated at IR wavelengths (Stahler & Palla 2004). The total luminosity emitted by a YSO has two components. One part, L_{star} , is emitted from the protostellar surface. In earlier stages of contraction, it is the gravitational potential energy difference between initial and final states. In later phases, it is produced by Deuterium burning within the protostar once the temperature in the centre reaches $\gtrsim 10^6$ K and is given by the Stefan-Boltzmann relation $L = 4\pi R^2 \sigma T_{\text{eff}}^4$ (Stahler & Palla 2004; Schulz 2012). Secondly, the matter infall converts its kinetic energy into radiation as it hits the protostellar surface at the accretion shock. The energy per unit time released is termed the accretion luminosity $L_{\text{acc}} = GMM_{\text{acc}}/R$. The above expression assumes that all of the gravitational potential energy is radiated away. However, in reality, it will only be a fraction given by the above expression. Some part will, e.g., get absorbed by the star. Some of the infalling material will also be affected by winds from the accretion disk and not reach the protostar (see, e.g., Offner & McKee 2011). The accretion luminosity described as above should therefore be interpreted as an upper limit.

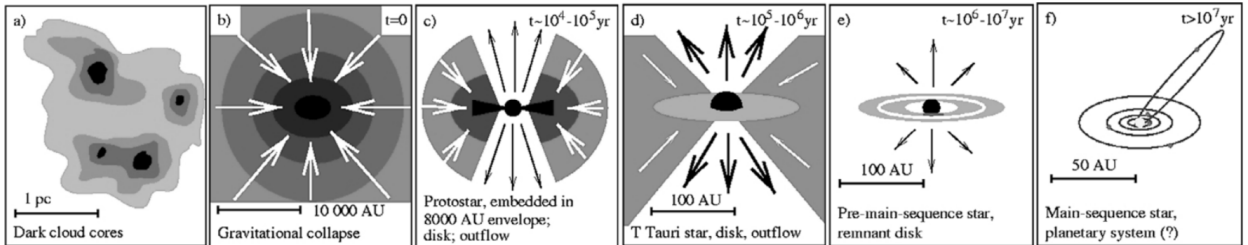


FIGURE 1.1 – The various steps of low-mass star formation. Within a giant molecular cloud, matter gathers into dense cores (a) which form protostars due to gravitational collapse (b). The protostars are surrounded by infalling envelopes and accretion disks (c). Eventually the protostar becomes hot enough to ignite nuclear fusion. Outflows and jets are formed and the accretion rate decreases (d). When the accretion phase ends, a young star surrounded by a protoplanetary disk is left (e). Adopted from Tielens (2021).

1.3.2 Massive stars

Theoretically, high-mass star formation can be divided into four phases (Zinnecker & Yorke 2007):

1. Compression: cold molecular cores form due to fragmentation of the parental GMC due to gravitational and turbulent influence.

2. Collapse: parts of the cores gravitationally collapse into pre-stellar objects.
3. Accretion: protostellar objects continue accreting material from their surrounding envelope – most likely through a disk. Hydrogen burning starts in the centre while accretion continues. The MYSOs emits UV radiation and UCH II regions of ionised gas form around the MYSOs. Protostellar jets and radiative feedback in form of winds develops. The accretion still persists.
4. Disruption: fully developed OB stars begin their influence of the surrounding environment. The parent molecular cloud is destroyed revealing OB associations or clusters. Radiation-driven winds, UV radiation and eventually SNe shape the ISM.

It seems that to some degree, high-mass star formation can be treated analogous to low-mass star formation. Collapsing massive cores, jets and outflows as well as circumstellar disks were observed also for massive YSOs (Kuiper et al. 2010, and references therein). However, the details regarding the formation of massive cores, the accretion to reach high masses as well as the effects of strong radiation from the forming MYSOs on the accretion flow remains debated. These aspects are discussed in more detail below.

The main challenge in comprehending early massive star formation can be formulated in the following question: how can a large enough clump of mass form a high-mass star rather than fragmenting into smaller entities forming several lower-mass stars? The various models proposed to solve this problem mainly differ in, firstly, where the material to make up the final star originates from and, secondly, at which time during the evolution it is gathered onto a single object. The turbulent core model (sometimes also called ‘monolithic core collapse’) suggests that the necessary mass is already localised within the dense (starless) cores from which high-mass stars will form and therefore exists before the gravitational collapse begins (McKee & Tan 2003). The initial core mass therefore reflects the final mass of the main-sequence star tying the IMF of cores and stars. They assume supersonic turbulence – higher than in low-mass star-forming regions – to prevent further fragmentation into less massive entities. This, however, induces high density gradients which would encourage fragmentation. Possibly, magnetic fields may present further stabilising conditions (Zinnecker & Yorke 2007, Sect. 4.1). However, Beuther et al. (2025, Sect. 2.4) argue that observations seem to not support significantly higher turbulence in high-mass star-forming regions compared to low-mass regions. Very high and accelerating ($\dot{M}_{\text{acc}} \propto t$) accretion rates, 10^{-4} – $10^{-3} M_{\odot} \text{ yr}^{-1}$, are required to overcome thermal radiation pressure (McKee & Tan 2003). The formation of accretion disks and outflows are compatible with this model and the timescale of MSF is compatible with $\sim 10^5$ yr (Beuther et al. 2025, Sect. 1.2. and references therein). So far, only few high-mass starless cores have been observationally confirmed (McKee & Ostriker 2007). Most remain as candidates (Ward 2017; Beuther et al. 2025, and references therein). On larger scales supporting evidence for the presence of turbulence in molecular clouds (MCs) exists: under the assumption of supersonically turbulent MCs, the star formation rate in the Milky Way has been successfully predicted (Krumholz & McKee 2005). Further, OB clusters with similar properties to Orion, i.e., with masses high enough to harbour massive stars, have been produced assuming turbulent initial conditions and correctly reproduced the observed initial mass function (Krumholz et al. 2012).

In contrast to the turbulent core model, competitive accretion introduced by [Bonnell et al. \(1997\)](#) assumes that massive stars grow by accretion material from their natal clump. Here, the dense cores are not required to reflect the mass of the final star prior to its formation. The challenge in the competition lies in two aspects: acquiring the most ideal location within the clump with respect to other cores and being the first to begin the stellar formation process. Cores at the centre of the clump are positioned in a higher density environment. Together with a high gravitational potential, central cores have a higher mass reservoir. Furthermore, the earlier the accretion starts, the more mass is still available. The higher the mass of the core becomes, the larger the gravitational potential and the larger its ‘sphere of influence’ on the rest of the clump, i.e., even more available mass ([Zinnecker & Yorke 2007](#), Sect. 4.2). This scenario predicts high- and low-mass star formation together with higher-mass stars in the centre and lower-mass stars in the outskirts of clusters. A situation as observed, e.g., in Westerlund 1 ([Ward 2017](#), Sect. 1.3.1. and references therein). The accretion in this model is essentially assumed to be spherically symmetric (Bondi-Hoyle-type process) with $\dot{M}_{\text{acc}} \propto M^2$. The IMF function observed in young clusters is reproduced by this model ([Bonnell et al. 2007](#)). However, the predicted accretion rates, $\sim 10^{-5} M_{\odot} \text{ yr}^{-1}$, are too low and would require longer pre-stellar phases for massive stars. In addition, radiative feedback and outflows should be accounted for. While accretion disks are predicted, they are smaller than in the turbulent core model due to dense environment ([Purser 2017](#), Sect. 1.3.2, and references therein).

Lastly, mergers (or coalescence) of multiple lower-mass stars were proposed to overcome radiation pressure and explain the densest OB clusters observed. The radiation pressure problem can be solved through other means (as discussed below). However, the stellar densities required for this scenario to work at extremely high $\sim 10^{6-8} \text{ pc}^{-3}$ ([Zinnecker & Yorke 2007](#), Sect. 4.3) – the upper limit of this value is about five times larger than in Orion ([Maud 2013](#)). It is therefore only relevant for extreme star-forming environments such as young globular clusters. While it may not be the principal formation mechanisms for massive star formation (MSF), it might be relevant for the formation of rapidly rotating high-mass stars which are believed to be progenitors of long-duration gamma-ray bursts ([Zinnecker & Yorke 2007](#)). We refer the reader to the reviews by [McKee & Ostriker \(2007\)](#); [Zinnecker & Yorke \(2007\)](#) for detailed descriptions of these models.

Comparing the evolution to low-mass stars, it is evident that certain processes (even if exact details may differ) such as cloud fragmentation and the formation of outflows (and disks?) are common to the formation of stars of all masses, even if the absolute scales of accretion and outflow rates are orders of magnitudes apart. The main difference lies in the presence of radiation feedback from MYSOs relevant only for high-mass star formation ([Beuther et al. 2025](#)). How can YSOs keep accreting enough material to become massive stars without radiation pressure halting spherical gravitational infall (as assumed in low-mass stars)? And in such little time? Young massive stars spend only $\lesssim 10^5 \text{ yr}$, around $\sim 15\%$ of their entire life, in their pre-stellar phase ([Schulz 2012](#)). Simulations of spherically symmetric accretion showed that for masses higher than $40 M_{\odot}$, radiation pressure stops accretion ([Kuiper et al. 2010](#)). However, observations show that stars with larger than $40 M_{\odot}$ and even $\gtrsim 200 M_{\odot}$ exists. To achieve the high accretion rates necessary to create more massive stars, the infall rate of matter must exceed the ‘outflow’ rate of the radiation. The Eddington luminosity describes the value at which the force exerted by radiation pressure equals the

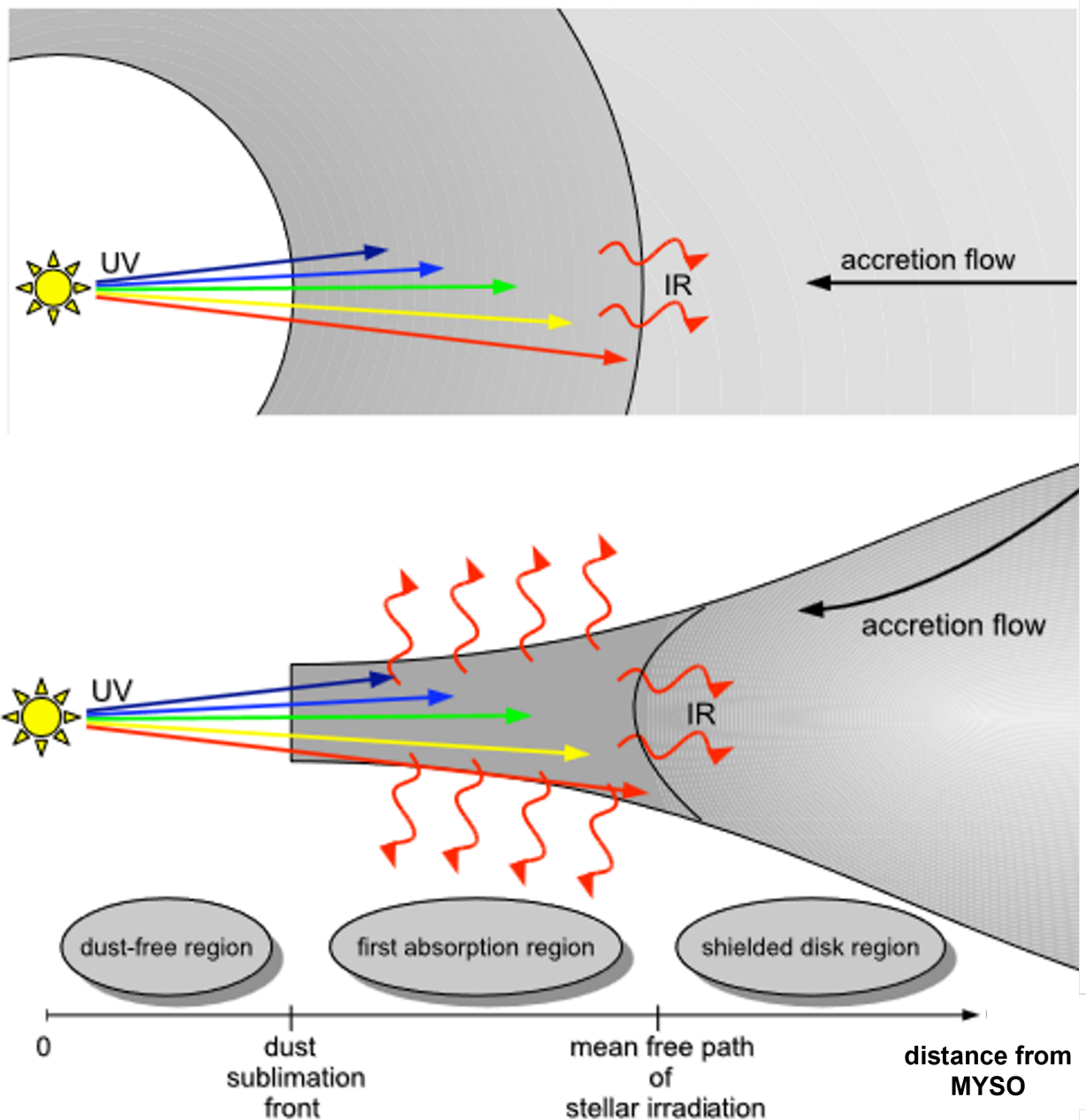


FIGURE 1.2 – **Top:** Radiation pressure influencing the accretion flow assuming spherical symmetry. Close to the MYSO its UV radiation destroys dust, farther away UV radiation is absorbed and re-processed into IR wavelengths. The main pressure is now exerted by this IR radiation. This ‘IR feedback’ eventually stops the accretion. **Bottom:** The same as above but for a axially-symmetric disk geometry. The heated disk in the absorption region is now able to radiate into vertical direction (presumably into a bipolar cavity). The radiation pressure into radial direction is reduced allowing the accretion to proceed. Adapted from [Kuiper et al. \(2010\)](#). The size of the regions is not to scale. They can be different for spherical and disk accretion.

spherical gravitational pull. If the luminosity exceeds this limit, radiation wins over gravity.

$$L_{\text{Edd}} = \frac{4\pi GMc}{\kappa_{\text{dust}}(\nu)}, \quad (1.5)$$

where c is the speed of light, G the gravitational constant, M the current mass of the protostar and $\kappa_{\text{dust}}(\nu)$ the dust opacity dependent on the frequency of the radiation. It describes the fraction of radiation absorbed by the infalling material (Zinnecker & Yorke 2007, see Sect. 3.4.2). As the accreted material originates from the envelope, it mainly consists of dust. The luminosity includes both the intrinsic contribution from the star as well as the accretion luminosity.

For the protostar to continue accreting material, the inequality must remain true: $L < L_{\text{Edd}}$. Either the protostar's luminosity must decrease, the mass and therefore the gravitational acceleration must increase or the dust opacity must decrease with respect to the assumed values in the ISM. As the opacity is frequency-dependent, the latter can, e.g., be achieved by assuming that the protostar is deeply embedded in an envelope. The emitted radiation is then absorbed by the dust in envelope and re-emitted at far-IR wavelengths. The infalling matter effectively sees a less energetic radiation field. Further, varying the intrinsic properties of dust particles such as increasing their size, e.g., by collisions (coagulation) can decrease the opacity. Reducing the overall dust content by destroying the grains is another possibility in decreasing the opacity (Zinnecker & Yorke 2007, Sect. 3.5.1). It has also been suggested that massive stars form in dust-depleted regions when intermediate-size (0.05–0.25 μm) grains are missing (Wolfire & Cassinelli 1987).

If spherical matter infall cannot produce the necessary high masses observed, deviations from the spherically symmetric geometry are necessary. As often in accretion problems, accretion disks are strong candidates. Observations of massive protostellar outflows provide indirect evidence for the presence of such disks. Far- and extreme-UV will effect the disk through photo-evaporation on timescales ($\sim 10^5$ yr) similar to the entire high-mass pre-stellar phase making disks hard to observed (Zinnecker & Yorke 2007, Sect. 3.5.2). Instead, the effects of the ionising radiation are visible as UCH II regions. Outflows effectively dissipate dense material from the envelope in polar directions of the protostellar system. Simulations showed that the radiation pressure affects these less dense regions carved by the outflows more than regions towards the disk plane. The radiation field seen by the infalling material is anisotropic, reduced towards the disk, allowing material to flow from the disk towards the protostar more easily. In addition, due to less material being present in the direction of the outflow, the escaping optical/UV radiation from the protostar are back-scattered less towards the disk, further reducing the impact of radiation pressure. Inevitably, the infalling material will encounter the ionising radiation. Here, the reduced opacity due to destruction or coagulation can allow the material to reach closer to the protostellar surface (Zinnecker & Yorke 2007, Sect. 3.5.2). Figure 1.2 illustrates the main difference between spherical accretion and accretion through a disk in terms of the effect of radiation pressure on the dust within the envelope or disk. Simulations have shown that accretion through a disk can produce stars with masses up to $\sim 140 M_{\odot}$ (Kuiper et al. 2010). For further details, we refer the reader to the reviews by McKee & Ostriker (2007); Zinnecker & Yorke (2007, and references therein).

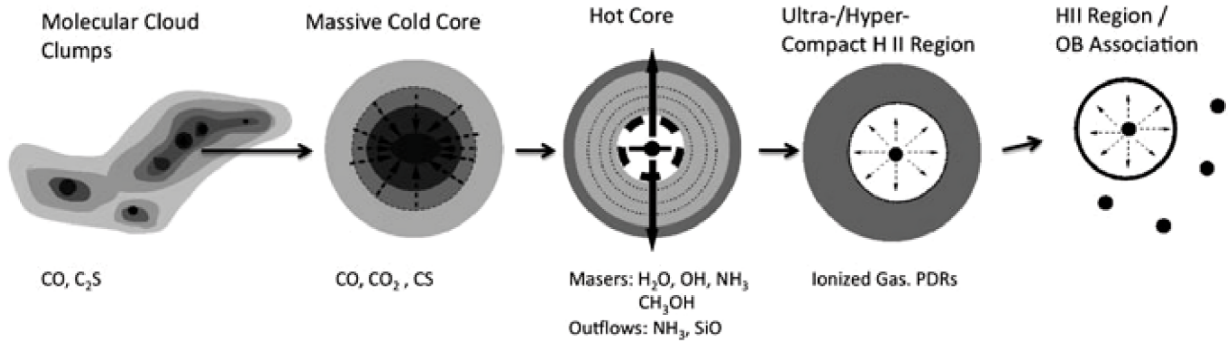


FIGURE 1.3 – High-mass star formation (Schulz 2012). A massive protostar develops from the gravitational collapse of a cold core within a fragmented GMC. The protostar continues to accumulate material. An accretion disk and outflows form while the MYSOs remain embedded in their dusty envelope. The luminosity of the protostellar object increases, ionising its surroundings and an UCH II region is created. Finally, the envelope is dissipated and the entire association or cluster of OB stars becomes visible.

1.4 Observations of Massive Young Stellar Objects

Observationally, massive star formation is divided into four stages (Beuther et al. 2007):

1. High-mass starless cores (HMSCs)
2. High-mass cores with accreting low- or intermediate-mass YSOs which will eventually become MYSOs.
3. Accreting high-mass protostellar objects (HMPOs) or MYSOs, i.e., $M \gtrsim 8 M_{\odot}$. At this stage the ionising radiation from the YSO forms an hyper-compact H II region (HCH II). Infalling gas is hindering the expansion of the HCH II.
4. Massive stars

Only a few HMSCs and massive cores with pre-MYSOs have been observationally confirmed (McKee & Ostriker 2007). Some MYSOs are associated with water (H₂O) and methanol (CH₃OH) maser emission. However, water maser emission has also been detected from low-mass YSOs. So the implications remain unclear. Further, MYSOs are associated predominately with hyper-compact (HC) H II regions (see Tab. 1.1). Once the MYSO evolves into a true massive star, the HCH II region expands and transitions into an ultra-compact (UC) H II region (Beuther et al. 2007). As UCH IIs lie in the transition phase between accreting MYSOs and final stars, they can still be associated with MYSOs towards the end of their accretion phase (Beuther et al. 2007).

Early B-type stars, i.e., spectral types B3V to B0V, with masses between 8 and 16 M_{\odot} possibly evolve similarly to low-mass stars (Zinnecker & Yorke 2007). As we will see later in this work, also MYSOs with B1V-type protostellar objects develop UCH IIs. A simple scaled-up version of low-mass star formation can therefore not be sufficient to explain their formation.

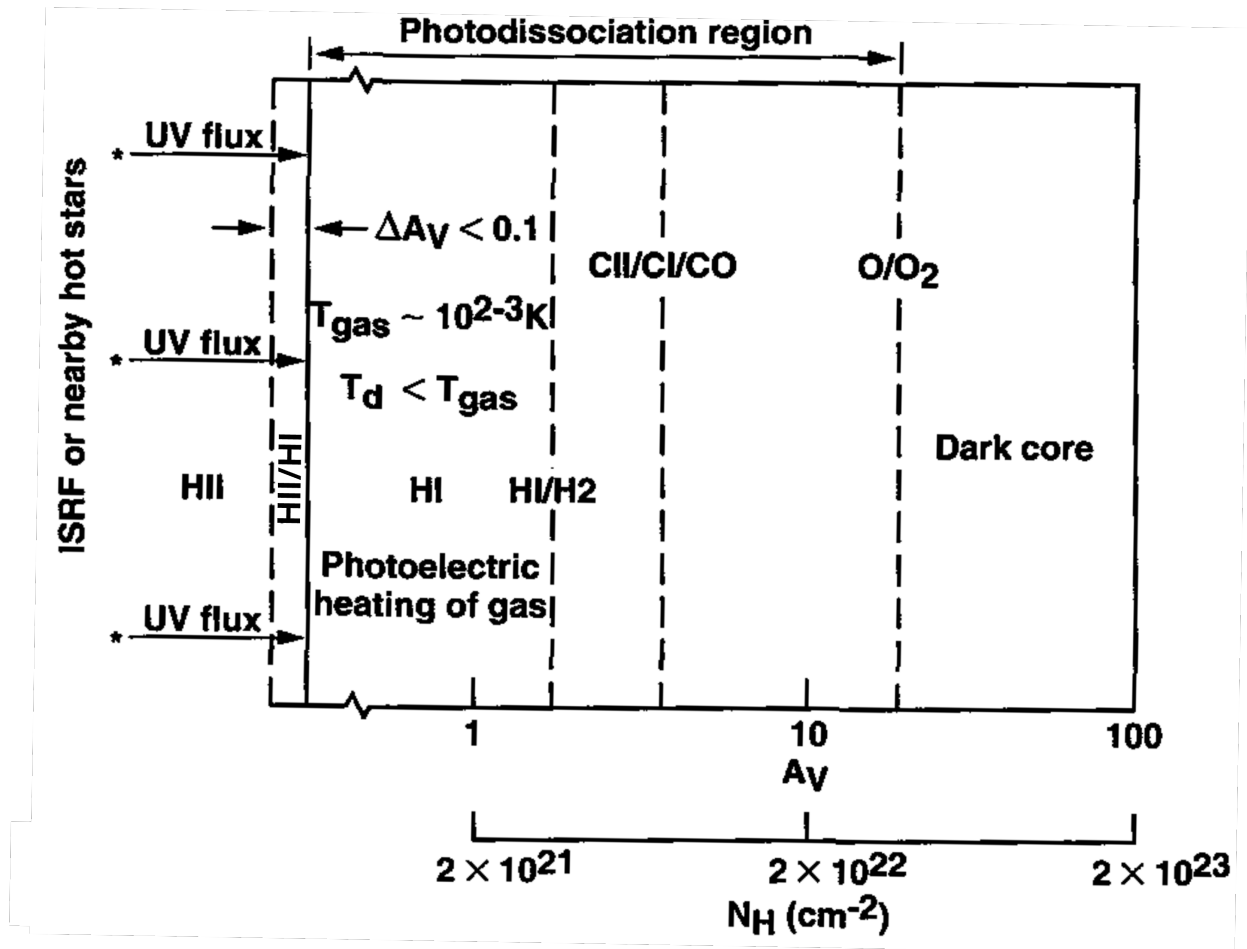


FIGURE 1.4 – Photodissociation region as the transition region between an H II region and the neutral interstellar medium. Adapted from [Hollenbach & Tielens \(1995\)](#).

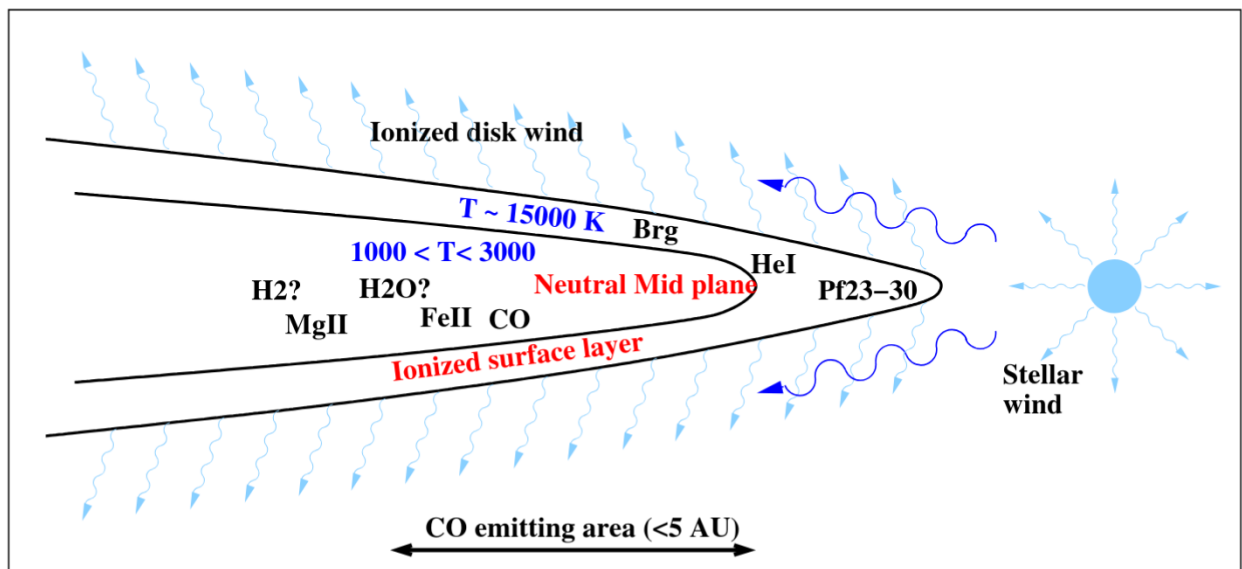


FIGURE 1.5 – Schematic view of the different regions in an accretion disk around a MYSO. Broad H I and He I recombination lines might originate from the ionised layer of the disk or from the disk wind. CO, ices, fluorescent Fe II may instead originate from a denser, colder area with the disk (see Sect. 9.6). Adapted from [Bik et al. \(2005\)](#).

1.4.1 Radiative feedback – compact H II regions and disk winds

The peak energy of the blackbody radiation from hot OB stars – and MYSO – lies around the ionisation potential of Hydrogen in the range UV wavelengths. The flux of ionising photons \dot{N}_{ionise} is between $\sim 10^{47-49} \text{ s}^{-1}$ for main-sequence stars of type B1 to O9 (Tielens 2005). The size of the photoionised (H II) region around the star is given by the equilibrium of the rate of ionisation and recombination. In the simplest case when the attenuation of radiation is neglected inside a medium of constant density n_e , the size is given by the Stroemgren radius

$$R_S = \left(\frac{3\dot{N}_{\text{ionise}}}{4\pi\alpha(T_e)n_e^2} \right)^{-1/3}, \quad (1.6)$$

where $\alpha(T_e)$ is the recombination rate coefficient for Hydrogen. For a discussion on the effects of dust and a density gradient in the ISM see, e.g., Williams (2021, Sect. 6.2.2–6.2.3). The edge of an H II region can be described by an ionisation front where the degree of ionisation changes almost abruptly. The thickness of the ionisation front is given by the mean free path of the photons and is significantly smaller than the size of the H II region (see Tielens 2005, Sect. 7.2.1). Within the front the density is higher compared to the rest of the ionised region and this allows heavier elements to be collisionally ionised and produce forbidden lines in spectra.

Photo-dissociation regions (PDRs) form at the interface between H II regions and the molecular cloud. Far-UV (6–13.6 eV) interact with the medium by ionising atoms, dissociating molecules and heating the gas. The structure of a PDR is shown in figure 1.4. Photons capable of ionising Hydrogen (>13.6 eV) are absorbed in thin transitions layer, the ionisation front. The ionisation energy of Oxygen (13.62 eV) is nearly identical to that of Hydrogen. Hence, ionised Hydrogen and Oxygen are expected to be found in the same regions. A similar situation is found for Nitrogen (N; $E_{\text{I} \rightarrow \text{II}} \sim 14.5 \text{ eV}$). Helium on the other hand requires almost twice the energy to be ionised (24.6 eV) and is thus mostly found in neutral form where Hydrogen is ionised (Dyson & Williams 1980). Photons with energies less than 13.6 eV dissociate H_2 , so we find mostly neutral Hydrogen H I adjacent to the ionisation front. The dissociation energy of H_2 (11.18 eV), of carbon monoxide (CO; 11.11 eV) and the first ionisation potential of carbon (11.26 eV) are similar (Ryden & Pogge 2021, Sect. 7.4). Therefore, a region where C I, C II, CO, H_2 and H I co-exist. Once the H_2 -destroying flux is reduced, the composition is dominated by H_2 . Even farther away from the ionisation front, molecular oxygen can form (Tielens 2005; Ryden & Pogge 2021).

MYSO create hyper-compact (HC) and ultra-compact (UC) H II regions by ionising their surrounding envelope – smaller and denser than those around main-sequence stars or even OB associations (see Tab. 1.1). HC H IIs are thought to be the precursors of UC H IIs. They have been discovered as a subgroup of UC H IIs, being about an order of magnitude smaller and two magnitudes denser (see Tab. 1.1). Apart from the size and density, HC H IIs show broad radio recombination lines (transitions with high quantum numbers $n \gtrsim 30$; see Sect. 4; Lequeux 2005) with $\Delta v \sim 40\text{--}50 \text{ km s}^{-1}$ or even $>100 \text{ km s}^{-1}$ (Hoare et al. 2007). In comparison, UC H IIs line widths are smaller on the order of $30\text{--}40 \text{ km s}^{-1}$ (Hoare et al. 2007). The broadening may be due to pressure broadening in these high-density environments or due to gas motion either due to accretion, outflows or rotation (Hoare et al. 2007). High

spatial and spectral resolution is required to distinguish the mechanisms. Further differences between UCH IIs and HCH IIs in terms of their radio spectra are discussed in [Hoare et al. \(2007, Sect. 3.1\)](#). The properties of HCH IIs described above suggest that they must be associated with earlier phases of high-mass star formation. Possibly, after the hot molecular core phase when radio continuum emission becomes observable and the mass and temperature of the MYSO has increased such that photoionising Lyman continuum radiation will be emitted ([Hoare et al. 2007](#)). The HCH II might be gravitationally trapped within the protostellar system at first while the accretion proceeds through the HCH II region. As the MYSO grows in mass and the flux of ionising photons increases, the H II region grows and expands nearly spherically except in the narrow range around the disk ([Hoare et al. 2007, Sect. 3.2.2.](#) and references therein).

A particular class of MYSOs with strong ionised stellar winds are luminous with $L_{\text{bol}} > 10^4 L_{\odot}$, have collimated outflows and are probably accreting although likely already fusing Hydrogen. These wind sources may be MYSO surrounded by an accretion disk. The ionised wind would originate due to the UV radiation from MYSO photo-evaporating the material at the surface of the disk (see [Fig. 1.5](#); [Bik et al. 2005](#); [Hoare et al. 2007, Sect. 3.2.3](#)). The inner regions of the disk remain molecular by self-shielding. Molecular Hydrogen H_2 at the boundary to the hotter region absorbs UV photons ($E = 11.2\text{--}13.6\text{ eV}$) preventing H_2 in the centre regions to be dissociated ([Ryden & Pogge 2021](#)). Wind sources are weaker in radio wavelengths than HCH IIs. However, similar to HCH IIs, the recombination lines *in the IR* are very broad with lines widths $\Delta v \gtrsim 100\text{ km s}^{-1}$. The presence of a rotating disk is further supported by HI recombination lines showing double peak line profiles (e.g., [Sim et al. 2005](#)). The main difference between MYSO with a disk wind and those with a HCH II lies in the origin of the observed ionised material: for wind sources the material comes from the disk and is part of the protostellar system. For HCH IIs it is the circumstellar matter that is ionised ([Hoare et al. 2007](#)).

1.4.2 Outflows

Accreting objects with magnetic fields and rotation exhibit bipolar outflows ([Bally 2016](#)). Such systems range from YSOs and symbiotic stars to accreting neutron stars and active galactic nuclei ([Bally 2016](#)). Low-mass YSO outflows and jets are quite ubiquitously found in our proximity as well as in prominent galactic and extra-galactic star-forming regions such as the Orion Nebula. Hundreds of outflows originating from YSOs were found within 1 kpc of the Sun ([Bally 2016](#)). Often, they are associated with Herbig-Haro objects – small nebular regions with optical emission lines tracing supersonic shock waves ([Bally 2016](#)). Their velocities span over a range of magnitudes from a few km s^{-1} to $\gtrsim 10^3\text{ km s}^{-1}$ ([Bally 2016](#)). Outflows are observed with various degrees of collimation from highly collimated parsec-scale jets to wide-angle disk winds. However, the detailed processes of gas flow from the accretion disk towards the protostar remain unclear thus far, even for low-mass stars.

Jets and outflows from MYSOs are less well studied than their low-mass counterparts as they are rare and located at larger distances. In addition, they remain obscured during a large part of their pre-stellar life and can only be identified with molecules in mm and masers in radio observations during their main-accretion phases. Despite the radiative feedback from the MYSOs themselves, outflows are observed. The expansion of photoionised regions

around MYSOs might even power outflows even further (Bally 2016). The morphologies of low- and high-mass outflows seem to be similar (Bally 2016). Jets and shells tracing low- and high-velocity shocks have been identified from MYSOs (Bally 2016, and references therein). The energetics, on the other hand, differ. MYSO outflows are faster and more powerful, although with spatial scales similar to those of lower-mass YSOs (on (sub-) parsec scales, 0.1–3 pc Ward 2017, Sect. 1.3.4). Physical reasons might include higher density environments for high-mass star-formation, the short pre-stellar phases or destructive influences from other (M)YSOs in their proximity. Due to the observational difficulties of MYSOs, selection effects and uncertainties in distance estimates and higher extinction cannot be excluded (Bally 2016).

In general, protostellar outflows (both from low-mass YSOs, MYSOs or even groups of YSOs) become observable due to interactions with the surrounding ISM. They are visible over a broad range of wavelengths from radio to UV. Emission lines can be utilised to derive the nature of their excitation and the properties of the emitting gas such as density and temperature as well as the radial velocities and proper motions of the outflowing material. The tools relevant for this work are discussed in section 9.8. Outflows and jets can have a variety of different properties. The outflowing gas can either be mostly molecular or ionised and originates from the protostellar system. In contrast, in HCH IIs and UCH IIs the radiation ionise the material in the surroundings of the MYSO. In particular, many MYSOs have very broad IR recombination lines with widths $\Delta v \sim 100\text{--}500 \text{ km s}^{-1}$ which might indicate dense, ionised winds (Bally 2016, Sect. 3.3).

Observations of molecular outflows from MYSOs can be used to distinguish the different formation scenarios of massive stars (see Sect. 1.3.2). In the turbulent core model, collimated outflows similar to those observed in low-mass YSOs can be present as the formation is essentially a scaled-up version of low-mass star-formation with outflows being connected to accretion. The conditions of the competitive accretion model are unfavourable for such outflows (Beuther & Shepherd 2005). Observations of early B-type MYSOs which can also already harbour HCH IIs are supportive of the similarities to low-mass outflows (Beuther & Shepherd 2005). An evolutionary scenario has been proposed for such B-type MYSOs under the assumption of the turbulent core model where the degree of collimation of the observed outflow changes with its evolution (see Fig. 1.6). In the early MYSO phase, accretion proceeds through a disk and collimated outflows are formed. As the MYSO produces an HCH II, an additional wider-angle wind can be observed. As the disk still exists while the HCH II forms, both the collimated jet and the wide outflow can co-exist. As the ionising radiation increases and the HCH II expands into a UCH II, the stellar wind dominates the outflow.

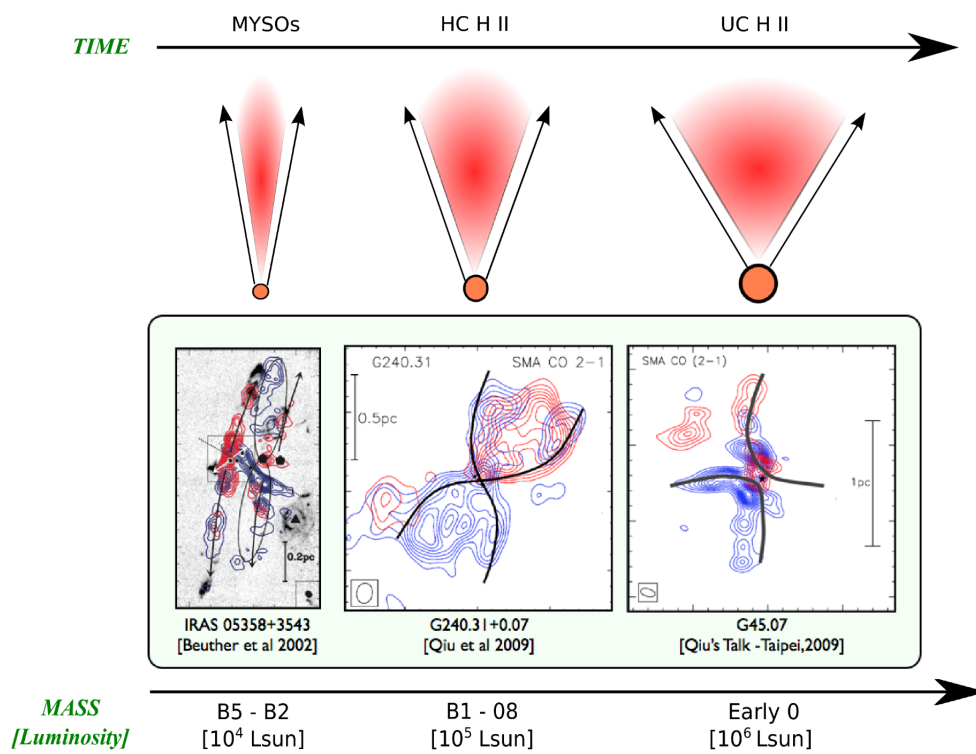


FIGURE 1.6 – Evolutionary sequence of MYSO outflows. The angle of collimation decreases the more the YSO evolves. Adopted from (Vaidya 2011) after (Beuther & Shepherd 2005).

2 Photometry

2.1 Luminosity, flux density and magnitude

The (*bolometric*) *luminosity* L is an intrinsic property of an astronomical source describing its total emitted radiation power across all wavelength or frequency bands. The *monochromatic luminosity* L_λ or L_ν refers to the total power in a certain spectral interval measured either in wavelength or frequency. The luminosity L is not a directly accessible parameter in experimental measurements. Instead, the radiation power received by an observer per unit wavelength or frequency and per unit area is the *monochromatic (or specific) flux density* F_λ or F_ν . It is noted that often this quantity is shortly referred to as flux.

The measured flux density depends both on the intrinsic luminosity of the source as well as on the distance d to the observer. Assuming that no radiation is absorbed and the velocity of the source is far less than the speed of light such that relativistic effects can be neglected, flux density and luminosity are related through the so-called *inverse square law*:

$$F = \frac{L}{4\pi d^2}. \quad (2.1)$$

To convert between a flux density at a specific wavelength F_λ to a density at a given frequency F_ν , the inverse relation $\nu = c/\lambda$ between wavelength and frequency has to be taken into account. The amount of frequency units $d\nu$ corresponding to one unit in wavelength space $d\lambda$ changes across the electromagnetic spectrum according to $d\nu = -c/\lambda^2 \cdot d\lambda$. The negative sign shows that the frequency unit decreases with increasing wavelength. In addition, the following equality holds: $\lambda F_\lambda = \nu F_\nu$. When the flux density of an astronomical source is discussed over a large spectral range, $\log \lambda F_\lambda$ ($\log \nu F_\nu$) is often plotted against $\log \lambda$ ($\log \nu$) to emphasise in which wavelength (frequency) range the source radiates the most power per decade (Glass 1999).

Historically, instead of flux densities, so-called *apparent magnitudes* have been used to compare the brightness of stars – later also of any astronomical object. The Greek astronomer Hipparchus was the first to use (bolometric) magnitudes m to describe the apparent brightness of stars. In his definition the brightest stars have magnitude 1 and the faintest stars magnitude 6. Important to note is that a higher apparent magnitude refers to a fainter-appearing star. In the nineteenth century, it had been noticed that the human eye responds to the difference in brightness of two objects not in a linear but a logarithmic way. Nowadays, the magnitude scale is defined such that a difference of 5 magnitudes of two objects 1 and 2 translates to a brightness ratio of 100:

$$\frac{F_2}{F_1} = 100^{(m_1 - m_2)/5}. \quad (2.2)$$

In a similar way, the total bolometric luminosity can be translated to a corresponding (bolometric) magnitude, referred to as *absolute bolometric magnitude* M_{bol} . As the flux density is measurable, but distance and therefore luminosity are often not easily accessible, alternatively, the absolute magnitude M can be defined through the apparent magnitude and imaging the object located at a distance of 10 pc. Using the inverse square law (2.1),

equation (2.2) can be written as:

$$\frac{F_{10}}{F} = 100^{(m-M)/5} = \left(\frac{d}{10 \text{ pc}} \right). \quad (2.3)$$

This definition is useful to compare the brightness of two objects independent of their distance even if their intrinsic luminosity is unknown. By isolating the quantity $m - M$, the connection between an object's absolute, apparent magnitudes and its distance d (in parsec) is illustrated by the *distance modulus*:

$$m_\lambda - M_\lambda = 5 \log_{10} d [\text{pc}] - 5. \quad (2.4)$$

2.2 Interstellar extinction

Dust in the interstellar medium scatters and absorbs radiation across the entire wavelength spectrum and re-emits radiation at longer (infrared) wavelengths. Depending on the amount of dust in the line-of-sight between observer and observed source and the wavelength of the radiation, the registered flux density and magnitude may be additionally decreased with respect to the inverse square law (2.1). This effect of attenuation by dust is referred to as *interstellar extinction* A_λ . It is measured in magnitudes and defined as follows:

$$A_\lambda = 2.5 \log_{10} \frac{F_\lambda^0}{F_\lambda}, \quad (2.5)$$

where F_λ^0 is the flux according to the inverse square law (2.1) and F_λ the observed flux density.

Trumpler (1930) proved the presence of absorbing material between stars for the first time. While studying the distribution of open clusters he realised that the distance modulus (2.4) has to be adjusted:

$$m_\lambda - M_\lambda = 5 \log_{10} d [\text{pc}] - 5 + A_\lambda. \quad (2.6)$$

The exact dependence of A_λ with wavelength (extinction curve or reddening law) is determined by the dust composition and size distribution. Based on Cardelli et al. (1989), the extinction is given relative to a reference wavelength λ_{ref} : $A_\lambda/A_{\lambda_{\text{ref}}}$. Often, λ_{ref} corresponds to the optical visual band $V \sim 4700\text{--}7000 \text{ \AA}$ of the Johnson-Morgan photometric system (Johnson & Morgan 1953; Johnson 1955). Instead of using the absolute interstellar extinction A_λ as defined above, some authors use the *selective extinction* $E_{\lambda_1-\lambda_2} = A_{\lambda_1} - A_{\lambda_2}$ instead. Then, the relative selective extinction is measured with respect to $\lambda_1 = B \sim 3600\text{--}5600 \text{ \AA}$ and $\lambda_2 = V$ Johnson bands (Bessell 2005):

$$\frac{E_{\lambda-V}}{E_{V-B}} = \frac{A_\lambda}{E_{V-B}} - \frac{A_V}{E_{V-B}} = R_V \left(\frac{A_\lambda}{A_V} - 1 \right), \quad (2.7)$$

where the first term is defined as the extinction curve $k_\lambda = A_\lambda/E_{V-B}$ and the second term $R_V = A_V/E_{V-B}$ the so-called *total to selective extinction ratio* (see below). Extinction curves, A_λ/A_V or $E_{\lambda-V}/E_{V-B}$ are empirically derived through parametric fits to photometric data of stars (see, e.g., Gordon et al. 2003).

Interstellar extinction is highly dependent on the line-of-sight as the amount of dust

particles varies depending on the direction. Extinction can be so high that certain regions cannot be observed in optical or UV wavelengths such as the Galactic Centre (Karttunen et al. 2007). Comparing extinction curves for different directions one notices that it is the slope of the function which predominantly changes. One defines the ratio R between the absolute interstellar extinction A_{λ_2} as defined above and the selective extinction $E_{\lambda_1-\lambda_2}$:

$$R_{\lambda_2} = \frac{A_{\lambda_2}}{E_{\lambda_1-\lambda_2}}. \quad (2.8)$$

Again, most often for normalisation $R_V = A_V/E_{B-V}$. R_V can provide an estimation on the average dust grain size (see Draine 2011, Ch. 22).

The most prominent observed phenomenon due to interstellar extinction concerns the *reddening* of starlight. The extinction curve is approximately inversely proportional to wavelength. It decreases towards longer, infrared (IR) wavelengths. Therefore, more distant stars appear redder than they should according to their spectral class as more blue and UV radiation is absorbed or scattered away from the emitted radiation along the line-of-sight.

Fahrion & De Marchi (2023) extend the extinction law for the 30 Doradus star-forming regions into the near-infrared up to $4.7 \mu\text{m}$ using the JWST imaging dataset of 30 Doradus (see Fig. 9.16). They find that the slope of the extinction curves in the LMC and the MW agrees at wavelengths $>1 \mu\text{m}$, but at shorter wavelengths is lower for the LMC compared to the MW (Fahrion & De Marchi 2023, Fig. 5). They conclude that the major difference between LMC and MW dust grains is the size distribution with larger grains in the LMC.

3 Spectroscopy

Astronomical spectroscopy studies the radiation of objects at the highest resolution in wavelength (or frequency) space. Using spectrographs, i.e., instruments that can decompose the light they detect as a function of wavelength, the most detailed information about an astronomical source can be obtained. To interpret a spectrum of an astrophysical source, detailed knowledge of atomic and molecular physics is required which in turn is based on quantum theories (see Sect. 4). Therefore, laboratory measurements on the intrinsic properties of atomic and molecular spectra are crucial. The structure of the energy levels, the precise wavelength of every transition and their strength are necessary to derive statements on the nature of an astronomical object and its surroundings. Only then can the following information be extracted for any observed line in a spectrum (after [Tennyson 2005](#)).

1. The elemental or molecular *composition* of a source can be deduced by identifying the atom, ion or molecule which produces a transition at the observed wavelength.
2. Knowing the strength of a transition, the *abundance* of an element can be determined as it is directly related to the number of atoms, ions or molecules undergoing the observed transition.
3. The motion of atoms, ions and molecules with respect to the observer in radial direction, referred to as the *radial velocity* v_{rad} , leads to the Doppler shift $\Delta\lambda$:

$$\frac{v_{\text{rad}}}{c} = \frac{\Delta\lambda}{\lambda} = \frac{\lambda_{\text{obs}} - \lambda_{\text{lab}}}{\lambda_{\text{lab}}}, \quad (3.1)$$

valid for the radial velocity of the source significantly less than the speed of light $v_{\text{rad}} \ll c$ which is usually the case. The central observed wavelength of a line is shifted compared to the rest wavelength determined in the laboratory. If an observed source (or parts of it) are moving away from the observer, the line is shifted towards longer wavelengths, it is said to be *red-shifted*. Similarly, a *blue-shifted* transition points to the source moving towards the observer.

4. Identifying the energy levels giving rise to the observed transition indicates the degree of excitation of an element. This can be utilised to derive physical conditions of the gas such as the *temperature* T or *density* n . In addition, T and n can be estimated by investigating the line profile and in particular its broadening. Collisions of atoms cause pressure broadening, which is more significant the higher the number of collisions, and, therefore, the density. Doppler broadening occurs due to the thermal motions of atoms. The higher the temperature, the higher the velocity, the more a line is ‘red-shifted’. The lower T , the lower the velocity, and the higher is the ‘blue-shifted’ component of the observed line. To separate the effects of pressure and Doppler broadening, very high-resolution spectra are required and is not possible with the spectrographs on JWST.
5. Electrons in atoms or molecules can interact with an external magnetic field and cause energy levels (with angular momentum > 0) to split into multiple components (see, e.g., the Zeeman effect). The separation between the resulting energy states is directly

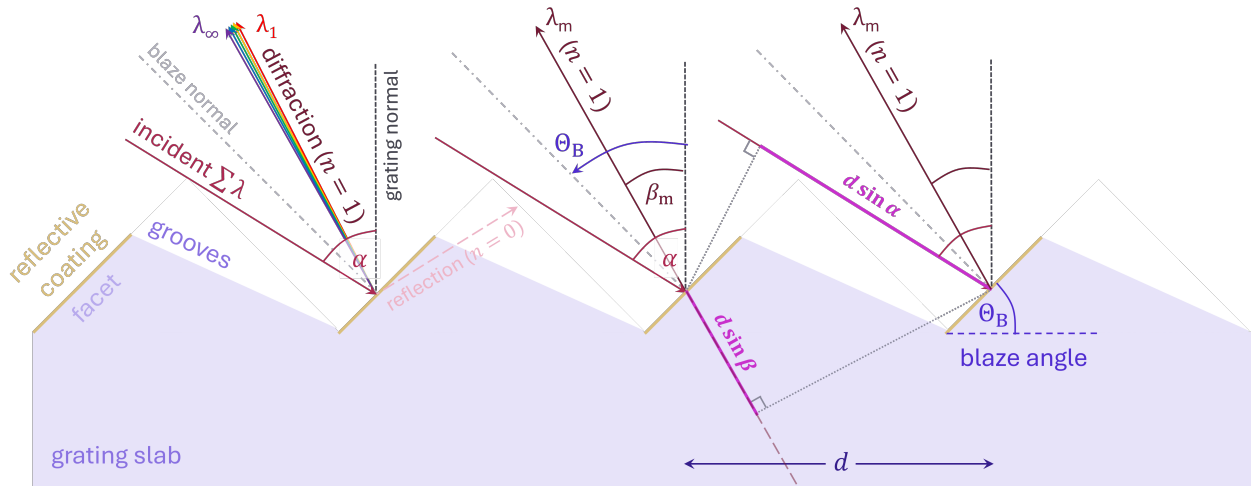


FIGURE 3.1 – Schematic crosssection through a blazed reflection grating. The geometry follows the specifications of the high-resolution gratings in MIRI (Wells et al. 2015). The left side of the graphic illustrates the diffraction of incident polychromatic radiation into several orders as well as wavelengths. The right part shows the path difference of wavefronts diffracted at different facets.

proportional to the magnetic field strength. Observing such splittings in a spectrum allows the estimation of the *local magnetic field*.

3.1 Basic principles of astronomical spectrographs

Although JWST’s primary mirror is the largest among current space telescopes, apertures of current ground-based telescopes are around 10 m. Next-generation telescopes with apertures up to three times larger $D \sim 30$ m are planned. Current ground-based IR spectrographs achieve spectral resolutions of $R \gtrsim 10^5$. Nevertheless, space-based IR – as optical – instruments have the big advantage of not being contaminated by telluric absorption and emission lines originating from Earth’s atmosphere. Toward the far-infrared (FIR), above $40 \mu\text{m}$, the atmosphere becomes particularly opaque, making ground-based FIR observations impossible. In addition, lower operating temperatures required in the IR can be achieved in space than on ground, increasing the sensitivity (Appenzeller 2013).

Astronomical spectrometers work as follows: light focused onto the telescope’s focal plane enters the spectrometer through a slit and is collimated. The resulting parallel light beam (described mathematically with plane waves) is split into its various wavelength components by a disperser. The dispersed monochromatic waves travel in different directions. Those entering the camera are recorded on different positions of the detector array. Three different dispersing elements exist: gratings, prisms and grisms. The MIRI/MRS and NIRSpec spectrometers all use blazed reflection gratings as their dispersers. They are discussed in more detail below. However, the basic principles behind measuring spectra can be applied to any disperser. For further information on the different gratings, see, e.g., Appenzeller (2013); Eversberg & Vollmann (2015); Palmer & Loewen (2005); McLean (2008). The optical design and the spectrometers of MIRI/MRS and NIRSpec and described in Wells et al. (2015) and Jakobsen et al. (2022), respectively.

Cutting narrow grooves into a plane slab of, e.g., aluminium, and coating the resulting

surface with a thin metal layer (gold for IR radiation, [McLean 2008](#)) produces blazed reflection gratings. The *blaze angle* Θ_B is defined as the angle between blaze and grating normals (see [Fig. 3.1](#)). Electromagnetic waves are reflected and diffracted at the narrow grooves whose size is comparable to the wavelength of incident light. Due to diffraction, the deflected waves propagate into different directions around the reflection direction. Waves deflected at one groove interfere with diffracted waves at another groove. The resulting intensity pattern can be derived as a product of incident light intensity, the diffraction pattern of a single groove and the interference function of all grooves (see, e.g., [Eversberg & Vollmann 2015](#), Ch. 2.5.1). If the diffracted wavefronts are in phase, constructive interference occurs and gives rise to maxima in the intensity distribution of the diffracted light. Maxima occur when the path difference Δl of waves between neighbouring grooves is an integer n multiple of the wavelength. The integer values n are referred to as *orders of diffraction*. Since light waves can reach the grooves at various incident angles α and be deflected in a range of diffraction angles β , the path difference depends on these two angles. Equation (3.2) is known as the *grating equation* and states the conditions for constructive interference. Note that in the equation below we assume that the incident light is perpendicular to the groove surface which is usually the case in practise.

$$\Delta l = n\lambda = d(\sin \alpha + \sin \beta), \quad (3.2)$$

where d is the distance between two adjacent grooves (see [Fig. 3.1](#)). Its inverse d^{-1} is called the *grating constant* G and gives the number of grooves per millimetre. In general, also the refractive indices of the reflective coating material as well as the medium in which the grating operates have to be considered as they determine its reflectivity.

The zeroth order ($n = 0 \iff \alpha = -\beta$) represents reflection without diffraction. It is not useful for spectroscopy as β is independent on wavelength. The different wavelength components of incident light cannot be separated. For any other diffraction orders, waves with different wavelengths are diffracted at different angles. A spectrum is produced. It is noted that incident and diffraction angles in equation (3.2) are defined as positive when the diffracted rays are on the left of the grating normal, and as negative when on the right.

For any pair of incident α and diffraction angle β and a certain Grating constant, the grating equation (3.2) can be satisfied for two wavelengths λ and λ' of successive orders n and $(n + 1)$: $n\lambda = (n + 1)\lambda'$. λ and λ' are diffracted into the same direction β . Order sorting filters or secondary dispersing elements must be utilised to prevent overlapping of different orders and the contamination of spectra (see [McLean 2008](#)). For more information on how this problem is handled for MIRI/MRS and NIRSpec, see, e.g., [Wells et al. \(2015\)](#) and [Jakobsen et al. \(2022\)](#), respectively.

In simple slit spectrometers, the intensity of the 0th order is the highest. The advantage of blazed reflection gratings lies in the possibility of adjusting the angle of the reflecting facets with respect to the grating plane such that the point of maximum intensity is shifted to a different order, usually the first ([Appenzeller 2013](#)). The maximum efficiency of the grating is achieved in the direction of reflection on the facet if no diffraction would occur. Incident and diffraction angles are related to the blaze angle by $(\alpha + \beta) = 2\Theta_B$. For MIRI/MRS gratings with $G \sim 50\text{--}270\text{ mm}^{-1}$, the blaze angle is 45° . For the high-resolution gratings ($G \sim 90\text{--}250\text{ mm}^{-1}$) on NIRSpec used for observation of S7A, $\Theta_B \sim 10\text{ deg}$.

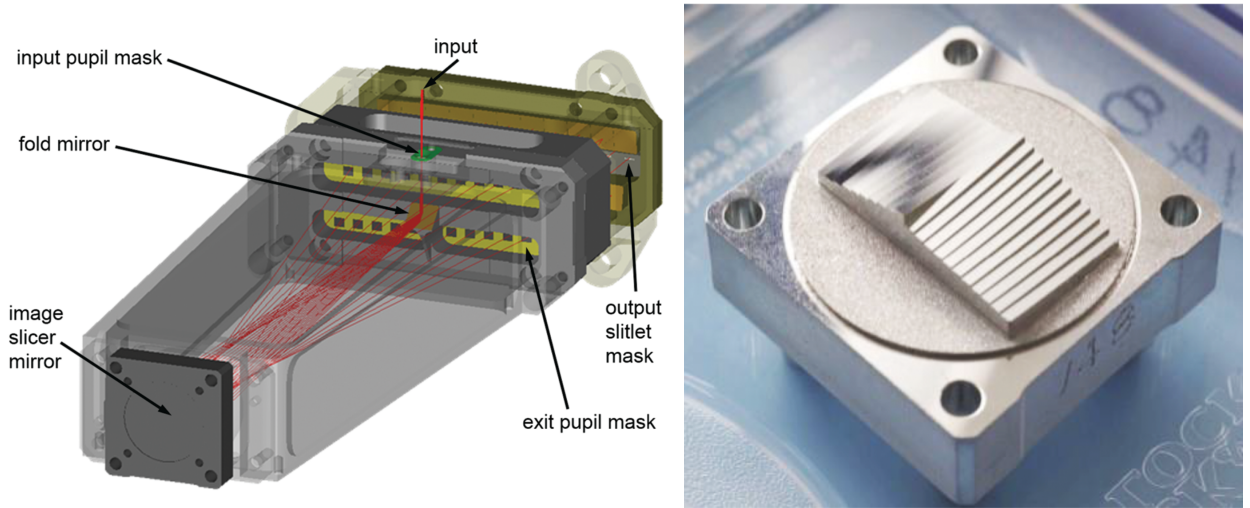


FIGURE 3.2 – Schematic of a MIRI IFU (left) and an image of the image slicer mirror (right). Figures are adapted from Wells et al. (2015).

The ability to separate two maxima of different wavelengths within a single order defines the resolution of the grating. The spectral resolution of a spectrograph is referred to as the resolving power R and is defined through the following ratio:

$$R = \frac{\lambda}{\Delta\lambda}, \quad (3.3)$$

where $\Delta\lambda$ is the smallest wavelength distance that can be resolved. Using the Doppler formula (3.1), the corresponding resolution can be found in the velocity space as $\Delta v = c/R$. It is useful for determining the velocity structure of astronomical objects and can, e.g., identify outflows. $\Delta\lambda$ can be defined through the Rayleigh criterion (6.1). However, instrumental effects will result in the broadening of a spectral line. Measurement of the FWHM of the PSF of a monochromatic line is a better estimate of $\Delta\lambda$ (Appenzeller 2013; Palmer & Loewen 2005). In practice, $\Delta\lambda$ is limited by the intrinsic spectral width of a line due to, e.g., Doppler, pressure broadening or the lifetime of an excited state.

3.2 Integral field spectroscopy

Conventional slit spectrographs as described in the previous section can only record source spectra *along the slit*, meaning in the direction of its orientation. To obtain complete spectroscopic information from an extended object over the entire foV of the telescope, several spectra with shifted slit positions have to be taken. To avoid such sequential observing procedures, integral field spectroscopy was developed. An image is rearranged by the integral field unit (IFU) to obtain spectral and two-dimensional spatial information in one observation. The foV of the instrument is sliced into multiple narrower parts by, e.g., an image slicing mirror and directed into different directions. A second mirror in the focal plane rearranges the image slices into a single strip matching the spectrograph entrance slit. In this case, Further post-processing allows the recorded spectra to be rearranged into 2D images for each wavelength. Combining all the 2D images yields a 3D data cube. Each spatial pixel of the data cube now contains a spectrum. Figure 3.2 illustrates the IFU as adopted for

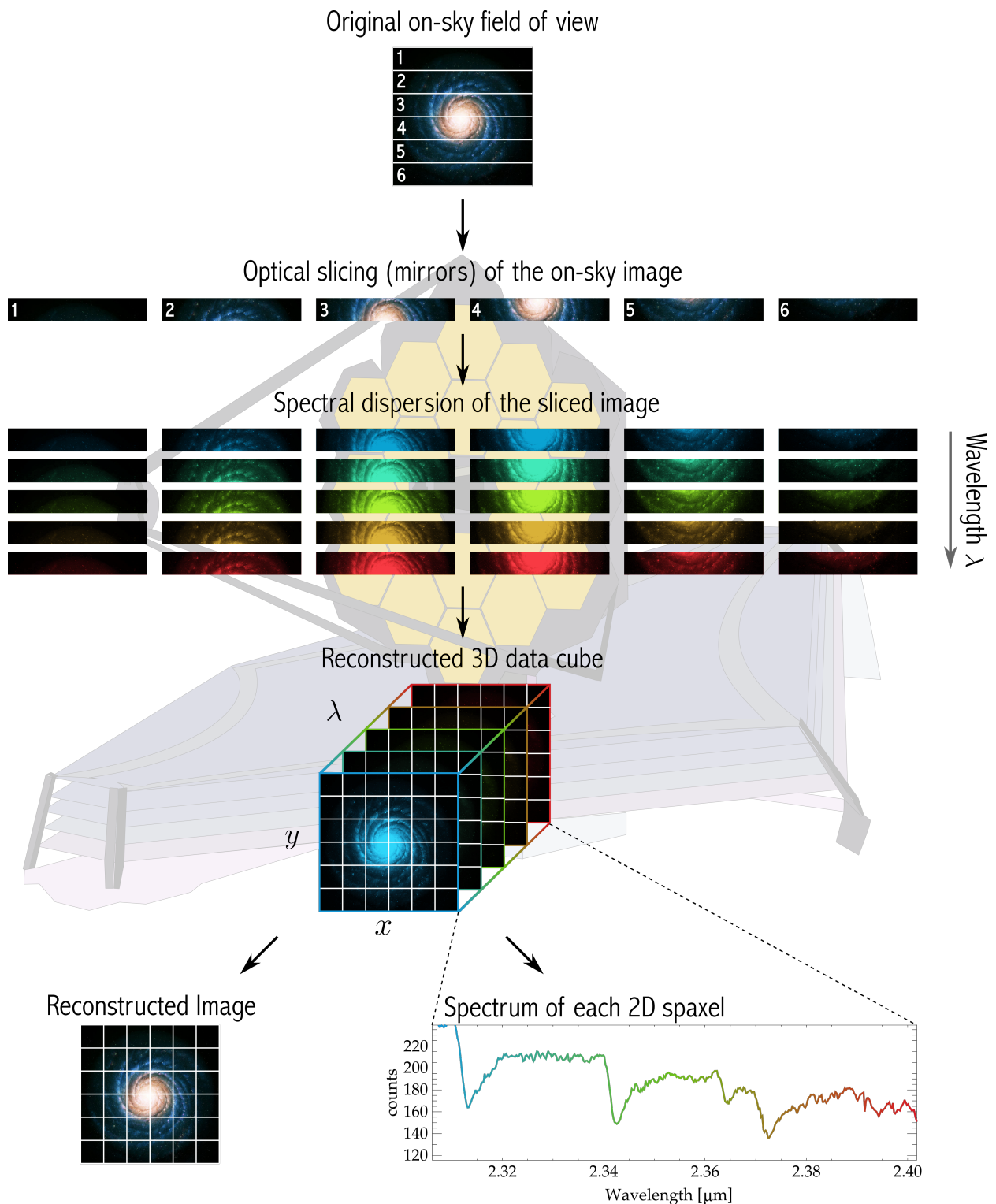


FIGURE 3.3 – The basic principle of an image slicing integral field spectrograph as adapted for NIRSpec and MIRI/MRS (Credit: [JWST Integral Field Spectroscopy documentation](#)).

MIRI/MRS. Figure 3.3 illustrates the principle of IFS. It is noted that apart from image slicers also other kinds of instruments exist to divide images into smaller segments. For further information on other types of IFUs see [McLean \(2008\)](#); [Appenzeller \(2013\)](#). All IFUs on JWST use Image Slicers. For details see the respective documentations for [NIRSpec](#) and [MIRI/MRS](#).

4 Origin of spectral lines

The following sections describe how emission (absorption) lines in spectra of astronomical objects are produced. A large part is based on quantum mechanical concepts and can be found in extensive detail in any such textbook. The connection to astrophysics can be found, e.g., in [Glass \(1999\)](#). Firstly, implications of the Schroedinger equation for the energy structure of hydrogen-like atoms are discussed (Sect. 4.1). Later chapters focus on more complex atoms and molecules (Sect. 4.3 and 4.5). Further, transition probabilities and different types of transitions relevant for the lines observed in the analysed MYSO spectrum (see Sect. 4.4) are discussed. Lastly, the energy structure of molecular Hydrogen H_2 is summarised.

4.1 Schroedinger equation and quantisation of energy levels

The non-relativistic time-independent Schroedinger equation can be used to determine the evolution of the wave function $\psi(\vec{r})$ of a quantum mechanical system. Consider a hydrogen-like system with a nucleus of charge $+Ze$ and a single electron. Note that the following considerations can be applied to atoms as well as ions, the term hydrogen-like simply limits the number of electrons to 1. For example, He^+ , C^{5+} , N^{6+} or O^{7+} can be described in the same matter as Hydrogen. The total energy of the system is composed of the kinetic energy of the electron, the first term in (4.1), and the potential energy – in this case – given by the Coulomb potential between nucleus and electron (second term).

$$\left[\frac{-\hbar^2}{2\mu} \nabla^2 - \frac{Ze^2}{4\pi\epsilon_0 r} \right] \psi(\vec{r}) = E\psi(\vec{r}), \quad (4.1)$$

where $\hbar = h/2\pi$ is the reduced Planck constant, ϵ_0 the electrical permittivity constant in vacuum, r the length of the electron position vector which corresponds to the distance of nucleus and electron. Finally, $\mu = (m_e M)/(m_e + M)$ is the reduced mass of the single-electron and nucleus (with mass M) system.

The solutions to the time-independent Schroedinger equation describe the allowed energy levels of the electron inside the atom as well as the spatial distribution of electric charge in space $-e|\psi(\vec{r})|^2$, also referred to as ‘orbitals’. There exists an infinite number of solutions $\psi_n(\vec{r})$ and each spatial wave function is associated with an energy E_n :

$$E_n = -\frac{\mu Z^2 e^4}{2\hbar^2 \epsilon_0^2} \frac{1}{n^2} = -R \frac{Z^2}{n^2}, \quad (4.2)$$

where R is the Rydberg constant summarising all constants in one value and n the principal quantum number. n can take any positive integer value (excluding 0) up to infinity and describes all allowed energy states of any hydrogen-like atom. Note that considering the special relativistic expression for the kinetic energy in equation (4.1) shifts the energy levels in (4.2). For Hydrogen, this reduces E_n of about 10^{-5} eV.

While deriving the solutions to equation (4.1) Schroedinger noticed that two additional quantum numbers related to the angular momentum are necessary to describe all electron orbitals [Schrödinger \(1926\)](#). Not only the energy levels are quantised but also the magnitude of the angular momentum of the atom $L = \sqrt{l(l+1)}\hbar$ with $l = 0, 1, \dots, n-1$ referred to as

the (electron) orbital angular momentum quantum number. Due to historic reasons, the values of l are denoted with letters (s, p, d, f, continuing alphabetically) instead of numbers. In addition to the magnitude of the angular momentum vector, also its z -component is quantised: $L_z = m_l \hbar$ with the magnetic quantum number $m_l = -l, -l+1, \dots, +l$. It is important to realise that the properties of the environment (e.g., presence of a magnetic field) influence the splitting of energy levels of an atom and change the observed spectra. For an completely isolated atom there is no preferred direction for the angular momentum in space. The electron orbitals for the same n , but different l and m_l are said to be degenerate as they have the same energy. Electrons making transitions from (n, l, m_l) to (n, l', m_l') produce the same spectral line (Carroll & Ostlie 2017). The presence of an external magnetic field, for example, gives the atom and its angular momentum a preferred direction and lifts the degeneracy of the orbitals shifting them to different energies and causing more lines to appear in the spectrum. This effect is known as the Zeeman effect.

Considering special relativistic effects introduces splittings to an atom's energy levels referred to as the fine structure of an atom. Conceptually, one can image the electron moving through an electric field due to the presence of the charged nucleus. According to the theory of special relativity this is equivalent to the electron experiencing a magnetic field when transferring reference frames from a moving electron to a moving nucleus. The electron does not only possess orbital angular momentum l , but also intrinsic angular momentum (spin) denoted by the quantum number s . Using perturbation theory, it can be shown that the spin-orbit coupling of both angular momenta causes the energy levels to split according to the total electron angular momentum $j = l \pm s$. The energy difference between the lowest and highest possible level due to the fine structure splitting is Foot (2011):

$$\Delta E_{\text{spin-orbit}} = E_{j=l+1/2} - E_{j=l-1/2} = \frac{\alpha^2}{nl(l+1)} E_n, \quad (4.3)$$

where α is the fine structure constant and E_n as defined in (4.2). Note that the energy levels including the effects of spin-orbit coupling can be directly obtained by using the Dirac formalism for relativistic quantum mechanics (Dirac 1928).

Apart from the electron also the nucleus possesses a magnetic angular momentum, the nuclear spin i . Together with the total electron angular momentum j this adds up to the final angular momentum $f = j \pm i$. Their interaction gives rise to atomic hyperfine structure – further energy levels. This additional splitting of energy levels is orders of magnitude smaller than the fine structure. For infrared spectra, the hyperfine structure is not relevant and is therefore not discussed further. Nevertheless, the hyperfine splitting of the ground state of the H atom (1s), the famous 21 cm H line, is important for mapping out star-forming regions in galaxies.

4.2 Energy spectrum of Hydrogen

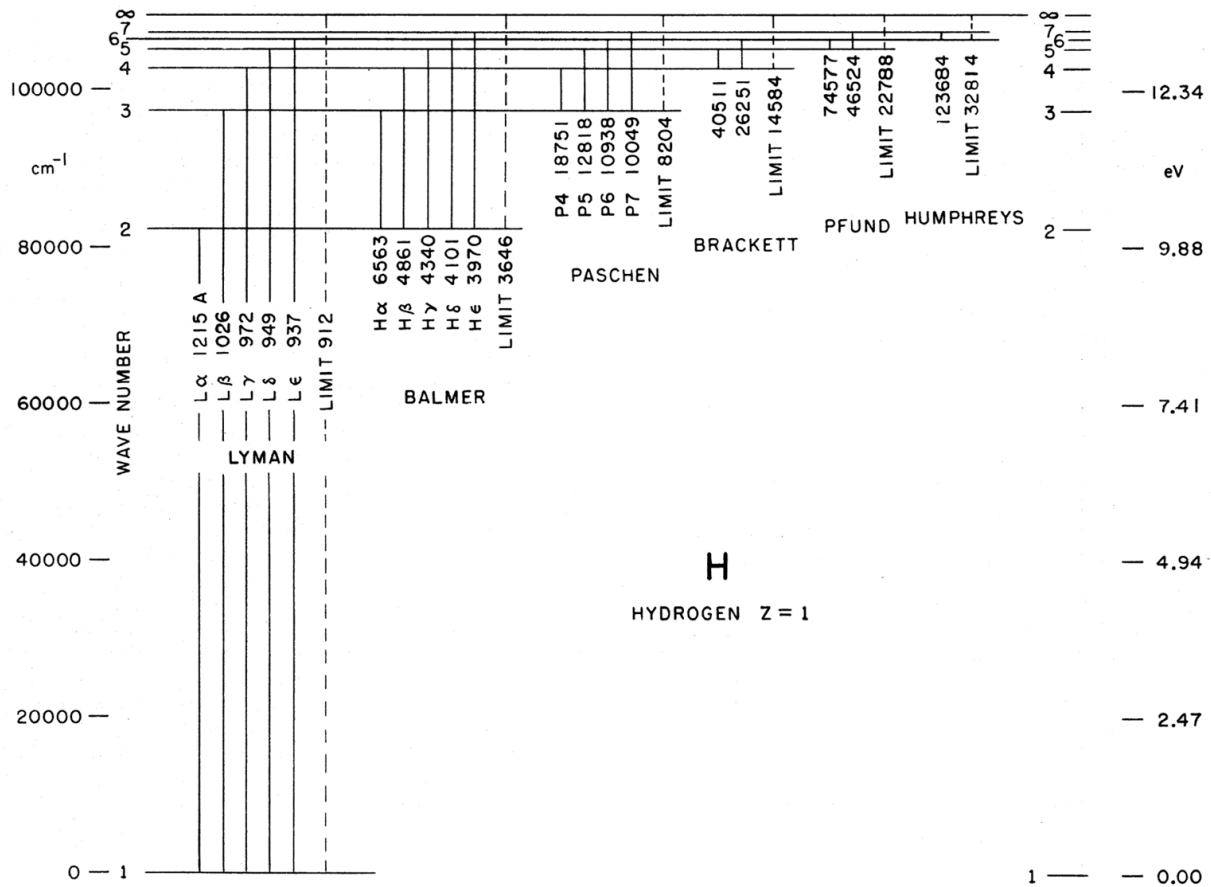


FIGURE 4.1 – Grotrian diagram of the energy levels E_n in a H atom. The Paschen (P), Brackett (Br), Pfund (Pf) and Humphreys (Hu) series are observable in the IR (adapted from [Merrill 1958](#)).

For the Hydrogen (H) atom, the energy levels are specified with the principal quantum numbers n . Configurations that only differ in l have the same energy and m_l becomes important only if an external magnetic field is present. In addition, the fine structure of Hydrogen is usually too small for astronomical applications. Only for more complex multi-electron systems does it become important (see Sect. 4.3). Transitions of H spectral lines are therefore only denoted by n . Again – due to historic reasons – the H spectrum is divided into several series named after their discoverers. Each series summarises the transitions of a lower energy level n_1 to all higher levels $n_1 < n_2 \leq \infty$ (or vice versa). The Balmer series ($n_1 = 2$) is important for optical spectra. Only from $n_1 = 3$ (Paschen series) on, the energy difference of the transitions becomes observable in the infrared. Transitions to (or from) the ground level $n_1 = 1$ are referred to as the Lyman series observable in the ultraviolet. Individual transitions within a series are marked with Greek letters representing the change in n : $\Delta n = 1$ denoted by α , $\Delta n = 2$ denoted by β and so on. This is continued for the most important transitions up to $\Delta n = 5$ indicated by ϵ . Transitions from higher energy levels are then denoted by the principal quantum number of the higher state n_2 , e.g., P8 for $n_2 = 8 \rightarrow n_1 = 3$ within the Paschen series. Figure 4.1 illustrates the energy levels in a so-called *Grotrian diagram* of the H atom and the various spectral line series.

4.3 Multi-electron systems

The Schroedinger equation (4.1) can be generalised for more electrons by summing up all their kinetic energies as well as the Coulomb potential between each electron and the nucleus as well as between pairs of electrons. This equation is no longer analytically solvable and approximations and numeric methods are required to calculate the energy structure. By convention, the configurations of multi-electron systems are described by the same quantum numbers nlm_l as the hydrogen-like atoms even though ‘orbitals’ as such do not exist anymore (see, e.g., discussion in Tennyson 2005, Ch. 4.2). In addition, the spin of single electrons becomes important for the structure of the atom. The Pauli exclusion principle states that two electrons cannot have the same set of quantum numbers $nlm_l s$. This statement gives rise to the ‘sub-shell’ structure of multi-electron atoms and ions. An important difference between the structure of single and multiple electron system is that the degeneracy of the n energy levels (or ‘shells’) is lifted with respect to l (see, e.g., discussion in Tennyson 2005, Ch. 4.4). The degeneracy of each nl configuration (or ‘sub-shell’) with respect to m_l persists but is duplicated as two electrons with opposite spin can populate each nlm_l ‘orbital’. Therefore, the total number of electrons in a nl configuration is $2(2l+1)$. When all nl sub-shells are filled with the maximum number of electrons, the complete configuration is referred to as closed. Whereas, when at least one sub-shell remains unfilled, the configuration is said to be open. The exponent of the nl configuration gives the number of electrons in that configuration. For the ground state of Iron (Fe) where all sub-shells are closed this is: $1s^2 2s^2 2p^6 3s^2 3p^6 3d^6 4s^2$. Even if the same notation is used to describe the electron configuration of an atom and an ion with the same number of electrons, the nucleus charge is not the same. Therefore, the energy levels and the transition energies differ. In the non-relativistic Schroedinger limit (4.2) they scale with Z^2 . Nevertheless, the energy structure and spectra of such systems are similar.

Each nl configuration has a multiplicity, meaning it hides multiple states with different energy originating in the change of quantum numbers of the atom as a whole. For most astrophysical cases, only energy states involving changes in the quantum numbers of all electrons are relevant. Therefore, the quantum numbers of the nucleus are often neglected. When writing energy levels in multi-electron systems, not only the quantum numbers of individual electrons but also the total orbital L and spin S momenta of all electrons have to be considered. Orbital and spin momenta of electrons in closed shells add up to zero and do not contribute to the state of the entire atom. Only quantum numbers of electrons in open shells have to be taken into account. In spectroscopic notation, the quantum numbers of sub-shells regarding individual electrons are denoted with small letters and referred to as the configuration of an atom or ion. Those of the entire atom are symbolised by large letters:

$$(n_1 l_1)^{\#e^-} (n_2 l_2)^{\#e^-} \dots {}^{2S+1} L_J^{(\circ)}. \quad (4.4)$$

As for hydrogen-like atoms, the orbital angular momenta are portrayed as letters (S, P, D, F, continuing alphabetically) instead of numbers. The exponent of the total orbital angular momentum illustrates the parity of the wave function. Parity is a symmetry property of a wave function describing how it changes under spatial inversion ($\vec{r} \rightarrow -\vec{r}$). If parity changes upon inversion the wave function is said to have odd parity and the energy level is marked

with ‘ \circ ’. If it does not change, the parity is called even and no additional mark is given. It has been established that for electric dipole transitions, the parity of the energy levels has to change, whereas for magnetic dipole and electric quadrupole transitions it remains the same (for the definition of dipole and quadrupole transitions, see Sect. 4.4.2–4.4.3).

4.4 Transitions

Transitions between the infinite but quantised energy levels can occur in different ways. Upward transitions (excitation), meaning a change from a lower to a higher energy level, occur if the energy difference E_{ij} between the two energy states i and j is provided to the electron:

$$E_{ij} = h\nu_{ij} = \frac{hc}{\lambda_{ij}}, \quad (4.5)$$

where h is the Planck constant. The electron can be excited either upon absorption of a photon (radiative excitation) or by thermal excitation through collisions without photon-absorption. Collisional excitation becomes important in warmer phases of the interstellar medium (ISM) where the electron density $n_e > 10^4 \text{ cm}^{-3}$. Upward transitions are always followed by downward transitions referred to as de-excitation. A photon is emitted with an energy corresponding to the difference of the two involved states. The time after which de-excitation occurs can be determined by either external effects such as the density of the ISM (see the following section) or by stimulated or spontaneous de-excitation governed by the lifetime of a transition. In case of stimulated emission, a photon with the correct energy is required to trigger the de-excitation of the electron. A second photon with the same energy is emitted. This is the basic working principle behind lasers. This mechanism is also important in astronomy when the photon and transition energies lie in the microwave regime (on mm and cm wavelength scales) giving rise to, e.g., H₂O masers (microwave amplification by stimulated emission of radiation). As stated in the previous chapter, many MYSOs have been associated with maser emission. However, stimulated emission is not relevant for the spectra discussed in this work and is therefore not further discussed.

4.4.1 Transition probabilities

Not all discussed transition mechanisms are equally likely. Radiative emission requires an atom to be in an excited state to be able to (spontaneously) emit a photon. The strength S_{ji} of an emission line depends on several quantities: the number of atoms in the excited state N_j , the energy difference between the upper level j and the lower level i as well as the rate or probability of an atom spontaneously emitting a photon of energy $h\nu_{ij}$ in the transition from level j to i denoted as A_{ji} and referred to as the Einstein A coefficient:

$$S_{ji} = N_j h\nu_{ji} A_{ji}. \quad (4.6)$$

The lifetime τ_j of an excited energy level j or the timescale of its decay is given by the inverse of the sum of all Einstein A coefficients over all possible downward transitions from

the upper level j (Tennyson 2005):

$$\tau_j = \left(\sum_{i < j} A_{ji} \right)^{-1}. \quad (4.7)$$

The different values of A_{ji} between different energy levels and whether transitions are considered ‘possible’ or not is discussed in the following two chapters.

Similarly, the strength S_{ij} of an absorption line due to interaction with a photon is

$$S_{ij} = N_i h \nu_{ij} B_{ij} \rho(\nu), \quad (4.8)$$

where N_i is the number of atoms in the energy level i , B_{ij} the Einstein B coefficient giving the absorption transition probability and $\rho(\nu)$ the energy density of radiation. Assuming a continuum radiation spectrum such as the Planck distribution for black-bodies, the Einstein A and B coefficients are related by Einstein (1916):

$$B_{ij} = \frac{c^3}{8\pi h \nu_{ji}^3} \frac{g_j}{g_i} A_{ji}, \quad (4.9)$$

where g is the degeneracy of the energy level i or j .

Whether the elements present in an astrophysical environment are revealed through absorption or emission lines in the spectrum depends on the properties of the medium, especially on the degree of excitation of the species and therefore the temperature. Also the geometry of observer, continuum light sources and diffuse ISM can influence the nature of the observed transitions. Absorption lines are often observed in stellar spectra as the fusion processes in the core provide a continuum light source which excites atoms in the upper, colder layers of the stars’ interior. These lines can already be observed in later stages of YSOs.

Whether de-excitation and therefore line emission is radiative or collisional depends on the density of collision partners (usually electrons) as it determines whether the excited electrons within atoms or ions have enough time to spontaneously de-excite or are incited to do so through interactions without the emission of a photon. This critical density n_c is given by the ratio of the timescales for radiative and collisional de-excitation between any two energy levels (Tennyson 2005):

$$n_c = \frac{\sum_{i < j} A_{ji}}{\sum_{i \neq j} q_{ji}}, \quad (4.10)$$

where q_{ji} is the probability of collisional de-excitation of level j to level i . If the atom or electron density is above n_c , collisions dominate the de-population of the upper energy level. Such emission lines provide a measure for the atom or electron temperature. Below n_c , emission is radiative and the atoms or electron density can be estimated.

4.4.2 Electric dipole transitions

In addition to radiative and collisional (de-)excitations and absorption having different probabilities, radiative transitions between different energy levels within the atom or ion are not equally likely as well. These probabilities can be derived considering the photon as a wave. An electromagnetic wave consists of an electric and magnetic field. The interaction of an atom or ion with an electromagnetic wave can be treated separately for the electric and the magnetic field. The most abundant and prominent lines in spectra are due to the interaction of the atom with the electric field component. In the electric dipole approximation, the amplitude of the electric field is assumed to be constant over the size of the atom. In other terms, the wavelength of radiation is much larger than the size of the atom. If the calculated transition rate has a finite value, the transition is called an electric dipole transition or short *allowed*. If the rate is zero, the transition is called *forbidden*. Whether a transition is allowed or forbidden can be evaluated using selection rules which summarise the conditions on the transition rates with the quantum numbers of the energy levels. The selection rules can be derived by imposing symmetry arguments on the electronic wave functions. They can be found in any astrophysical textbook discussing spectra such as [Tennyson \(2005\)](#), [Dopita & Sutherland \(2003\)](#) or [Draine \(2011\)](#).

4.4.3 Forbidden lines

If the transition probability between two energy levels is very small or even zero, the electric dipole approximation becomes insufficient. A similar calculation to the one described in the previous section replacing the electric with the magnetic field gives rise to magnetic dipole transitions. One can also consider higher orders in the electric dipole approximation to get transitions driven by electric quadrupoles. Both magnetic dipole and electric quadrupole transitions are considerably less probable than electric dipole transitions. While electric dipole transitions have lifetimes in the order of $\tau_{\text{el.dipole}} \sim 10^{-7}\text{--}10^{-9}$ s, those of magnetic dipole transitions are $\tau_{\text{mag.dipole}} \sim 10^{-3}$ s and of electric quadrupole transitions $\tau_{\text{el.quadrupole}} \sim 1$ s ([Tennyson 2005](#)). The long lifetimes of forbidden transitions indicate that they only occur if there are no other possible decay channels, neither radiative nor collisional. Therefore, such transitions only become important in astronomical low-density environments such as the ISM. The mean time between collisions becomes so long (between 10 and 10^4 s) that electrons in atoms and ions return to lower energy levels radiatively after the intrinsic lifetime of their current energy level. Lines originating in this way are referred to as *forbidden* and denoted by square brackets []. The most common forbidden transitions in the infrared (IR) originate from singly ionised iron, denoted as [Fe II].

4.5 Quadrupole transitions in molecular hydrogen H₂

Molecules have lower binding energies than the ionisation energies of atoms. They are therefore found in cooler astronomical environments with temperatures up to about 8000 K ([Tennyson 2005](#)) such as in molecular clouds, cool stars, planetary atmospheres and comets. The most simple molecules consist of two atoms of the same species in a linear geometrical configuration and are called homo-nuclear diatomic molecules. The following discussion will be focused on the diatomic molecule H₂ as it is the most abundant molecule in the

universe and the most frequent molecule detected in the line structure of the analysed MYSO spectrum (see Sect. 9.5.2). However, the general considerations on the energy structure can also be applied to other diatomic molecules.

The energy structure of molecules is more difficult to describe than for atoms for two reasons: on the one hand, electrons can now move about (at least) two positively charged nuclei. On the other hand, the relative motion of the nuclei in form of vibration and rotation introduces additional energy states compared to atoms. Within the Born-Oppenheimer approximation, the wave function of nuclei and electrons can be treated separately. Based on the high ratio of nucleus to electron mass, the nuclei are assumed to be fixed and only the electrons move. In this case, the total energy spectrum of a molecule can be separated into a sum of electronic levels due to Coulomb interactions as well as the vibrational and rotational states of the nuclei. The rotational and vibrational modes are assumed to be independent as the energy changes between vibrational levels are $\sim 10^6$ times greater than between rotational states (Dopita & Sutherland 2003). The repulsive Coulomb potentials between the two nuclei and the electrons as well as the attractive potential between nuclei and electrons create characteristic potential energy curves as a function of the separation of the two atoms (see Fig. 4.2). These curves describe the electronic states of the molecule. The electronic energy states are in turn separated into vibrational energy levels characterised by the vibrational quantum number v . This additional quantisation occurs due to the relative displacement of two nuclei with respect to each other along their connecting internuclear axis ('vibration' or 'stretching'). Figure 4.2 shows potential curves for the ground, first and second excited electronic states for H_2 as well as the vibrational levels within each electronic state.

Additionally, each vibrational energy level splits into several rotational states characterised by the rotational quantum number J . Rotational levels arise due to the rotation of the molecule around one of the two axis perpendicular to the internuclear axis. A molecular spectral line can arise due to the change in multiple motions. For example, in the mid-infrared the pure rotational spectrum within one vibrational level of H_2 can be observed. Towards the near-infrared transitions between rotational levels of different vibrational levels are dominant. In spectroscopic terms, these levels are therefore known as rotational-vibrational (or short ro-vibrational) transitions.

Transitions between different electronic states lie in the optical and UV wavelength regime. Similar to atomic energy levels, the electronic states of molecules are subject to fine and hyperfine structure splitting. As they are not relevant for the study of infrared spectra, they will not be further discussed.

As H_2 is a linear homo-nuclear molecule, it does not possess a permanent dipole moment as the centre of mass and charge are the same (Genzel 1992). Therefore, it does not exhibit dipole transitions, but can only radiate in less probable electric quadrupole transitions. Quadrupole radiation from H_2 is often observed when the gas, e.g., in molecular clouds, is heated to sufficient temperatures by collisions or other non-thermal processes (Glass 1999). Ro-vibrational transitions are specified by the upper and lower vibrational quantum numbers v as well as by the change in rotational quantum number J . For molecular transitions, vibrational transitions are often accompanied by a change in J (Tennyson 2005). Molecular selection rules state that the change in rotational quantum number $\Delta J = J' - J'' = 0$ or $\Delta J = \pm 2$. These rules arise from the allowed (anti-)parallel proton spin orientations (as

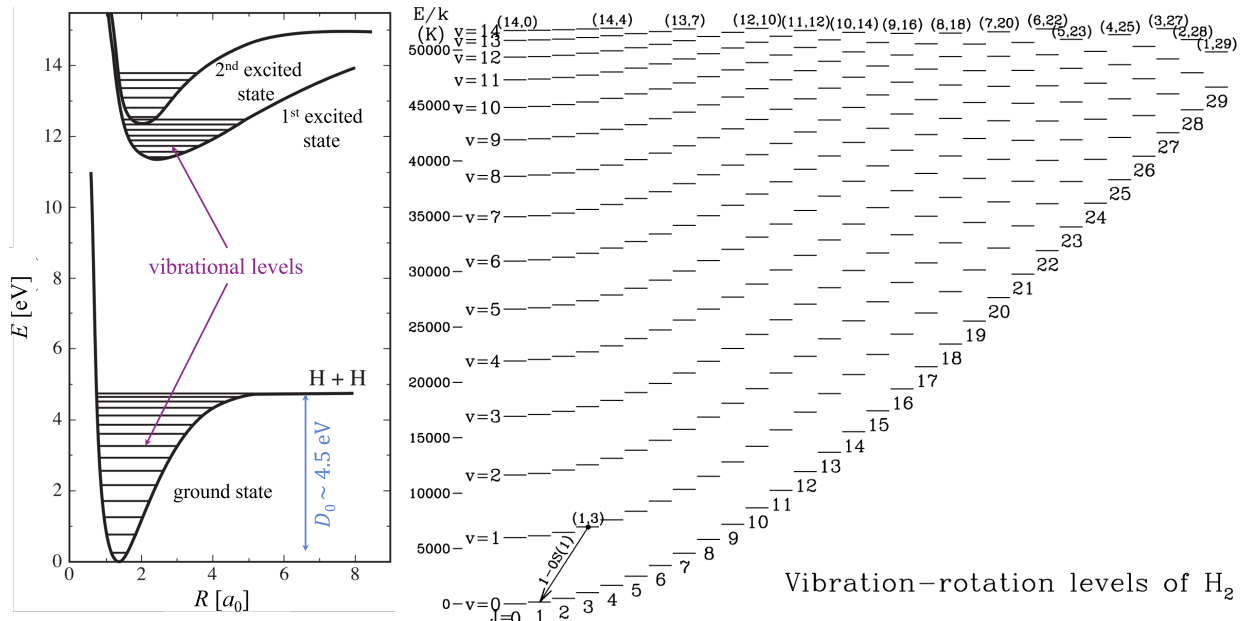


FIGURE 4.2 – **Left:** Potential energy curves for the ground, first and second excited electronic states of H₂ as a function of atomic separation R (in units of the Bohr radius a_0). For large R , the molecule is dissociated into two H atoms. The required dissociation energy is $D_0 = 4.5$ eV. The vibrational levels within each electronic state are depicted by horizontal lines. **Right:** Ro-vibrational energy levels of the electronic ground state of H₂ for $J \leq 29$. A single energy level is denoted by a pair of vibrational and rotational quantum numbers (v, J) . The important ro-vibrational 1–0S(1) transition from $(v', J') = (1, 3)$ to $(v'', J'') = (0, 1)$ at $\lambda = 2.12 \mu\text{m}$ is indicated. The figures were adapted from Draine (2011).

fermions, protons need to satisfy the Pauli exclusion principle). Each change in J is denoted by a letter followed by the rotational quantum number of the lower state. Summarised, the ro-vibrational transitions of H₂ are denoted by

$$v'-v''\text{S}(J'') \text{ if } \Delta J = +2, \quad (4.11)$$

$$v'-v''\text{Q}(J'') \text{ if } \Delta J = 0 \text{ and } J' = J'' \neq 0, \quad (4.12)$$

$$v'-v''\text{O}(J'') \text{ if } \Delta J = -2, \quad (4.13)$$

where v', J' are the quantum numbers of the upper level and v'', J'' of the lower level. Any changes in the vibrational quantum number are allowed. However, transitions with $\Delta v = \pm 1$ are the most pronounced. One of the strongest ro-vibrational transitions observed in IR spectra is 1–0S(1) at $\lambda = 2.12 \mu\text{m}$ and is often observed in YSO spectra as well (see Sect. 9.5.2). Vibrational transitions which change by more than one ($\Delta v > 1$) are called overtones (Tennyson 2005). This nomenclature is often encountered in the literature regarding the CO molecule rather than H₂. Figure 4.2 depicts the ro-vibrational levels of electronic ground state of H₂.

5 Infrared Photodetectors

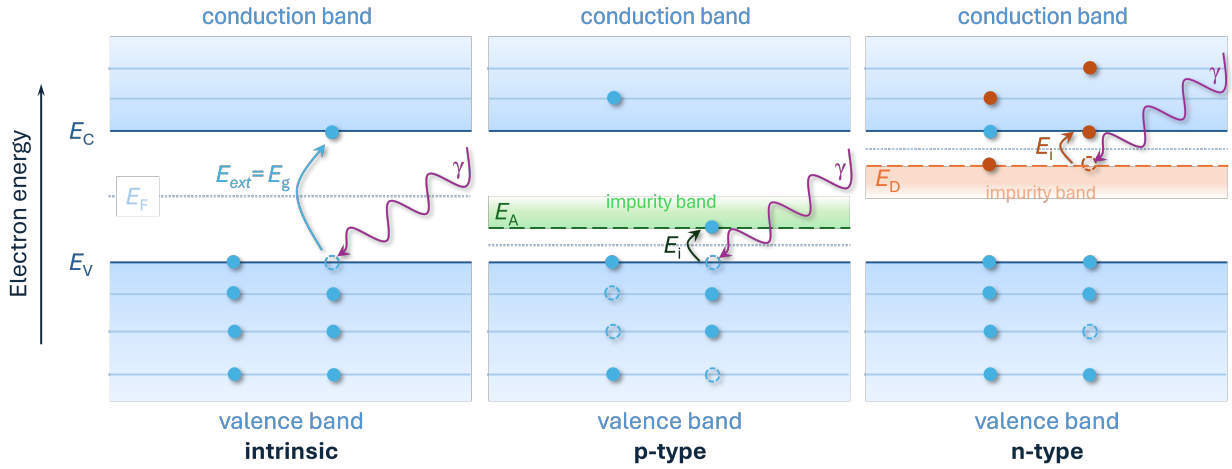


FIGURE 5.1 – Energy band diagram of an intrinsic, a p-type and a n-type semiconductor.

As the IR detectors used in JWST instruments operate differently from CCDs which are often used in ground-based telescopes, the optical (HST ACS) and ultraviolet (WFC3/UVIS) instruments on the HST or X-ray satellites, a short introduction to their photon collection principle is given. For more details on the IR detectors and the detailed solid state physics behind them, please consult [Rieke \(2007, 2021\)](#).

The most commonly used photo-detection principle is based on creating photo-electrons upon photon-absorption in a detector material. Detectors based on this photo-electric effect respond to individual photons and are referred to as photodiodes. The electrons produce a measurable current proportional to the number of incident photons. An ideal detector would detect all incoming photons within its spectral response (the wavelengths regime in which the detector is sensitive) while preserving all their properties. In reality, the output signal is a combination of noise and only a fraction of the incoming photons.

Several parameters are used to characterise the performance of detectors. Two examples are linearity and quantum efficiency. Linearity rates the linear proportionality of incoming photons to the actual output signal. Quantum efficiency (QE) describes the fraction of incident photons being converted into a detectable signal. In other words, the number of electrons with respect to the number of absorbed photons. For more parameters describing detector performance, see, e.g., [McLean \(2008, Ch. 1.5.2\)](#).

As we are considering detectors that detect photons through absorption, the absorption coefficient of the detector material is important as photons that do not free electrons cannot be detected. The absorption coefficient is a proportionality factor based on the absorption cross-section of a material that relates the incoming photon flux to the flux absorbed in a material of a certain thickness. In short, it describes the efficiency of photon-absorption. The quantum efficiency is decreased by the reflection of photons at every surface before the detector volume is reached.

5.1 Intrinsic and extrinsic semiconductors

Near- and mid-infrared photodetectors operate on different forms of photoconductivity. Photoconductivity means the electric conductivity of a material is increased (or its resistivity decreased) upon the absorption of photons. Apart from photon illumination, the conductivity of semiconductors can be altered in further ways such as a change in temperature or the presence of impurity atoms which add energy states between the valence and conduction bands reducing the energy necessary to excite electrons. Intrinsic (pure) semiconductors can detect photons with an energy larger than the binding energy of the electrons in a semiconductor crystal. This binding energy is also called bandgap energy E_g and presents the minimal energy required to excite electrons from the valence to the conduction band (solid state physics terms for ground and excited states). The cut-off wavelength λ_c is then the longest wavelength up to which detectors can detect photons:

$$\lambda_c = \frac{hc}{E_g}, \quad (5.1)$$

where h is the Planck constant and c the speed of light. E_g depends on the semiconducting material. Therefore, the choice of material can increase or decrease the spectral response of the detector. For optical detectors, materials with higher bandgap energy – usually based on silicon – are used than for the near-IR (NIR). The materials used for NIR and mir-IR (MIR) photon detection are discussed below in section 5.2.1–5.2.2.

In extrinsic photoconductors, an electron is produced upon photon absorption through an ‘impurity’ atom, that is, from an atom that is not the same element as the semiconductor. These impurity atoms add energy states between the valence and conduction band of the intrinsic semiconductor reducing the excitation energy for electrons. The higher the concentration of impurity atoms, the greater the quantum efficiency. Based on the element chosen for the impurity atoms, p- and n-type semiconductors can be constructed. P-type semiconductors have fewer valence electrons than the semiconductor atoms. They ‘accept’ electrons from the semiconductor crystal to fill their valence band while leaving ‘holes’ in the crystal. N-type semiconductors have an additional electron than necessary to form the crystal bond. This electron can be easily excited to the conduction band. Therefore, in extrinsic photoconductors, instead of being directly excited from the valence into the conduction band, electrons can either be excited onto an energy level introduced by the impurities (p-type) or from the impurity level to the conduction band (n-type). Figure 5.1 illustrates a simplified energy band structure of the different types of semiconductors as well as the change of charge population upon photon absorption within the semiconductor.

For extrinsic semiconductors, the bandgap energy in equation (5.1) is replaced by the ionisation energy E_i of the impurity atom, that is the energy between the impurity level and the highest level in the valence band (p-type) or the lowest level in the conduction band (n-type). As $E_i < E_g$, the cut-off wavelength increases enabling operation towards longer wavelengths. The absorption coefficients proportional to the photo-ionisation cross-sections of the impurity element are approximately three orders of magnitude less than for the intrinsic semiconductors (Rieke 2021). Therefore, detectors based on extrinsic photoconductivity must have larger volumes to achieve high enough quantum efficiency for a reasonable output signal.

Electrons cannot only be excited through photon interaction but also thermally. The population of allowed energy states by electrons follows the Fermi-Dirac distribution function:

$$f(E) = \frac{1}{1 + e^{(E-E_F)/kT}}, \quad (5.2)$$

where E is the energy level, E_F the Fermi level, k the Boltzmann constant and T the temperature. With increasing temperature, the probability of electrons populating the conduction band increases. The Fermi level is defined such that $f(E_F) = 0.5$. For any T , E_F defines states that are likely populated ($E < E_F$) and those that are likely unoccupied ($E > E_F$). The current produced due to thermal excitation is referred to as dark current as the signal is produced even though the detector is not illuminated and presents a source of noise. To reduce the amount of thermal electrons, IR detectors have to be cooled to $\lesssim 100$ K. Since the relevant excitation energy for MIR detectors based on extrinsic photoconductivity is smaller than for intrinsic photoconductors used in NIR, MIR instruments have to be cooled more than those for the NIR.

5.2 IR Detector arrays

IR detector arrays are manufactured with semiconducting materials with smaller band gap energies than silicon ($E_g = 1.14$ eV). Intrinsic photo-absorption would yield a cut-off wavelength at $\lambda \sim 1 \mu\text{m}$ (5.1). Difficulties in the manufacturing process of CCDs with other semiconductors than Si lead to IR arrays being developed in a ‘hybrid’ approach (McLean 2008). Detection of IR radiation and electronic pixel read-out are separated. IR detector arrays can be described as ‘sandwiches’: the IR sensor and the readout-integrated circuit (ROIC) chip are connected through Indium bumps which join the each pixel in the sensor to its output amplifier (see Fig. 5.2). The entire structure is referred to as *focal plane array* (FPA) or *sensor chip assembly* (SCA). Even though the principle of photon detection and electron conversion remain similar to CCDs, charge storage, transfer and read-out methods differ. How electric charge is stored in IR arrays depends on the type of array used and are discussed in the following sections 5.2.1–5.2.2. The readout process does not follow the charge-coupling principle utilised in X-ray CCDs (see, e.g., Siemiginowska et al. 2011, Ch. 3), but each pixel is readout sequentially using Complementary Metal-Oxide-Semiconductors (CMOSs; McLean 2008).

5.2.1 HgCdTe Photodiodes

The most commonly used detectors in the near-infrared are HgCdTe (Mercury-Cadmium-Telluride) photodiodes based on intrinsic photoconductivity. They can operate at relatively high temperatures (30–90 K) and the cut-off wavelength can be increased by increasing the amount of Mercury. Detector sizes with 2048×2048 pixels are standard since 2008 (McLean 2008) and are used in all NIR instruments on JWST. HgCdTe detectors have previously been employed on the *Near-Infrared Camera and Multi-Object Spectrograph* (NICMOS) on-board HST as well as on the NIR instruments of the *Wide-Field Infrared Survey Explorer* (WISE; Wright et al. 2010). While the arrays on NICMOS in 1997 employed only 256×256 pixels, the WISE arrays have 1024 pixels, half the size of those used on JWST. In theory,

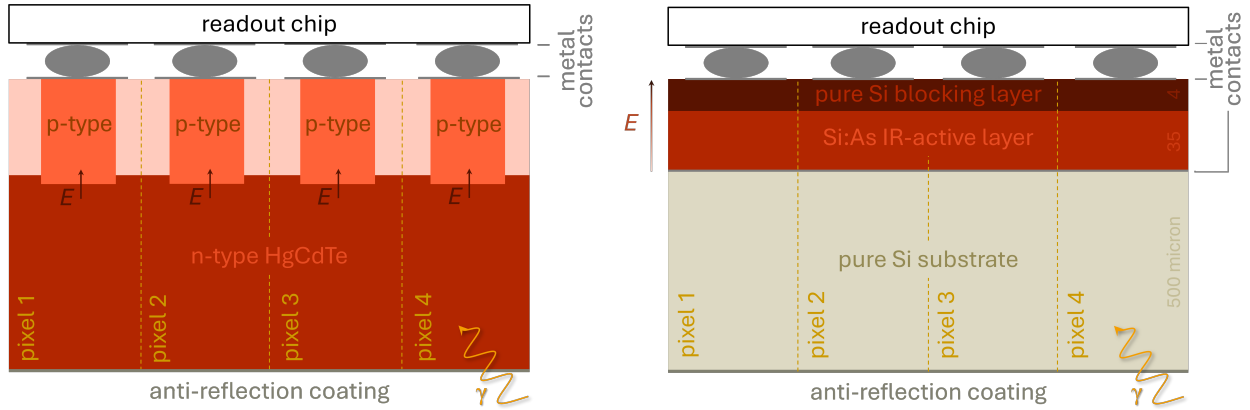


FIGURE 5.2 – Simplified structure of the photo-sensitive HgCdTe (left) and IBC detector arrays (right). Both arrays are back-illuminated. The IR sensor and the readout chip are connected through Indium bumps. The depletion region (for HgCdTe) and the electric field E across the IR-active and blocking layers (for IBC) are indicated. The numbers on the right of IBC detector layout indicate the thickness as adopted for MIRI on-board JWST.

HgCdTe photodiodes can be fabricated to longer cut-off wavelengths up to $\lambda_c \sim 15 \mu\text{m}$ (Rieke 2007, 2021). However, for astronomical purposes, the smaller band gap allows too high dark current rates. A different method was discovered to detect MIR radiation (Sect. 5.2.2).

To achieve detectors with high quantum efficiency, HgCdTe photodiodes are constructed with a pn-junction: one side of detector is made from a n-type material and the other side from a p-type semiconductor. As the additional electrons introduced by the n-type impurity atoms can easily be freed, they combine with p-type atoms missing an electron for complete crystal structure. Close to the junction, a ‘contact’ voltage builds up. The resulting potential difference creates an electric field that accelerates electrons across the junction and depletes the region of charge. When electrons are produced in the n-type HgCdTe layer upon photon-absorption, charges diffuse towards the depletion region created by the pn-junction. They cross the depletion region due to the potential field producing a current. The current is recorded and presents the rawest form of data. Figure 5.2 illustrates the detection principle inside a HgCdTe photodiode. For further details on HgCdTe arrays see, e.g., Rieke (2007, 2021) or McLean (2008).

5.2.2 Impurity band conduction detectors

As stated in the previous section, photodiodes operate only on intrinsic absorption and can be constructed up to $\lambda_c \sim 15 \mu\text{m}$ (Rieke 2007, 2021). For photon-detection in the MIR another technique based on extrinsic absorption has to be used. Impurity band conduction (IBC) detectors are doped with a very high concentration of impurity atoms (usually n-type). The resulting separation between the impurity atoms is small enough to allow the electron wave function of one atom to extend with a non-negligible probability to the next (also known as the ‘tunnel’-effect). Electrons are transferred between impurity atoms increasing the electric conductivity without the absorption of photons and hence, without elevating electrons into the conduction band. In traditional (extrinsic) photoconductors this would lead to an additional noise source and is therefore undesirable. Instead, in IBC detectors, an additional layer in the detector substrate is used to block the ‘tunneling’ electrons producing

dark current.

The IBC detectors used in astronomy are made from arsenic doped silicon Si:As, an n-type semiconducting material. The basic structure is shown in figure 5.2. The photon detection in back-illuminated detectors (as those on-board JWST) proceeds as follows: photons pass through an anti-reflection coating and travel through a pure thick silicon substrate onto which all subsequent layers are grown before entering the IR-active layer of Si:As. Here, the extrinsic photon-detection takes place. This detection layer is followed by an intrinsic blocking layer (made of silicon) preventing (at sufficiently low temperatures) thermally-generated electrons to pass. Due to the lack of impurity atoms, the electrons do not have enough energy to enter the conduction band of silicon. The photo-electrons, however, can cross the blocking layer as they have been excited into the conduction band through photon-absorption. An electric field across the IR-active and the blocking layer drives the photo-electrons to the amplifiers in the readout chip.

In an IBC detector array, there are no physical boundaries between pixels. All pixels reside on a single slab of silicon with the IR-active and blocking layers are grown on top. A pixel is defined by the electric field generated between two electric contacts, one separating the IR-active and blocking layers and one at the indium bumps between the detector and the readout chip (see Fig. 5.2).

Even though IBC detectors exhibit lower quantum efficiencies than HgCdTe photodiodes, they are sensitive over an extensive wavelength range from 5 to $28\ \mu\text{m}$ with a low dark current. They have a long history in IR missions: the spectrometer on-board the *Infrared Space Observatory* (ISO; [Kessler et al. 1992](#)), the *Midcourse Space Experiment* (MSX; [Mill et al. 1994](#)), MIR instruments on the *Spitzer Space Telescope* ([Werner et al. 2004](#)), the IR camera on the Japanese mission *Akari* ([Murakami et al. 2007](#)) and the *Wide-Field Infrared Survey Explorer* (WISE; [Wright et al. 2010](#)) were IBC detectors. The biggest technical advance has been achieved by increasing the detector size and therefore the number of pixels on the silicon substrate. The latest generation devices on-board WISE and JWST have 1024×1024 pixel arrays. Further information on IBC detectors in general can be found, e.g., in [Herter \(1994\)](#); [Rieke \(2007, 2021\)](#) and for the mid-IR instrument on JWST, e.g., in [Rieke et al. \(2015\)](#); [Argyriou \(2021\)](#).

6 JWST

The *James Webb Space Telescope* (JWST; Gardner et al. 2023; Rigby et al. 2023a) is a near-infrared (NIR) and mid-infrared (MIR) space observatory launched on the 25th of December 2021 into the second Lagrange point (L2) of the Earth-Sun system. The mission was developed in an international collaboration between NASA, the European and Canadian Space Agencies. The 6.5 m primary mirror consists of 18 hexagonal segments. The instruments are protected from solar radiation by a large sun shield (see Fig. 6.1). As an IR observatory, JWST has been designed with high sensitivity to observe the most distant objects in our universe. Its lifetime is limited by its fuel amount which will enable it to perform science observations for the next 20 years.

JWST was designed as a successor to both the *Hubble* Space Telescope (HST) and the *Spitzer* Space Telescope. Three main arguments justify the need for a new IR space observatory: for ground-based IR telescopes, the Earth’s atmosphere is a substantial obstacle. Not only does it absorb large parts of the IR wavelength band, but also produces a substantially high background through its warm layers that is 10^6 – 10^7 time higher than in space (Gardner et al. 2023). Additionally, molecules in the atmosphere produce dominant emission and absorption lines contaminating spectra. The HST has high thermal self-emission dominating at wavelengths above $1.7\ \mu\text{m}$ as it is not cooled down enough (which was not necessary as the main instruments operate in the near-infrared below $1.7\ \mu\text{m}$, visible and ultra-violet). Further, HST has only 16% of the light-collecting area compared to JWST. *Spitzer*, although being a near- and mid-infrared space observatory and therefore cold, has due to its small primary mirror ($D = 0.85\ \text{m}$) less than 2% the collecting area (Gardner et al. 2023). Table 6.1 compares the main characteristics of the imaging detectors and spectrographs of the three telescopes.

JWST hosts four scientific instruments on-board: a Near-IR Camera NIRCam (NIRCam; Gardner et al. 2023; Rieke et al. 2023), a Near-IR spectrograph (NIRSpec; Gardner et al. 2023; Böker et al. 2023), a Near-IR Imager and Slitless Spectrograph (NIRISS; Gardner et al. 2023; Doyon et al. 2023) and a Mid-IR Instrument performing both imaging and spectroscopy (MIRI; Wright et al. 2023; Gardner et al. 2023). In the following, the instruments which

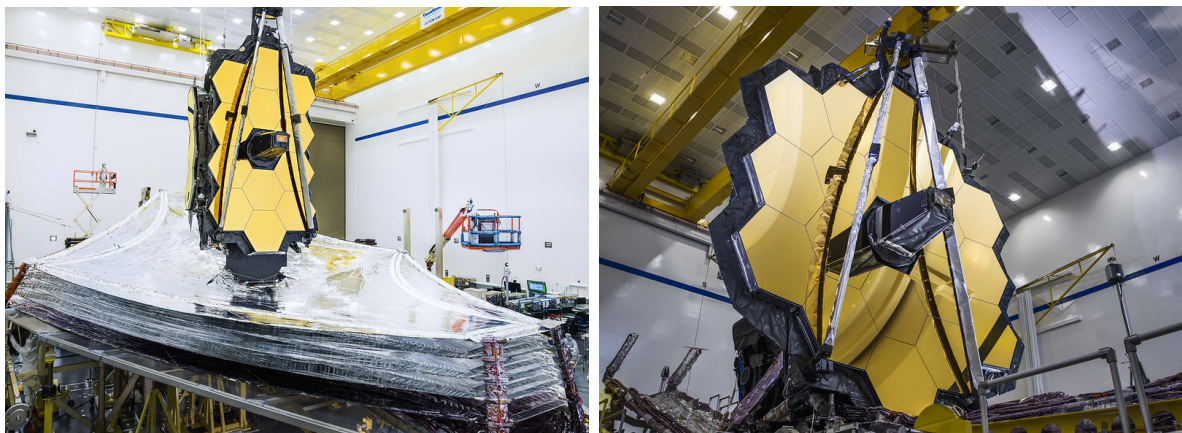


FIGURE 6.1 – **Left:** JWST after an successful sun shield deployment test. **Right:** The fully deployed 6.5 m diameter primary mirror with its 18 hexagonal segments (Image Credit: NASA/Chris Gunn).

provided the data for the analysis in this work are introduced in more detail, namely NIRC*am* (see Sect. 6.2.1), NIR*Spec* (see Sect. 6.2.2) and MIRI (see Sect. 6.2.3).

TABLE 6.1 – Comparison of JWST imaging and spectroscopic (IFU) instruments with their predecessor cameras and spectrographs on HST and *Spitzer*. I compare the size of the primary mirror (aperture), the wavelength coverage, the field of view and the pixel sizes for the imaging and IFU detectors as well as the resolving powers R of the spectrographs.

Telescope (Aperture)	Instrument	Wavelength Range [μm]	Pixel size	$R = \lambda/\Delta\lambda$	Field of View
JWST (6.5 m)	NIRC <i>am</i>	0.6–2.3	0''031	-	4'4 × 2'2
		2.4–5.0	0''063		
	NIR <i>Spec</i> IFU	0.6–5.3	0''1	100, 1000, 2700	3''1 × 3''2
	MIRI Imaging	5.6–25.5	0''11–0''33	-	74'' × 113''
	MIRI/MRS IFU	4.9–27.9	0''196–0''273	3710–1330	3''2 × 3''7 to 6''6 × 7''7
HST (2.4 m)	WFC3/IR	0.8–1.7	0''135 × 0''121	210–130	136'' × 123''
	NICMOS	0.8–2.5	0''043–0''2	200	11'' × 11'' to 51''2 × 51''2
<i>Spitzer</i> (0.85 m)	IRAC	3.19–9.34	1''2	-	5'2 × 5'2
	MIPS @24 μm	21.5–26.2	2''55 × 2''60	-	5'4 × 5'4
	IRS	5.3–38	-	90–600	-

NOTES. Low-resolution spectrographs (part of MIRI or MIPS on *Spitzer*) accompanying imaging instruments are not included in the comparison.

REFERENCES. For the JWST instruments see the text. For HST: IR-imager on the Wide-Field Camera 3 (WFC3/IR; [Marinelli & Green 2024](#)) and the Near Infrared Camera and Multi-object Spectrometer (NICMOS; [Thatte 2009](#)). For *Spitzer*: Infrared Array Camera (IRAC; [Fazio et al. 2004](#)), Multi-band Imaging Photometer (MIPS; [Rieke et al. 2004](#)) and Infrared Spectrograph (IRS; [Houck et al. 2004](#)).

6.1 Diffraction limited resolution

The resolution of any telescope is limited by diffraction. The theoretical limit can be derived considering the diffraction of light by a circular aperture and calculating the conditions for destructive interference (see, e.g., [Karttunen et al. 2007](#)). The intensity pattern of radiation due to the diffraction through a circular aperture is given by the Airy disk. By definition, the diffraction limit on the resolution is defined by the first minimum of the interference

pattern and is known as the Rayleigh criterion:

$$\sin \theta \sim \theta = 1.22 \frac{\lambda}{D}, \quad (6.1)$$

with λ the wavelength of the radiation and D the diameter of the aperture. In addition, the small-angle approximation was used to determine the minimal angular distance θ that can be resolved. For a constant D , the longer the wavelength, the higher θ , thus the lower the diffraction-limited resolution. To achieve the same resolution limit with IR as with optical telescopes, a larger aperture is necessary. JWST as the first IR space observatory can achieve this goal.

6.2 Instruments

JWST has three NIR instruments and one MIR instrument on-board. NIRCam, NIRSpec and MIRI are relevant for the analysis in this work. They are explained in detail in the sections below. For further details, see the JWST user documentation under <https://jwst-docs.stsci.edu/>.

6.2.1 NIRCam

The Near-Infrared Camera (NIRCam; [Gardner et al. 2023](#); [Rieke et al. 2023](#)) performs imaging in 29 different filters in the 0.6–5.0 μm wavelength interval. NIRCam consists in total of 10 HgCdTe detector arrays, each with 2048×2048 pixels across two fully redundant modules A and B. The inner 2040×2040 pixel array is light-sensitive. The outer 4-pixel wide border consists of reference pixels required for calibration. Each module consists of four short (0.6–2.3 μm) wavelength detectors separated by 4–5'' gaps and one long (2.4–5.0 μm) wavelength detector. Due to the same number of pixels over a smaller detector area, the resolution of the short wavelength detectors (0''031/pixel) is higher than the resolution of the long wavelength detectors (0''063/pixel). Each module covers an area of $2'2 \times 2'2$ including the short wavelength detector gaps. Additionally, modules A and B are separated by a 44'' gap (see [Fig. 6.2](#)). NIRCam obtains images simultaneously with modules A and B using all 10 detectors. Combining both modules, NIRCam's total field of view spans 9.7 arcmin^2 without the separating gap of module A and B (see [NIRCam Imaging documentation](#)). NIRCam's resolution is diffraction-limited. The point-spread function (PSF) is Nyquist sampled at 2 μm and 4 μm ([Rieke et al. 2023](#)). All relevant filters for this work and the PSF full-width at half-maxima (FWHM) are reported in [table 6.2](#).

In addition to the filter-imaging described above and which is relevant to this work, NIRCam also offers four additional scientific observing modes: coronagraphic imaging, wide-field slit-less spectroscopy, time-series imaging and grism time-series spectroscopy. For more information on these modes, please consult the [JWST NIRCam documentation](#).

6.2.2 NIRSpec

The Near-Infrared Spectrograph (NIRSpec; [Gardner et al. 2023](#); [Böker et al. 2023](#)) performs NIR spectroscopy in the 0.6–5.3 μm interval using either fixed slits, a microshutter assembly for multi-object spectroscopy or an integrated field unit (IFU; [Böker et al. 2022](#)). This

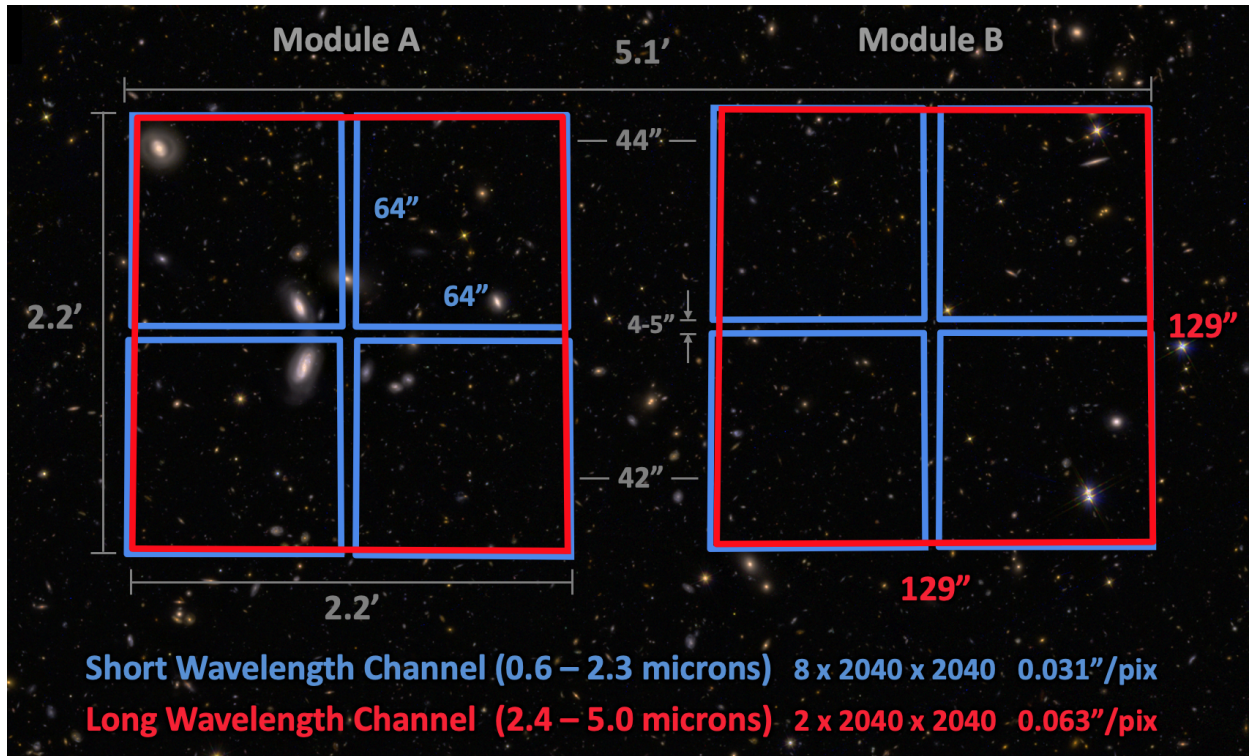


FIGURE 6.2 – NIRCam’s field of view across all 10 detectors in two redundant modules A and B. Each module consists of four (blue) short wavelength and one (red) long wavelength detector. Each short and each long wavelength detector has the same dimensions, whereas, the short wavelength detectors are smaller than the long wavelength detectors and have a higher resolution. NIRCam obtains images simultaneously with modules A and B using all 10 detectors. Combining both modules, NIRCam has a 9.7 arcmin^2 field of view (see [NIRCam Imaging documentation](#)).

TABLE 6.2 – All narrow (N), medium (M) and wide (W) NIRCam and MIRI filters of the 30 Doradus observation, their wavelength range, PSF sizes and general scientific use.

Filter	Wavelength [μm]	PSF FWHM ^a	Scientific use ^b
NIRCam			
F090W	0.795–1.005	0''033	Continuum, extinction of background stars
F187N	1.863–1.885	0''064	Hydrogen Pa α , strong shocked atomic emission
F200W	1.755–2.227	0''066	Continuum, extinction of background stars
F335M	3.177–3.537	0''111	Aromatic IR Bands: PAH, CH ₄
F444W	3.881–4.982	0''145	PAH bands, continuum
F470N	4.662–4.733	0''160	H ₂ O–O S(9), shocked molecular emission
MIRI			
F770W	6.581–8.687	0''207	broad PAH emission bands, continuum
F1000W	9.023–10.891	0''269	Silicate absorption bands, continuum
F1130W	10.953–11.667	0''375	broad PAH emission bands, continuum
F1800W	16.519–19.502	0''591	Silicate absorption bands, continuum

NOTES. ^(a) See [NIRCam Filters documentation](#) and [MIRI Filters documentation](#). ^(b) See the [30 Doradus project proposal](#) as well as the [NIRCam PSF](#) and [MIRI Filters](#) documentations.

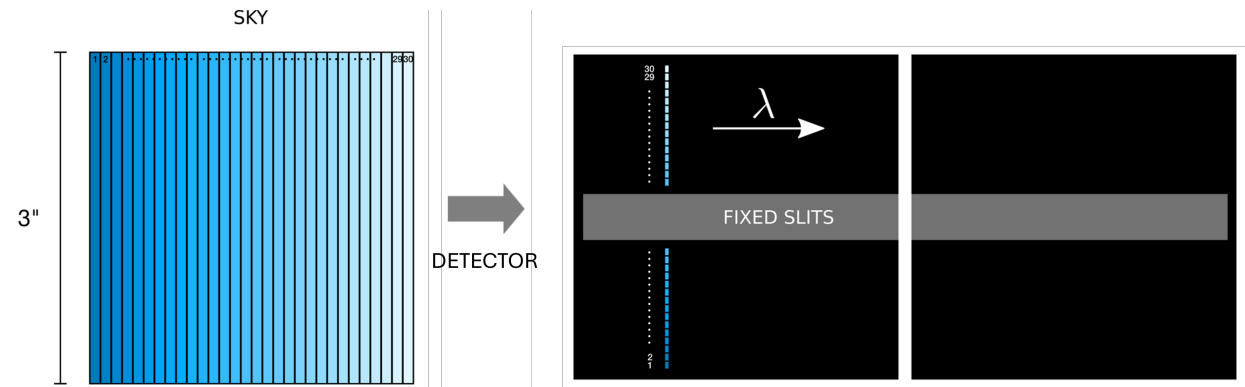


FIGURE 6.3 – Illustrated view of the 30 ‘virtual’ slice positions on the NIRSpec IFU $3'' \times 3''$ aperture (left) and the positions of the recorded spectra on two detectors NRS1/2 (right). The dispersion direction is indicated by the white arrow. Due to the gap between NRS1 and NRS2, a slit-dependent wavelength loss is present (see [NIRSpec IFU documentation](#)).

analysis makes use of NIRSpec IFU data. Therefore, here, we only focus on the IFU’s properties. More information on the other instruments can be found in the [JWST NIRSpec documentation](#).

Integral Field Spectroscopy (IFS) combines imaging and spectroscopy into a single exposure. Light reaching the telescope is directed by slicing mirrors to dispersive elements, producing spectra for each slice on a detector. Essentially, the IFU captures spectra simultaneously at each spatial pixel (or ‘spaxel’) of the imaging detector. After pipeline processing, the resulting 3D data cube has two spatial dimensions and one spectral dimension (see Sect. 3.2).

The NIRSpec IFU allows for spatially resolved imaging spectroscopy over a $3'' \times 3''$ sky region at three different spectral resolutions: $R \approx 100, 1000,$ and 2700 , either using a prism or a grating as the dispersive elements. The IFU aperture is separated into 30 slices (‘virtual slits’), each measuring $0''.103 \times 3''.2$, using slicing mirrors. The final reconstructed image is projected onto 900 spatial pixels (spaxels), each $0''.103 \times 0''.105$. To obtain spectra for each spaxel, the slices are rearranged into a line of individual slit images. Each slit image is independently dispersed by the dispersive element and recorded onto a different part of the detector array, ensuring the spectra do not overlap (see Fig. 6.3).

NIRSpec uses two HgCdTe detector arrays (see Sect. 5.2.1), NRS1 and NRS2, to record the spectra. Spectra acquired with high-resolution gratings span both detectors. However, due to a physical gap between the detectors, the wavelength range of the high-resolution spectra falling into the gap, is not accessible. The lost wavelengths depend on the ‘virtual’ slit and the grating (see [NIRSpec IFU documentation](#) and Tab. 6.3).

NIRSpec was designed to achieve high sensitivity. As a result, the detector pixels are relatively large and undersample the PSF almost over the entire wavelength range. Higher spatial resolution is recovered by a practise referred to as ‘dithering’ (see Sect. 6.4) to improve the PSF sampling (Böker et al. 2022).

The resolution of the NIRSpec images is diffraction-limited only above $>3.17 \mu\text{m}$, i.e., the PSF FWHM measures $\sim 0''.17$ at $5.3 \mu\text{m}$ (Jakobsen et al. 2022, see). The FWHM of the PSF at $2.5 \mu\text{m}$ is $0''.08$ and is comparable to the optical cameras on the HST.

TABLE 6.3 – NIRSpec long-pass (LP) filter and high-resolution (H) grating combinations relevant to this work, their corresponding spectral wavelength and the filter-dependent gaps. The spectral resolution is given both as a dimensionless quantity R as well as the maximally resolvable spread in wavelength and velocity space (see [NIRSpec Filters documentation](#)).

Filter/Grating	λ [μm]	Gap ^a [μm]	$R = \lambda/\Delta\lambda$	$\Delta\lambda$ [μm]	Δv [km s^{-1}]
F100LP/G140H	0.97–1.89	1.40780–1.48580	1839–3803	0.0005	163–79
F170LP/G235H	1.66–3.17	2.36067–2.49153	1875–3697	0.0009	160–81
F290LP/G395H	2.87–5.27	3.98276–4.20323	1931–3746	0.0015	155–80

NOTES. ^(a) The wavelength range of the gap depends on the slit. The given ranges quote the minima and maxima across all 30 slits. Therefore, emission lines are still observable in this range.

6.2.3 MIRI

The Mid-Infrared Instrument (MIRI; [Wright et al. 2023](#); [Gardner et al. 2023](#)) enables MIR imaging and spectroscopy from 4.9–27.9 μm through various observing modes: filter and coronagraphic imaging across nine and four photometric bands, respectively, low-resolution spectroscopy with fixed slits or slit-less and medium-resolution spectroscopy (MRS) with four IFUs. The MIRI imager and the MIRI/MRS IFU are relevant for this work and will be described in more detail below. For all other modes, relevant information can be found in the [JWST MIRI documentation](#).

MIRI detectors are Si:As (silicon doped with arsenic, an n-type dopant) IBC detector arrays with a total of 1024 pixels (see Sect. 5.2.2). Three such Si:As IBC arrays are used in total: one in the imaging module and the remaining two for short and long wavelength medium-resolution spectroscopy (see Fig. 6.4 and Fig. 6.5). With a pixel size of 0''11/pixel for the imaging array, the filter-imaging foV spans 112''6 \times 73''5. Only a fraction of the entire light-sensitive array is used for filter-imaging. Similar to NIRCcam, four pixels at the beginning and end of each row are reference pixels to monitor electronic variabilities. In addition, one half of the detector array is used for filter-imaging and the other for coronagraphic images. One array utilised for coronagraphy can also be added to filter-imaging whenever the calibration is valid (see [MIRI Imaging documentation](#)). The MIRI foV is significantly smaller than the foV of NIRCcam. This has to be kept in mind when planning observations with both instruments. All MIRI imaging filters are broadband filters. Four of them target prominent MIR silicate and dust features (see Tab. 6.2). MIRI imaging is diffraction-limited across all bands. The imaging sensitivity is limited by astronomical background at $\lambda < 15 \mu\text{m}$ and by thermal emission from the telescope above 15 μm (see Sect. 6.3 for more on the infrared background relevant to space missions).

The Medium Resolution Spectrometer (MRS; [Wells et al. 2015](#); [Argyriou et al. 2023](#)) consists of four IFUs (referred to as Channel 1–4) delivering spectro-photometric data between 4.9 and 27.9 μm with a spectral resolving power of $R \sim 3500$ –1500. The basic working principle of an IFU has been summarised in the previous section 6.2.2 and in section 3.2. In short, an IFU splits its field of view into spatial slices which act as ‘virtual’ slits. Each slice produces a spectrum. Only in post-processing three-dimensional data cubes with two spatial and one spectral dimensions are constructed.

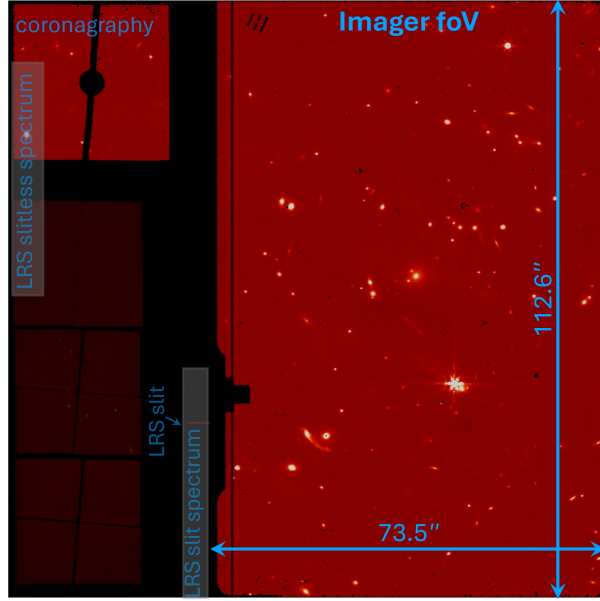


FIGURE 6.4 – The MIRI imager detector array and its distribution for filter-imaging, coronagraphic imaging and low-resolution spectroscopy. The highlighted filter-imaging foV on the right takes up the largest part of the detector. The four arrays on the left are used for coronagraphy. The position of the slit and slitless spectra is also indicated (Credit: [JWST MIRI Imaging documentation](#)).

The foV (as well as the pixel size) of the IFUs increases from $3''.2 \times 3''.7$ at $\sim 5 \mu\text{m}$ to $6''.6 \times 7''.7$ towards the long-wavelength cut-off at $\sim 28 \mu\text{m}$ (see Fig. 6.5). Each IFU consists of three sub-bands referred to as SHORT (A), MEDIUM (B) and LONG (C) which divide the total MIRI/MRS wavelength range in twelve photometric bands. Technically speaking, the last sub-band (4C) extends to $28.7 \mu\text{m}$. Unfortunately, the quantum efficiency drops to $\sim 5\%$ at $\sim 27.9 \mu\text{m}$ and decreases further at longer wavelengths. We cut-off the 4C spectra at $27.5 \mu\text{m}$ as we noticed significant noise which would make any flux measurements unreliable. Observations can be obtained simultaneously with the four IFUs, but using only one sub-band. The spectra of each slit are distributed across two detectors: sub-band spectra of channel 1 and 2 are recorded on MIRIFUSHORT and of channel 3 and 4 on MIRIFULONG (Fig. 6.5). Three exposures provide the full spectrum over the entire spectral range of the IFUs. The PSF increases significantly towards the long-wavelength end of the spectral range. To ensure useful spatial scaling, the pixel size and spatial slice width increase with wavelength. This also gradually reduces the number of slices in the IFU channels (see Fig. 6.5). Table 6.4 summarises the properties of the four MIRI/MRS IFUs.

Due to reasons described in chapter 5, MIRI requires a lower operational temperature due to the increased background at longer wavelengths. As the only MIR instrument, it is the coldest instrument on-board JWST cooled down to $\lesssim 6.7 \text{K}$ (Rieke et al. 2015). The temperature can be controlled to a very high level of accuracy and can be assumed to be constant during observations.

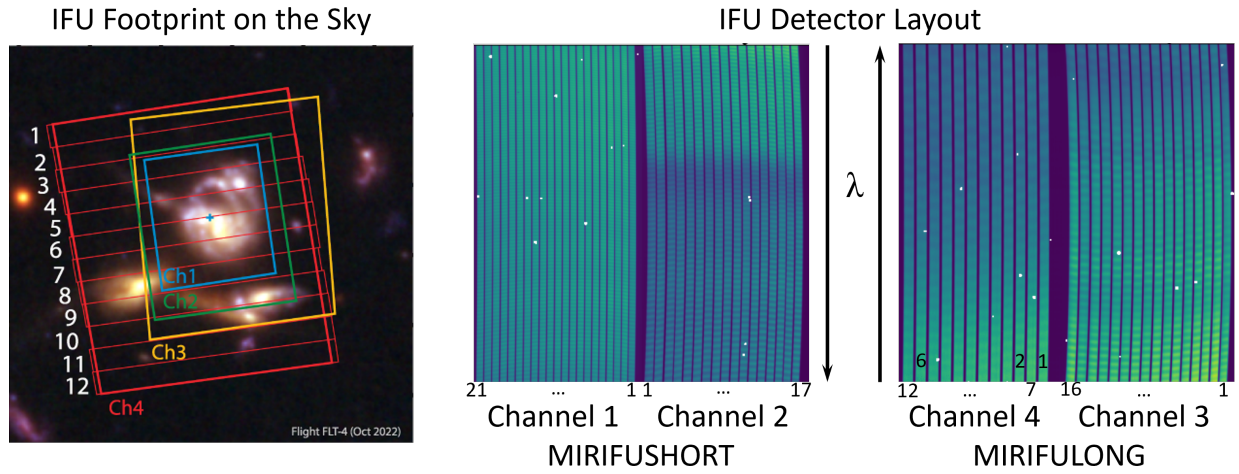


FIGURE 6.5 – MIRI/MRS IFUs foV (left) and their increasing dimensions towards channel 4. The 12 slices of Ch4 IFU are also indicated. The IFU detector layout (right) placing the slit spectra of two channels on one Si:As detector. The number of slices is indicated by the numbers at the bottom of the figure. The arrows indicate the dispersion direction (Credit: [Argyriou \(2021\)](#) and [JWST MIRI/MRS documentation](#)).

TABLE 6.4 – The four MIRI/MRS IFU channels, their field of view, wavelength coverage, pixel size and their resolving power (see [Argyriou et al. \(2023\)](#) and [MIRI Filters documentation](#)).

IFU	FoV	Sub-band	Wavelength [μm]	Pixel size	$R = \lambda/\Delta\lambda$	$\Delta\lambda$ [μm]	Δv [km s^{-1}]
Ch1	$3''2 \times 3''7$	SHORT (A)	4.90–5.74	$0''196$	3320–3710	0.002	90–80
		MEDIUM (B)	5.66–6.63		3190–3750	0.002	94–80
		LONG (C)	6.53–7.65		3100–3610	0.002	97–83
Ch2	$4''0 \times 4''8$	SHORT (A)	7.51–8.77	$0''196$	2990–3110	0.003	100–96
		MEDIUM (B)	8.67–10.13		2750–3170	0.003	109–95
		LONG (C)	10.02–11.70		2860–3300	0.004	105–91
Ch3	$5''2 \times 6''2$	SHORT (A)	11.55–13.47	$0''245$	2530–2880	0.005	118–104
		MEDIUM (B)	13.34–15.57		1790–2640	0.008	167–114
		LONG (C)	15.41–17.98		1980–2790	0.008	151–107
Ch4	$6''6 \times 7''7$	SHORT (A)	17.70–20.95	$0''273$	1460–1930	0.01	205–155
		MEDIUM (B)	20.69–24.48		1680–1770	0.01	178–169
		LONG (C)	24.19–27.90		1630–1330	0.02	184–225

6.3 Infrared Background

Science observations with JWST are performed against an astronomical and instrumental IR background. The main astrophysical IR background radiation originates, on the one hand, from the so-called zodiacal cloud of the Solar System which describes the thermal emission from interplanetary dust particles. The zodiacal dust reflects the sunlight below $\sim 3\ \mu\text{m}$ and emits in the IR above $\sim 3\ \mu\text{m}$. Due to its origin in the Solar System, its contribution is strongly dependent on the ecliptic latitude. In addition, due to temperature variations the zodiacal dust emission is dependent on the day of the year (Rigby et al. 2023b). Similarly, interstellar dust grains in the Galaxy contribute emitting in the spectral range of JWST through broad emission features from polycyclic aromatic hydrocarbons (PAHs). As interstellar dust originates from the Galactic plane, its contribution increases towards low Galactic latitude. This contribution is time-independent.

Even though the JWST mirrors are cooled to temperatures around 37 K, the self-emission from the mirrors, the sun shield and other components of the spacecraft cannot be avoided (Rigby et al. 2023a). It becomes dominant at wavelengths above $15\ \mu\text{m}$ and, therefore, has especially to be taken into account for the mid-IR instrument (see Fig. 6.7).

The contribution of the discussed background sources is not only limited to the amount seen by the field of view (foV) of the instrument, but increases slightly due to ‘stray light’, i.e., scattered emission from outside of the foV (Rigby et al. 2023b). For more details on the JWST background model (see Rigby et al. 2023b).

As the LMC is located at high galactic latitude, the contribution of the galactic ISM dust to the background is about one magnitude smaller than for observations towards the Galactic centre (see Fig. 6.7). Therefore, the background observation taken for the spectro-photometric data of the MYSO S7A analysed in this work focuses solely on the MIR bands. Figure 6.6 shows the position of the background field with respect to the science observation. It is located within a region of little local ISM emission to focus the calibration on the self-emission and the contribution from zodiacal dust.

6.4 Dithering

Dithering describes the practice of performing multiple exposures of the same field slightly offset with respect to each other. It is used to compensate for detector gaps (see Sect. 6.2.2), bad pixels and uncertainties in the flat-field calibration. In addition, it can improve the spatial and spectral resolution by improving pixel sampling (Böker et al. 2022). For each JWST instrument pre-defined dither patterns exist which are optimised for point-like or extended targets as well as for different background levels. See the respective instrument documentations for further information or starting from the general [Dithering documentation](#) webpage.

6.5 Detector readout patterns and exposure time

IR pixel arrays are complementary metal oxide semiconductor (CMOS) arrays where each pixel has its own readout amplifier. Even though, charge coupled devices (CCDs) have initially been used in IR astronomy, they produce high read-out noise in the low temperature environment required in the IR (Rieke 2007). While being exposed to IR radiation, detectors

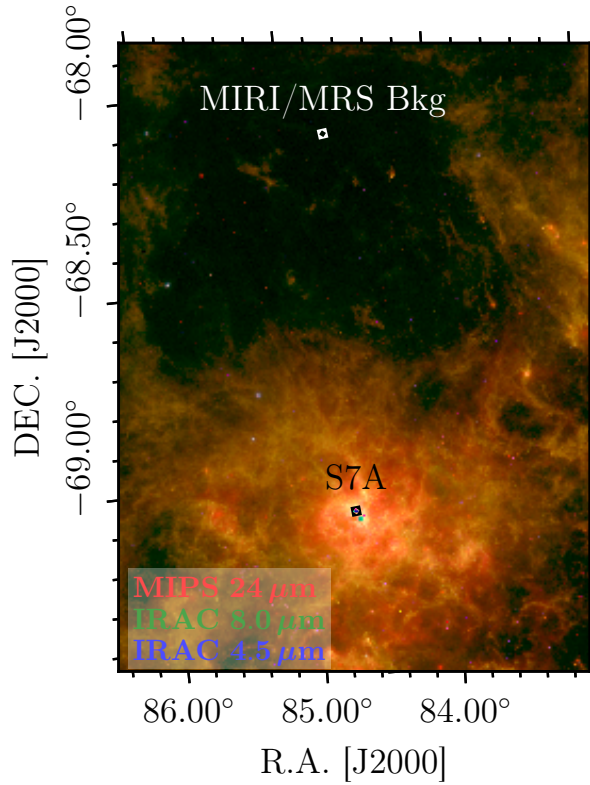


FIGURE 6.6 – *Spitzer* three-colour image (Meixner et al. 2006) illustrating the position of the science and MIRI/MRS background observations.

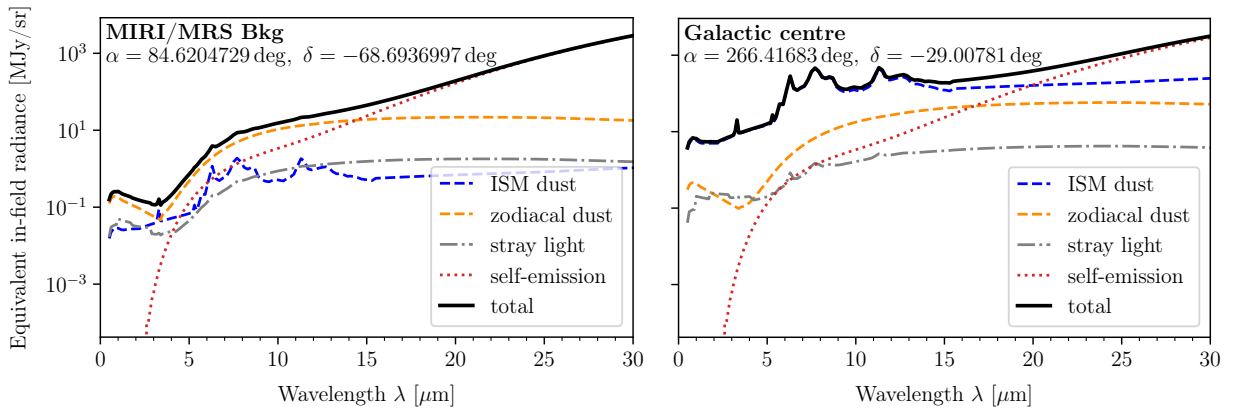


FIGURE 6.7 – JWST infrared background model for the background observation in the LMC (left) and for the Galactic Centre (right). The Galactic dust contribution (ISM and zodiacal) is about one order of magnitude less across the entire wavelength range for the LMC than towards the Galactic centre. The background contribution was calculated for the day of the YSO observation, the 20th June, using the [JWST Backgrounds Tool](#). The Galactic Centre is not observable with JWST on this day and a different date was chosen. The total background changes more significantly with direction than with time.

accumulate charge carriers while being read out multiple times according to readout patterns. The read-out process is non-destructive, i.e., charge is not erased until the exposure is completed. Unlike in CCDs, charge is not transferred between pixels.

Figure 6.8 illustrates the readout process for a single pixel of a NIRC*am* detector, but it can be applied also for the other instruments. An exposure consists of multiple integrations where charge accumulates and creates a ‘ramp’. Depending on the chosen readout pattern, a certain number of frames and skips (together also called samples) are combined into a group. The readout pattern also defines whether all individual frames or group averages (together with the first frame of the integration) are saved. For the readout patterns that average over multiple frames in an integration, the first read-out frame is always saved. On the one hand, it increases the dynamic range of the image. If saturation occurs in subsequent frames and the averaging cannot determine a photon count rate, the first frame may be used instead if it is not saturated as well. On the other hand, contamination by a cosmic ray would require the integration to be discarded. The initial frame would again be useful in case it has not been affected by the cosmic ray. However, to measure the slope of the ramp with only one frame, the bias offset has to be precisely characterised. An integration combines multiple groups into a ‘ramp’. After a set integration time (see Eq. 6.2), the charge is cleared from the pixels (reset).

$$T_{\text{integration}} = T_{\text{frame}} \cdot (N_{\text{groups}} \cdot N_{\text{samples}} - N_{\text{skips}}), \quad (6.2)$$

where $T_{\text{frame}} = 10.73677$ s is the time required to read-out the full light-sensitive detector through four outputs simultaneously and $N_{\text{samples}} = N_{\text{frames}} + N_{\text{skips}}$. As no data is acquired in the last skipped frame in an integration, it is subtracted. For MIRI detectors $N_{\text{skips}} = 0$. Note that the time necessary for reset is not included in the integration.

Finally, multiple identical integrations are executed sequentially to obtain an exposure. The exposure time therefore describes the total photon collection time at each dither position. Due to the use of readout patterns in JWST observations, the exposure time is not selected directly by the user but through the choice of three parameters: a readout pattern which defines the number of samples N_{samples} , the number of groups per integration (‘ramp’) N_{groups} which defines the integration time (see Eq. 6.2) as well as the number of integrations (‘ramps’) per exposure $N_{\text{integrations}}$.

$$T_{\text{exp}}^{\text{dither}} = T_{\text{integration}} \cdot N_{\text{integrations}} (+N_{\text{resets}} \cdot T_{\text{frame}}), \quad (6.3)$$

where $N_{\text{resets}} = N_{\text{integrations}} - 1$ are additional reset frames before an integration for MIRI detectors where no signal is acquired. The additional time for these resets only applies for MIRI. The reset time equals the read-out time for a single frame.

In case of a mosaic image, the total exposure time reported in the fits header accounts for the number of dithers per pointing N_{dithers} and the number of pointings (or visits) $N_{\text{pointings}}$ to cover the desired field:

$$T_{\text{exp}}^{\text{mosaic}} = T_{\text{exp}}^{\text{dither}} \cdot N_{\text{dithers}} \cdot N_{\text{pointings}}. \quad (6.4)$$

Table 6.5 reports the average exposure time for the science observation of 30 Doradus across the entire mosaic as reported in the header of the final calibrated mosaic image.

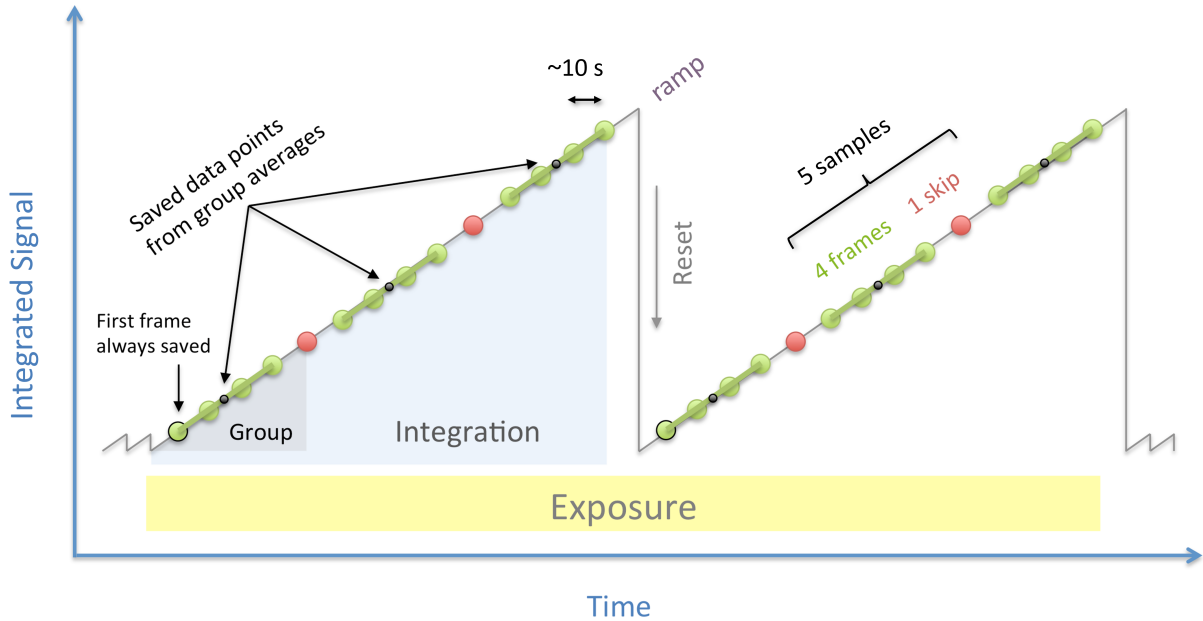


FIGURE 6.8 – General readout principle for a single pixel in JWST (NIRCam) detectors. An exposure consists of multiple integrations where charge accumulates and creates a ‘ramp’. Integrations are composed of groups which are (often) averages of readout frames. It takes approximately 10s to readout the light-sensitive pixel arrays in a NIRCam detector. The pixels are reset after an integration is completed. An astronomer can select a readout pattern, e.g., defining the number of frames in a group, the number of groups in one integration as well as the number of integrations per exposure. All parameters together yield the exposure of a dither. The figure was adapted with minor changes from the [JWST NIRcam Detector Readout Pattern documentation](#).

The accumulating-charge technique used for read-out allows ‘up-the-ramp’ fitting to determine the count rate obtained over the time of an integration. Advantages of this technique include the possibility of cosmic ray rejection and the reduction of readout noise. Each detector readout results in a so-called data frame. It is possible to choose to skip a readout frame which will not be considered in calculating the photon count rate. As data has been saved on-board of the satellite, this saves space and reduces the data load.

The pre-defined readout patterns have a couple of advantages. Firstly, they limit the science data volume which otherwise would overload the storage space onboard the satellite. At the same time, the reduced data rate allows longer exposures which might be necessary to achieve to desired scientific goal. Secondly, they maximise the dynamic range of an image, i.e., the ratio between the smallest and largest pixel value. Therefore, bright stars and faint diffuse structures can successfully be imaged together. Thirdly, they increase the signal-to-noise ratio in regions of high background.

TABLE 6.5 – Readout patterns, their number of samples N_s and frames N_{fr} used in different observing modes. For all instruments and filters, the number of groups per integration N_{gr} , the number of integrations per exposure N_{int} , the number of dithers N_{dith} , the total number of pointings N_p as well as the average exposure time T_{exp} is listed.

Instrument	Pattern	N_s	N_{fr}	Filter	N_{gr}	N_{int}	N_{dith}	N_p	T_{exp} [s]
NIRCam	BRIGHT1	2	1	F090W, F335M	9	1	5	4	913
				F200W, F444W	5	2	10	4	1020
	SHALLOW2	5	2	F187N, F470N	6	1	5	4	1449
MIRI	FASTR1	1	1	F770W, F1000W, F1800W	8	4	10	2	971
				F1130W	12	4	10	2	1415
				MRS All	30	3	4	1	1021
NIRSpec	NRSIRS2RAPID ^a	1	1	All	5	1	8	1	700

NOTES. ^(a) NRSIRS2RAPID has a larger $T_{\text{frame}} = 14.59$ s as the readout pattern was improved to reduce $1/f$ noise and reference pixels are sampled more frequently (see [Rauscher et al. \(2011\)](#) and [IRS2 readout documentation](#)). An additional reset frame at the beginning of each exposure was included.

7 Data overview

For our analysis, we use the publicly available observations of the central star cluster R136 in NGC 2070 in the 30 Doradus star-forming region in the Large Magellanic Cloud. Exposures were obtained during the Early Release Observations #02729 (PI: Pontoppidan) in June 2022. All uncalibrated data products can be downloaded from the Barbara A. Mikulski Archive for Space Telescopes ([MAST](#)). The technical details of the observations can be found [online](#) in the proposal overview.

The raw data products are processed with the [JWST Calibration Pipeline](#) version 1.14 ([Bushouse et al. 2023](#)) and the Calibration Reference Data System version 11.17.22 (CRDS; [Greenfield & Miller 2016](#)). The Calibration Reference Data System (CRDS) manages all instrument-specific reference files necessary for calibrating raw data products. Science calibration reference files include, e.g., flat fields, bad pixel masks, information on the dark current for each pixel, and photometric calibration files. Further, parameter reference files configure the default arguments for a particular pipeline stage depending on the used instrument mode. A CRDS *context* contains file mappings that point to the correct reference files for a given instrument and pipeline version. Knowledge of the CRDS context is important as reference files are continually updated based on in-flight data analysis to improve the instrument performance. For the datasets used in this work, the CRDS contexts are: `jwst_1237.pmap` (NIRCam images), `jwst_1241.pmap` (MIRI images and MIRI/MRS data cubes) and `jwst_1231.pmap` (NIRSpec data cubes).

NIRCam observations were performed in the three wide-band filters F090W, F200W, F444W, the two narrow-band filters F187N, F470N, and the medium filter F335M. Wide-band filters reveal background/foreground stars, YSOs as well as diffuse emission. The medium filter together with wide-band MIRI filters traces PAH and silicate emission features (see [Tab. 6.2](#)). The two narrow-band filters show shocked atomic and molecular H emission. To cover the $7'4 \times 4'4$ field of R136 and its surrounding bubble with NIRCam's field of view, four visits are necessary. The imaging is performed using a standard FULLBOX dither pattern (see [Sect. 6.4](#)) and a BRIGHT1 readout pattern ([Sect. 6.5](#)) for medium and wide-band filters and a SHALLOW2 pattern for narrow-band filters. Five dithers were obtained for each filter. The total dataset consists of 20 individual exposures per filter.

MIRI exposures in four wide-band filters F770W, F1000W, F1130W and F1800W are read-out using the FASTR1 pattern. The dither strategy follows the 10-point LARGE CYCLING pattern. MIRI images only a subregion of the NIRCam mosaic field covering R136 but only $\sim 50\%$ of its shell towards the north-west. Two MIRI imager tiles (and the coronagraph, see [Fig. 6.4](#)) yield a final area coverage of $\sim 6 \text{ arcmin}^2$ which is about $\sim 20\%$ of the region covered by NIRCam.

IFU spectral imaging is focused on the massive young stellar object S7A in the north-west of R136. The source resolves into multiple point sources as shown in HST/WFCP3 images ([Sect 9.1](#)). To achieve high resolution spectra in the $1\text{--}5 \mu\text{m}$ band, NIRSpec observations are taken in three long-pass filters paired with high-resolution gratings: F100LP/G140H, F170LP/G235H and F270LP/G395H. NIRSpec exposures are read out using the improved

NRSIRS2RAPID pattern to reduce $1/f$ noise (Rauscher et al. 2011, 2014). As the source is assumed to be extended towards longer wavelengths, an 8-point LARGE CYCLING dither pattern was chosen.

MIRI/MRS observations are performed with all four IFU channels across all twelve sub-bands. A 4-point dither pattern and the FASTR1 readout pattern is used.

No dedicated background observations were performed for the NIRC*am*, MIRI imaging and NIRSpec IFU observations. Only for MIRI/MRS IFS a dedicated background observation was taken, mainly to establish the thermal self-emission that is the most prominent background source at MIR wavelengths (see Sect. 6.3; Fig. 6.6 and Fig. 6.7). A field without apparent point-sources and little emission from the local ISM was chosen. The readout-pattern FASTR1 is the same as for the science observations, but a 2-point dither pattern is sufficient. Together with 25 groups per integration and three integrations per exposure this yields an average exposure time of 427 s.

The average exposure time for each observing mode and filter is summarised in table 6.5. It is noted that due to dithering and the combination of images into mosaics, the exposure time is not uniform in the final images.

8 Data Reduction

The complete pipeline processing from the downloaded uncalibrated files to the final science products involves three stages both for Imaging and IFS. In each stage several calibration steps are performed. Stage 1, also referred to as **Detector1**, corrects for several detector effects. It is therefore run for all instruments and modes and is discussed first (see below). There exist a number of MIRI-specific detector effects that have been studied by [Morrison et al. \(2023\)](#). These are beyond the scope of this work and are not discussed.

For NIRC*am* and MIRI/MRS, processing beyond the default calibration steps is necessary to achieve satisfactory science products. This includes additional noise corrections or detector effects as well as astrometric alignment. These steps are either not included in the general JWST pipeline processing or do not achieve satisfactory results therein and separate tools are used. Section 8.1 discusses the three pipeline stages and important calibration steps as well as additional corrections in the context of NIR and MIR Imaging. Section 8.2 discusses the pipeline stages focusing on IFS. All pipeline stages are mostly run with default parameters. Only when they differ, they are explicitly mentioned in the sections below.

Detector1 corrects for detector-specific effects. Pixel values in uncalibrated exposures are DNs. Firstly, pixel values are checked for reliability and flagged based on their imperfections. Such include dead pixels without any value, hot pixels exhibiting excessive dark current or pixels with low quantum efficiency (QE). Pixel values are also checked for saturation and saturated pixels are masked. Secondly, the bias level measured by the reference pixels not illuminated by radiation is subtracted from the light-sensitive array. Further, the non-linearity of the detector signal due to non-constant gain or QE is corrected and the dark current subtracted. For NIR instruments, additionally, an overall ‘super’-bias level is subtracted and ‘ghost’ images from previous exposures are deleted. For MIRI several MIRI-specific corrections have to be performed (see [Morrison et al. 2023](#)). Subsequently, the `jump_detection` step detects large changes in the ADU values of consecutive frames (or groups if only averages were saved) identifying saturation or cosmic ray (CR) hits which produced a large amount of electric charge. Saturated or contaminated groups are excluded. Finally, the slope of each integration ramp is determined to convert counts to count-rates. After successful slope fitting, the final **Detector1** output files are 2D partially calibrated count-rate exposures in units of DN/s. For further details on the **Detector1** pipeline stage, see [Detector1 documentation](#) and references therein.

8.1 NIRC*am* and MIRI Imaging

The uncalibrated exposures are processed in five (four) steps to obtain calibrated mosaic images of NGC 2070 in each of the six (four) NIRC*am* (MIRI) filters. Figure 8.1 illustrates the complete data reduction process. The three pipeline stages common for NIR and MIR Imaging modes are **Detector1**, **Image2** and **Image3**. NIRC*am* images require additional low frequency ($1/f$) noise correction. For NIR and MIR images astrometric alignment is necessary for which the *Gaia* DR3 point source catalogue ([Gaia Collaboration et al. 2023](#)) is chosen.

It is noted that the exact order of the calibration steps within a pipeline stage depends on

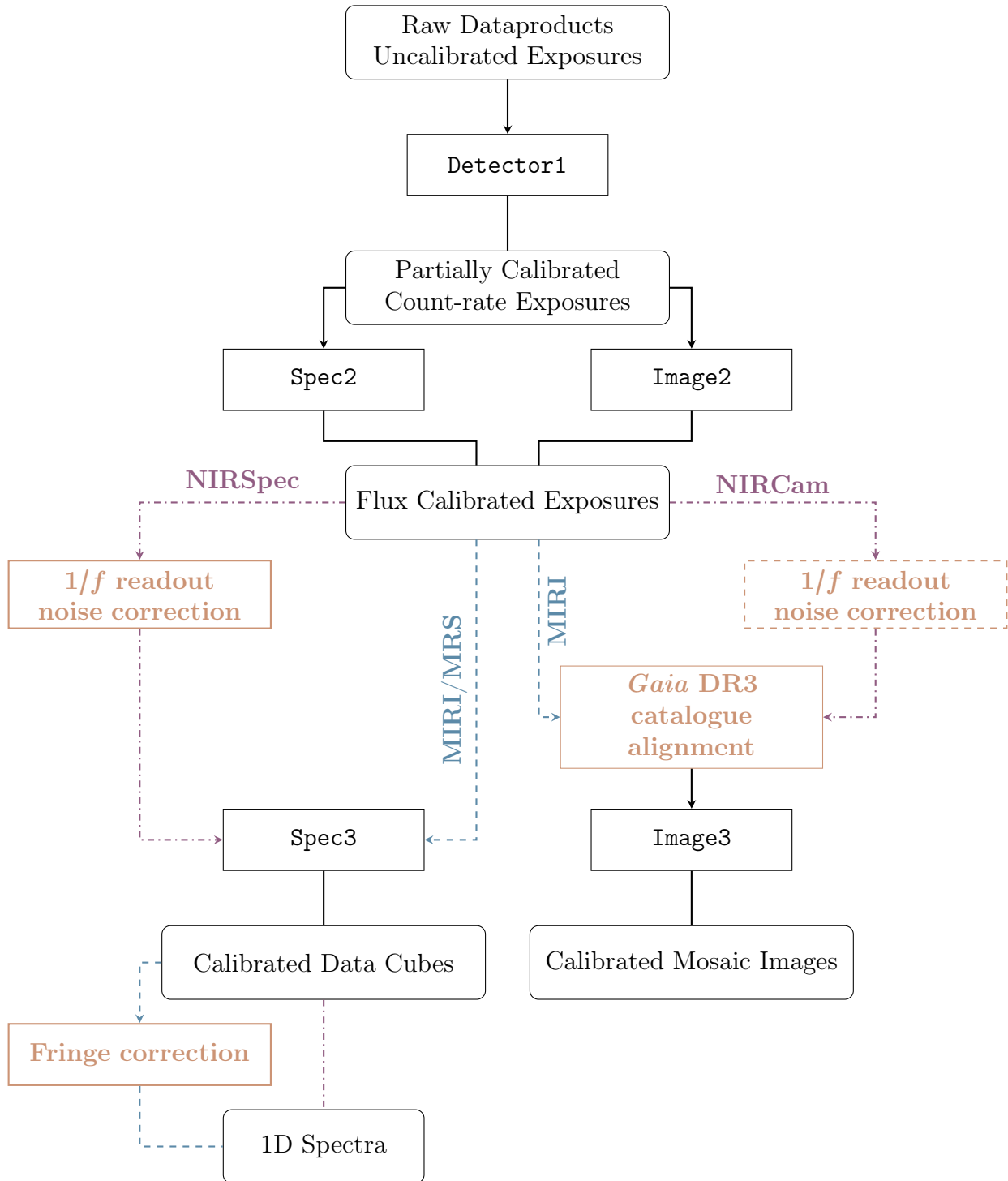


FIGURE 8.1 – Pipeline processing of uncalibrated NIRCам, NIRSpec and MIRI data products. After flux calibrated exposures are obtained with the `Image2/Spec2` steps, the processing differs for NIR and MIR instruments. The dashed lines focus on MIRI and dashed-dotted on NIRCам/NIRSpec. Additional calibration steps not performed with the default pipeline are marked in colour. Details on the individual steps can be found in the text.

the instrument and the observing mode used. For further corrections and instrument-specific calibrations, please consult the [JWST Science Calibration Pipeline documentation](#) (Bushouse et al. 2023), the [Detector1](#), [Image2](#) and [Image3](#) documentations and the references therein.

Image2 processes the partially-calibrated count-rate exposures produced in the **Detector1** pipeline stage. In a first step, the detector pixel coordinates are converted to R.A. and DEC. based on the attitude information of the pointing during the observation. Further, exposures are divided by flat fields. These calibration frames record variations in the response of single pixels. If a background observation was requested, it is subtracted. Additional corrections are applied to MIRI data. Below $10\ \mu\text{m}$, scattering and multiple reflections between the anti-reflection at the backside and metal coatings at the frontside of the Si:As detector (see Fig. 5.2) cause an additional ‘cruciform’ diffraction pattern along the row and column directions (e.g., [Argyriou et al. 2023](#)). It becomes particularly pronounced for bright sources. Finally, raw data counts are flux calibrated and converted into physical units. The primary conversion factor relates count-rates in DN/s to surface brightness in MJy/sr. A secondary factor for $\mu\text{Jy}/\text{arcsec}^2$ is also reported in the header. The above steps produce flux-calibrated images in units of MJy/sr.

1/f noise correction The NIR detector readout electronics generate low frequency correlation ($1/f$) noise which appears as horizontal stripes spanning over the entire detector width. This noise depends mainly on the temperature of the electronics and is correlated between pixels. Sampling of the reference pixels reduces the contribution of $1/f$ noise by a few electrons, but is not sufficient. The official JWST calibration pipeline does currently not include any steps to further mitigate $1/f$ noise ([1/f noise documentation](#)). However, external publicly available packages can be used instead. In this work, we use the python script [image1overf](#) provided by Chris Willott on the **Image2** output files. This method is the most widely used in literature, including in the previous data reduction of the same dataset by [Fahrion & De Marchi \(2023\)](#). However, running this correction did not result in major changes compared to exposures calibrated with the default pipeline. We assume that the highly variable background is the reason. Nevertheless, we proceed the following data reduction steps on the $1/f$ -noise-corrected exposures.

Image3 is the final pipeline stage producing science images or mosaics. As the spacecraft pointing information is subject to uncertainties, the world coordinate system (WCS) information of the calibrated **Image2** exposures is refined by using point-like sources common to multiple images (**tweakreg** step). The background between single exposures is not constant. To avoid background variations in the final mosaic, the background is matched between exposures comparing overlapping regions (**skymatch**). Images are checked for possible CR contamination that may have been missed in the **Detector1** stage (**outlier_detection**). Intersecting sky areas are searched for ‘sources’ that do not appear in multiple images as CRs hits can be treated as moving targets changing their position on the detector during a few consequent exposures. Finally, exposures for each filter are combined into final science images. Bad pixels masked during the **Detector1** stage are excluded. The final fits files have multiple extensions. Apart from the science arrays, also error arrays reporting the

standard deviation for each pixel value, several variance arrays for individual noise contributions (poisson, readout, flat field) and information on the number of individual exposures contributing to a pixel value in the final mosaic are included.

***Gaia* DR3 alignment** The `tweakreg` step in `Image3` pipeline stage is not sufficient to correctly align individual exposures. Instead, the JWST/HST Alignment Tool (JHAT; Rest et al. 2023) performs better astrometric alignment by comparing star positions measured in NIRC*am* images with those reported in the *Gaia* DR3 catalogue. JHAT corrects the WCS information of the `Image2` output files after the initial WCS assignment. `Image3` is run with the `tweakreg` step switched off.

8.2 Near- and Mid-infrared IFS

The uncalibrated spectra are processed in three (four) steps to obtain calibrated spectra and 3D data cubes of S7A in each of the three (twelve) NIRSpec (MIRI/MRS) bands. Figure 8.1 illustrates the complete data reduction process. The three pipeline stages common for NIR and MIR Imaging modes are `Detector1`, `Spec2` and `Spec3`. The `Detector1` stage is very similar for NIRC*am*, NIRSpec and MIRI and was discussed above. MIRI/MRS spectra have to be additionally corrected for ‘fringing’ (see below).

It is noted that the exact order of the calibration steps within a pipeline stage depends on the instrument and the observing mode used. For further corrections and instrument specific calibrations, please consult the JWST Science Calibration Pipeline documentation (Bushouse et al. 2023), the `Detector1`, `Spec2` and `Spec3` documentations and references therein.

`Spec2` processes the partially-calibrated count-rate exposures produced in the `Detector1` pipeline stage. For spectroscopic data, these exposures have one spectral dimension, the dispersion direction, and a spatial dimension (along a ‘virtual’ slit). In a first step, the detector pixel coordinates are converted to R.A. and DEC. based on the attitude information of the pointing during the observation. Further, exposures are divided by flat fields. These calibration frames record variations in the response of single pixels. If a background observation was requested, it is subtracted. For NIRSpec exposures, it is a simple image-from-image subtraction as for `Image2`. For MIRI/MRS data, the background is subtracted during `Spec3` using a different method (see below).

In contrast to the image calibration pipeline, the $1/f$ noise correction for NIRSpec is incorporated in the official pipeline and applied at this stage. NIRSpec exposures are additionally corrected for light losses in the optical system. Due to scattering not all light captured from the source reaches the diffraction gratings.

For MRS data, several issues contaminating spectra have to be addressed. Scattering and multiple reflections between the anti-reflection at the backside and metal coatings at the frontside of the Si:As detector (see Fig. 5.2) cause spectral ‘fringing’ discussed separately below. Due to the design of the MRS detector layout, neighbouring slices do not corresponds to neighbouring regions on the sky. In addition, slices are periodically offset in wavelength. Neighbouring pixels in different slices do not record the same wavelength. Emission lines appear in a step-like pattern in the detector images (see Fig. 8.2). Internal reflections cause the

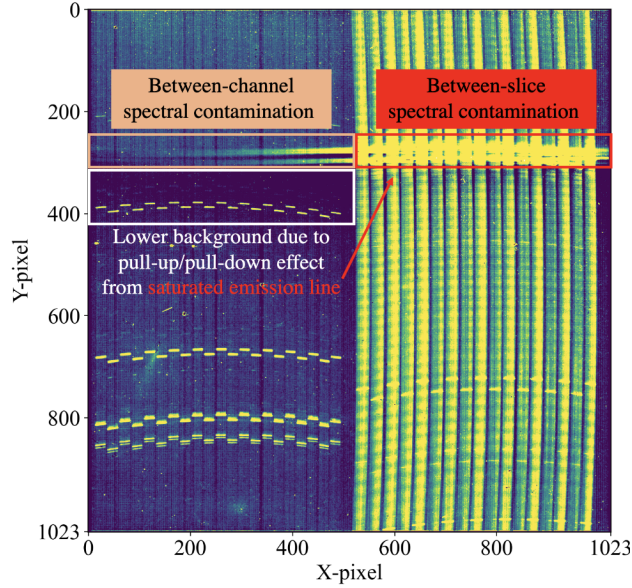


FIGURE 8.2 – MRS artifacts associated to bright emission lines in the detector image. Figure adapted from [Argyriou et al. \(2023\)](#).

PSF to be broadened in along-slice direction. Bright emission lines extended across multiple slices in the detector and produce fainter emission features at other wavelengths which do not originate from the observed astrophysical target (see Fig. 8.2). This contamination can extend not only between different slices in a single channel, but propagate to a different channel whose spectra are recorded on the same detector. Moreover, electronic cross talk decreases (pull-down) or increases (pull-up) the signal close to bright emission lines ([Dicken et al. 2022](#)). Except for spectral fringing, no corrections are applied in the pipeline. Inspecting the detector plane images is therefore an important step in analysis of MRS data cubes. Further details on the MRS issues can be found in [Argyriou et al. \(2023\)](#) and in the [MRS known issues documentation](#). Apart from spectral fringing, none of the above described artifacts are present in the MRS spectrum of S7A.

Finally, raw data counts are flux-calibrated and converted into physical units. For spectroscopic observations, 2D sensitivity maps are constructed that relate each pixel’s count rate (DN/s) to surface brightness (MJy/sr) based on wavelength and the pixel area. Only scalar conversion factors are reported in the header (for MJy/sr and $\mu\text{Jy}/\text{arcsec}^2$). The photometric response of MIRI/MRS detectors decreases with time. The 2D sensitivity array contains corrections derived from observations of standard stars. The above steps produce calibrated count-rate exposures in units of MJy/sr.

Spec3 is the final pipeline stage for spectroscopic data and produces 3D data cubes and 1D spectra from the 2D detector exposures. Exposures are checked for possible CR contamination that may have been missed in the **Detector1** stage (**outlier_detection**). For NIRSpec, the final data cubes still had a relatively high CR contamination rate. CRs deposit a large amount of charge at a very particular energy and position in the detector. In 1D spectra, CRs resemble emission line features. However, they can be easily be identified comparing suspicious emission lines with corresponding image slices in the data cubes.

For MIRI/MRS data, a so-called ‘master’ background is subtracted to achieve a higher

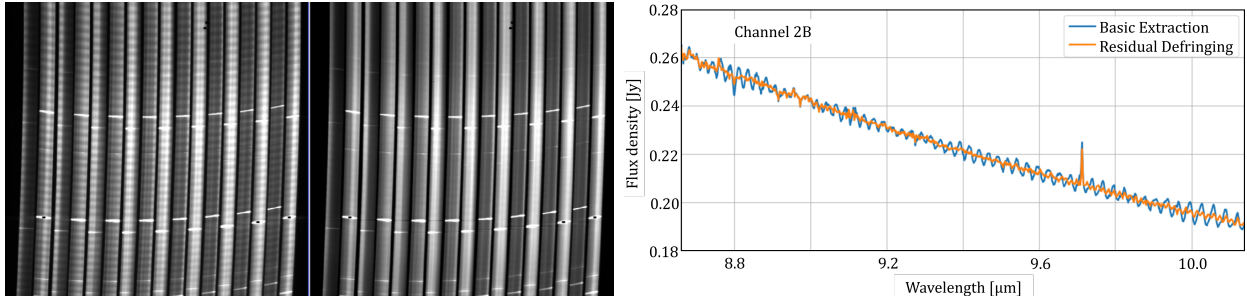


FIGURE 8.3 – MRS Fringing. Figures adapted from the [MRS known issues documentation](#).

signal-to-noise ratio than with the simple technique used in `Image2` or `Spec2`. Background observations are processed through the entire pipeline prior to science data using the same set of parameters. From the 3D background data cubes, a 1D spectrum is extracted and subsequently interpolated by wavelength of each pixel in the 2D spectra recorded by the detector to create an image. The resulting 2D array is subtracted from the science data.

Finally, 3D science data cubes are created (`cube_build`) and 1D spectra are extracted from pre-defined apertures (`extract_1d`). In this work, spectra from the 3D data cubes are extracted using a custom extraction routine instead of the `extract_1d` step in the `Spec3` pipeline to improve the selection of aperture sizes. The spectral extraction is discussed in section 9.3.1.

MIRI/MRS Fringing Several internal reflections between different layers of the Si:As detector (see Fig. 5.2) allow interference as a function of wavelength. This spectral ‘fringing’ manifests itself in strong periodic variations of the recorded signal in dispersion direction across the entire detector array. The modulations become particularly dominant in the continuum emission of 1D spectra (see Fig. 8.3). If not addressed, ‘fringing’ can easily be confused with emission features in 1D spectra. Further, weak emission lines are lost and large uncertainties in continuum fitting are introduced. Even though the frequencies of the ‘fringe’ patterns are known, modulations can occur at additional frequencies. For further details on the origin of spectral ‘fringing’ see, e.g., [Argyriou et al. \(2020\)](#).

Two optional fringe identification and correction steps are present in the pipeline: `fringe` in `Spec2` and `residual_fringe` in `Spec3`. The details of the methods used to remove ‘fringing’ are reported in the [MRS known issues documentation](#). In addition to the residual fringe correction performed in the `Spec2` stage, further fringe correction is performed when extracting 1D spectra with a custom routine. As the spectral extraction from a defined aperture sums the flux of multiple pixels, previously unidentified fringe contamination could be enhanced. Our custom routine tries to correct the contamination by fitting the periodic signals. Even though, all the above mentioned corrections have been performed, residual ‘fringing’ is still present in the extracted spectra. As this work focuses on spectral emission features, spectra have been examined by eye for ‘fringing’ residuals and contaminated regions excluded from further analysis.

9 IFU emission line spectrum of massive YSO S7A

The spectroscopic data accompanying the NIRC*am* and MIRI Imaging of the 30 Doradus region focuses on the $\sim 20 M_{\odot}$ YSO S7A (as referred to in [Walborn et al. 2013](#)) located towards the north-east of the central massive star cluster R136 in NGC 2070. S7A is part of a ‘double source’ complex together with a second YSO S7B ([Walborn et al. 2013](#)). Their angular separation is $\sim 4''$. They are embedded in a dust pillar located in the north-east of R136 ([Walborn et al. 2013](#)) and oriented towards the super-cluster (see Fig. 9.8). In the optical, in particular in the *Y*-band, S7A dominates over S7B ([Walborn et al. 2013](#)). For wavelengths longer than the *J*-band and especially in the NIR and MIR, S7B is brighter than S7A which hints towards a younger nature of S7B with respect to S7A. S7A/B are two of the brightest and reddest IR sources in 30 Doradus that have been known since the 90s, but only one detailed spectroscopic observation has been performed (see [van Gelder et al. 2020](#), and summary below). The increasing foV of the MIRI/MRS IFUs reveals S7B at the longest MIR wavelengths starting with an partial image at $\sim 11.6 \mu\text{m}$ (3A).

The following chapter summarises the previous studies both on S7A/B as these sources have always been discussed together. The most striking features of the system are first discussed in the context of NIRC*am* and MIRI images (Sect. 9.2). Subsequent chapters focus on the spectra and images extracted from the JWST IFU cubes. This work especially focuses on the emission line spectrum and several parameters are derived using line ratios.

9.1 Previous studies

The first record of S7A/B is reported by [Hyland & Jones \(1991\)](#) and [Hyland et al. \(1992\)](#) who had for the first time detected a bright IR source at the same position in ground-based NIR images in the *J* ($1.25 \mu\text{m}$) and *K* ($2.2 \mu\text{m}$) obtained with the Anglo-Australian Telescope in 1982. The source was identified as a high-mass protostellar candidate (P1; IRS-124) through its highly increased *J* – *K* colour. In addition, [Hyland et al. \(1992\)](#) present the first NIR spectrum (2.0 – $2.45 \mu\text{m}$) with a resolving power of $R = 140$. [Rubio et al. \(1992\)](#) confirm the presence of a protostar (IRS-N-1 therein) in a new set of *J*, *H* ($1.65 \mu\text{m}$), *K* images of the same region obtained in 1991 using the Las Campanas Observatory (LCO) in Chile.

The system was then resolved by [Rubio et al. \(1998\)](#) into two individual sources IRSN-122 (S7A) and IRSN-126 (S7B) in another set of *JHKs*¹ images at LCO. [Brandner et al. \(2001\)](#) continued the NIR photometric study of the central 30 Dor region including S7A (30Dor-NIC12b therein) and S7B (30Dor-NIC12d therein) with ground-based *JHK* images from the ESO/MPI 2.2m telescope and space-based NIR Imaging using HST/NICMOS.

[Walborn et al. \(1999\)](#) compare HST/NICMOS NIR images with HST/WFPC2 optical images. A ‘nebular arc’ is detected around S7A both in the optical as well as in the IR. This shell is clearly visible in NIRC*am* and NIRS*pec* images (see Fig. 9.2) where JWST resolves a brightness and therefore density gradient. Additionally, [Walborn et al. \(1999\)](#) point out three other very red IR sources near S7A. The NIRC*am* F090W image resolves seven faint objects close to S7A. A further source appears in the NIRC*am* F200W image and is also present in the narrow-band filter F187N tracing the Hydrogen $P\alpha$ line as well as the medium

¹The *Ks* filter is a modified *K* filter with a narrower FWHM which reduces the thermal background for IR observations with ground-based telescopes ([Rubio et al. 1998](#)).

filter F335M exposing PAH features.

Further NIR photometric data was acquired during the Spitzer Space Telescope Legacy Program ‘Surveying the Agents of a Galaxy’s Evolution’ (SAGE; Meixner et al. 2006), the ‘Infrared Survey Facility (IRSF) Magellanic Clouds Point Source Survey’ (Kato et al. 2007) and the ‘VISTA Magellanic Clouds’ survey (VMC; Cioni et al. 2011), all discussed in Walborn et al. (2013). SAGE and IRSF NIR images of the LMC are accompanied by point source catalogues. S7A (S7B) can be matched to SSTISAGEMA/C J053846.84-690505.4 (SSTISAGEMA J053847.02-690501.7) in the SAGE IRAC Source Archive/Catalogue and 05384685-6905058 (05384701-6905019) in the IRSF source catalogue. There are no matches in the SAGE MIPS catalogues and hence no photometric data on S7A/B in the MIR as the detector is oversaturated at the source position.

Using the updated NIR photometric measurements from the surveys described above as well as optical upper limits and IR fluxes from HST/WFPC2 F555W ($\gtrsim 22$ mag for both S7A/B) and F814W (20.4 mag for S7A and 21.2 mag for S7B), Walborn et al. (2013) fit YSO models computed by Robitaille et al. (2006, 2007) to the spectral energy distributions. For S7A, the best-fit model predicts a stellar luminosity $L_* = 3.0 \times 10^4 L_\odot$, effective temperature $T_{\text{eff}} = 2.0 \times 10^4$ K, stellar mass $M_* = 15.2 M_\odot$, envelope mass $M_{\text{env}} = 1.6 \times 10^2 M_\odot$, almost no disk mass ($M_{\text{disk}} = 0.04 M_\odot$) as well as an interstellar extinction of $A_V = 3.2$. S7B is anticipated as a Class I object with stellar luminosity $L_* = 7.3 \times 10^4 L_\odot$, effective temperature $T_{\text{eff}} = 1.7 \times 10^4$ K, stellar $M_* = 23.4 M_\odot$ and envelope $M_{\text{env}} = 71.5 \times 10^2 M_\odot$ masses, no disk mass as well as an interstellar extinction of $A_V = 0.1$.

Nayak et al. (2016) investigate the relation between massive star formation and molecular clumps. Previously, it has been found that the bolometric luminosity of MYSOs correlates with the clump mass (e.g., Purser 2017). Such clumps can be studied using CO molecules, in particular the $^{12}\text{CO}(2-1)$ and $^{13}\text{CO}(2-1)$ transitions in radio, e.g., with the Atacama Large Millimeter/Submillimeter Array (ALMA; Indebetouw et al. 2013). Firstly, Nayak et al. (2016) find that S7A (therein J84.695932-69.083807) and S7B (therein J84.695173-69084857) are associated with $^{12}\text{CO}(2-1)$ and $^{13}\text{CO}(2-1)$ clumps (S7A: clump ID 13, 14, 25; S7B: clump ID 15 in their tables 1 and 2). Previously, Indebetouw et al. (2013) had discussed this association (S7A: clump 11, S7B: clump 21 in their table 3) and estimated a clump velocities of $v_{11} = 248.2 \text{ km s}^{-1}$ and $v_{21} = 250.1 \text{ km s}^{-1}$. Secondly, they use SAGE IRAC photometric measurements and far-infrared (FIR) completeness limits from the Herschel HERITAGE point source catalogues (Meixner et al. 2013; Seale et al. 2014) to obtain mass and luminosity estimates by fitting SEDs with the Robitaille et al. (2007) YSO models. Mass $M_*^{\text{S7A}} = 21.8_{-8.07}^{+12.0} M_\odot$, $M_*^{\text{S7B}} = 19.0_{-5.87}^{+10.5} M_\odot$ and luminosity $L_*^{\text{S7A}} = 5.62_{-4.16}^{+6.49} \times 10^4 L_\odot$, $L_*^{\text{S7B}} = 5.62_{-4.16}^{+6.49} \times 10^4 L_\odot$ estimates agree within the uncertainties with the previous result of Walborn et al. (2013).

A detailed spectral analysis of S7A/B is for the first time performed by van Gelder et al. (2020) using the X-Shooter intermediate resolution slit spectrograph on the Very Large Telescope (VLT; Vernet et al. 2011) in the UV-Blue, visible and NIR bands (300–2500 nm). The slit length of $0''.6$ for the NIR observations results in a resolving power of $R = 8100$. Unfortunately, the observations suffered from bad seeing conditions (FWHM $\sim 2''.2$). The spectrum of S7A show a continuum in the UVB band (300–550 nm) continuously decreasing, until it disappears $\sim 1 \mu\text{m}$ and reappears $\sim 1.5 \mu\text{m}$. Photospheric Hydrogen Ba and He I absorption features are detected. Photospheric lines allow, firstly, the measurement of the

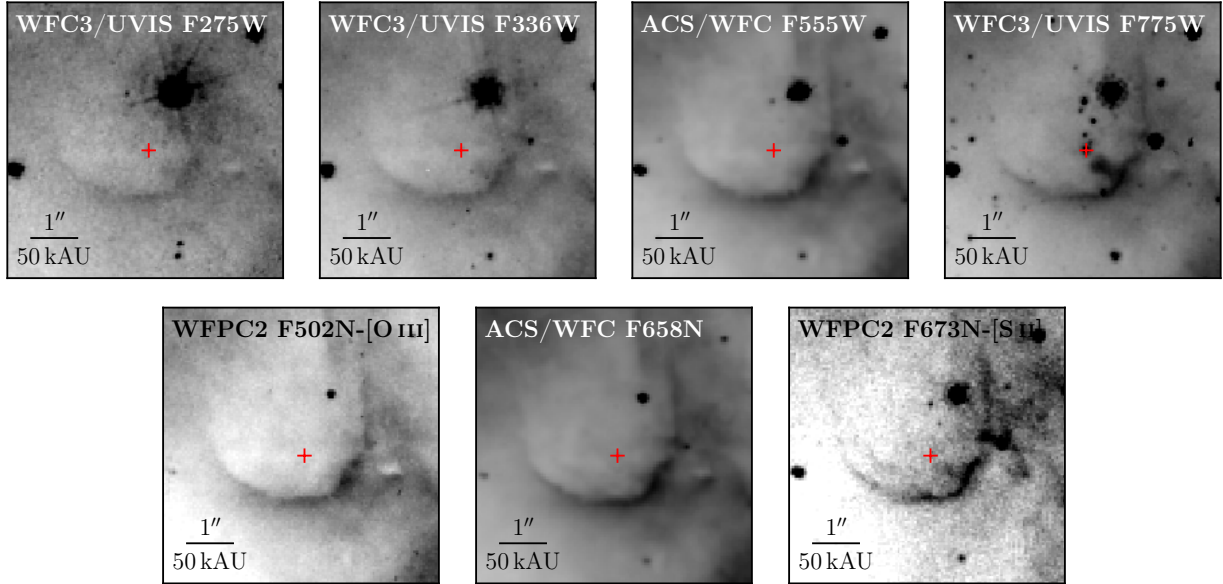


FIGURE 9.1 – HST images of S7A. North is up and east to the left. The arc around S7A is clearly visible across various broad-band filters in UV (F336W) and optical (F555W, F775W) as well as in narrow-band filters (F502N-[O III], F658N-H α , F673N-[S II]). In the WFC3/UVIS F275W filter the arc is still visible, but significantly fainter. The central YSO as well as several other point sources become prominent in F775W. In addition, F775W reveals bright extended emission towards the south-west between the YSO and the arc.

radial velocity of the central YSO to $264.7 \pm 2.3 \text{ km s}^{-1}$ and secondly, the classification of the YSO as a B1V star. H α / β , Hydrogen Pa series and Hydrogen Br γ line emission trace accretion features onto the YSO. Additionally, Fe II 1687.8 nm line emission and CO overtones hint to the presence of a disk. [Fe II] 1.64 μm (not detected for S7A) and H $_2$ 2.12 μm emission lines trace outflow features. The above described spectral features and their implications for the existence of a physical process (accretion, disk, outflow) are used by [van Gelder et al. \(2020\)](#) to classify S7A as a massive YSO. Further, the extinction A_V is estimated around 5 mag from comparing the X-shooter spectrum with a B1 V star model with varying A_V ([Kurucz 1993](#); [Castelli & Kurucz 2003](#)).

The spectrum of S7B shows a continuum over all X-shooter bands, many emission lines, but no photospheric absorption lines or CO bands. The detection of broad H α / β , Hydrogen Pa series, Hydrogen Br γ , Fe II 1687.8 nm, [Fe II] 1.64 μm and H $_2$ 2.12 μm line emission classify S7B as a massive YSO. Moreover, the Pa series lines are double-peaked at velocities of -355 km s^{-1} and -265 km s^{-1} with a stronger blue-shifted component. The blue-shifted component is observed also in the [Fe II] 1.64 μm line, though it appears weaker. [van Gelder et al. \(2020\)](#) suggest a high velocity outflow with ‘bullets’, i.e., density and temperature enhancements, or a binary system to explain this observation. Further, the extinction A_V is estimated around 5 mag from comparing the X-shooter spectrum with a B0 V star model with varying A_V ([Kurucz 1993](#); [Castelli & Kurucz 2003](#)). These spectral analyses and their results mark the first time in literature that S7A/B have officially been promoted from YSO candidates to YSOs. [van Gelder et al. \(2020\)](#) also estimate photometric measurements from the X-shooter spectra. Table 9.1 lists all archival photometric data available on S7A.

TABLE 9.1 – Summary of archival photometric data available for S7A.

F275W	F336W	<i>B</i>	<i>V</i>	<i>G</i>	<i>R</i>	<i>I</i>	F658N ^a	Inst/Survey	Ref
...	>22	20.4	...	HST WFPC2 ^b	W13
24(1)	>24	21.25(3)	...	HST/WFC3 UVIS ^c	S16
...	23.8(1)	21.192(8)	20.53(8)	HST/ACS WFC ^{c,d}	S16
...	...	>17.9(4)	>17.8(4)	>17.5(4)	>17.4(5)	>17.2(5)	...	X-Shooter ^e	G20
<i>Y</i>	<i>J</i>	<i>H</i>	<i>Ks</i> ^f	[3.6]	[4.5]	[5.8]	[8.0]		
...	>14.34	...	11.04	IRPS@AAT	H92 ^g
...	>14.80	...	11.22	LCO	R92
...	...	12.18	11.82	40arcsec	
...	16.57	14.83	13.00	LCO 2.5 m	R98
...	17.46(9)	15.30(6)	13.21(5)	HST NICMOS ^h	B01
...	13.0	13.7(2)	12.3(1)	2MASS ⁱ	C03
...	13.0	13.8(1)	12.3(1)	2MASS ⁱ	C12
...	13.0	13.7(2)	12.3(1)	10.20(4)	SPIREX ^k	M05
19.5(3)	16.83(8)	...	13.13(2)	VISTA	W13
...	16.13(9)	14.81(5)	12.99(2)	IRSF	K07
...	10.26(6)	9.31(5)	8.25(5)	...	IRAC	M06
...	14.9	14.0	12.7	IRSF	K16 ^m
...	18.087(89)	15.95(4)	HST/WFC3 IR ^j	S16
>17.5(3)	>16.6(2)	>14.8(3)	>13.2(3)	X-Shooter ^e	G20

NOTES. Uncertainties on the photometric measurements are noted in brackets, e.g., 6.00(6) = 6.00 ± 0.06. The catalogue ID's (if exist) are stated in the References below. ^(a) H α filter. ^(b) The *VI* photometry was determined from the F555W ($\sim V$) and F814W ($\sim I$) filters. ^(c) *I* \sim F775W. ^(d) *V* \sim F555W. ^(e) Photometric upper limits determined from the X-shooter spectrum. ^(f) For H92 and R92, *K* photometry. Following R98 (included) this column represents the *Ks* band. ^(g) H92 provided dereddened magnitudes (upper row) in addition to apparent magnitudes (lower row). ^(h) The *JHKs* photometry was obtained through colour transformations from the F110W, F160W and F205W filters. ⁽ⁱ⁾ F110W ($\sim YJ$), F160W ($\sim H$). ^(k) *JHKs* photometry from 2MASS, [3.6] $\sim L$ (3.5 μ m). ^(l) The source is unresolved in 2MASS images.

REFERENCES. H92: Hyland et al. (1992), ID IRS124; R92: Rubio et al. (1992), ID IRS1; R98: Rubio et al. (1998), ID IRSN-122; B01: Brandner et al. (2001), ID 30Dor-NIC12b; C03: Cutri et al. (2003), ID 2MASS05384682-6905054; C12: Cutri et al. (2012), ID 2MASS05384682-6905054 and 2MASS05384682-6905053; M05: Maercker & Burton (2005), ID 101; M06: Meixner et al. (2006), ID SSTISAGEMA/C J053846.84-690505.4; K07: Kato et al. (2007), ID IRSF05384685-6905058; W13: Walborn et al. (2013); S16: Sabbi et al. (2016), ID HTTP053846.871-690505.58; K16: Kim et al. (2016), ID 05384685-6905058; G20: van Gelder et al. (2020).

9.2 NIRCcam and MIRI view

The diffraction-limited IR cameras on JWST provide us with the highest spatial resolution data for S7A across a wide wavelength range in the IR from 0.97 to 27 μm revealing different extended structures around the YSO. The ‘nebular arc’ mentioned by [Walborn et al. \(1999\)](#) (Fig. 9.1) becomes clearly visible in NIRCcam F090W, F187N- $P\alpha$ and F200W images (Fig. 9.2). The shell is about $0''.7$ (~ 35 kAU) away from the YSO in south-west direction and spans $\sim 3.5''$ (~ 175 kAU) from east to west. It appears to have two arms, one extending towards the east (S1 in Fig. 9.3) and the other towards the north (S2 in Fig. 9.3). An additional third arm extending out into south-west can be seen in F187N, although significantly fainter than the other two (see also S3 in Fig. 9.3). In addition, JWST resolves a brightness gradient decreasing towards the edges of the shell.

F090W resolves an additional extended structure towards the south-west of the YSO. It is more prominent in HST WFC3/UVIS F775W (see Fig. 9.1). It appears separated from the YSO. The emission starts $\sim 0''.1$ (~ 5 kAU) away from S7A. The emission reaches the shell structure and seems to be interacting with the material in the shell as their overlap marks the brightest part of the shell. In addition, the shell seems to be shaped by this emission as the curvature of the shell differs from that of the second arm (S2 in Fig. 9.2; F090W). It appears to be pushed away by what seems to be a powerful outflow from the massive YSO. Protostellar outflows are often observed to be bipolar as so-called Herbig-Haro objects in lower-mass YSOs (e.g., review in [Reipurth & Heathcote 1997](#)). The one-sidedness of S7A’s outflow could be explained by a decrease in density towards the north-east compared to the south-west. Alternatively, the proto-stellar system might be oriented such that the second part of the outflow is obscured by the diffuse dust structure (see below). It might additionally have travelled further outwards due to lack of obstacles.

NIRCcam F335M, MIRI F770W and F1130W trace PAHs and silicate emission in a complicated structure around S7A. The entire emission is concentrated in the region behind the shell. Only the second arm of the shell (S2 in Fig. 9.2; F090W) appears in these images as well (also in F444W). However, the central region is dominated by the PSF of the YSO. The orientation of the shell as well as the PAH emission are curved towards the north-east. The strong radiation pressure from the near-by star cluster R136 might be responsible for this shape.

Additionally, [Walborn et al. \(1999\)](#) point out three other fainter ‘very red’ IR sources near S7A. It remains unclear which sources they were referring to exactly. The NIRCcam F090W image resolves seven faint objects close to S7A. For five point sources located towards the north of the YSO (P1–5 in Tab. 9.2), only HST WFC3/UVIS F775W (see Fig. 9.1) counterparts can be identified. For the northern-most source (P5 or 053846.878–690504.57 in Tab. 9.2), additional fainter emission is seen in HST ACS/WFC F555W and WFC3/UVIS F336W (Fig. 9.1). However, in F336W the emission is largely contaminated by the diffraction spikes of eclipsing binary OGLE LMC-ECL-21481 ([Graczyk et al. 2011](#)) – the brightest source in the field. The sixth source is the faintest one in the sample and appears only in the F090W image towards the east of S7A.

A further source (C1; yellow mark in Fig. 9.2) appears in the F187N- $P\alpha$, F200W and F335M images. C1 can also be identified in F444W–F1130W images, but is increasingly overshadowed by the NIRCcam and MIRI PSF of S7A. The non-existence of C1 in F090W and

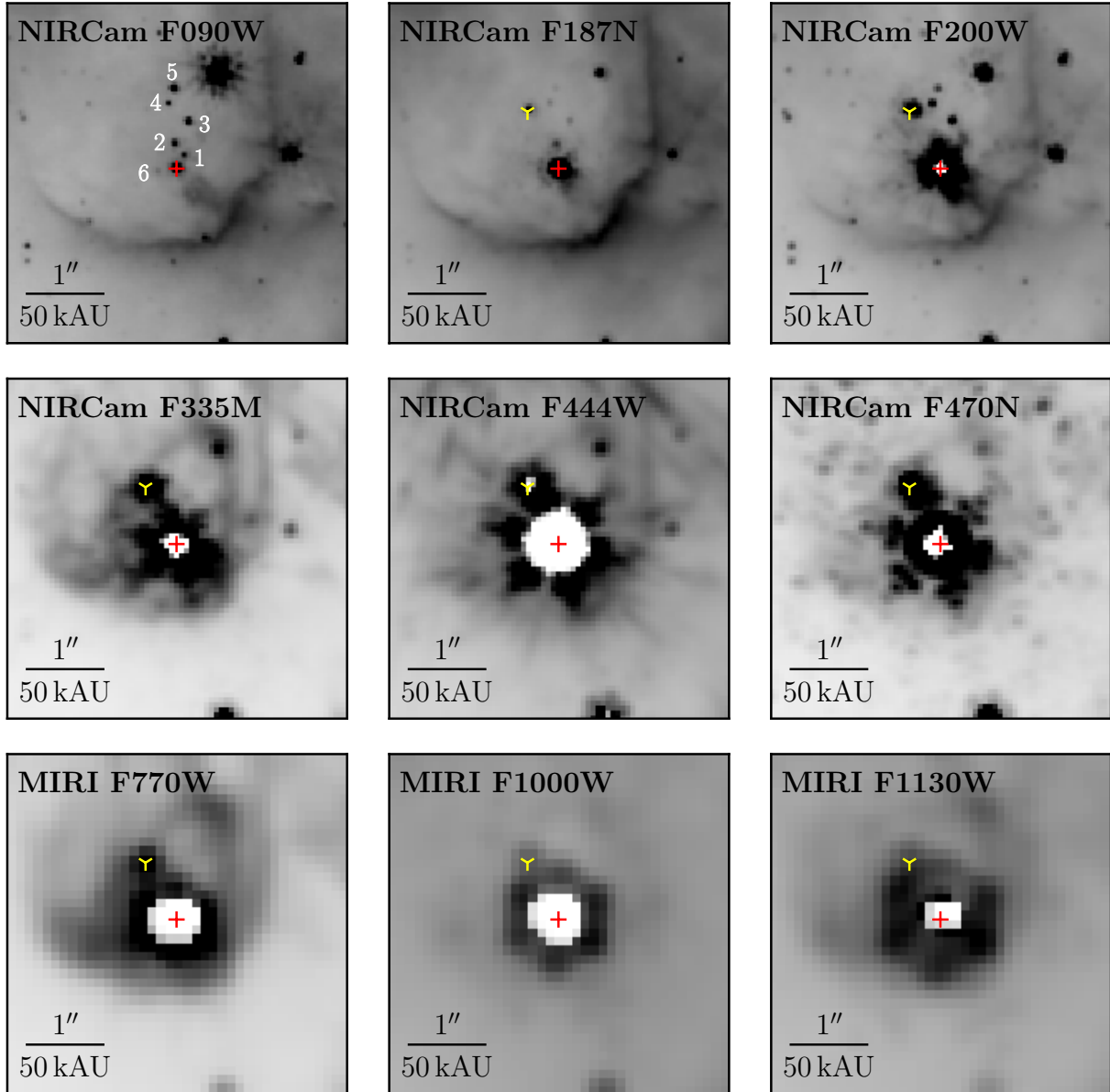


FIGURE 9.2 – NIRCam and MIRI images of S7A. The red cross marks the position of S7A. The yellow marker highlights the position of point source C1 becoming brighter towards longer wavelengths and, therefore, a strong protostellar candidate. The two narrowband filters F187N ($P\alpha$) and F470N (H_2 $2.12\mu\text{m}$) highlight atomic and molecular Hydrogen emission. The other discussed point sources near to S7A are indicated by numbers.

its high brightness in F200W strongly point to an infrared excess and the general spectral shape to a protostellar origin (see Sect. 9.3.2 and Sect. 9.4).

9.3 NIRSpec and MIRI/MRS IFU spectra – Methods

9.3.1 Spectral Extraction

In the continuum frames of NIRSpec and MIRI/MRS, the source appears point-like. In the following, we refer to this central point-like object as the YSO S7A (see Fig. 9.3). To compare NIRCcam and NIRSpec images, an astrometric correction is required. We perform a 2D centroid fit to determine the exact position of S7A in the NIRCcam F090W image and the NIRSpec F100LP/G140H continuum frames using the `photutils.centroids.centroid_2dg` routine. An adjustment of $0''.208$ in R.A. and $0''.267$ in DEC. is required to align the source in both observations. The final position of S7A – as determined from the fit to the *Gaia*-aligned NIRCcam data – is (R.A., DEC.) = (84.695327, -69.084905).

To account for higher diffraction at longer wavelengths and thus the increasing PSF size with increasing wavelength, we adopt a conical aperture meaning the initial aperture is scaled with the Rayleigh criterion ($1.22 \lambda/D$) across all NIRSpec bands and MIRI/MRS channels.

$$r_{\text{aperture}} = \frac{f_{\text{rc}} \cdot 1.22 \cdot \lambda/D}{2} \cdot 206264.806 + r_{\text{init}}, \quad (9.1)$$

where $f_{\text{rc}} = 1.5$ an empirical correction factor to account for the increased PSF size with respect to the diffraction limit, $D = 6.5$ m the primary mirror diameter, 206264.806 the conversion factor between rad and arcsec, and r_{init} the initial radius of the aperture at $0''.2$ ($0''.3$) for NIRSpec (MIRI/MRS).

Due to inaccuracies in the astrometry, the source was shifted in the MIRI/MRS cubes with respect to the position in the NIRSpec cubes. Therefore, the spectrum was extracted from a slightly different position (R.A. 84.6956537, DEC. -69.0846748).

Only the MIRI/MRS observations had a dedicated background field which was subtracted from the science cubes. This results in an offset between the flux density measured by NIRSpec F290LP and MIRI/MRS 1A. To match the flux density in both detectors, we scaled the NIRSpec flux density in all three bands with a factor of 0.91 to get a continuous spectrum.

Motivated by the results of the continuum-subtracted line emission maps (see Sect. 9.3.3), Figure 9.3 shows selected emission maps with various structures. Figure 9.3 includes substructures indicated by circles and ellipses from which I suggest to extract separate spectra for further investigation. The substructures are primarily selected based on the variation of brightness in the emission maps. In this work, I focus on three of the marked regions: the red circle showing the position of the YSO, the ellipse including both the YSO and the knot and the shell region S1A. The blue circles in the lower panel of Figure 9.3 indicate the emission region of the knot with respect to the YSO. As these regions lie very close together and overlap, I decided to investigate their combined region (red ellipse YSO+Outflow) instead of separately. Only the regions marked in red in Figure 9.1 use a conical aperture for the spectral extraction. All others are extracted without scaling their size. However, their size has been chosen above the FWHM of the PSF of the longest wavelength NIRSpec filter F290

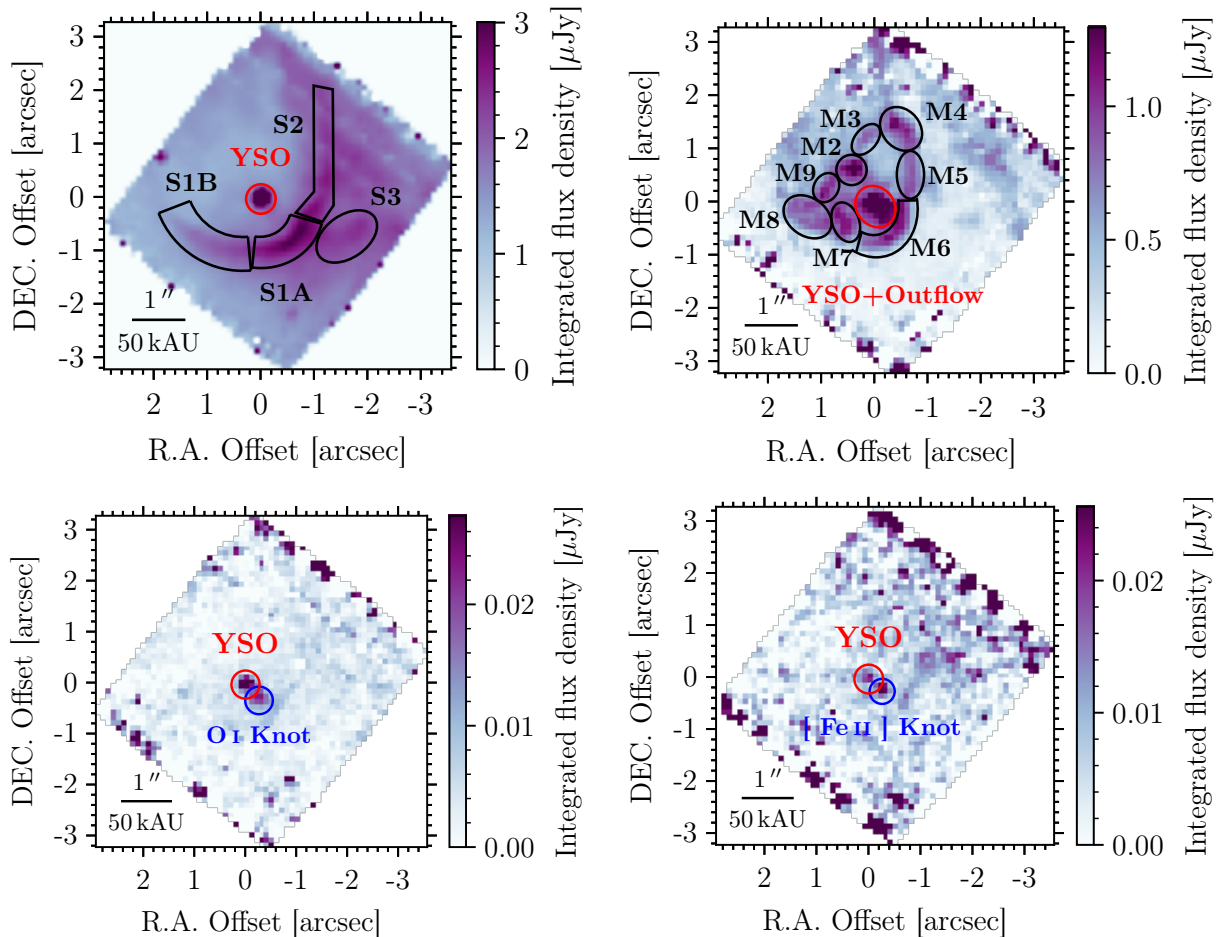


FIGURE 9.3 – NIRSpect emission maps showing spectral extraction regions for various structures detected around YSO.

(see Tab. 6.3). The extended structures and the transitions dominating the emission are further discussed in sections 9.5 and 9.8.

9.3.2 Contamination by other point sources and possible multiplicity

S7A first appears as a clear point source in NIRSpect data only around $1\ \mu\text{m}$ even though the IFU cube provides data starting at $\sim 0.97\ \mu\text{m}$. The NIRCcam images reveal further point sources in the vicinity of S7A. P1–5 (Fig. 9.2) are detected with HST WFC3/UVIS F775W (see Fig. 9.1). Table 9.2 includes the photometric measurements from the HST point source catalogue (Sabbie et al. 2016) for P1–5. P1–5 can only be clearly identified in F090W. P3–5 additionally appear in F200W, however P1–2 are covered by the PSF size of S7A. The emission of P5 fades away with increasing wavelength and no emission is seen longer than F335M. In F187N all five sources (P1–5) are significantly fainter than S7A. P6 is visible only in F090W and is significantly fainter than P1–5. For any longer wavelength filters the PSF of S7A hides P6. In addition, C1 is particularly interesting as it appears only in filters longer than F187N. It presents a strong protostellar candidate.

None of the point-sources P1–6 can be resolved with NIRSpect. Comparing the NIRSpect continuum frame at $1\ \mu\text{m}$ with the NIRCcam F090W image (Fig. 9.2), S7A together with P1 appear as a single point source in NIRSpect and fall into r_{init} (Fig. 9.4). As the extraction

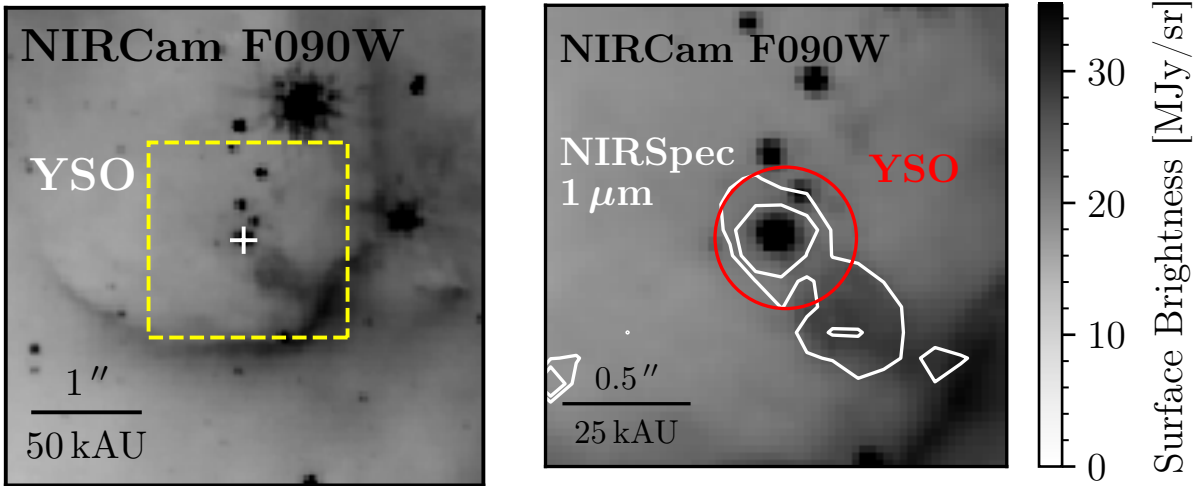


FIGURE 9.4 – NIRCcam F090W image (left) and a closer look at S7A and its outflow (right). The region shown on the right is indicated by the yellow square. Contours outlining $1\ \mu\text{m}$ continuum emission from NIRSpec (right). The red circle shows the smallest extent of S7A in the NIRSpec data and r_{init} for spectral extraction.

radius grows according to equation (9.1), likely also P2 will contribute to the measured flux density. However, I am mainly interested in emission lines in this work. Based on the faintness of P1–5 in F187N, I conclude that similar behaviour in longer narrow-band filters can be expected, namely, the flux density of P1–5 significantly less than that of S7A. Therefore, I presume P1–5 do not have significant emission line flux compared to S7A. I therefore neglect the knowledge of their presence in my emission line analysis.

Apart from the possible contamination of apparent point sources, true multiplicity of S7A has to be considered especially as MYSOs predominantly form in groups. The radius of the emission from S7A detected at the lowest NIRCcam wavelengths ($\sim 0.9\ \mu\text{m}$) is $0''.1$. This corresponds to $\sim 5\ \text{kAU}$ ($\sim 0.02\ \text{pc}$) at a distance of 50 kpc. Therefore, the S7A system is on the same size scale as hyper-compact H II regions (see Kurtz 2005, Tab. 3) which are of the order of magnitude of single or binary star systems (Kurtz 2005). If S7A is in fact an unresolved binary system of a higher-mass YSOs with a lower mass companion, the massive protostar would dominate the luminosity of the system.

TABLE 9.2 – HST WFC3/UVIS (F775W) and WFC3/IR (F110W, F160W) photometric measurements for S7A, point sources P1–6 and C1. The HST photometry was adopted from the HTTP Source Catalogue (Sabbi et al. 2016).

ID ^a	HTTP ID	R.A. DEC. ^b [J2000]	F775W	F110W	F160W
S7A	053846.871–690505.58	05:38:46.874–69:05:05.66	21.25±0.03	18.09±0.09	15.95±0.04
P1	053846.853–690505.42	05:38:46.861–69:05:05.49	22.7±0.1	20.4±0.1	21±2
P2	053846.875–690505.27	05:38:46.883–69:05:05.34	22.22±0.01	20.1±0.1	18.88±0.02
P3	053846.844–690504.99	05:38:46.852–69:05:05.06	21.8±0.1	20.6±0.2	19.5±0.032
P4	053846.891–690504.76	05:38:46.898–69:05:04.83	22.32±0.01	20.72±0.02	19.55±0.03
P5	053846.878–690504.57	05:38:46.885–69:05:04.64	21.04±0.05	20.52±0.03	20.06±0.01
P6	-	05:38:46.926–69:05:05.72	-	-	-
C1	053846.943–690504.84	05:38:46.941–69:05:04.91	27±2	21.23±0.05	18.74±0.04

NOTES. The magnitudes are given in the Vega system. The point sources are detected in HST WFP3/F775W, but cannot be resolved in WFP3/IR making the photometric data unreliable. The F110W and F160W photometry is reported for completeness. ^(a) ID used in this work. ^(b) R.A./DEC is given in the NIRCcam frame. The coordinates were determined using the PSF photometry software `starbugII` (Nally 2023). There is an intrinsic shift between the HST and JWST coordinates of $\sim 0''.11$ in R.A. and $\sim 0''.07$ in DEC.

9.3.3 Identification and Continuum-subtracted Line Emission Maps

The first step towards deriving physical parameters from line ratios is the identification of the species and exact transitions giving rise to the emission lines. In addition, the IFU allows to map the spatial distribution of single emission lines across its foV. This section describes the steps applied to identify emission lines and create their continuum-subtracted emission maps.

The same steps are applied for NIRSpec and MIRI/MRS data cubes (see Sect. 9.3.1). The only difference lies in the handling of the spectral extraction from the 3D data cubes. For NIRSpec data, spectra are extracted from single spaxels within a 11×11 pixel square size aperture around the YSO and added to increase the signal-to-noise ratio. Due to the additional spectral fringe correction for MIRI/MRS data (Sect. 8.2), the spectrum for emission line identification is extracted from an aperture $r_{\text{init}} = 0''.6$ using the custom extraction routine (Sect. 9.3.1).

To find the line centres of the emission lines for further investigation, I use the `fitting.find_lines_derivate()` routine of the `specutils` python package (version 1.16.0). Emission lines are identified through searching for zero crossings in the spectrum derivative. In general, the routine can detect absorption as well as emission lines. At this stage, I am only interested in the emission lines. Any detected lines flagged as absorption lines are excluded from the next steps. The algorithm identified several fluctuations in the continuum of the spectrum as emission lines. Therefore, a flux threshold is set above which the algorithm considers a spectral bin part of an emission line or the continuum. The threshold was chosen by eye such that the fraction of true emission lines is maximised and that of false detections minimised. However, setting such a threshold results in only the brightest emission lines being detected. Performing line detection on the spectrum without previous continuum subtraction is, therefore, insufficient. To increase the sample of detected emission lines, a

generic continuum is fit with `fitting.fit_generic_continuum()` to the spectrum excluding the previously detected emission lines. Firstly, the routine smooths the input spectrum to remove emission lines or noise peaks. Secondly, a 1D Chebyshev polynomial of the first kind and third degree (see the `astropy.Chebyshev1D` model) is fit to the spectrum. The fitted continuum is subtracted from the input spectrum and the line detection routine is re-run with a lower flux-threshold. Possible fainter lines missed by the algorithm are identified by eye from the spectrum and through investigating individual slices of the IFU cube. These were added to the detected line table for further investigation.

For each detected emission line, a sub-cube within a small spectral window $[\lambda_c - \Delta\lambda, \lambda_c + \Delta\lambda]$ around the line centre is created. This sub-cube is used both for spectral extraction and emission line fitting as well as for the line-emission maps. For all NIR wavelengths, the window is $2\Delta\lambda = 0.01 \mu\text{m}$ wide. It gradually increases in MIRI data towards longer wavelengths from $0.014 \mu\text{m}$ in 1A to $0.08 \mu\text{m}$ in 4C due to the decreasing spectral resolution. The width is chosen based on the 1D spectrum to cover the full extent of the broadened emission line as well as a portion of the surrounding continuum. To isolate the line from the continuum emission, the local continuum around the emission line is fit and subtracted. As before, the `fitting.fit_generic_continuum()` function is used. Spectra are extracted from the sub-cube and the continuum is fitted and subtracted spaxel-by-spaxel. A continuum-subtracted spectral cube is created. For MIRI/MRS data, this step is repeated twice: once for the spectral cube and once for the extracted spectrum.

In the NIR bands, the line density is relatively high. In several cases the selected spectral window was large enough to capture not only one, but two or sometimes even more emission lines. To account for several lines, the `fitting.find_lines_derivate()` routine is run again on the sub-cube spectra. In this case, the line model consisted of a sum of several Gaussians – one for each emission line. M0 maps were re-created by cutting further sub-cubes out of the larger continuum-subtracted sub-cube covering each emission line.

To illustrate the spatial distribution of each emission line, so-called moment 0 (M0) maps are created from the continuum-subtracted sub-cubes using the `spectral-cube` python package (version 0.6.5). Such maps show the integrated line flux under an emission line and are calculated by integrating the measured flux density in a small spectral window around an emission line over the spectral dimension – in this case, the wavelength.

$$M_0 = \int_0^\infty F_\lambda d\lambda. \quad (9.2)$$

Emission maps are not only useful for the illustrating the spatial distribution of line transitions, but also for the identification of possible CRs or bad pixels that were missed by the calibration pipeline (Sect. 8).

To determine the central wavelength λ_c of the broadened emission lines for identification of the species and its transition, a Gaussian profile $f(\lambda)$ is fit to each line.

$$f(\lambda) = A \exp\left\{-\frac{(\lambda - \lambda_c)^2}{2\sigma^2}\right\}, \quad (9.3)$$

where A is the amplitude and σ the standard deviation of the emission line. Least-squares fitting with the Levenberg-Marquardt algorithm was performed using the `astropy.modeling`

library.

The observed spectrum was redshift-corrected using the systemic velocity $v_r = 267.4 \text{ km s}^{-1}$ of the 30 Doradus region determined from optical observations of the H α line (Torres-Flores et al. 2013). It is noted that van Gelder et al. (2020) derived a velocity for the protostar from observed photospheric absorption lines (see Sect. 9.1). This paper was discovered after the complete line identification pipeline was already run. Their determined radial velocity for the protostar is $v_r = 264.7 \text{ km s}^{-1}$. A $\sim 3 \text{ km s}^{-1}$ velocity difference cannot be resolved by the highest resolution gratings on NIRSpec ($R \sim 2700$; $\Delta v \sim 110 \text{ km s}^{-1}$). Therefore, previous results using the general 30 Doradus velocity can be adopted for further analysis.

The determined central wavelengths are compared to the vacuum wavelengths of known transitions in the IR. The observed emission lines were identified with the help of the IR line lists provided by the ISO Spectrometer Data Centre at the Max Planck Institute for extraterrestrial physics, the Atomic Line List version 3.00b5 (van Hoof 2018), the NIST Atomic Spectra Database (Kramida et al. 2023) as well as the Gemini H $_2$ line list. A tolerance of $\Delta\lambda = 0.001 \mu\text{m}$ was chosen for filtering the above line catalogues. If no ID could be found, the tolerance was increased gradually in steps of $0.001 \mu\text{m}$. A definite line transition could be attributed to most of the emission lines within $\Delta\lambda = 0.002 \mu\text{m}$. The matched lines were checked for plausibility by comparing them to other lines in the spectrum of the same species. Multiple lines originating from the same upper levels or multiplets are more likely to be present than isolated lines. Emission lines for which the above line lists were not sufficient to provide a clear ID, spectra of other YSOs, planetary nebulae or other photoionised regions such as the Orion nebula were considered (see also the discussion in Sect. 9.5.3). Blended and unresolved lines returned several identifications for an assumed single line. They are combined with brackets in table B.1 and are excluded from further analysis.

About 250 emission lines were observed and are listed in table B.1. For eight of detected lines, the current ID is either uncertain or remains entirely unidentified (see Sect. 9.5.4). Such lines are marked with question marks in table B.1. The most abundant lines are Hydrogen recombination lines. H $_2$ transitions hold the second place. Further, Helium fine-structure transitions and forbidden transitions from heavier elements are present. Additionally, O I fine-structure transitions, forbidden as well as allowed Fe II lines were identified. We note that the presented line catalogue is complete for transitions with fluxes $\gtrsim 10^{-17} \text{ erg s}^{-1} \text{ cm}^{-2}$ (see Sect. 9.3.4). Additional weaker lines, especially from H I and H $_2$ transitions could be present, but have a too low line-to-continuum ratio to be detected by the pipeline or be successfully fitted by a Gaussian profile.

Hydrogen and Helium recombination lines and certain forbidden lines ([Fe II] $4.67 \mu\text{m}$, [Ar II] $6.99 \mu\text{m}$, [Ni I] $11.31 \mu\text{m}$, [Ne II] $12.81 \mu\text{m}$) originate from the central YSO as well as from a C-shaped shell or arc around the YSO. Most forbidden lines trace the MYSO, the shell and/or the diffuse medium around the source. Molecular Hydrogen emission originates from the MYSO and is distributed in the complex diffuse structure around the YSO. The H $_2$ distribution closely follows the distribution of PAHs observed in the NIRCcam F335M filter (see Fig. 9.2). Ro-vibrational H $_2$ transitions additionally seem to extend further out from the region of the YSO towards the north-west. Mean M0 maps showing the most prominent features are illustrated in figure 9.5. Hydrogen recombination lines are discussed further in section 9.5.1, H $_2$ transitions in section 9.5.2 and forbidden lines in section 9.5.1.

Examining all M0 maps and the individual slices of the IFU cubes, emission from a knot

towards the north-west of the YSO was identified in O I and [Fe II] transitions. H₂ emission lines appear to be extended towards the south-west covering the MYSO and the knot. M0 maps for these transitions are shown in figure 9.6. This knot emission is further discussed in section 9.8.

To determine the kinematics of the observed structures, moment 1 maps are created. The first moment of an emission line is calculated as $M_1 = \int \lambda F_\lambda d\lambda$. To accurately determine additional radial velocity shifts with respect to the general velocity of the YSO, the exact transition wavelengths of the observed lines have to be known. Unfortunately, no additional velocity structures are resolved in any of the observed transitions. Most observed (and redshift-corrected for the radial velocity of S7A) wavelengths of the emission lines are blue-shifted with respect to their lab wavelengths (see Tab. B.1). The differences in velocity space lie between $\Delta v \sim -40 \text{ km s}^{-1}$ and $\sim +25 \text{ km s}^{-1}$ – consistently below the spectroscopic resolution. Some individual transitions are shifted even further than the above range: H₂ 1–0 O(2) 2.6268 μm , H₂ 2–1 Q(6) 2.6269 μm , H₂ 3–2 Q(9) 2.90 μm , H₂ 3–2 O(4) 3.40 μm , H₂ 0–0 S(16) 3.55 μm , H I 6–5 7.46 μm , H I 11–9 22.34 μm , and [Fe III] 22.93 μm with $\Delta v \sim -126, -131, -103, -76, -125, +85, +79, +47 \text{ km s}^{-1}$, respectively. However, also these lie below the instrumental resolution. We emphasise again that the velocities have at least an uncertainty of $\sim 3 \text{ km s}^{-1}$ due to the choice of the systemic velocity of the system (see discussion above). The H₂ 1–0 O(2), 2–1 Q(6), 0–0 S(16) lines are blended with H I lines. The large blueshift is the result of only a single Gaussian fit.

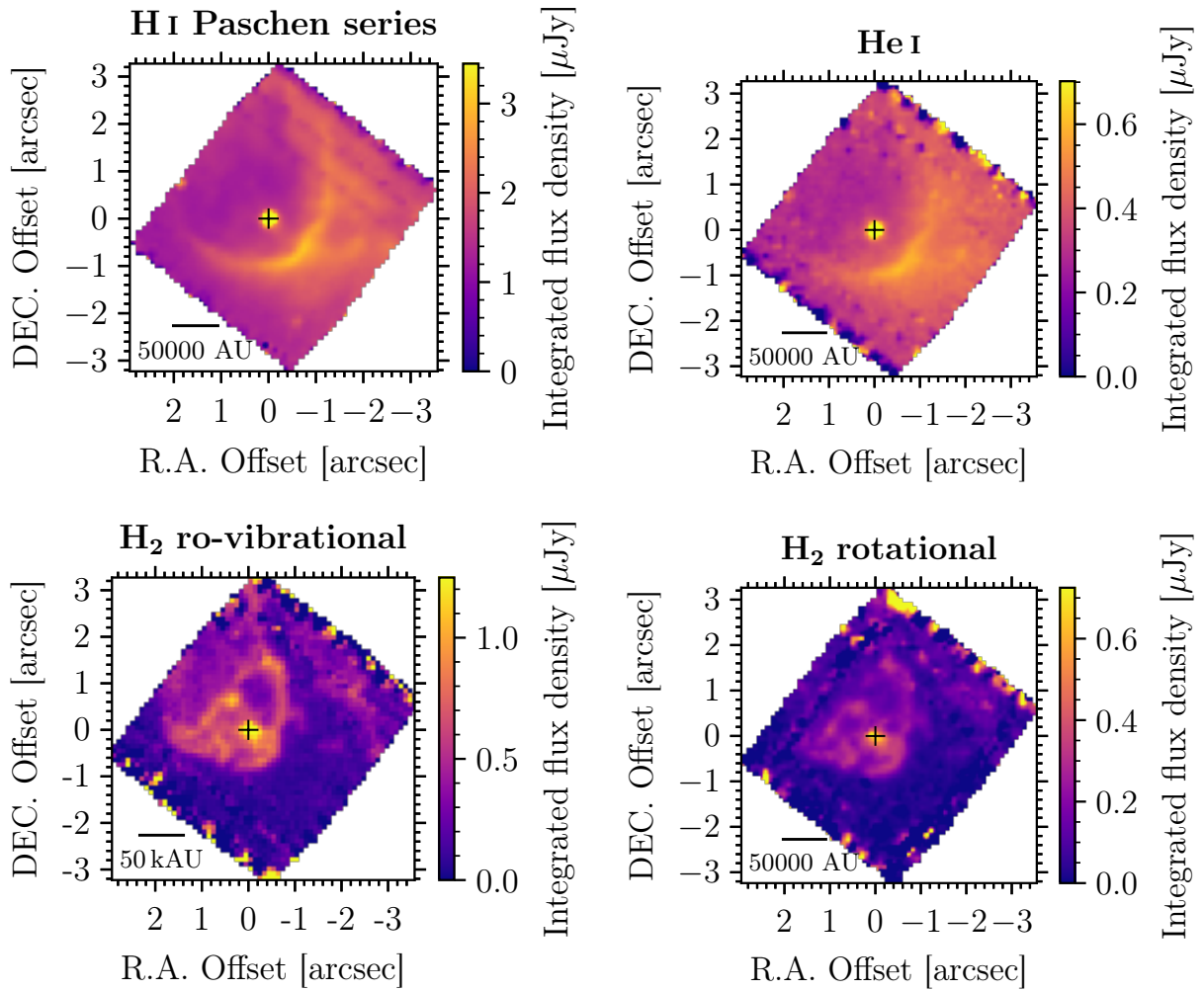


FIGURE 9.5 – Mean moment 0 maps showing the most prominent observed emission line morphologies. The averaging was performed over all emission lines showing similar features across the NIRSpc bands. The fitted position of the YSO is shown with the black cross.

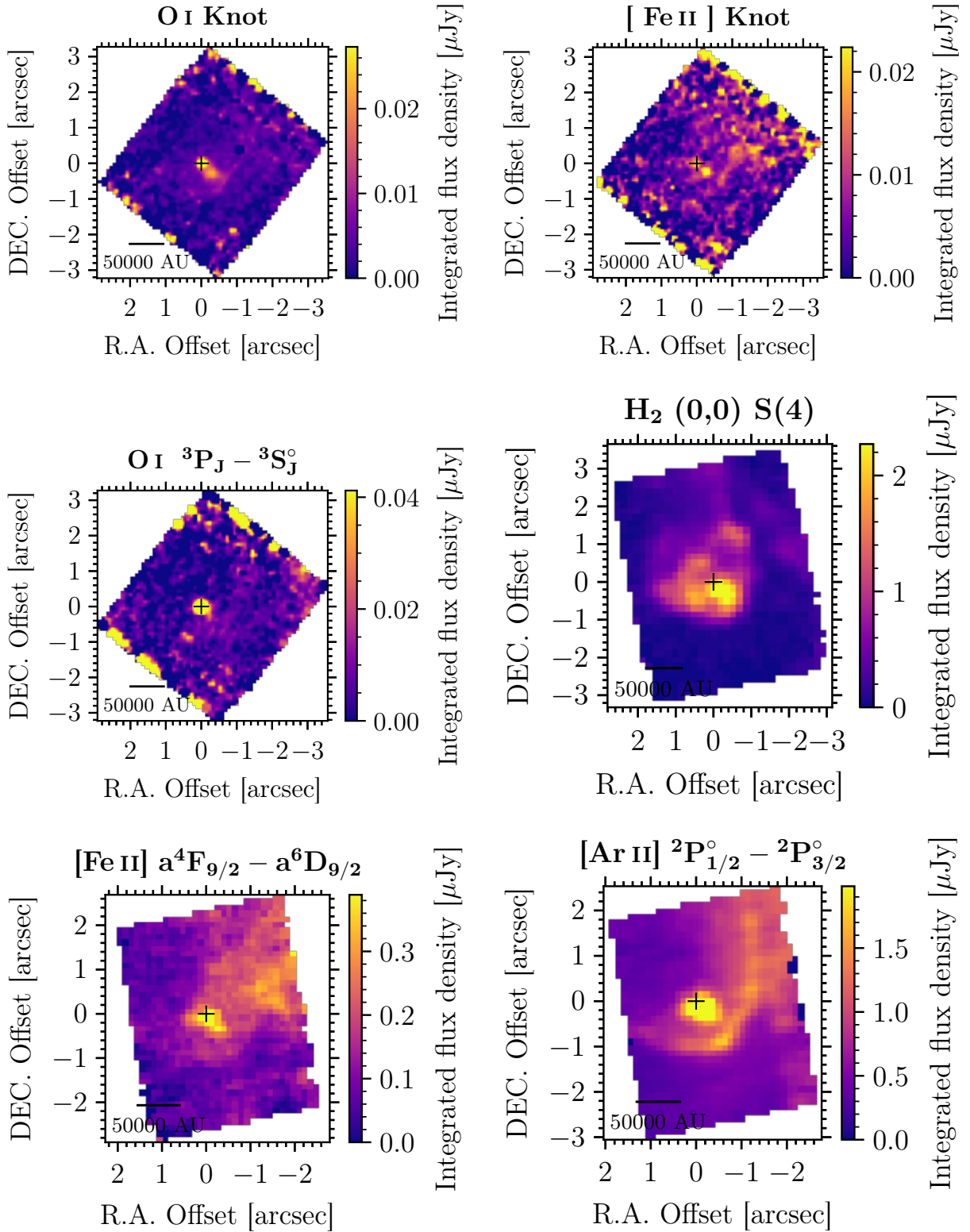


FIGURE 9.6 – Moment 0 maps showing the transitions tracing the possible stellar outflow. The M0 maps in the top row present mean maps. Averaging was performed over multiple O I and [Fe II] emission lines showing the knot feature. It is noted that the foV of MIRI/MRS towards longer wavelengths increases.

9.3.4 Line Flux

Since several diffuse structures were detected around the YSO (see M0 maps), separate spectra are extracted from the central object, the C-shaped shell, the extended H₂ emission region and the knot. Emission line fluxes are calculated with the automated line fitting algorithm (ALFA; Wesson 2016). As a first step, the continuum is estimated using an m data point wide ‘moving window’ and calculating the flux value below which 25% of the data falls (25th percentile). The default size of the window is $m = 100$. It can be adjusted for more complex continua. Due to high variability in the continuum of the F290, 1C, 2B/C, 3A spectra, the window was reduced to 20–40 data points.

After subtracting the fitted continuum, ALFA constructs a synthetic spectrum with Gaussian profiles for all emission lines in a catalogue using a genetic algorithm. In this work, the emission line catalogue is supplied by the user and is based on the emission lines in table B.1.

The genetic algorithm works as follows: it first creates a number (population size) of synthetic spectra and evaluates their goodness of fit. Secondly, the code keeps a certain percentage (breeding fraction) of the best generated spectra and creates a new set of synthetic spectra with parameters chosen from the best fits until the population size is reached once again (breeding). Thirdly, 10% of the best-fit parameters are altered with a random mutation function (see Wesson 2016, Eq. 1). The previous two steps are repeated for a number of generations. The population size, the breeding fraction, the mutation function and the number of generations can be altered. For the JWST spectra of S7A, the change of these parameters did not have any significant impact on the quality of the final fit. Instead, the initial guess for the velocity of the source and the resolution of the spectrum had to be adjusted to reproduce the line fluxes of bright Hydrogen emission lines. ALFA calculates uncertainties on the line fluxes according to an empirical relation (see Lenz & Ayres 1992; Wesson 2016, Eq. 2) based on the noise level at the centre wavelength of the respective line. The signal-to-noise ratio is determined from the root-mean-square of the residuals after subtracting the continuum and the estimated line flux.

The NIR spectra also contain blended lines. After the synthetic spectra have been constructed, ALFA checks whether any line centres provided in the catalogue fall into the half-width at half-maximum of a fitted line at the calculated spectral resolution. Such blended lines are marked in the final line list. The total flux of the blended lines is reported nevertheless although it does not have any scientific use. We do not include these fluxes in the lines table E.1. Further, the estimated spectral resolution by ALFA is consistently larger than the actual resolution of the spectra. We therefore mark blended lines ourselves by inspecting the line shapes (see Sect. 9.3.3).

For MIRI/MRS 1A, 2A and 3B spectra, ALFA did not converge while estimating velocities and spectral resolutions and was therefore not able to reproduce the observed spectra. Line fluxes in these two bands are calculated manually by integrating over the fitted Gaussian profile after subtracting a locally fit pseudo-continuum similar to the procedure described in section 9.3.3:

$$F(\lambda) = \int_{-\infty}^{+\infty} f(\lambda) d\lambda = A\sigma\sqrt{2\pi}, \quad (9.4)$$

where $f(\lambda)$ is the flux density as defined in equation (9.3). The calculated lines fluxes, their uncertainties as well as the full-width half-maxima (FWHM) are summarised in table E.1. The calculated line fluxes are given in $\text{erg s}^{-1} \text{cm}^{-2}$. However, in some works the SI unit W m^{-2} is used instead. The conversion factor is 10^{-3} from cgs to SI units. I note that the FWHM reported by ALFA seem to be larger compared to those estimated from Gaussian fits. In general, the FWHM determined via Gaussian fits show a larger variation between different lines whereas those of SC are the same for several subsequent lines. Successful ALFA fits and the residuals between observed and fitted spectra are shown in Appendix E.2.

9.4 General spectral features

Figure 9.7 shows the spectral energy distribution (SED) of S7A over the entire wavelength range ($0.97\text{--}27\ \mu\text{m}$) covered by NIRSpec and MIRI/MRS IFUs. Several characteristics of YSO spectra can be identified. The rising contribution of the continuum towards the MIR, clearly shows the infrared excess and implies the presence of an envelope around the young protostar. The continuum in the NIR as well as in the MIR is superimposed by several broad absorption and emission features. Figure A.1 shows the spectrum separately for the two instruments where these broad features appear more clearly. The first broad band in absorption around $2.8\text{--}3.3\ \mu\text{m}$ is primarily attributed to water (H_2O) ice. Absorption around $\sim 4.3\ \mu\text{m}$ with a distinct shape points to solid CO_2 . The peak of the feature together with its shape and strength depend on the environment of the molecule and whether it exists in pure form or is mixed with other (e.g., H_2O) ices or whether is in gas or solid-state phase (e.g., van Dishoeck 2004; Boogert & Ehrenfreund 2004; Boogert et al. 2015; Sturm et al. 2023). Interstellar ices form by condensing on cold dust grains (Lequeux 2005; Boogert et al. 2015). The second broad absorption feature around $10\ \mu\text{m}$ is a silicate band. Such broad absorption bands of ices and silicates are generally detected in protoplanetary disks or the cold outer parts of envelopes around YSOs (van Dishoeck 2004).

The broad emission features centred at $3.3\ \mu\text{m}$, $3.4\ \mu\text{m}$, $6.2\ \mu\text{m}$, $7.7\ \mu\text{m}$, $8.6\ \mu\text{m}$, $11.3\ \mu\text{m}$, $12.7\ \mu\text{m}$ originate from warm dust. They are known since the 1970s and were originally referred to as unidentified IR bands (UIRs) as their detailed composition remained unknown. In the 1980s, these features have been attributed to aromatic molecules containing Carbon (C) and Hydrogen atoms where the C atoms are arranged into ring structures. Nowadays, they are summarised under aromatic infrared bands (AIBs). The features in the S7A spectrum listed above are mainly due to polycyclic aromatic hydrocarbons (PAHs) containing multiple such C rings. PAHs have been observed in almost every type of astrophysical object where UV radiation exists to excite them (e.g., Tielens 2008, and references therein). In addition, PAHs are important for the formation of other molecules such as molecular Hydrogen (see Sect. 9.5.2) as well as for the heating and cooling of their environment (Lequeux 2005; Draine 2011).

Furthermore, the spectrum is dominated by a high number of emission rather than absorption lines. In general, observed spectra of YSOs and their features vary widely as they depend highly on the parameters of the protostellar system itself such as the mass of the YSO and the density of its surrounding medium, the orientation of the system towards the observer as well as on the presence of foreground molecular clouds (Bowey & Adamson 2001). This work focuses on the identification of the narrow emission lines and their implications

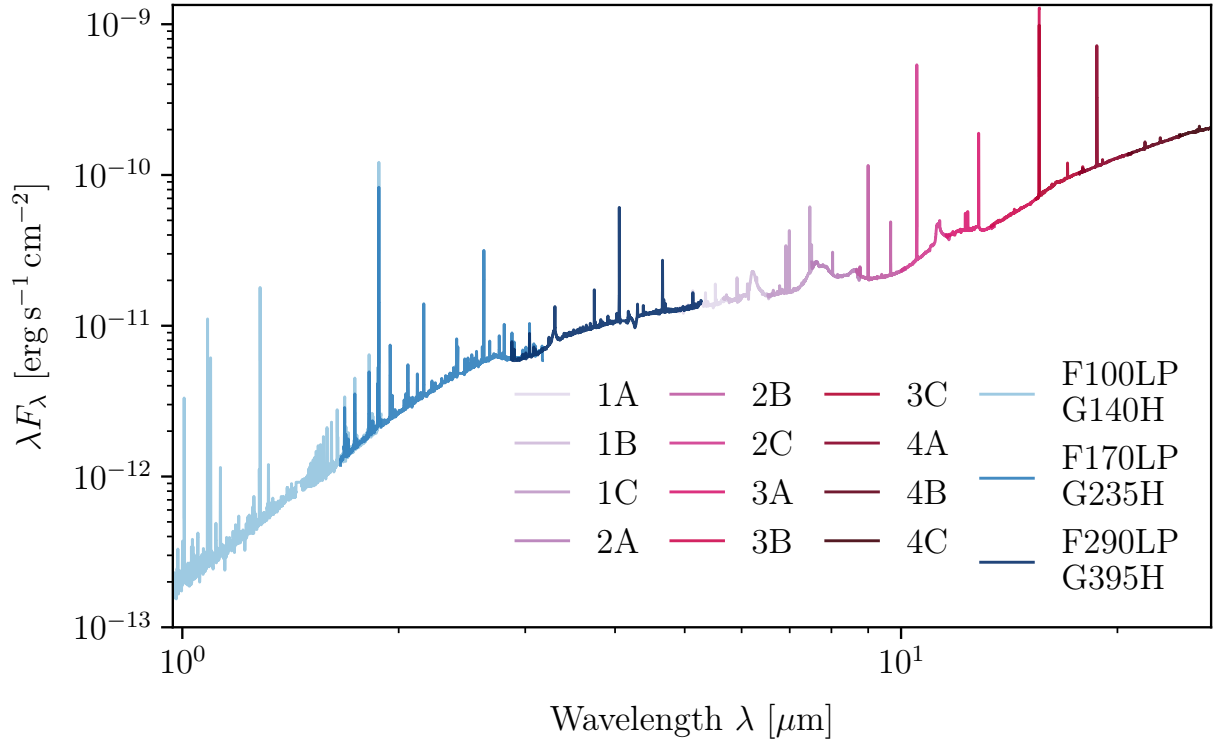


FIGURE 9.7 – Observed NIRSpec and MIRI/MRS SED of S7A spanning a wavelength range of 0.97–27 μm . The different colors in each panel indicate the different filters/gratings of NIRSpec and IFU channels of MIRI/MRS.

on the conditions of the circumstellar medium. With the advantages of the IFUs, spatially resolved emission line maps reveal striking diffuse structures around the YSO.

NIRSpec and MIRI/MRS spectra of point source C1 are shown in figure A.4. C1 can be identified as a source for $\lambda > 1.7 \mu\text{m}$ (NIRSpec F170 filter). For wavelengths longer than $\sim 12 \mu\text{m}$ C1 is covered by the MIRI/MRS PSF of S7A. The measured flux densities are about 2 orders of magnitudes lower compared to S7A. The distribution of emission lines appears similar, although the relative strengths are different. The most prominent spectral differences include the non-detection of the water ice absorption feature around $\sim 3.3 \mu\text{m}$ and CO_2 ice around $4.3 \mu\text{m}$. The broad PAH emission features and the silicate absorption between $9 \mu\text{m}$ and $11 \mu\text{m}$ are significantly stronger for C1 than for S7A. The weak PAH emission feature around $3.4 \mu\text{m}$ is more pronounced in C1 than S7A.

9.5 NIRSpec and MIRI/MRS IFU spectra – Spectral Lines

To understand the atomic and molecular environment in which the YSO is located in, the brightest spectral emission lines are investigated. Hydrogen line ratios can be employed to estimate mass accretion rates onto the central protostar (e.g., Jones et al. 2022, and references therein). Further, the NIRCам F090W image points to a possible single-sided outflow. Certain line transitions such as H_2 or $[\text{Fe II}]$ have been associated with protostellar jets (e.g., Davis et al. 2011). H_2 and $[\text{Fe II}]$ line ratios can be employed to derive the dominating excitation mechanism – shock- or photo-excitation (Bally et al. 2007; Bally 2016, and references therein).

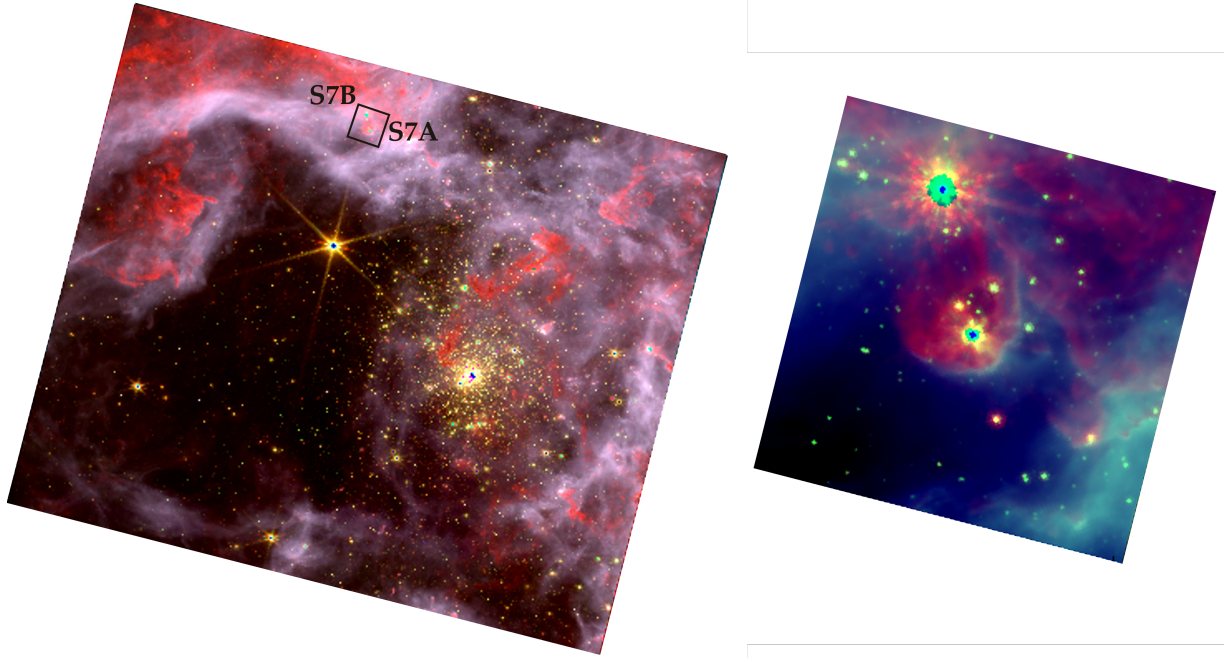


FIGURE 9.8 – Three-colour Near-IR image of the central cluster NGC 2070 with R136 in 30 Doradus and the position of S7A/B (left). A closer look at S7A/B (right). Red: F335M, green: F200W, blue: F187N.

9.5.1 Transitions tracing the MYSO and the shell

Recombination lines Hydrogen and Helium lines originate from the region of the YSO as well as from a C-shaped shell around the YSO as can be seen in the M0 maps in Figure 9.5. These lines are the result of electron-ion recombination



and the subsequent radiative cascades of the excited states. In optically thin environments, collisional excitation does not play a role. The 1st excited state for H I lies at ~ 10 eV and for He I at ~ 24 eV. Assuming a plasma temperature of $\sim 10^4$ K and a Maxwellian distribution of electrons, the electron energies are around ~ 1 eV – too low to excite H I or He I. Even for higher plasma temperatures, H I would be ionised before excited by electron collisions (Pradhan & Nahar 2011).

There are two main cases of recombination in low-density environments. Case A describes the case of an optically thin plasma where the H I column density is low enough such that ionising radiation (mainly H I Lyman photons) escapes after recombination. As a result, the total ionisation state of the plasma is reduced. Shock-heated regions with very high temperatures ($T \gtrsim 10^6$ K) and collisionally ionised Hydrogen but a small fraction of neutral H I are well approximated with case A recombination (Draine 2011). Case B recombination applies to the opposite case of an optically thick plasma with respect to H I-ionising radiation. The photons emitted during recombination will be re-absorbed, ionising another neutral Hydrogen atom. Hence, the ionisation of the gas is not reduced by transitions to the ground state of Hydrogen. The UV Lyman transitions (with high principal quantum numbers of the upper level n_2) will scatter until they are converted into a Balmer and Ly α line (or

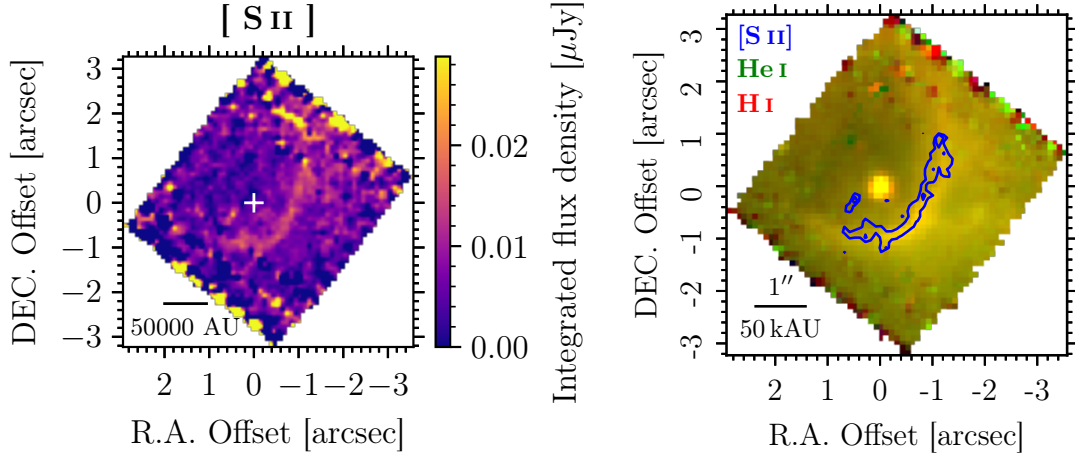


FIGURE 9.9 – **Left:** Mean M0 map of the observed [S II] transition. The white cross indicates the fitted position of S7A. **Right:** Comparison of shell emission from H I (red), He I (green) recombination lines and [S II] transitions (blue contours). The [S II] emission originates from the inner part of the shell and is less extended compared to H I and He I towards the star cluster.

two-photon continuum) (Ferland 1999). This case is applicable for H II regions around massive O and B-type stars. For massive YSOs, the situation is similar and calculations of extinction (Sect. 9.7.1) and electron temperatures and densities derived from line ratios assume case B recombination (e.g., Bary et al. 2008; Davis et al. 2011). There exists also the intermediate case C recombination. The Lyman UV lines are not completely optically thick and are not fully absorbed. In addition, these Lyman lines as part of the UV continuum may induce fluorescent transitions in O I and Fe II ions (see Sect. 9.5.3 and 9.6.1). The optical and IR cascades will then be stronger than assumed for case A (Ferland 1999).

The Hydrogen recombination lines are the most abundant lines in the MYSO and shell spectra ($N = 101$) with fluxes around 10^{-14} – 10^{-17} erg s $^{-1}$ cm $^{-2}$. The brightest H I lines being the P α 1.87 μ m, Br α 4.05 μ m, Pf α 7.46 μ m and H I (13 – 9) 14.2 μ m transitions with fluxes around $F \sim 10^{-14}$ erg s $^{-1}$ cm $^{-2}$ for the YSO. 15 Helium fine-structure transitions ($F \sim 10^{-15}$ – 10^{-17} erg s $^{-1}$ cm $^{-2}$) were found which are also formed by recombination (Draine 2011). Apart from the YSO, the shell region S1A (see Fig. 9.3) is the most pronounced in both H I and He I lines. In the brightest part of the shell (S1A in Fig. 9.3), the P α 1.87 μ m transition is by far the brightest line (Fig. A.3). The flux density $F \sim 10^{-13}$ erg s $^{-1}$ cm $^{-2}$ is nearly a magnitude higher than for the YSO. Similar observations can be made for He I lines. Here, the brightest transitions lies at 1.08 μ m with a flux density ratio of ~ 6 between the shell region S1A and the YSO. Towards the edges of the shell (regions S1B and S2) the intensity of He I is reduced compared to H I emission. In general, He I emission originates from the same regions as H I emission tracing the same structures although weaker and more compact. This observation is similar to (ultra- or hyper-compact) H II regions where a hot central source ionises large amounts of surrounding gas (Ward 2017). The NIRSpec and MIRI/MRS spectra extracted for S1A are shown in figure A.3 and the calculated flux densities are reported in table E.2. For wavelengths longer than ~ 13.5 μ m (Ch-3B), S7A and the shell can no longer be distinguished as two separate structures due to the large PSF and are not included in the analysis.

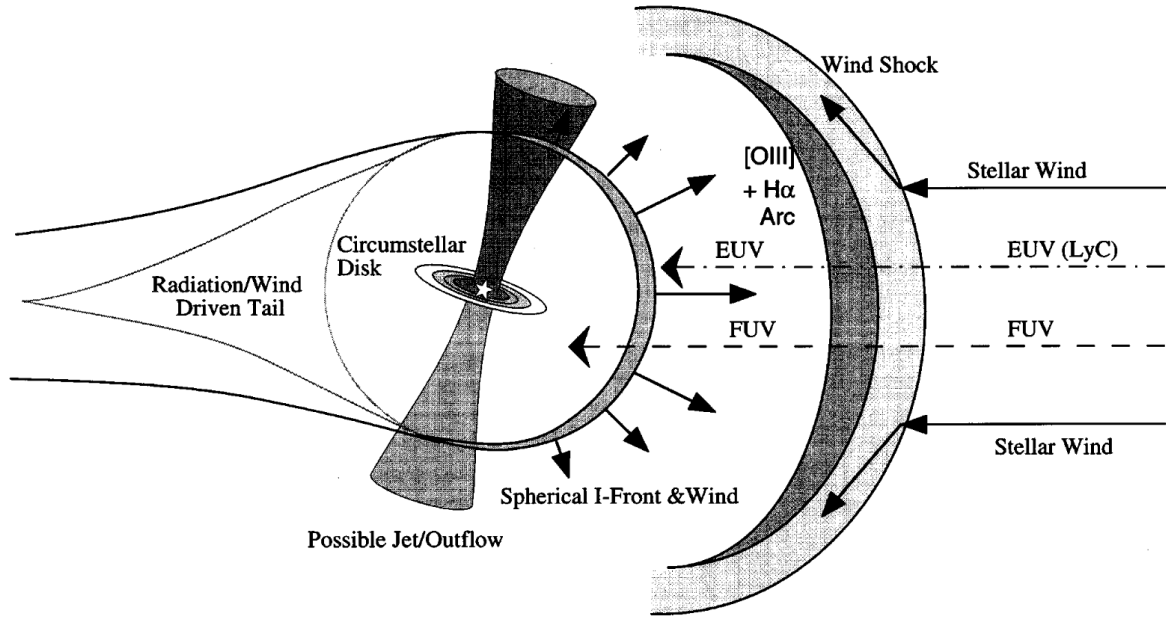
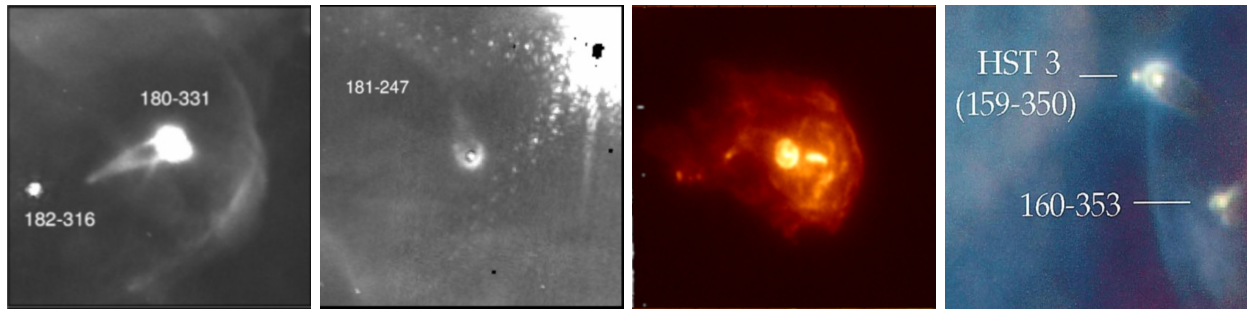


FIGURE 9.10 – **Upper panel:** Narrow-band images of PROPLYDs. The first two images from the left: NIRCcam F187N $P\alpha$ (Habart et al. 2024), VLT/MUSE $[O\ I]$ of PROPLYD 244–440 (Kirwan et al. 2023) and a three-colour composite HST image, R: $[N\ II]$, G: $H\alpha$, B: $[O\ I]$ (Bally et al. 1998). **Lower panel:** Schematic illustrating the processes of PROPLYDs or externally illuminated YSOs (Bally et al. 1998).

Forbidden Transitions The MYSO and the shell appear in (electric-dipole) forbidden lines of heavier elements as well (see M0 maps in Fig. 9.6 and Fig. C.4). Forbidden lines are excited in collisions with electrons. During the collision, the electrons lose kinetic energy. Therefore, collisional excitation cools the gas. In general, forbidden lines originate in a lower-density medium, in particular lower than the critical density of a transition (see Eq. 4.10), than electric-dipole transitions such that the excited state with a low transition probability has enough time to survive possible collisional de-excitation.

27 forbidden transitions from heavier elements such as Carbon (C), Neon (Ne), Sodium (Na), Silicon (Si), Phosphorus (P), Sulphur (S), Chlorine (Cl), Argon (Ar), Potassium (K), Iron (Fe) and Nickel (Ni) are present. The excitation stages range from neutral species (C, Ni) over single-ionised (Ne, S, Cl, Ar, Fe) and double-ionised (Ne, Na, P, S, Ar, K, Fe) to triple-ionised (S, Cl, K). All elements and their ionisation stages are consistent with observations of photo-ionised regions around O and B stars (Draine 2011). All observed transitions are listed in table B.1 and the flux densities extracted from the position of the YSO in table E.1 and those from the shell in E.2.

The photo-ionising radiation responsible for the recombination lines close to S7A and in the shell has a different origin. H I and He I at position of the YSO are ionised by the UV radiation of the massive YSO itself. Photons with energies up to 46 eV must be present to triple-ionise Potassium as the $[\text{K IV}]^3\text{P}_1 - ^3\text{P}_2$ transition is present (Fig. C.4). The radiative feedback from S7A might be creating an HC H II region expanding into an UC H II region. Alternatively, the photo-ionising may be photo-evaporating the surface of the circumstellar disk (see discussion in Sect. 1.4.1). The shell is formed by external radiation from the nearby star cluster R136 and traces the stationary ionisation shock front at pressure equilibrium from the stellar winds of the R136 cluster and winds from the YSO (Johnstone et al. 1998; Bally et al. 1998). Such arcs around YSOs have been first discovered in the Orion Nebula. S7A strongly resembles the so-called PROtoPLanetary Disks (PROPLYDs; O’Dell et al. 1993; O’Dell & Wen 1994) or *externally illuminated* YSOs (Bally et al. 1998). Figure. 9.10 shows a few examples of NIRCcam and HST images of PROPLYDs in Orion. More examples can be found, e.g., in Habart et al. (2024) and in Ricci et al. (2008). In this work, the first PROPLYD outside of the Galaxy and around a high-mass YSO is presented. Many PROPLYDs show tails of ionised emission and a bright ionisation front close to the YSO interpreted as photo-evaporating circumstellar disks (Johnstone et al. 1998; Bally et al. 1998). These observations are missing in the system of S7A.

The ionised shells have been found to be bright not only in H α (see also the HST images of S7A in Fig. 9.1), but also in optical forbidden lines of [N II], [O I], [O III] and [S II]. Using HST/WFC2 archival images (Walborn et al. 2002), shell emission – but not emission from the YSO – could be confirmed also in [O III] 0.63 μm , [S II] 0.6717 + 0.6731 μm and H α lines (see Fig. 9.1). In the NIRSpc and MIRI data, we also find evidence for ionised Helium through the IR He I recombination lines and further NIR and MIR forbidden transitions of [Ni I], [Fe II], [S II], [Fe III], [Ne II], [S III], [Ar III], [K III], [S IV], [Ne III] – in order of increasing ionisation potentials (see Fig. C.4 for the M0 maps of the observed transitions). The corresponding transitions and estimated line flux densities are summarised separately in table E.2. Shell emission from [Cl II] and [P III] cannot be confirmed due to the bad sampling of the MIRI/MRS M0 maps around the position of the YSO. However, the surrounding emission in the rest of the foV resembles that of confirmed lines, especially for [P III]. In addition, there appears to be a layering of elements in the shell. Apart from the bright H I and He I emission, we detect a faint shell structure in the [S II] 1.03–1.04 μm lines (see Fig. C.4 and Fig. 9.9). This structure is less prominent and less extended in the direction of the star cluster.

While the dimensions of the distances between YSOs and arcs lie on AU scales at distances of the Orion nebula $\sim 400\text{--}500\text{ pc}$, the shell around S7A is about $0''.7$ away from the YSO in south-west direction which corresponds to $\sim 35\text{ kAU}$ at a distance of $\sim 50\text{ kpc}$.

The shell around S7A appears to have two arms (S1 and S2 in Fig. 9.3) with a possible fainter third arm (S3). The brightest region in the shell – S1A – overlaps with the diffuse emission seen in the HST (Fig. 9.1) and NIRCcam F090W (Fig. 9.2) images. It likely corresponds to an outflow or jet associated with S7A and seems to interact with the material in the shell. It may either excite the atoms and ions present in the shell and shift the pressure equilibrium of the ionisation front away from the YSO. Alternatively, the out-flowing material from S7A itself might be penetrating the ionisation front being ionised in the process and therefore contributing to the increased brightness.

9.5.2 Molecular Hydrogen Lines

H₂ transitions detected in the YSO spectrum can be separated into ro-vibrational and purely rotational transitions. The latter are S-branch transitions within the lowest vibrational $v = 0$, S-branch transitions within $v = 1$ and the S(9) transition within $v = 2$. Molecular Hydrogen emission originates from the YSO and is distributed in the complex diffuse structure around the YSO (see Fig. 9.5). Both the ro-vibrational and purely rotational H₂ emission morphology closely follows the distribution of PAHs observed in the NIRCcam F335M filter (see Fig. 9.2). Ro-vibrational H₂ transitions additionally seem to extend further out from the region of the YSO towards the north-west (see Sect. 9.8.1).

The close correlation of H₂ may seem surprising at first glance. However, when considering H₂ formation in the ISM, the connection becomes clear. H₂ is mostly formed at the surface of small interstellar dust grains. After Hydrogen atoms get bound to the grain surface, their diffusion leads to two atoms encountering each other and forming H₂. The energy released in this reaction is about 4.5 eV (Draine 2011). It is both enough to overcome the binding energy of the H atoms and the grain as well as to leave the formed H₂ molecule in an excited state. It was found that H₂ formation on dust in the way described above requires very low grain temperatures in the range of 11–13 K. With more complex chemical scenarios temperatures up to 25 K can be reached (Lequeux 2005).

The formation of H₂ via radiative association ($\text{H} + \text{H} \rightarrow \text{H}_2^* \rightarrow \text{H}_2 + h\nu$) does not occur. Two H atoms combining directly into an excited level and emitting the excess energy is not an efficient reaction as H₂ does not possess a dipole moment. Therefore, no permitted transitions exist for de-excitation and electric quadrupole transitions have very low probabilities. The second possibility of forming H₂ with the help of a third H atom carrying away the excess energy via a collision requires very high densities ($n_{\text{H}} > 10^{11} \text{ cm}^{-3}$) which do not exist in any phase of the ISM (Lequeux 2005).

H₂ (together with [Fe II]) were also identified as tracers of protostellar parsec-scale jets (e.g., Eislöffel 2000; Stanke et al. 2002) as well as outflows in early B-type YSOs (Varricatt et al. 2010, Fig. 6) such as S7A. Inspecting the calculated line profiles for the H₂ lines (Sect. 9.8.1) and M0 maps (e.g., Fig. 9.6), shows that the molecular emission close to the YSO is clearly extended in the direction of the diffuse emission detected in HST and NIRCcam F090W images. As a molecule, the presence of H₂ suggests a shocked gas component in a low-excitation stage at $T \sim 2 \times 10^4 \text{ K}$ with low radial velocities $v_{\text{rad}} \sim 10\text{--}30 \text{ km s}^{-1}$ (Bally et al. 2007). Observations suggest that this gas phase does not originate solely from the interaction of an outflow with ambient medium, but part of the outflow itself must be molecular (Bally et al. 2007; Ray et al. 2023). The H₂ in the medium must survive the shocks introduced by the outflows. At typical densities of $n_e \sim 10^4 \text{ cm}^{-3}$, the timescale for H₂ to form on dust grains is around $2 \times 10^5 \text{ yrs}$ which is comparable to the dynamical time scale of an outflow (O’Connell et al. 2004). Further discussion on the correlation of protostellar jets, shocks and H₂ emission follows in section 9.8.

9.5.3 O I transitions

The observed O I transitions at $1.13 \mu\text{m}$, $1.32 \mu\text{m}$, $2.89 \mu\text{m}$ and $3.10 \mu\text{m}$ result from fluorescent excitation either due to strong UV lines of abundant species such as H I or He I or continuum UV background radiation from hot stars. The $1.13 \mu\text{m}$ transition originates from line

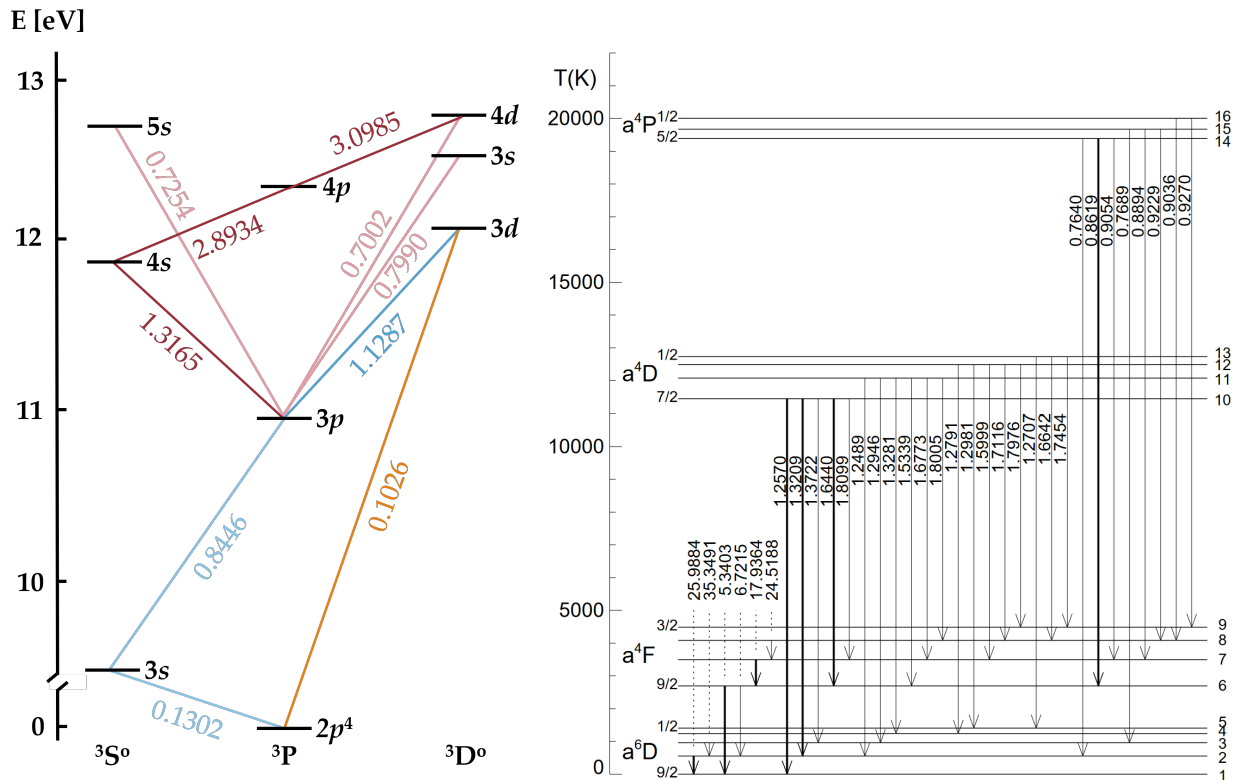


FIGURE 9.11 – **Left:** O I energy level diagram for the triplet states involved in continuum (red) and Ly β fluorescence (blue). The orange line shows the O I $3P_2 - 3D^{\circ}$ transition resonant to the Ly β line at $0.102572 \mu\text{m}$. The wavelengths of the transitions are given in μm . The splittings according to the different total angular momentum quantum numbers J are not indicated as they cannot be resolved in the spectra. **Right:** The 16 lowest Fe II energy levels giving rise to NIR and MIR [Fe II] transitions. The diagram is adapted from [Koo et al. \(2016\)](#).

fluorescence. A coincidence exists in the energy difference of the Ly β 1.02572 μm and the O I 1.02576 μm transition from the ground state $1s^2 2s^2 2p^4 \ ^3P_2$ to $^3D^\circ$. Such transitions are also referred to as *resonant*. Due to the high abundance of H I in the interstellar medium, the Ly β recombination line has a very high intensity. The 1.02572 μm Ly β photons ‘pump’ the O I atoms to the $^3D^\circ$ state. The highly populated $^3D^\circ$ state can then radiately decay giving rise to IR 1.13 μm line as well as the 0.8446 μm optical and 0.1302 μm UV lines (see Fig. 9.11). This line fluorescence mechanism was first described by Bowen (1947) and is also referred to as *Bowen fluorescence*. Alternatively, Bhatia & Kastner (1995) refer to the same process as *photoexcitation by accidental resonance*.

The 1.32 μm , 2.89 μm and 3.10 μm lines originates due to continuum fluorescence due to the UV radiation from S7A. The population of the $4s^3S_1^\circ$ state is higher due to the UV photons than expected if only collisional excitation is present. The excited state decays to $3p^3P_1$ via spontaneous emission of 1.32 μm photons. The situation is similar for the other two transitions involving $4s^3S^\circ$, $4p(3p)^3P$ and $4d^3D^\circ$ multiplets (see Fig. 9.11). Lucy (2002) identified the longer wavelength transitions originating from UV pumping for the first time and gives a detailed theoretical overview.

Comparing the flux of the 1.13 μm and 1.32 μm lines is utilised to determine whether continuum of line fluorescence is the dominating excitation process (Porter et al. 1998). Measuring the equivalent width of the 1.13 μm and 1.32 μm transitions is further used to estimate which process is dominating (Mathew et al. 2018). In addition, 0.7002 μm , 0.7254 μm and 0.7990 μm lines are also often identified in spectra when continuum fluorescence plays a significant role (Mathew et al. 2018).

The M0 maps of the O I lines show that the emission does not only coincide with the position of the YSO, but also with that of the knot. The O I lines must originate in partially ionised gas environments where sufficient O I is present similar to the edges of H II regions following the H I ionisation front as the ionisation energy of O I at 13.618 eV is very close to the H I ionisation energy at 13.598 eV. Fluorescent O I lines have been previously discovered not only in star-forming regions such as the Orion nebula (e.g., Marconi et al. 1998; Peeters et al. 2024) but also in Be stars (e.g., Mathew et al. 2012), galactic Herbig Ae/Be stars (e.g., Mathew et al. 2018) and massive YSOs (e.g., Porter et al. 1998).

The significant decrease of flux at the knot (see Sect. 9.8.1 and Fig. 9.19) compared to the YSO position ($\sim 60\text{--}70\%$) suggest that O I is removed from the partially ionised region close to the YSO by an outflow. Enough far UV radiation ($\lambda < 13.6\text{ eV}$) still reaches $0''3\text{--}0''4$ away from the YSO, exciting the O I atoms, but not ionising them.

The de-reddened $F(1.13\ \mu\text{m})/F(1.32\ \mu\text{m})$ flux ratio is 2.5 ± 0.5 – smaller than 6.2 – suggesting continuum fluorescence is dominant over line fluorescence according to (Porter et al. 1998). Comparing the strength of the 1.13 μm further to the 2.89 μm and 3.10 μm continuum fluorescent lines, their de-reddened ratios are: $F(1.13\ \mu\text{m})/F(2.89\ \mu\text{m}) = 5.7 \pm 1.3$ and $F(1.13\ \mu\text{m})/F(3.10\ \mu\text{m}) = 13.8 \pm 3.5$. Most of the massive YSOs studied by Porter et al. (1998) showing O I emission (with the exception of one), however, show Ly β as the dominating mechanism. The dust envelope of S7A must be optically thin enough for far-UV radiation from the central protostar to escape it as H I and He I recombination lines are observed. Radiation with energies $>13.6\text{ eV}$ and even $\sim 24.6\text{ eV}$ must be present in order to ionise H I and He I atoms. Ly β photons with energies around 12 eV are therefore not stopped by the envelope. The central B1V-type protostar could have strong Lyman absorption lines.

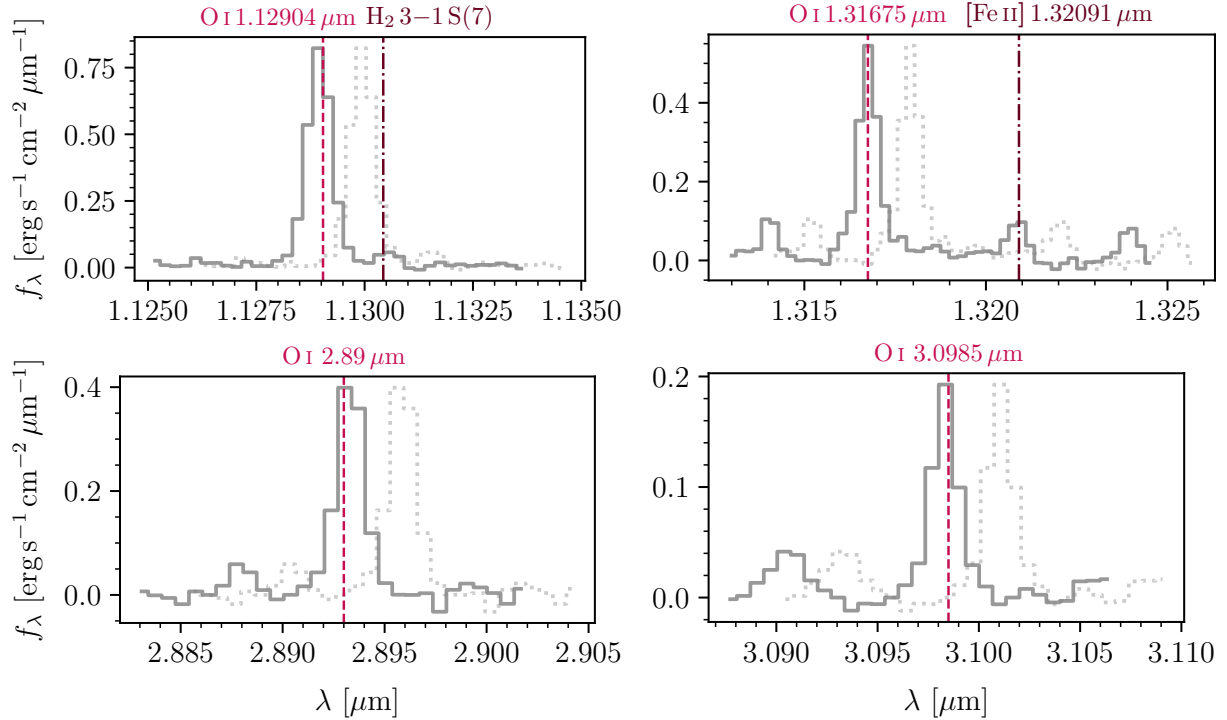


FIGURE 9.12 – O I spectral lines. The solid line shows the continuum-subtracted and redshift-corrected spectrum. The dotted line shows the continuum-subtracted observed spectrum.

However, [van Gelder et al. \(2020\)](#) only mention Balmer absorption lines. The Lyman lines might also be reprocessed in a case B recombination scenario (see Sect. 9.5.1).

9.5.4 Unidentified transitions

Several studies on YSOs, have identified permitted atomic transitions from heavier metals such as Na I, Ca I, Mg I, fluorescent Mg II, Al I (e.g., [Antoniucci et al. 2008](#); [Bik et al. 2005](#); [Davis et al. 2011](#)). Most of the unidentified lines have transitions matching the observed wavelengths. However, most of these transitions involve high orbitals and are therefore not confidently identified. Some of these transitions are discussed below. Furthermore, fluorescent Fe II is discussed in the literature to be a tracer of disks in intermediate and high-mass YSOs (see, e.g., [Porter et al. 1998](#); [Lumsden et al. 2012](#)). Several of the unidentified transitions up to $\sim 3 \mu\text{m}$ are possible Fe II transitions and are discussed in section 9.6.1.

The $1.050 \mu\text{m}$, $1.113 \mu\text{m}$ and $1.840 \mu\text{m}$ transitions could be Ca I or Mg I transitions. However, also Fe II lines are present. Which of these elements is more likely to be present in the spectrum of S7A cannot be distinguished at the resolution of spectrum and the observed line fluxes. In addition, transitions of Ca I and Mg I at these particular elements were not found in the literature YSO spectra (e.g., [Davis et al. 2011](#)). It is noted that the $1.113 \mu\text{m}$ line shows a peculiar arc-like morphology close to the YSO in the M0 map (Fig. C.5).

The $5.000 \mu\text{m}$, $5.217 \mu\text{m}$ and $8.409 \mu\text{m}$ transitions have a match to the high excitation H₂ 9–8 Q(8), 13–11 O(5), 9–8 O(8) lines. The 13–11 O(5) transition has a vacuum wavelength of $5.220 \mu\text{m}$. The wavelength offset to the observed transition seems too large to be a confident match. The emission is originating solely from the position of the YSO as for the

5.000 μm transition. The 8.409 μm line shows no distinct morphology in the M0 map. As no H_2 transitions are observed between vibrational states between $v = 4-8$, it is unlikely such highly excited isolated states are present. The wavelength range around 5 μm is covered both by NIRSpec F290 and MIRI 1A. However, the 5.000 μm and 5.217 μm lines are only observed in the NIRSpec data. Several atomic lines of heavier metals have transitions at wavelengths similar to the observed such as Na I 5.216 μm or Al I 8.41 μm . However, most involve high orbitals. The same argument applies for the He I 5.002 μm and C I 5.220 μm and 8.410 μm transitions.

The MIR line observed at 15.753 μm ($F < 1.54 \times 10^{-15} \text{ erg s}^{-1} \text{ cm}^{-2}$) is close to several Na I transitions involving very high orbitals. For example, the 15.754 μm line from $2p^6 26p \ ^2P^\circ$ to $2p^6 13s \ ^2S$. No identifications of Na I lines at NIR wavelengths do not favour recombination as a possible explanation for the presence of such lines. Similar arguments can be applied for the 15.755 μm transitions of Ar I. The M0 map of this transitions is undersampled and is not of help for the identification.

9.6 Disk tracers – CO bandhead emission and fluorescent Fe II

9.6.1 Comparison to the NIR X-shooter spectrum

As stated in section 9.1, [van Gelder et al. \(2020\)](#) studied the spectrum of S7A with X-shooter. However, only a limited number of emission lines is discussed in their context of identifying massive YSO and not line fluxes are given. Therefore, we can only discuss the detection or non-detection of emission lines in either spectra. When comparing the X-shooter and JWST spectra, one has to keep in mind that the X-shooter spectrograph has a higher spectral resolution in the NIR ($R = 8100$) than NIRSpec ($R \sim 2700$). They detect Br γ , [Fe II] 1.64 μm and H_2 2.12 μm emission which can be confirmed with JWST spectra. The H I Paschen series is flagged as a weak emission feature and a residual from Earth's atmosphere. With NIRSpec and MIRI, the Paschen series from P δ to P α is clearly detected with the P α transition being one of the strongest emission lines in the entire spectrum. The [Fe II] 1.64 μm transition was not detected in the X-shooter spectrum. However, with NIRSpec we detect this transition with a flux of $(2.96 \pm 0.49) \times 10^{-16} \text{ erg s}^{-1} \text{ cm}^{-2}$. Confusion with residual nebular emission is the most probable explanation.

CO emission [van Gelder et al. \(2020\)](#) also detect weak CO bandhead emission from the first overtone $v = 2-0$ ($\sim 2.3 \mu\text{m}$). Although no CO bandheads had been detected by our pipeline, upon second look we do find evidence for weak CO 2–0 and 3–1 bandhead emission ($F \sim 3 \times 10^{-16} \text{ erg s}^{-1} \text{ cm}^{-2}$; see Tab. E.1). The CO molecule is the second most abundant molecule in the universe – after H_2 ([Draine 2011](#)). In YSOs, CO emission is thought to originate in the inner regions of circumstellar accretion disks (see Fig. 1.5) which are mainly made up of neutral gas with very high densities $n > 10^{11} \text{ cm}^{-3}$ and temperatures between 2500–5000 K ([Jones et al. 2022](#), Sect. 4.5 and references therein). CO emission is detected more frequently in galactic YSOs with mass accretion rates around $10^{-5} M_\odot \text{ yr}^{-1}$ and where the density is high enough to self-shield against UV radiation from the central protostar. The only detection of weak CO emission from YSOs in the LMC have been found in S4, S5-E and S7A ([van Gelder et al. 2020](#)) and a single source in the SMC ([Ward et al. 2017](#)).

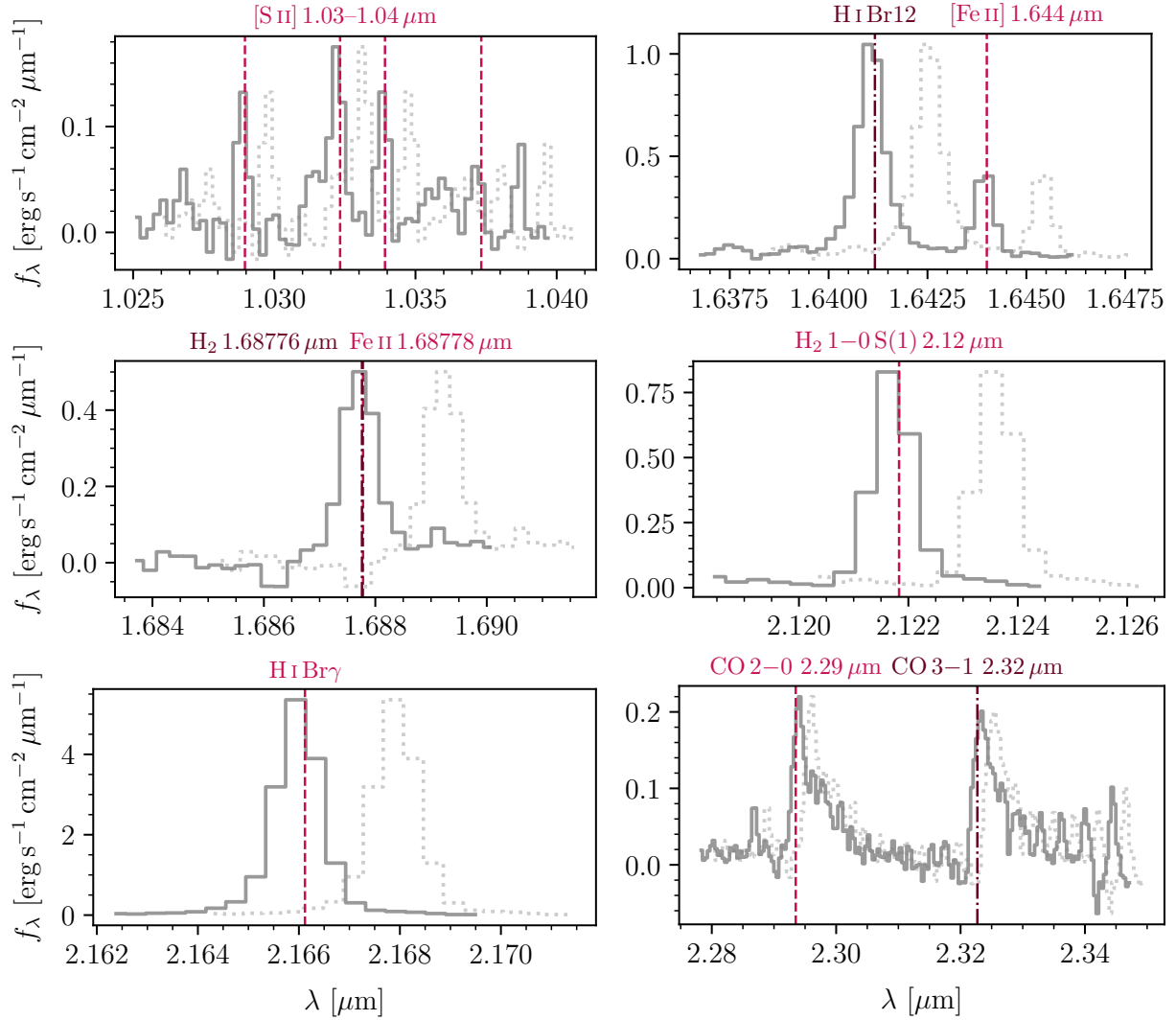


FIGURE 9.13 – Selected NIR spectral lines discussed in [van Gelder et al. \(2020\)](#) (Sect. 9.6.1) and in S9 (Sect. 9.6.2). The solid line shows the continuum-subtracted and redshift-corrected spectrum. The dotted line shows the continuum-subtracted observed spectrum. The dashed-dotted vertical lines show the observed wavelength as determined from Gaussian fits to the lines.

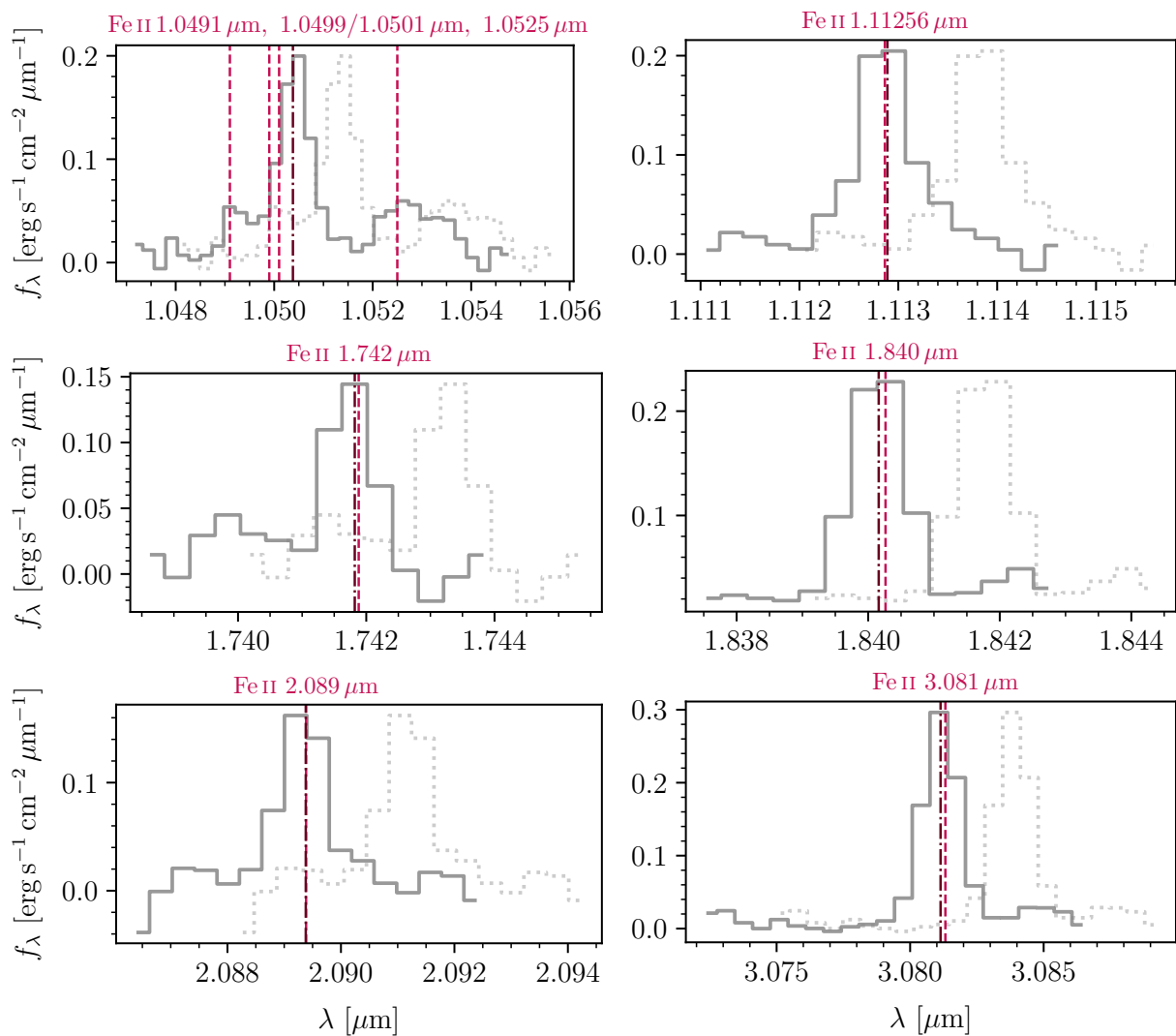


FIGURE 9.14 – Fe II spectral lines discussed in section 9.6.1. The solid line shows the continuum-subtracted and redshift-corrected spectrum. The dotted line shows the continuum-subtracted observed spectrum. The vertical dashed line marks the position of Fe II transitions discussed in the text. The vertical dash-dotted line shows the observed redshift-corrected wavelengths estimated from Gaussian fits to the lines observed in the spectrum.

The most probable explanation of this observation is the reduced metallicity of the LMC and SMC which leads to an overall decrease of CO abundance and affects the properties of dust grains. Together with a higher UV radiation field (Welty et al. 2006), the temperature and density within the disk may be altered to unfavourable conditions for either the presence of CO or its detection in low- and medium-resolution spectra at the distance of the LMC (see discussion in Jones et al. 2022). Additionally, apart from being associated with inner regions of accretion disks, CO emission is also thought to be formed in accretion flows from the disk to the central object (Martin 1997) as well as optically thick stellar winds (Carr 1989; Davis et al. 2011).

Fluorescent Fe II Both CO bandhead and fluorescent Fe II are discussed in the literature to be tracers of disks in intermediate and high-mass YSOs (see, e.g., Porter et al. 1998; Lumsden et al. 2012). The IR Fe II lines resulting from H I Ly α or H I Balmer continuum fluorescence (Lucy 1995; Porter et al. 1998). The fluorescent Fe II 1.68778 μm $c^4\text{F}_{9/2} - z^4\text{F}_{9/2}^\circ$ transition cannot be separated from H₂ 1–0S(9) transition at 1.68776 μm in the NIRSpc spectrum (see Fig. 9.13). The M0 map displayed in figure C.1 shows emission only from the central YSO region without tracing the surrounding morphology (Fig. 9.5). However, several other identified H₂ are similarly located solely at the YSO. In addition, the ro-vibrational line H₂ 1–0Q(11) at 2.635 μm originating from the same upper level is detected. This line is probably a blend of contributions of H₂ and Fe II. Other Fe II transitions at 1.840 μm ($c^4\text{F}_{7/2} - z^4\text{F}_{7/2}^\circ$) and 2.089 μm ($c^4\text{F}_{3/2} - z^4\text{F}_{3/2}^\circ$) originating from the same multiplet are also observed (Fig. 9.14 and Fig. C.1). Porter et al. (1998, see their Tab. 2) had detected four other Fe II lines in massive YSO spectra at 1.050 μm , 1.690 μm , 1.741 μm and 2.091 μm (see Fig. 9.15). In addition, further fluorescent transitions exist around 1.050 μm and 1.113 μm (also mentioned in Porter et al. (1998), although not detected in any of their sources; see Fig. 9.15). Unfortunately, Porter et al. (1998) do not specify the exact terms involved in the transition. The transitions at 1.690 μm and 2.091 μm mentioned by Porter et al. (1998) are the transitions at 1.688 μm and 2.089 μm discussed above. The 1.113 μm and 1.741 μm transitions could correspond to the observed lines at 1.11256 μm , 1.74180 μm (Fig. 9.14) corresponding to Fe II transitions at 1.11286 μm $b^4\text{G}_{5/2} - z^4\text{F}_{3/2}^\circ$ and 1.74188 μm $c^4\text{F}_{7/2} - z^4\text{D}_{7/2}^\circ$. However, a considerable wavelength offset is still present. Only the unidentified transitions at the observed wavelength $\lambda_{\text{obs}} = 1.84016 \mu\text{m}$, 2.08938 μm and 3.08114 μm have no considerable offset to the Fe II 1.84026 μm $c^4\text{F}_{7/2} - z^4\text{F}_{7/2}^\circ$, 2.08939 μm $c^4\text{F}_{3/2} - z^4\text{F}_{3/2}^\circ$ and 3.08132 μm $c^4\text{P}_{5/2} - z^4\text{P}_{5/2}^\circ$, respectively (see Fig. 9.14). The M0 maps reveals the emission being concentrated to the YSO (Fig. C.1).

The detection of CO and Fe II emission (likely the broad ice absorption features discussed in Sect. 9.4 as well) are indicative of an circumstellar disk. Studies of larger samples ($N = 76$) of Galactic MYSOs have identified CO *together with* Fe II emission only towards a handful ($N = 6$) of objects (Cooper et al. 2013). Those with Fe II emission exhibit full Brackett series and weak or not H₂ emission. Ward (2017) suggests that this observation could imply an evolutionary sequence where younger MYSOs exhibit CO bandheads and only at later stages Fe II. Comparable studies towards the LMC contain only limited numbers of MYSOs (Ward 2017, seven out of nine show Fe II, none CO emission). Their (non-) detections are therefore not statistically significant. Due to the presence of strong H I and

He I recombination lines, S7A exhibits either a HCH II region or a photo-evaporating disk (see Sect. 1.4.1 and Sect. 9.5.1). At this stage, the accretion rate is significantly lower than in the main accretion phase and accretion disks are likely to either be optically thin due to the increasing UV radiation (Ward 2017). Under the assumption that CO and Fe II are present in the inner regions of disks (see Fig. 1.5), the detection of their emission means the UV radiation is reaching the inner disk.

9.6.2 Comparison of S7A and S9 spectra

Reiter et al. (2019) obtained a NIR spectrum (0.8–2.5 μm) of YSO S9 (30 Dor YSO in their work; R.A. 84.703995, DEC. –69.079110) with the Folded-Port Infrared Echellette (FIRE; Simcoe et al. 2013) spectrograph on the Magellan/Baade telescope with a spectral resolution of $R = 4800$. As in the spectrum of S7A, H I and He I recombination is detected. The respective H I and He I line fluxes are significantly higher for S7A than S7B. The He I recombination lines are ~ 4 – 5 times stronger for S7A, the $\text{Br}\gamma$ transition flux is even ~ 15 times that of S9. Due to the proximity of the two sources ($D \sim 6$ pc), they have likely formed from the same molecular cloud. This would suggest the same elemental abundances present in both YSOs. The higher line fluxes for S7A must result from higher ionising radiation due to either a higher mass and higher stellar UV photons and therefore a higher class and older YSO or a higher mass accretion rate in an earlier evolutionary stage. The masses of S7A and S9 are similar and around $\sim 20 M_{\odot}$ (Nayak et al. 2016).

Highly excited [S III] 0.90+0.95 μm lines are identified in the S7B spectrum. The NIRSpec data available for S7A starts around 0.97 μm . The presence of these [S III] transitions can not be confirmed. In contrast to S9, [S II] 1.03–1.04 μm transitions are observed.

CO absorption Further, CO bandheads at 2.3–2.4 μm have been detected in absorption. The CO lines in the spectrum of S7A are detected in emission. CO absorption lines have been detected in low-mass G-, K- or M-type and asymptotic giant branch stars (see, e.g., S3K in van Gelder et al. 2020; Nandakumar et al. 2018), T Tauri stars as well as in YSOs with high mass accretion rates (e.g., Carr 1989; Calvet et al. 1991). In YSOs, CO bandheads are typically observed in emission and are utilised to trace circumstellar disks (see e.g., Ilee et al. 2013). CO molecules form in the inner regions of the disk where the temperature is low enough for photodissociation to destroy the molecules ($T < 4 \times 10^4$ K; Calvet et al. 1991). Calvet et al. (1991) found that CO emission is more likely to be found in hot stars than CO absorption. The observed NIR spectrum shows CO in emission or absorption depending on the mass accretion rate from the disk onto the star and the amount of radiation from the star reaching the disk. The radiation from the central object increases the surface temperature of the accretion disk. If the surface temperature is higher than effective temperature of the entire disk, CO emission is observed. In the opposite case, CO absorption is present. Therefore, under the assumption of a temperature for the central star, the observation of CO absorption or emission in a YSO spectrum indicates the mass accretion rate. However, the opacity of the disk cannot be asserted with this method as calculations with optically thick and thin disks yielded the presence of CO emission (Carr 1989; Calvet et al. 1991). Whether accretion disks are optically thick or thin can be assessed from the observations of the CO molecule in addition to the continuum infrared excess. The infrared excess will be

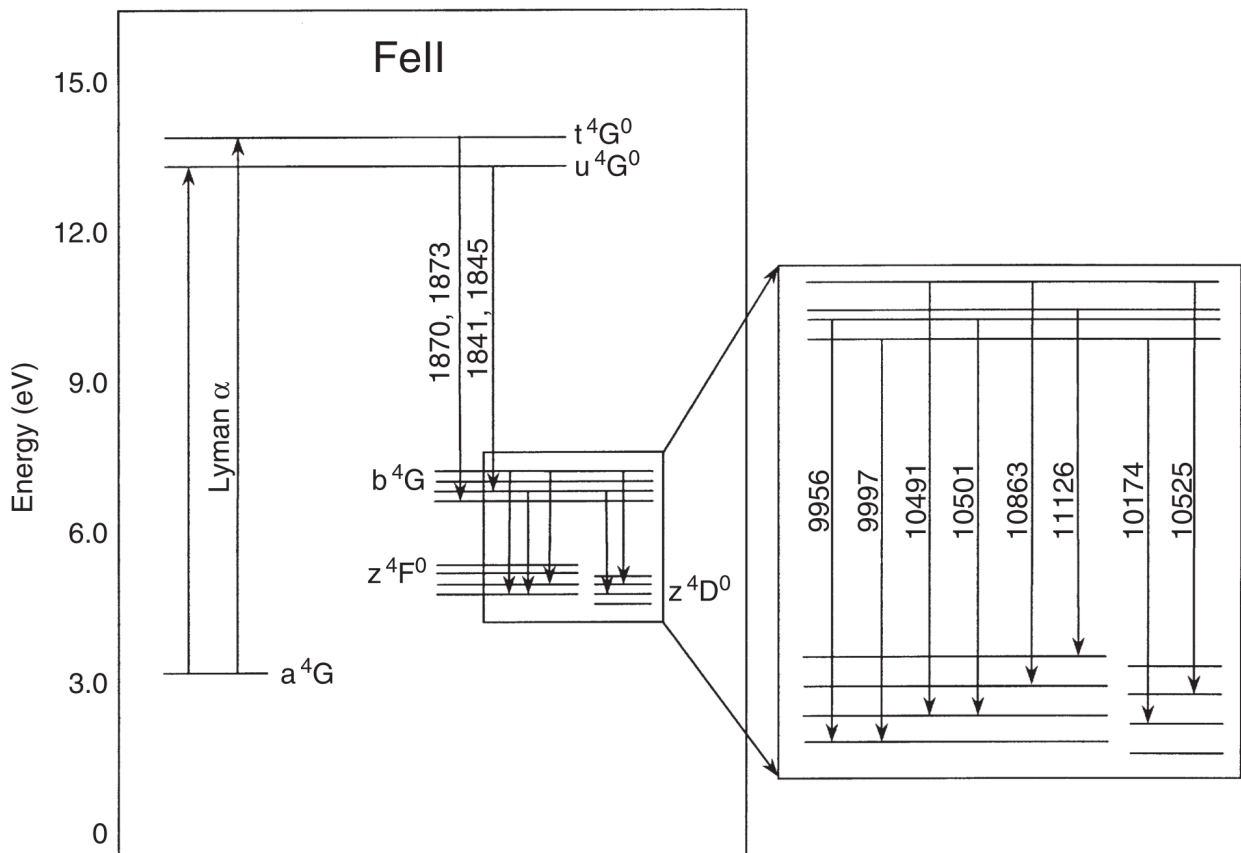
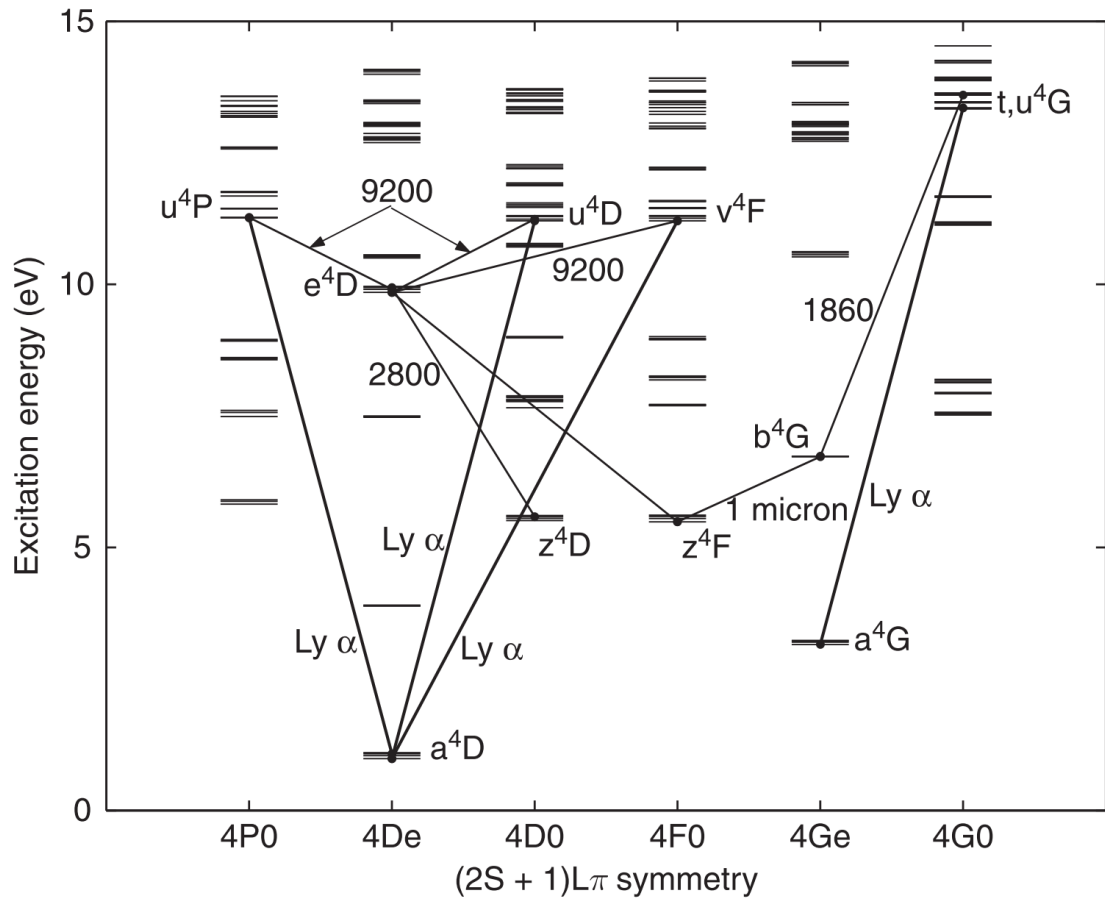


FIGURE 9.15 – Fe II energy level diagram illustrating fluorescence lines. The figures were adapted from Pradhan & Nahar (2011).

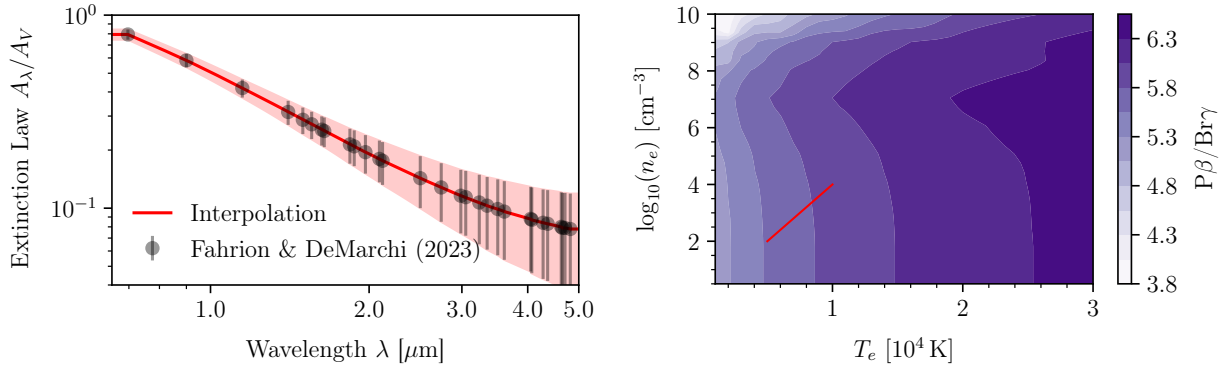


FIGURE 9.16 – **Left:** Extinction law derived by [Fahrion & De Marchi \(2023\)](#) for 30 Doradus. The red line represents an interpolation to the published data points. **Right:** H I $P\beta/Br\gamma$ line ratios under case B recombination as calculated by [Hummer & Storey \(1987\)](#). The red line shows the subspace assumed in this work for the calculation of extinction.

higher for optically thick compared to thin disks.

The estimated stellar temperature of S7A $T_* \sim 2 \times 10^4$ K would suggest mass accretion rates less than $\sim 10^{-4}$ – $10^{-5} M_\odot \text{yr}^{-1}$. However, their calculations only include temperatures up to 10^4 K. In addition, the assumed disk models have been developed for low-mass YSOs and through only limited observational detections of disk-like features it remains unclear if the same theory can be applied for MYSOs ([Reiter et al. 2019](#), and references therein). An extensive study on CO bandhead emission in MYSOs and its correlation with circumstellar disks can be found in [Ilee et al. \(2013\)](#). Their results show that CO emission is likely to originate close to the central source in an optically thin disk and that MYSOs form via disk accretion. They also tested models with similar assumptions of [Calvet et al. \(1991\)](#), mainly a disk heated through viscous flux and external irradiation from the protostar. However, none of these models provided a good fit to the observed CO profiles.

Furthermore, apart from being associated to inner regions of accretion disks, CO emission is also thought to be formed in accretion flows from the disk to the central object ([Martin 1997](#)) as well as optically thick stellar winds ([Carr 1989](#); [Davis et al. 2011](#)).

9.7 H I lines as accretion tracers

The mass accretion rate \dot{M} onto a protostar independent of the exact accretion mechanism is an indicator of the evolutionary stage of an YSO. Mass accretion rates are generally observed to decrease over time as the protostar grows. \dot{M} can be determined from the excess luminosity formed at the accretion shock at the proto-stellar surface compared to the intrinsic emission from the photosphere ([Calvet et al. 2004](#)).

9.7.1 Extinction Correction

To derive physical properties from the observed emission lines, flux densities have to be corrected for extinction and converted to luminosities. In this work, I estimate the extinction by comparing measured line flux density ratios to their theoretically predicted values. On the one hand, transitions from certain species which are separated in wavelength and share the same upper energy level can be utilised for this purpose as their ratio then only depends

on the extinction and physical constants. This method also does not depend on the specific excitation mechanism. H_2 and $[\text{Fe II}]$ lines ratios are common species which have been used for NIR observations (e.g., [Davis et al. 2011](#), and references therein). On the other hand, the so-called Balmer decrement – the sequence of Balmer line ratios with respect to $\text{H}\beta$ – can be used in optical observations as these pairs are approximately independent of electron temperature and at low densities also of electron density ([Draine 2011](#)). For the NIR, H I recombination lines of higher principal quantum numbers are used. The choice of the exact transitions depends on the available spectral range. The prediction of line ratios requires H recombination theory ([Storey & Hummer 1995](#)) and the assumption of a particular temperature and density for the gas. For YSOs, case B recombination is assumed (see, e.g., [Bary et al. 2008](#)).

In this work, two sets of lines are necessary to estimate the extinction towards the YSO and the shell and towards the knot as the emission is traced by different species. I use $\text{H I Pa}\beta$ (4–3) $1.28 \mu\text{m}$ to $\text{Br}\gamma$ (7–4) $2.16 \mu\text{m}$ ratio following [Jones et al. \(2022\)](#) for the YSO. In the context of YSOs, the H_2 1–0S(1) to 1–0Q(3) ratio is also often utilised ([Davis et al. 2011](#), and references therein). However, the Q(2), Q(3) and Q(4) transitions at $2.413 \mu\text{m}$, $2.424 \mu\text{m}$, $2.437 \mu\text{m}$ fall into the detector gap (see Sect. 6.2.2) and therefore cannot be used. Instead, I choose the H_2 1–0S(3) and 1–0Q(5) lines to estimate the extinction towards the region of the YSO and its outflow. For the knot region, the $[\text{Fe II}]$ transitions at $1.257 \mu\text{m}$ and $1.644 \mu\text{m}$ are suitable as they share the same upper level.

Measured flux densities of the relevant emission lines are converted to luminosities using the inverse square law (2.1) assuming a distance to the LMC of $d = 49.59 \pm 0.54 \pm 0.09 \text{ kpc}$ ([Pietrzyński et al. 2019](#)). The observed luminosity L_λ^{obs} is converted to the intrinsic luminosity corrected for extinction using equation (2.5) ([Jones et al. 2022](#)):

$$L_\lambda^{\text{corr}} = L_\lambda^{\text{obs}} 10^{0.4A_\lambda} = L_\lambda^{\text{obs}} 10^{0.4E_{B-V}k_\lambda}, \quad (9.6)$$

where the relation $A_\lambda = k_\lambda E_{B-V}$ was used. The above relation can be formulated for the measured flux densities in the same way. We adopt the extinction curves derived by [Fahrion & De Marchi \(2023, their Tab. A.1\)](#) for the 30 Doradus region (see Fig. 9.16) and the average value for $R_V = 4.4 \pm 0.9$ derived for the core of the Tarantula Nebula around R136 ([Brands et al. 2023](#)). Values between 3 and 4.5 have been obtained for the entire 30 Doradus region from various studies (e.g., [De Marchi & Panagia 2014](#); [De Marchi et al. 2016](#)).

The selective extinction E_{B-V} is estimated using the chosen line ratios. Using the $\text{H I Pa}\beta$ (5–3) $1.28 \mu\text{m}$ and $\text{Br}\gamma$ (7–4) $2.16 \mu\text{m}$ transitions, the relative extinction is

$$E_{B-V} \cdot (k_{\text{Pa}\beta} - k_{\text{Br}\gamma}) = A_{\text{Pa}\beta} - A_{\text{Br}\gamma} = 2.5 \log_{10} \left[\frac{(\text{Pa}\beta/\text{Br}\gamma)_{\text{obs}}}{(\text{Pa}\beta/\text{Br}\gamma)_{\text{exp}}} \right], \quad (9.7)$$

where $k_{\text{Pa}\beta}$ and $k_{\text{Br}\gamma}$ are the extinction curves evaluated at the wavelengths of the respective transitions.

The line intensities for H I recombination lines assuming case B recombination (see Sect. 9.5.1) have been calculated by [Hummer & Storey \(1987\)](#) for various temperatures and densities. The expected line ratios can be derived from their look-up tables. We follow [Jones et al. \(2022\)](#) and [Reiter et al. \(2019\)](#) and adapt electron densities $10^2 \text{ cm}^{-3} \leq n_e \leq 10^4 \text{ cm}^{-3}$

and electron temperatures $5 \times 10^3 \text{ K} \leq T_e \leq 10^4 \text{ K}$. The entire parameter space covered by [Hummer & Storey \(1987\)](#) and the subspace assumed in this work are illustrated in figure 9.16. For the lower limiting case ($T_e = 5 \times 10^3 \text{ K}$, $n_e = 10^2 \text{ cm}^{-3}$), the Pa β /Br γ line ratio is:

$$\frac{1.84 \times 10^{-1}}{3.30 \times 10^{-2}} = 5.58, \quad (9.8)$$

and for the upper limit ($T_e = 10^4 \text{ K}$, $n_e = 10^4 \text{ cm}^{-3}$):

$$\frac{1.62 \times 10^{-1}}{2.75 \times 10^{-2}} = 5.89. \quad (9.9)$$

I adapt the mean value 5.74 ± 0.16 as the expected Pa β /Br γ line ratio interpreting the difference to the upper and lower bounds as an uncertainty. Together with the observed ratio $(\text{Pa}\beta/\text{Br}\gamma)_{\text{obs}} = 1.58 \pm 0.04$ (Tab. E.1), the relative extinction (Eq. 9.7) equals -1.40 ± 0.04 . Using the interpolated extinction law, we get the selective $E_{B-V} = 1.70 \pm 0.52$ and visual extinction $A_V = 2.60 \pm 0.95$. [Reiter et al. \(2019\)](#) get a similar $A_V = 2.46 \pm 0.57$ (see their Tab. 5) for the 30 Dor YSO (see Sect. 9.6.2) derived from the same H I line ratio. They assumed a lower ratio $R_V = 3.41$ – an average value for the LMC – and the extinction curves derived by [Gordon et al. \(2003\)](#). However, the average R_V in 30 Dor is estimated to be higher around 4.5 as derived by [De Marchi et al. \(2016\)](#).

We emphasise that the above extinction estimation assumes a certain temperature and density range. However, NIR line ratios corrected in such a way can also be employed to estimate temperature and density *after* extinction correction. [Ueta & Otsuka \(2021\)](#) pointed out this ‘chicken-egg’ problem and proposed an iterative algorithm to ensure proper temperature, density and extinction estimates. A correct treatment of this issue is important as a wide range of temperatures and densities have been estimated for various YSOs (e.g., summary in [Edwards et al. 2013](#); [Cooper et al. 2013](#)). For the scope of this work, we do not apply their described technique to be able to compare our results with previous works using the same T , n assumptions. It is the goal of future studies to use the *proper plasma analysis practice* of [Ueta & Otsuka \(2021\)](#) and investigate the implications of more rigorously determined extinction on the estimated luminosity and the derived physical quantities such as the mass accretion rate.

For the Br γ line, the extinction correction yields a flux of $F_{\text{corr}} = (1.94 \pm 0.36) \times 10^{-14} \text{ erg s}^{-1} \text{ cm}^{-2}$ compared to the observed value $F_{\text{obs}} = (5.97 \pm 0.10) \times 10^{-15} \text{ erg s}^{-1} \text{ cm}^{-2}$. Using equation (9.6), the intrinsic Br γ line luminosity is $L_{\text{Br}\gamma} = (5.71 \pm 1.08) \times 10^{33} \text{ erg s}^{-1} = 1.49 \pm 0.28 L_{\odot}$. Using the extinction and observed flux in [Reiter et al. \(2019\)](#), the Br γ luminosity for S9 is $(3.35 \pm 0.29) \times 10^{-2} L_{\odot}$ – about two orders of magnitude less than that of S7A. As the H I lines are believed to be correlated with accretion. A higher line luminosity points to an earlier evolutionary stage for S7A than for S9.

We compare the Br γ luminosity with the bolometric luminosity $L_{\text{bol}} = 2.66 \times 10^4 L_{\odot}$ derived from the SED fitting (see Sect. 9.7.3). It has been found for low-mass T Tauri stars, intermediate mass Herbig Ae/Be stars and MYSOs that the Br γ luminosity lies between $10^{-2} L_{\text{bol}} \lesssim L_{\text{Br}\gamma} \lesssim 10^{-6} L_{\text{bol}}$ ([Pomohaci et al. 2017](#), Fig. 5). The Br γ luminosity of S7A $L_{\text{Br}\gamma} \sim 6 \times 10^{-5} L_{\text{bol}}$ falls into the upper range of this relation.

9.7.2 Accretion luminosity

The kinetic energy of infalling material onto a protostar is converted into radiation at the accretion shock at the protostellar surface (Pomohaci et al. 2017). This radiation ionises the material around the protostar and is described as the accretion luminosity of a YSO. The H I Br γ (7–4) 2.16 μm and Humphreys α (7–6) 12.27 μm transitions have been shown to be correlated with the accretion luminosity (e.g., Calvet et al. 2004; Mendigutía et al. 2011; Rigliaco et al. 2015). For Br γ , the empirically derived relation is (Mendigutía et al. 2011):

$$\frac{L_{\text{acc}}^{\text{Br}\gamma}}{L_{\odot}} = (0.91 \pm 0.27) \cdot \log_{10} \frac{L_{\text{Br}\gamma}}{L_{\odot}} + (3.55 \pm 0.80), \quad (9.10)$$

where $L_{\text{Br}\gamma}$ is the extinction corrected luminosity of the Br γ transition calculated from the measured flux density at the position of the YSO (Sect. 9.3.1 and Fig. 9.3). The above relation (as also the one for the Humphreys α line in Rigliaco et al. 2015)) was derived for an galactic YSO sample with solar metallicity abundances and intermediate-mass Herbig Ae/Be stars ($1 M_{\odot} \leq M_{\star} \leq 6 M_{\odot}$). On the one hand, the lower metallicity of the LMC is not expected to influence equation (9.10). The number of UV photons with energies above 13.6 eV capable of ionising Hydrogen in a low-metallicity environment (such as the LMC or SMC) is similar to a solar-metallicity environment as shown by Kudritzki (2002). We note that (Ward et al. 2016, 2017) investigating MYSOs in the LMC and SMC determine higher accretion rates for sources in the SMC compared to the Galaxy. (Ward et al. 2017) suggest the reduced metallicity ($0.2 Z_{\odot}$) as a possible reason. No significant difference has been observed in the sample of the LMC (Ward et al. 2016). On the other hand, the origin of the recombination lines has been established to be in accretion funnels in low-mass T Tauri stars, but in disks for higher mass Herbig Be stars. Pomohaci et al. (2017) argue that as the ionising radiation is originating in the accretion shock regions for both types of YSOs despite the origin of the recombination lines, the relation can be applied for MYSOs. Most studies on MYSOs apply this relation without further discussion (e.g., Cooper et al. 2013; Jones et al. 2022). We utilise equation (9.10) for the sake of comparison. Then, the accretion luminosity of S7A is $L_{\text{acc}}^{\text{Br}\gamma} = (3.71 \pm 1.68) L_{\odot}$.

9.7.3 Stellar parameters from SED fitting

To constrain the stellar parameters of S7A, in particular the stellar radius R_{\star} , mass M_{\star} , bolometric luminosity L_{bol} , effective temperature T_{eff} , we fit synthetic SED models to the spectrum. We apply the Robitaille (2017) models convolved with the JWST filters (Richardson et al. 2024). The models assume an accretion scenario where a central source in an ambient medium is surrounded by an accretion disk, infalling envelope and bipolar cavities. Each of the characteristics can be optionally selected. As such, the models span a wide range of evolutionary stages for YSOs from their earliest deeply-embedded sources to the latest pre-main sequence stars where the central source starts to dominate the SED at optical wavelengths. All possible combinations are summarised in model sets (see Robitaille 2017, Tab. 2). Based on the observed features of the spectrum, we include all above mentioned properties and choose the `spubhmi` set. This set contains 280 000 models calculated with the 3D radiative transfer code Hyperion (Robitaille 2011, 2017).

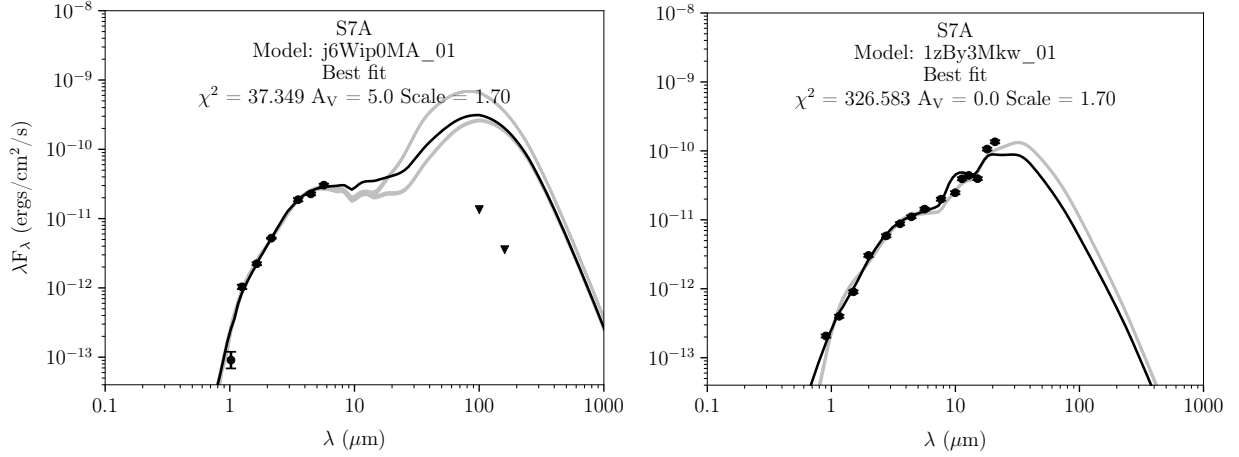


FIGURE 9.17 – **Left:** Best fit SED models using literature photometric data from HST/WFC3 F775W, VISTA *YJHKs*, IRAC (see Tab. 9.1) as well as Herschel 90% confidence limits on 100 μm /160 μm . **Right:** Best-fit SED using JWST spectra convolved with broadband NIRC*am* and MIRI filters.

TABLE 9.3 – JWST NIRC*am* and MIRI broad-band photometry derived from the observed spectra by convolving with the filter transmission curves. The uncertainties correspond to 5% of the estimated flux densities.

Filter	Wavelength ^a [μm]	F [$\text{ergs s}^{-1} \text{cm}^{-2}$]	F [mJy]	δF [mJy]
NIRC <i>am</i>				
F090W	0.62–0.78	2.34×10^{-13}	6.24×10^{-2}	3.12×10^{-3}
F115W	0.76–1.00	3.57×10^{-13}	1.54×10^{-1}	7.70×10^{-3}
F150W	1.33–1.48	6.20×10^{-13}	4.54×10^{-1}	2.27×10^{-2}
F200W	1.76–2.23	1.58×10^{-12}	2.03	1.01×10^{-1}
F277W	2.42–3.13	2.20×10^{-12}	5.40	2.70×10^{-1}
F356W	3.14–3.98	2.54×10^{-12}	1.05×10^1	5.23×10^{-1}
F444W	3.88–4.98	2.61×10^{-12}	1.63×10^1	8.16×10^{-1}
MIRI				
F560W	5.05–6.17	2.60×10^{-12}	2.69×10^1	1.34
F770W	6.58–8.69	2.74×10^{-12}	5.11×10^1	2.55
F1000W	9.02–10.89	2.54×10^{-12}	8.22×10^1	4.11
F1130W	10.95–11.67	3.49×10^{-12}	1.49×10^2	7.43
F1280W	11.59–14.12	3.53×10^{-12}	1.89×10^2	9.44
F1500W	13.53–16.64	2.70×10^{-12}	1.99×10^2	9.96
F1800W	16.52–19.50	6.02×10^{-12}	6.39×10^2	3.19×10^1
F2100W	18.48–23.16	6.74×10^{-12}	9.42×10^2	4.71×10^1

NOTES. ^(a) The wavelength range is given by the half power wavelengths where the transmission of the filter drops to 50% of its maximum (see [NIRC*am*](#) and [MIRI Filter documentation](#)).

TABLE 9.4 – Best-fit parameters from the SED fits using the models of [Robitaille \(2017\)](#) convolved with JWST filters ([Richardson et al. 2024](#)).

	T_{eff} [K]	R [R_{\odot}]	L [L_{\odot}]	M^a [M_{\odot}]	ID	N_{data}	N_{fits}	χ^2
Photometry	1.1×10^4	69	5.5×10^4	19	j6Wip0MA_01	8	8	37
JWST spectra	1.8×10^4	16	2.7×10^4	16	1zBy3Mkw_01	15	4	327
	1.0×10^4	46	2.1×10^4	15	ZRmqCLyy_06	11(4) ^b	1	358

NOTES. ^(a) Masses are derived from the zero-age main sequence mass-luminosity relation (9.11) using the best-fit luminosity shown in the column before. ^(b) The flux densities for the MIRI filters sensitive to PAH emission and silicate absorption F770W, F1000W, F1130W and F1800W are used as absolute upper limits.

The models required photometric data as an input. Most of the observations of S7A performed with NIRcam and MIRI (except F090W and F187N filters) are substantially dominated by the PSF (see Fig. 9.2) and accurate photometric measurements can not be obtained. Instead, we convolve the observed NIRSpect and MIRI/MRS spectrum with the transmission curves of NIRCcam and MIRI filters and obtain photometric flux densities for each of the broad-band filters using the `pyphot` python package. The results are summarised in table 9.3. We compare the best-fit models obtained with the convolved flux densities and with literature photometric data summarised in table 9.1. For the SED fit, we choose the VISTA $YJHK$, the available IRAC bands as well as the 90% confidence limits on the completeness of far-infrared ($100 \mu\text{m}$, $160 \mu\text{m}$) SPIRE data as in ([Nayak et al. 2016](#)). The fluxes obtained with Spitzer IRAC are higher than those measured with JWST. The higher spatial resolution of NIRSpect and MIRI can now resolve the YSO and the shell which was previously not possible with Spitzer. The lower flux densities follow from utilising the extracted spectrum only at the position of the YSO and excluding the shell, whereas the photometric data includes both contributions.

We fit the models utilising the provided python package `sedfit`. The best-fit is chosen by the lowest χ^2 value of all fitted models. The best-fit SED models for both sets of data are shown in figure 9.17 and the best-fit parameters summarised in table 9.4. Due to the limited number of successful fits, standard deviations on the fitted parameters could not be estimated. Markov-Chain Monte-Carlo simulations could be performed assuming prior distributions for the parameters to estimate uncertainties. Unfortunately, this lies beyond the scope of this work. Therefore, I stress that the best-fit luminosity and radius to only used to perform order of magnitude estimations. The limitations of the [Robitaille \(2017\)](#) models in the context of MYSOs are discussed below.

The mass can be inferred from the zero-age main sequence (MS) mass-luminosity relation. Alternatively, pre-main sequence evolutionary tracks can be employed to estimate the mass [Nandakumar et al. \(2018\)](#). The detection of an HCH II region around S7A (see Sect. 9.5.1) indicates that the MYSO has already evolved towards the main sequence ([Churchwell 2002](#); [Beuther et al. 2007](#); [Hoare et al. 2007](#)). Hence, we use the MS relations. We know from the previous study by [van Gelder et al. \(2020\)](#), the central source in S7A is a B1V type star. We therefore apply the $M_{*}-L_{\text{bol}}$ derived for O- and B-type stars ([Hohle et al. 2010](#)) to infer the

mass of S7A from the bolometric luminosity obtained from the SED fit:

$$M \propto L_{\text{bol}}^{0.27}. \quad (9.11)$$

With $L_{\text{bol}} = 2.66 \times 10^4 L_{\odot}$, the mass of S7A is $M_{*} \sim 16 M_{\odot}$. It appears that the luminosity from the SED fit is overestimated by about a factor 2 compared to the mean luminosity for (galactic) B1V stars (e.g., $L_{\text{B1V}} \sim 1.25 \times 10^4 L_{\odot}$, $M_{\text{B1V}} \sim 12 M_{\odot}$, [Hohle et al. 2010](#), Tab. 4). As the [Robitaille \(2017\)](#) models have been developed for low-mass YSOs, the fitted physical parameters must be treated with care.

Properties of protostellar objects depend on their accretion rates ([McKee & Tan 2003](#), Sect. 6 and references therein). The [Robitaille \(2017\)](#) models were developed primarily for lower-mass protostars with lower mass accretion rates than MYSOs. As such, they include radiation produced by accretion processes under specific conditions (see discussion in [Zhang & Tan 2011](#)) leading to the accretion luminosity being generally underestimated. MYSOs have higher accretion rates than low-mass YSOs. Their luminosity, however, is dominated by nuclear burning – initially, Deuterium, and eventually, Hydrogen burning ([McKee & Tan 2003](#)). Nevertheless, accretion continues even after they reach the main sequence ([Ward 2017](#)). The estimated luminosity for the central source is too large if part of the accretion luminosity is attributed to the intrinsic luminosity of the star. As the effective temperature and the radius are non-linearly connected with the luminosity of a star via $L_{*} = 4\pi R^2 \sigma T_{\text{eff}}^4$, our best-fit R_{*} and T_{eff} are possibly over- or underestimated. Therefore, for modelling SEDs of MYSOs, the [Zhang & Tan \(2018\)](#) models that accurately consider accretion onto the protostar are more appropriate for estimating accurate stellar luminosities and radii. For the previous versions of the SED models by [Robitaille et al. \(2006, 2007\)](#), [De Buizer et al. \(2017\)](#) found that masses are generally slightly overestimated by ([Robitaille et al. 2006, 2007](#)) compared to [Zhang & Tan \(2018\)](#). A more detailed comparison of the two different sets of models can be found in [Saral et al. \(2017\)](#); [De Buizer et al. \(2017\)](#).

Furthermore, the SED models assume Galactic ISM dust grain models ([Kim et al. 1994](#)) and a Galactic gas-to-dust ratio of ~ 100 ([Sewiło et al. 2013](#)). This is relevant for other parameters calculated by the model such as the envelope infall rate or the disk-to-envelope mass ratio as well as the extinction A_V ([Robitaille 2017](#)). The extinction is calculated separately using observed line ratios (see Sect. 9.7.1). As we do not have any far-IR coverage $>24 \mu\text{m}$, the disk and envelope parameters will not be well constrained as the peak of emission is unknown ([Saral et al. 2017](#)). For the parameters (R_{*} , T_{eff} , L_{*}) we are interested in, the lower LMC metallicity ($\sim 0.5 Z_{\odot}$ [Westerlund 1997](#); [Choudhury et al. 2021](#); [Hocdé et al. 2023](#)) will have an influence on the star formation rate as well as stellar mass ([Mannucci et al. 2010](#)). Further, the unique location of S7A in close proximity to NGC 2070 is heavily affected by the radiative feedback of massive stars. In addition, the observed PAH emission as well as silicate absorption in the spectrum influences the calculated photometry and as such the shape of the SED especially at MIR wavelengths $\gtrsim 6 \mu\text{m}$. A second fit treating the MIRI filters sensitive to PAH emission and silicate absorption as absolute upper limits yielded an even higher best-fit radius, but a comparable mass to the previous result (see Tab. 9.4). These are crucial at constraining the fits ([Rogers et al. 2024a](#)), however, the PAH emission is not included in the [Robitaille \(2017\)](#) models ([Whitney et al. 2008](#); [Sewiło et al. 2013](#)). The metallicity as well as the PAH emission in the spectrum of S7A will influence the fitted

stellar parameters.

It is also noted that deriving the mass from the MS mass-luminosity relation might not be a valid approach as ongoing contraction, accretion as well as Deuterium and Hydrogen burning will affect the evolution of the protostar and therefore its properties. For example, (Hosokawa et al. 2010) found in their simulations of MYSOs with high accretion rates that they can swell up to ~ 2 orders of magnitude during their evolution. The stellar mass should therefore be estimated from comparing the fitted stellar luminosity and effective temperature with evolutionary pre-main sequence tracks in a Hertzsprung-Russell diagram (Nandakumar et al. 2018; Rogers et al. 2024b).

9.7.4 Mass accretion rate

For high-mass protostars, the observed luminosity is dominated by accretion. Once the protostars evolves, the intrinsic stellar luminosity will become the main radiation source Zinnecker & Yorke (2007). From the accretion luminosity, the mass accretion rate onto the central protostar \dot{M}_* can be estimated assuming a mass M_* and radius R_* for the YSO. We apply the best-fit values obtained from the SED fit described in the previous section.

Without any further assumptions on the type of accretion process, \dot{M}_* balances the gravitational energy loss by the infalling material onto the protostar and the radiation emitted at the shock:

$$\dot{M} \leq \frac{L_{\text{acc}} R_*}{GM_*} \quad (9.12)$$

with G the gravitational constant. The mass accretion rate of S7A is then $\lesssim 10^{-7} M_{\odot} \text{yr}^{-1}$. To produce a star with a certain mass M_* in $\sim 2 \times 10^5$ yr, Zinnecker & Yorke (2007) estimate that an average accretion rate of $5 \times 10^{-6} (M_*/M_{\odot}) M_{\odot} \text{yr}^{-1}$ is required. For the estimated mass of S7A, this would yield $8 \times 10^{-5} M_{\odot} \text{yr}^{-1}$. For MYSOs in the main accretion phase, accretion rates are about 10^{-3} – $10^{-4} M_{\odot} \text{yr}^{-1}$ are reported. I conclude that S7A is a more evolved source where the accretion has already significantly decreased.

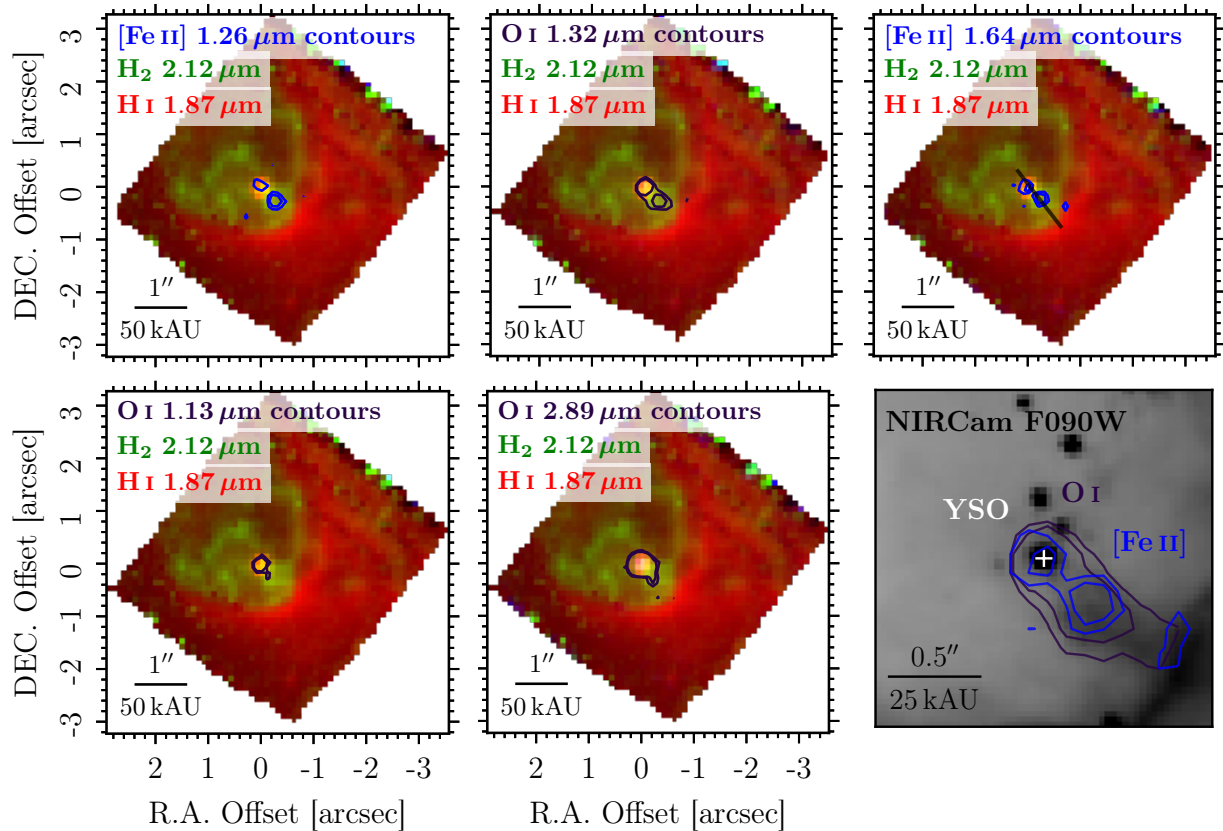


FIGURE 9.18 – Two colour images showing the YSO and the shell in Hydrogen (red) and the H_2 morphology (green). The emission lines showing knot emission are illustrated by blue ([Fe II]) and violet (O I) contours. The image showing the [Fe II] $1.64 \mu\text{m}$ emission also shows the jet axis along which line profiles are calculated (Sect. 9.8.1). The last image in the second row compares the O I (violet) and [Fe II] (blue) transitions with emission seen in the NIRCcam F090W image. The contours are drawn from mean M0 maps combining all observed O I and [Fe II] transitions showing knot emission, respectively.

9.8 Knot emission – a protostellar outflow

Emission from a knot towards the north-west of the YSO was identified in O I and [Fe II] lines in addition to extended H₂ emission around the protostar. Figure 9.18 shows the most prominent O I and [Fe II] emission lines with respect to the shell and the H₂ emission around S7A. Comparison to observations of other YSOs in the literature and the discussions in sections 9.5.2, 9.5.3, 9.5.1 and 9.6.1, let us identify this knot as an outflow from massive YSO S7A.

The three O I triplet transitions lie in the NIR at 1.13 μm (³D₁^o – ³P₀^o; Fig. C.3), 1.32 μm (³S₁^o – ³P₁; Fig. C.3) and 2.89 μm (³P_J – ³S₁^o; Fig. 9.6). The observed 2.89 μm line is most likely a blend of several transitions from the different total angular momentum states of the ³P level to ³S₁^o. We include the 1.13 μm and 2.89 μm lines tracing the knot emission. However, as seen in Fig. 9.18, the emission does not clearly originate from the position of the knot compared to the O I 1.32 μm (and [Fe II]) lines. The emission is primarily centred on the YSO. Only a slight extent towards the south can be identified through the contours. In addition, the emission from the 2.89 μm transition is radially extended around the YSO compared to the emission at shorter wavelengths due to the increased PSF size.

Three NIR [Fe II] emission lines are observed at 1.26 μm (*a*⁴D_{7/2} – *a*⁶D_{9/2}), 1.32 μm (*a*⁴D_{7/2} – *a*⁶D_{7/2}) and 1.64 μm (*a*⁴D_{7/2} – *a*⁴F_{9/2}). The 1.32 μm line is observed in the F100 spectrum, but the M0 maps shows only faint emission (see Fig. C.2) and the calculated line flux is one magnitude lower with a large uncertainty compared to the other two transitions (see Tab. E.1). The only [Fe II] transition in the MIR showing knot emission lies at 5.34 μm (*a*⁴F_{9/2} – *a*⁶D_{9/2}; Fig. 9.6). The line observed at 4.67 μm (*a*⁴F_{3/2} – *a*⁶D_{1/2}) is blended with the H I transition. The MIRI IFU foVs of channel and 4C are too large to identify any knot emission so close to the YSO. The [Fe II] MIR M0 map at 17.9 μm (*a*⁴F_{7/2} – *a*⁴F_{9/2}; Fig. C.4) suffers from a spectral sampling problem and does not allow any emission morphology to be seen (see Nisini et al. 2024, for details). The 26.0 μm transition (*a*⁶D_{9/2} – *a*⁶D_{7/2}; Fig. C.4) has a double-peak structure. However, keeping the enlarged foV (together with the large PSF and less spatial resolution) in mind, one peak shows the YSO whereas the other traces the shell around S7A.

In the mean M0 maps showing NIR H₂ ro-vibrational and purely rotational transitions (Fig. 9.5), no knot emission can be identified. Only in the M0 maps of MIR rotational lines (Fig. 9.6) does a bright extended emission shifted towards the position of the knot become visible. However, the line profiles discussed in the following section clearly show that the H₂ emission is extended to the knot position also in the NIR.

The only other emission line in the MIR apart from the H₂ lines and the [Fe II] 5.34 μm transition showing knot emission is possibly the [Ar II] 6.98 μm (²P_{1/2}^o – ²P_{3/2}^o) transitions. The [Ar II] seems to resemble the H₂ YSO+knot morphology. However, it remains unclear whether this statement is true. The spatial resolution and the increased PSF might fool the eye.

H₂ and [Fe II] emission lines are associated with protostellar outflows (Nisini et al. 2002). On the one hand, molecular H₂ emission traces a colder and denser medium. On the other hand, forbidden [Fe II] transitions point to a second component with a higher temperature allowing the Fe ions to be collisionally excited and a lower density such that the excited states have enough time to de-excite radiatively via less probable transitions.

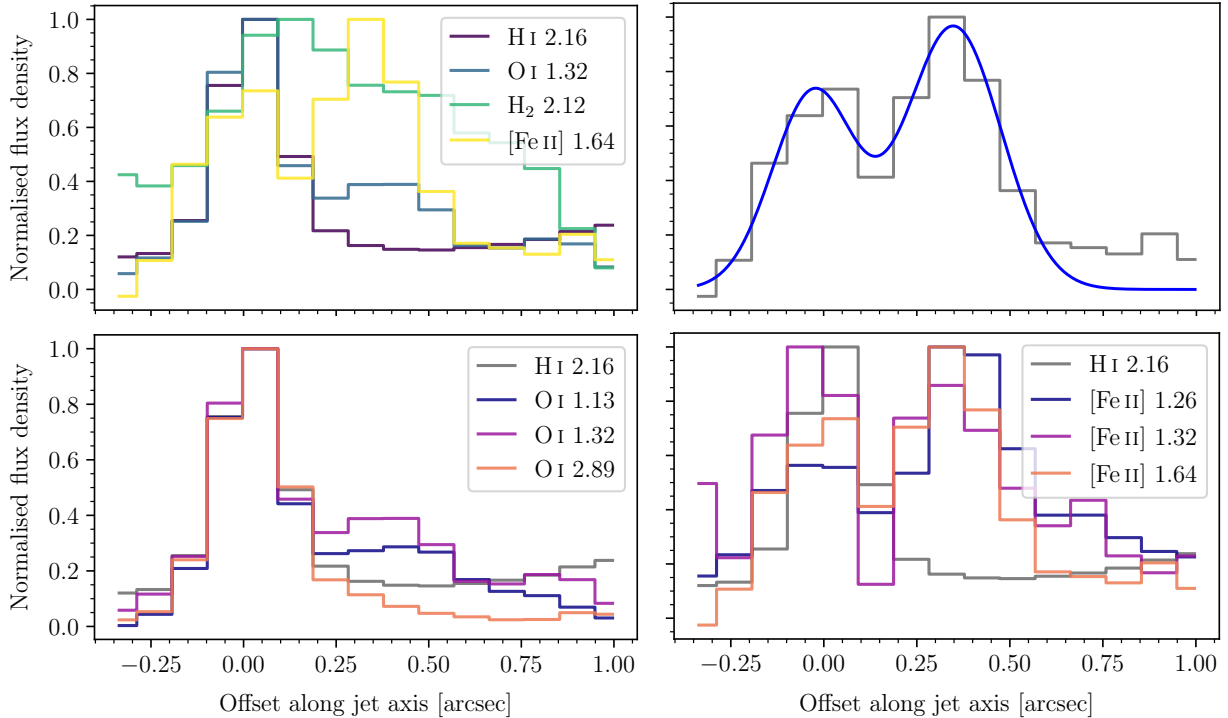


FIGURE 9.19 – **Upper left:** Line profiles along the jet-axis for transitions showing knot emission in M0 maps and H I Br γ 2.16 μm . The flux density of each transition was normalised to its maximum value. **Upper right:** A two-component Gaussian fit (blue) to the line profile of the [Fe II] 1.64 μm transition. The observed spectrum is shown in gray. **Lower left (right):** Line profiles of H I 2.16 μm compared to profiles of several O I ([Fe II]) transitions.

9.8.1 Line Profiles

We compare line profiles of observed transitions which do not show knot emission (H I) in their M0 maps along the jet axis with those showing knot emission ([Fe II], O I, H₂). I define the jet axis as the axis connecting the fitted YSO position (at 0'') and the knot of emission (see Fig. 9.18). I calculate line profiles along the jet axis using the `scimage.measure.profile_line()` routine. I fit two Gaussian components to determine the peak position of the emission and the offset of the knot with respect to the YSO. Figure 9.19 compares the line profiles of the H I 2.16 μm emission line with [Fe II], O I, H₂ emission lines showing knot emission discussed in the previous section. In addition, I compare different [Fe II] and O I with each other. Table 9.5 lists the fitted offsets from the maxima of the (multi) Gaussian fits.

The H I 2.16 μm profile is solely centred around the YSO. The increase of flux towards 1'' away from the YSO is due to the presence of the shell. The fitted centre of the H I 2.16 μm peak is shifted to $0''.03 \pm 0''.02$ away from the YSO position determined from continuum images. Accretion onto the YSO or wind originating from the disk might explain the offset of emission (Davis et al. 2011, and references therein). The H₂ 2.12 μm profile is extended along the entire axis without a clear separation into two components. The two component fit reported in table 9.5 is insufficient to characterise the shape of the profile. The peak emission is shifted from the YSO position by about 0''.2. The H₂ emission drops to $\sim 75\%$ of that at the peak position at 0''.25 and remains nearly constant until it drops further to $\sim 60\%$

TABLE 9.5 – Offset of emission peaks for various emission lines along the jet axis. The line profiles are illustrated in Fig. 9.19.

	H I Br γ 2.16 μm	O I 1.13 μm	O I 1.32 μm	O I 2.89 μm
1st peak	0''03 \pm 0''02	0''012 \pm 0''002	0''008 \pm 0''005	0''026 \pm 0''005
(YSO position)	2 \pm 1 kAU	0.6 \pm 0.1 kAU	0.4 \pm 0.3 kAU	1.3 \pm 0.3 kAU
2nd peak	-	0''31 \pm 0''04	0''37 \pm 0''02	-
(knot emission)	-	16 \pm 2 kAU	19 \pm 1 kAU	-
	H ₂ 2.12 μm	[Fe II] 1.26 μm	[Fe II] 1.32 μm	[Fe II] 1.64 μm
1st peak	0''17 \pm 0''05	<-0''05	<-0''05	<0''02
(YSO position)	9 \pm 3 kAU	<-2.5 kAU	<-2.5 kAU	<1 kAU
2nd peak	0''72 \pm 0''05	0''40 \pm 0''04	0''3 \pm 0''1	0''35 \pm 0''02
(knot emission)	36 \pm 3 kAU	20 \pm 2 kAU	15 \pm 5 kAU	18 \pm 1 kAU

around 0''55. It significantly decreases around 0''75.

Both the [Fe II] and O I (1.13 μm and 1.32 μm) profiles show a double peak structure with one maximum coinciding with the position of the YSO, the second maximum being shifted by 0.3''. While the [Fe II] (1.64 μm and 1.26 μm) emission peaks at the second maximum, i.e., the knot position, with a \sim 25–30% increase compared to the first maximum, the O I (1.13 μm and 1.32 μm) emission is \sim 60–70% higher at the YSO. The [Fe II] 1.32 μm that could not be visualised in the M0 map, shows a clear double peak profile similar to 1.26 μm and 1.64 μm . In contrast to 1.26 μm and 1.64 μm , the emission is \sim 15% higher at the YSO. However, the abrupt drop at 0''1 and subsequent increase within a single bin point to a purely statistical variation rather than a physical one. The O I 2.89 μm emission does not show a double peak profile. However, the profile shows an extended tail towards the direction of the knot.

The clear double peak profiles of the [Fe II] emission as well as the extended H₂ emission are further evidence for a protostellar outflow. The fitted position of the second [Fe II] peak places the hotter, less dense medium of the central region outflow close to the YSO at \sim 0''35 away. The peak of H₂ emission is clearly offset to the YSO. The very broad profile of the H₂ emission shows that the outflow extends further away, tracing cool and dense gas towards the edges of the outflow, possibly on the boundaries to bow shocks (e.g., Bally et al. 2007).

9.8.2 Shock- or photo-excitation?

H₂ and [Fe II] transitions associated with protostellar outflows can be used to estimate the dominating excitation mechanism. There exist two main mechanisms for producing vibrationally excited H₂: firstly, pumping by UV radiation (11–13.6 eV) from OB stars – or in this case, from the MYSO itself – to a higher electronic state. The decay to the ground electronic state populates high vibrational levels with $v \geq 3$ (Dinerstein 1995). The subsequent cascades to the ‘vibrational ground state’ $v = 0$ radiate as optical and infrared fluorescent emission lines. The population of states is often referred to as ‘top-down’. Secondly, thermal excitation through inelastic collisions following a shock. In contrast to UV excitation, the states are populated ‘bottom-up’. However, in dense environments with high UV flux densities (photo-dominating regions) with $n_{\text{H}} \gtrsim 10^{4-5} \text{ cm}^{-3}$, collisions occur frequently enough to thermalise the lower energy levels and de-excitation is collisional. This occurs when the density of collision partners (usually electrons) is higher than the critical density n_c (Eq. 4.10) of a particular transition. For the lowest vibrational transitions of H₂, $n_c \sim 10^5 \text{ cm}^{-2}$. In this case, the line ratios are equivalent to those in the shock-excitation scenario (Habart et al. 2005; Rosenberg et al. 2013). To determine the dominating excitation mechanism despite the degeneracy of UV excitation, not only H₂ lines, but also the Br γ and [Fe II] transitions can be utilised. Fe I has a low ionisation potential ($E_{\text{I}} \sim 7.9 \text{ eV}$; see Tab. D.1) and can be ionised by UV radiation which leaves H neutral. In photo-ionised regions where H is ionised, Fe is therefore more likely to be in higher ionisation stages. The ~ 16 lowest energy levels in Fe II give rise to the observed NIR and MIR transitions (see Fig. 9.11). They have low excitation temperatures with the highest upper levels having temperatures $T \lesssim 12000 \text{ K}$ and are thus easily excited in post-shock regions (Koo et al. 2016). On the one hand, in dense regions with a significant UV radiation field, apart from H₂ transitions, also the Br γ transition – as one of the brightest H recombination lines in the NIR – will be present (see Sect. 9.7). On the other hand, shock-excited regions will show both H₂ and [Fe II] emission (Rosenberg et al. 2013). Fe will initially be locked in dust grains. The presence of shock as dust destructors releases Fe into the ISM enhancing its abundance and, subsequently, emissivity (Koo et al. 2016). However, it is noted that H₂ and [Fe II] do not trace the same type of shocks. [Fe II] is expected for high velocity J-type shocks with velocities $v_s \gtrsim 50 \text{ km s}^{-1}$ which would dissociate H₂ (Hollenbach et al. 1989; Nisini et al. 2002). Instead, H₂ emission is expected from slower non-dissociative continuous- (C) or jump- (J) type shocks ($v_s \lesssim 20 \text{ km s}^{-1}$). In C-type shocks, gas properties such as density and temperature change gradually from the post- to the pre-shock region. In J-type shocks, these conditions change abruptly (Shull & Draine 1987; Draine & McKee 1993). The observed spatial correlation of H₂ and [Fe II] emission points to the simultaneous presence of different shocks and excitation conditions within the jet/outflow which are either unresolved or coincide in projection (Nisini et al. 2002).

Most of the observed H₂ lines originate from vibrational levels with $v \lesssim 3$ with only 8 transitions involving $v = 4-5$. The flux densities for the latter transitions are consistently about one order of magnitude smaller than for the former. This is the first indication for shock-excitation as the dominant excitation mechanism. To obtain further evidence for the knot emission tracing a protostellar outflow, we investigate Br γ , H₂ and [Fe II] line ratios to find evidence for shock-excitation. As seen in the line profiles in the previous section, the

H₂ emission is extended over the spectral extraction of the YSO and the knot. Therefore, I compare H₂ line ratios in the YSO+outflow region and [Fe II] transitions in the knot as the emission from the YSO and knot can be separated (see Fig. 9.3).

First, the observed flux densities have to be corrected for extinction. As discussed in the previous section, the H₂ and [Fe II] lines have a different spatial extent. Therefore, extinction towards the YSO+outflow and knot region traced by H₂, Br γ and [Fe II], respectively, has to be estimated separately. In the context of YSOs, the H₂ 1–0S(1) to 1–0Q(3) ratio is also often utilised (Davis et al. 2011, and references therein). However, the Q(2), Q(3) and Q(4) transitions at 2.413 μm , 2.424 μm , 2.437 μm fall into the detector gap (see Sect. 6.2.2) and can therefore not be used. Instead, I choose the H₂ 1–0S(5) and 1–0Q(7) lines to estimate the extinction towards the region of the YSO and its outflow. For the knot region, the [Fe II] transitions at 1.257 μm and 1.644 μm are suitable as they share the same upper level. Intrinsic line ratios in an optically thin plasma are simply given by the ratio of their Einstein *A* coefficients (spontaneous transition probabilities) multiplied by the ratio of the line energy or frequency (see Eq. 4.6):

$$\frac{I_1}{I_2} = \frac{A_1 \cdot h\nu_1}{A_2 \cdot h\nu_2}, \quad (9.13)$$

with A_i , ν_i the Einstein *A* coefficient and the frequency of the respective transition. With the transition probabilities of Wolniewicz et al. (1998) for H₂ and of Nussbaumer & Storey (1988)² for [Fe II]

$$\frac{I_{\text{S}(5)}}{I_{\text{Q}(7)}} = \frac{3.95 \times 10^{-7} \cdot 0.6754 \text{ eV}}{2.34 \times 10^{-7} \cdot 0.4960 \text{ eV}} = 2.27, \quad (9.14)$$

$$\frac{I_{1.644}}{I_{1.257}} = \frac{4.65 \times 10^{-3} \cdot 0.7542 \text{ eV}}{4.83 \times 10^{-3} \cdot 0.9863 \text{ eV}} = 0.74. \quad (9.15)$$

The observed H₂ ratio in the YSO+outflow region is $F_{\text{S}(5)}/F_{\text{Q}(7)} = 0.70 \pm 0.15$. Using the same extinction law as in section 9.7, the selective extinction $E_{B-V} = 4.06 \pm 0.53$ (Eq. 9.7) and the absolute visual extinction $A_V = 1.08 \pm 0.26$. Analogously, for the knot region and with $F_{1.644}/F_{1.257} = 1.12 \pm 0.10$: $E_{B-V} = 0.86 \pm 0.54$ and $A_V = 5.10 \pm 3.35$. The observed and corrected flux densities for the relevant H₂, Br γ and [Fe II] transitions are summarised in table 9.6. The Br γ transition was corrected for extinction using the same lines as in section 9.7, although with the measured line ratio in the YSO+outflow region (stated in Tab. 9.6).

In the past there have been discrepancies between extinction derived from optical and NIR [Fe II] line ratios involving the 1.644 μm and 1.257 μm transitions. The values for the optical extinction A_V derived from 1.644/1.257 would be about twice as high as those from 1.644/1.320 and in conflict with those derived from optical [Fe II] lines (Nisini et al. 2005). The lines are relatively faint in our spectra and their observed flux densities exhibit large uncertainties, especially the 1.320 μm transition (see Tab. 9.6 or Tab. E.1). Therefore, the derived visual extinction covers a very large range (see above and Tab. 9.6). In our data, both 1.644/1.257 and 1.644/1.320 yield high $A_V \sim 5$ and agree as their uncertainties are large. The results stay the same when more updated transition probabilities are used. Therefore, I

²The more updated transition probabilities from Deb & Hibbert (2011) yield the same ratio for the 1.257 μm and 1.644 μm transitions.

proceed with estimating the extinction towards the knot region with the 1.644/1.257 line ratio.

Extinction-corrected H₂ line ratios are quoted in table 9.7 with the expected ratios from photo- or shock-excitation. The estimated 1–0S(0)/S(1) and 1–0S(2)/S(1) ratios are due to their large uncertainty indicative for both photo- and shock-excitation. The 2–1S(1–3) to 1–0S(1) ratios are consistent with shock-excitation with a post-shock temperature around 3000 K. Apart from H₂ line ratios also the relative intensity of 1–0S(1) to Br γ is used to identify H₂ shock-excitation if the ratio is larger than 1. Otherwise, photo-excitation dominates (Dale et al. 2004; Yeh et al. 2015; Reiter et al. 2019; Jones et al. 2022). From the de-reddened flux densities in table 9.6, 1–0S(1)/Br γ = 1.60 ± 0.49 indicating shock-excitation.

To investigate the possibility of confusing shock-excitation with UV photo-excitation in a high density region, I also compute [Fe II]/Br γ and [Fe II] 1.257/1.644 and 1.320/1.644 ratios. The expected and estimated line ratios in the knot region are shown in table 9.8. The expected 1.257/1.644 and 1.320/1.644 are from Hartigan et al. (2004) and were computed for pre-shock density $n_{\text{H},0} = 10^{3-5} \text{ cm}^{-3}$ and shock velocities of $v_s = 30-50 \text{ km s}^{-1}$. The above line ratios remain constant under these conditions. The [Fe II] lines are consistent with shock-excitation, however, the uncertainties are large. The H lines ratios with respect to the 1.644 μm transition do not indicate the presence of a shock. However, it is noted that the knot emission is located very close to the emission region of the YSO (see Fig. 9.3). The spectrum extracted at the knot position is therefore likely to be contaminated by the emission of the YSO. In addition, the H I (and He II) emission does not drop to zero outside the YSO and shell regions (see Fig. 9.5) indicating that interstellar H and He that are not directly related to the YSO and its outflow are excited as well. Radiative feedback from the near-by stellar cluster NGC 2070 has likely influenced the environment by increasing the ionisation fraction of the ISM in which S7A is forming. Therefore, comparing [Fe II] with H I lines for indication of shock-excitation is likely not applicable in this case.

In conclusion, the observed H₂ spectrum dominated by transitions from $v \lesssim 3$ and only few from higher vibrational states with $v = 4-5$ (see Tab. B.1) together with the presented H₂ and [Fe II] line ratios indicate the presence of shocks as the primary excitation mechanisms for the observed H₂ and [Fe II] transitions in the region of the YSO and towards the knot emission. A protostellar outflow is the most probable origin of the shocks. Nevertheless, photo-ionisation will also play a role considering the higher H₂ transitions and the presence of a B1V protostar ionising H and He.

Furthermore, the [Ne II] transition at 12.8 μm has been determined to be directly proportional to J shock velocities (Hollenbach & McKee 1989; van Dishoeck 2004, Ch. 8.1.1). However, the spatial resolution of the MIRI/MRS datacube is not sufficient to identify whether the emission is originating from the knot region or only the MYSO.

TABLE 9.6 – Observed and extinction-corrected line flux densities from the YSO+Outflow and knot region.

Transition	λ_{lab}^a	observed			A_V^d	corrected
		F^b	δF^b	FWHM ^c		$F \pm \delta F^b$
YSO+Outflow						
P β	1.28216	2.09×10^{-14}	2.36×10^{-16}	126	4.00 ± 1.45	$(1.03 \pm 0.11) \times 10^{-13}$
Br γ	2.16612	8.37×10^{-15}	1.34×10^{-16}	141		$(1.80 \pm 0.21) \times 10^{-14}$
1-0S(0)	2.22329	6.19×10^{-16}	5.34×10^{-17}	141		$(9.55 \pm 1.22) \times 10^{-15}$
1-0S(1)	2.12183	1.53×10^{-15}	5.12×10^{-17}	138		$(2.88 \pm 0.81) \times 10^{-14}$
1-0S(2)	2.03376	4.90×10^{-16}	2.67×10^{-17}	138		$(1.06 \pm 0.10) \times 10^{-14}$
1-0S(3)	1.95756	1.06×10^{-15}	3.91×10^{-17}	155	1.08 ± 0.26	$(2.70 \pm 0.21) \times 10^{-14}$
2-1S(1)	2.24772	4.02×10^{-16}	3.26×10^{-17}	141		$(5.97 \pm 0.75) \times 10^{-15}$
2-1S(2)	2.15422	1.43×10^{-16}	2.20×10^{-17}	141		$(2.46 \pm 0.44) \times 10^{-15}$
2-1S(3)	2.07348	3.45×10^{-16}	3.27×10^{-17}	138		$(6.92 \pm 0.86) \times 10^{-15}$
Knot						
P β	1.28216	8.51×10^{-15}	6.02×10^{-17}	126	9.21 ± 4.60	$(1.71 \pm 0.13) \times 10^{-14}$
Br γ	2.16612	2.14×10^{-15}	2.93×10^{-17}	130		$(2.98 \pm 0.16) \times 10^{-15}$
[Fe II]	1.25702	2.36×10^{-16}	1.14×10^{-17}	125		$(8.60 \pm 1.70) \times 10^{-16}$
[Fe II]	1.32091	6.50×10^{-17}	1.28×10^{-17}	126	5.10 ± 3.35	$(2.17 \pm 0.42) \times 10^{-16}$
[Fe II]	1.64400	2.63×10^{-16}	2.00×10^{-17}	111		$(6.34 \pm 1.34) \times 10^{-16}$

NOTES. ^(a) Vacuum lab wavelength in micron; ^(b) in $\text{ergs}^{-1} \text{cm}^{-2}$; ^(c) in kms^{-1} , ^(d) in mag.

TABLE 9.7 – Extinction-corrected H₂ line ratios with respect to the 1-0S(1) transition in the YSO+outflow region (S7A-M1). Line ratios derived for UV photo-excitation and excitation by interstellar shocks with different postshock temperatures in a high density environment ($n_{\text{H}_2} = 3.0 \times 10^5 \text{cm}^{-3}$) are quoted in rows two to six (Ward et al. 2016, Tab. 4).

	1-0S(0)	1-0S(2)	1-0S(3)	2-1S(1)	2-1S(2)	2-1S(3)
S7A-M1	0.33 ± 0.10	0.37 ± 0.11	0.94 ± 0.27	0.21 ± 0.06	0.09 ± 0.03	0.24 ± 0.07
Photo ^a	0.4-0.7	0.4-0.6	-	0.5-0.6	0.2-0.4	0.2-0.3
Shock 1000 K ^b	0.27	0.27	0.51	0.005	0.001	0.003
Shock 2000 K ^b	0.21	0.37	1.02	0.083	0.031	0.084
Shock 3000 K ^b	0.19	0.42	1.29	0.21	0.086	0.27
Shock 4000 K ^b	0.19	0.44	1.45	0.33	0.14	0.47

REFERENCES. ^(a) Black & van Dishoeck (1987), ^(b) Hollenbach & Shull (1977); Shull & Hollenbach (1978).

TABLE 9.8 – Extinction-corrected [Fe II] and H I line ratios with respect to the $1.644\ \mu\text{m}$ transition in the knot region.

	$P\beta$	$\text{Br}\gamma$	1.257	1.320
Knot	27 ± 6	4.70 ± 1.02	1.36 ± 0.39	0.34 ± 0.10
Shock	$<1^a$	$<1^b$	1.04^c	0.27^c

REFERENCES. ^(a) Labrie & Pritchett (2006), ^(b) Reiter et al. (2019),
^(c) Hartigan et al. (2004).

10 Summarised Conclusions

I analyse high spatial and spectral resolution integral field observations of B1V-type massive young stellar object (MYSO) S7A located in the 30 Doradus star-forming region in the Large Magellanic Cloud using NIRSspec and MIRI/MRS on JWST. We focus on the identification of the observed emission lines in the available 0.9–27.5 μm wavelength range. Continuum-subtracted line-emission maps reveal several extended structures around the MYSO, its radiative feedback and outflow as well as the new protostar C1 (see Fig. 10.1).

We observe strong and broad ($\Delta v \gtrsim 130 \text{ km s}^{-1}$) H I and He I recombination lines. Continuum-subtracted line-emission maps reveal the emission originates from the MYSO and a C-shaped shell $\gtrsim 35 \text{ kAU}$ away from the protostellar system. In addition, various electric-dipole forbidden transitions from heavy elements such as Carbon, Iron and Nickel are detected. The line-emission maps place their origin at the position of the MYSO, the shell as well as the interstellar medium (ISM) within the source is embedded. These collisionally excited transitions have different origins. The partially-ionised ISM can be explained by the presence of the highly-active environment under the influence of the UV radiation of the young massive star cluster R136. The spherical emission close to the MYSO within a $\sim 0.02 \text{ pc}$ radius is created by the UV radiation from the MYSO indicating that Hydrogen burning has already commenced. Photons with energies up to 46 eV must be present to triple-ionise Potassium as the $[\text{K IV}]^3\text{P}_1 - ^3\text{P}_2$ transition is present. The emission can either be interpreted as an hyper-compact H II region or a photo-evaporating disk. The C-shaped shell presents an ionisation front created by the interaction of stellar winds from the massive star cluster R136 and the MYSO. The identification of a double-ionised Neon ($[\text{Ne III}]^3\text{P}_1 - ^3\text{P}_2$) emission line suggests photon energies of $\sim 41 \text{ eV}$. Similar structures are observed around low-mass YSOs in the Orion Nebula and referred to as externally-illuminated low-mass YSOs or protoplanetary disks in the literature.

A high abundance of H_2 ro-vibrational transitions is observed across the entire spectrum. Line-emission maps reveal a complex morphology around S7A. It closely resembles that of PAH dust emission observed in the NIRCcam F335M image. The H_2 emission is the brightest at the position of S7A and appears to be extended compared to the size of the emission region seen in H I and He I recombination lines (for further discussion see below).

The near-infrared H I Br γ line flux density can be utilised to estimate the accretion luminosity onto the central YSO. The energy radiated away from the accretion shock at the YSO's surface ionises Hydrogen atoms. In the infrared, the recombination of Hydrogen ions and electrons can be observed. The accretion luminosity is derived from an empirical relation for intermediate-mass YSOs. It has previously been shown to apply also to more massive YSOs. The estimated accretion luminosity for S7A is $L_{\text{acc}} = (3.71 \pm 1.68) L_{\odot}$. From L_{acc} , an upper limit on the mass accretion rate onto the central YSO can be estimated assuming spherically infalling gas if the stellar radius and mass are known. To estimate the stellar parameters, I perform a spectral energy distribution fit. I estimate the mass of the central source using the mass-luminosity relation for OB stars ($M \propto L_{\text{bol}}^{0.27}$) to $\sim 16 M_{\odot}$ from the best-fit radius $\sim 16 R_{\odot}$ and luminosity $\sim 2.66 \times 10^4 L_{\odot}$. Then, the mass accretion rate is $\lesssim 10^{-7} M_{\odot} \text{ yr}^{-1}$ – two order of magnitude smaller than predicted average for the main accretion phases of MYSOs. The estimated accretion rate together with the ionised region around the YSO suggests an evolved MYSOs where accretion is significantly reduced and

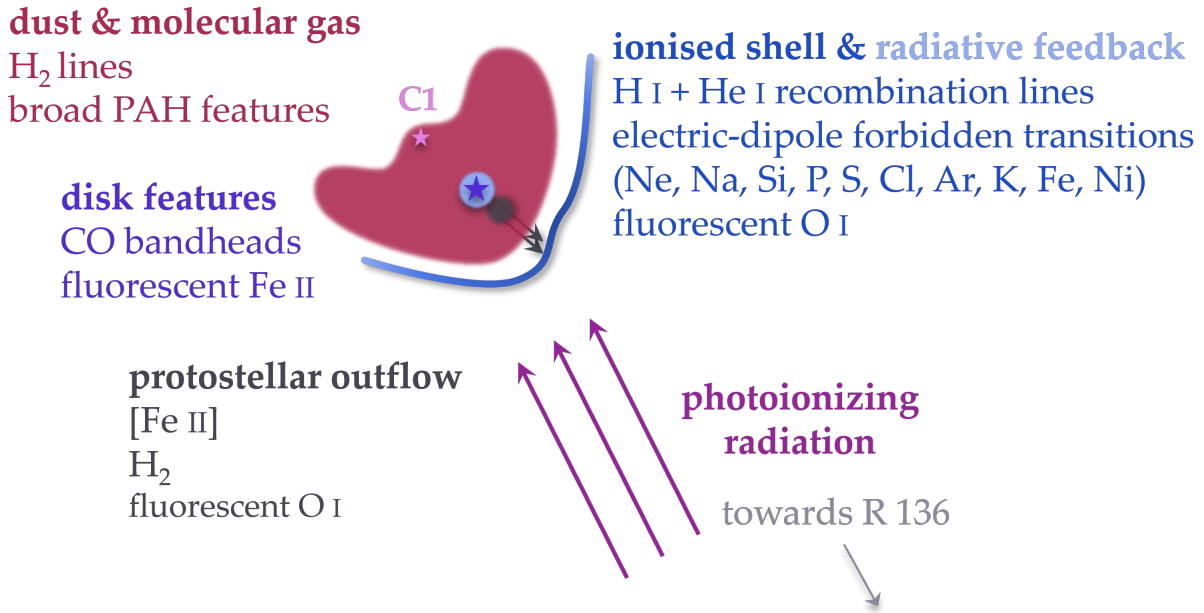


FIGURE 10.1 – Schematic view of the physical processes identified in and around S7A: extended H_2 and PAH morphology, C-shaped shell, protostellar outflow, radiative feedback from S7A as well as point source C1.

the radiation from the star is dominating the observed luminosity.

Weak CO 2–0 and 3–1 bandhead emission at $2.29 \mu\text{m}$ and $2.32 \mu\text{m}$ can be interpreted as a tracer of the inner molecular regions of an accretion disk. Fluorescent Fe II transitions are also thought to be indicative of accretion disks in MYSOs, however, presumably at later stages of evolution. Five such transitions at $1.688 \mu\text{m}$, $1.742 \mu\text{m}$, $1.840 \mu\text{m}$, $2.089 \mu\text{m}$, $3.081 \mu\text{m}$ have been identified in the spectrum of S7A.

Further, O I and [Fe II] line-emission maps reveal emission from a knot close to S7A. Combining the spectral data with NIRCcam F090W and HST F775W images suggests a protostellar outflow extending until the C-shaped shell – about $\sim 35 \text{kAU}$ ($\sim 0.1 \text{pc}$) from S7A. The symmetry of the C-shaped shell is broken where it meets the outflow shifting the ionisation front away from the MYSO. Line profiles of the O I and [Fe II] with respect to H I lines along the defined jet axis show clear double peaks. [Fe II] profiles reveal the knot emission has a maximum at $10\text{--}20 \text{kAU}$ away from S7A. The NIRCcam F090W images shows that the emission of the outflow begins $\sim 5\text{--}8 \text{kAU}$ away from the emission region of S7A. The H_2 profile does not show a clear separation of emission from the MYSO and the position of the knot. Instead intensity of the H_2 emission is more extended and covers both the S7A and the knot while gradually decreasing with increasing distance from S7A. I interpret the results as additional evidence for the presence of an outflow. Combined H_2 and [Fe II] emission are often utilised in the study of YSOs as tracers of jets and outflows as they indicate shock-excited gas. Comparing observed and extinction-corrected line ratios of prominent H_2 and [Fe II] lines with theoretical calculations indeed suggests the knot-emitting gas is shock-excited. The O I transitions are pre-dominantly excited by continuum fluorescence rather than line fluorescence. The evolved stage of S7A and therefore the presence of UV radiation explain the observed lines. The reason why weak O I emission is additionally observed in the knot as the [Fe II] and H_2 lines remains unclear. It indicates, however,

despite the evidence for shock-excitation of the knot emission that UV excitation is present nonetheless.

Finally, the increased resolution of NIRC*am* allowed us to identify an additional point-like source, C1, ~ 52 kAU away from S7A (see Fig. 10.1). This source only appears in NIRC*am* images at wavelengths longer than $2 \mu\text{m}$. The extracted NIRSpec and MIRI/MRS spectra ($\lambda = 1.7\text{--}11.7 \mu\text{m}$) reveal a rising continuum towards the mid-infrared. The observed spectral features identify C1 as another YSO.

References

- Antonucci, S., Nisini, B., Giannini, T., & Lorenzetti, D. 2008, *A&A*, **479**, 503
- Appenzeller, I. 2013, *Introduction to Astronomical Spectroscopy*, Cambridge Observing Handbooks for Research Astronomers No. 9 (Cambridge; New York: Cambridge University Press)
- Arce, H. G., Shepherd, D., Gueth, F., et al. 2007, in *Protostars and Planets V*, ed. B. Reipurth, D. Jewitt, & K. Keil, 245
- Argyriou, I. 2021, *Calibration of the MIRI Instrument on Board the James Webb Space Telescope*, PhD thesis
- Argyriou, I., Glasse, A., Law, D. R., et al. 2023, *A&A*, **675**, A111
- Argyriou, I., Wells, M., Glasse, A., et al. 2020, *A&A*, **641**, A150
- Bally, J. 2016, *ARA&A*, **54**, 491
- Bally, J., Reipurth, B., & Davis, C. J. 2007, in *Protostars and Planets V*, ed. B. Reipurth, D. Jewitt, & K. Keil, 215
- Bally, J., Sutherland, R. S., Devine, D., & Johnstone, D. 1998, *AJ*, **116**, 293
- Bary, J. S., Matt, S. P., Skrutskie, M. F., et al. 2008, *ApJ*, **687**, 376
- Bekhti, N. B., Flöer, L., Keller, R., et al. 2016, *A&A*, **594**, A116
- Bessell, M. S. 2005, *ARA&A*, **43**, 293
- Beuther, H., Churchwell, E. B., McKee, C. F., & Tan, J. C. 2007, in *Protostars and Planets V*, ed. B. Reipurth, D. Jewitt, & K. Keil, 165
- Beuther, H., Kuiper, R., & Tafalla, M. 2025, *arXiv e-prints*, [arXiv:2501.16866](https://arxiv.org/abs/2501.16866)
- Beuther, H. & Shepherd, D. 2005, in *Astrophysics and Space Science Library*, Vol. 324, *Astrophysics and Space Science Library*, ed. M. S. N. Kumar, M. Tafalla, & P. Caselli, 105
- Bhatia, A. K. & Kastner, S. O. 1995, *ApJS*, **96**, 325
- Bik, A., Kaper, L., Thi, W.-F., & Waters, R. 2005, *IAU Symp.*, 227, 53
- Black, J. H. & van Dishoeck, E. F. 1987, *ApJ*, **322**, 412
- Böker, T., Arribas, S., Lützgendorf, N., et al. 2022, *A&A*, **661**, A82
- Böker, T., Beck, T. L., Birkmann, S. M., et al. 2023, *PASP*, **135**, 038001
- Bonnell, I. A., Bate, M. R., Clarke, C. J., & Pringle, J. E. 1997, *MNRAS*, **285**, 201
- Bonnell, I. A., Larson, R. B., & Zinnecker, H. 2007, in *Protostars and Planets V*, ed. B. Reipurth, D. Jewitt, & K. Keil, 149
- Boogert, A. C. A. & Ehrenfreund, P. 2004, in *Astronomical Society of the Pacific Conference Series*, Vol. 309, *Astrophysics of Dust*, ed. A. N. Witt, G. C. Clayton, & B. T. Draine, 547
- Boogert, A. C. A., Gerakines, P. A., & Whitet, D. C. B. 2015, *ARA&A*, **53**, 541
- Bowen, E. J. 1947, *Q. Rev. Chem. Soc.*, **1**, 1
- Bowey, J. E. & Adamson, A. J. 2001, *MNRAS*, **320**, 131
- Brandner, W., Grebel, E. K., Barbá, R. H., Walborn, N. R., & Moneti, A. 2001, *AJ*, **122**, 858
- Brands, S. A., de Koter, A., Bestenlehner, J. M., et al. 2023, *A&A*, **673**, A132
- Bushouse, H., Eisenhamer, J., Dencheva, N., et al. 2023, *JWST Calibration Pipeline*, Zenodo
- Calvet, N., Muzerolle, J., Briceño, C., et al. 2004, *AJ*, **128**, 1294
- Calvet, N., Patino, A., Magris, G. C., & D'Alessio, P. 1991, *ApJ*, **380**, 617
- Cardelli, J. A., Clayton, G. C., & Mathis, J. S. 1989, *ApJ*, **345**, 245
- Carr, J. S. 1989, *ApJ*, **345**, 522
- Carroll, B. W. & Ostlie, D. A. 2017, *An Introduction to Modern Astrophysics*, 2nd edn. (Cambridge: Cambridge University Press)
- Castelli, F. & Kurucz, R. L. 2003, in *IAU Symposium*, Vol. 210, *Modelling of Stellar Atmospheres*, ed. N. Piskunov, W. W. Weiss, & D. F. Gray, A20
- Choudhury, S., de Grijs, R., Bekki, K., et al. 2021, *MNRAS*, **507**, 4752

- Churchwell, E. 2002, *ARA&A*, **40**, 27
- Cioni, M. R. L., Clementini, G., Girardi, L., et al. 2011, *A&A*, **527**, A116
- Cooper, H. D. B., Lumsden, S. L., Oudmaijer, R. D., et al. 2013, *MNRAS*, **430**, 1125
- Cutri, R. M., Skrutskie, M. F., van Dyk, S., et al. 2003, VizieR Online Data Catalog, **2246**, II/246
- Cutri, R. M., Skrutskie, M. F., van Dyk, S., et al. 2012, VizieR Online Data Catalog, **2281**, II/281
- Dale, D. A., Roussel, H., Contursi, A., et al. 2004, *ApJ*, **601**, 813
- Davis, C. J., Cervantes, B., Nisini, B., et al. 2011, *A&A*, **528**, A3
- De Buizer, J. M., Liu, M., Tan, J. C., et al. 2017, *ApJ*, **843**, 33
- De Marchi, G. & Panagia, N. 2014, *MNRAS*, **445**, 93
- De Marchi, G., Panagia, N., Sabbi, E., et al. 2016, *MNRAS*, **455**, 4373
- Deb, N. C. & Hibbert, A. 2011, *A&A*, **536**, A74
- Dicken, D., Rieke, G., Ressler, M., et al. 2022, *Proc. SPIE*, **12180**, 121802R
- Dinerstein, H. L. 1995, in *The Analysis of Emission Lines*, ed. M. Livio & R. Williams, Space Telescope Science Institute Symposium Series (Cambridge: Cambridge University Press), 134–157
- Dirac, P. A. M. 1928, *Proceedings of the Royal Society of London Series A*, **117**, 610
- Dopita, M. A. & Sutherland, R. S. 2003, *Astrophysics of the Diffuse Universe*, Astronomy and Astrophysics Library (Berlin: Springer)
- Doyon, R., Willott, C. J., Hutchings, J. B., et al. 2023, *PASP*, **135**, 098001
- Draine, B. T. 2011, *Physics of the Interstellar and Intergalactic Medium*, 1st edn., Princeton Series in Astrophysics Series No. 19 (Princeton: Princeton University Press)
- Draine, B. T. & McKee, C. F. 1993, *ARA&A*, **31**, 373
- Dyson, J. E. & Williams, D. A. 1980, *Physics of the Interstellar Medium*
- Edwards, S., Kwan, J., Fischer, W., et al. 2013, *ApJ*, **778**, 148
- Einstein, A. 1916, *Zur quantentheorie der strahlung* (Verlag u. Druck Gebr. Leemann)
- Eislöffel, J. 2000, *A&A*, **354**, 236
- Eversberg, T. & Vollmann, K. 2015, *Spectroscopic Instrumentation: Fundamentals and Guidelines for Astronomers*, Springer Praxis Books (Berlin, Heidelberg: Springer)
- Fahrion, K. & De Marchi, G. 2023, *A&A*, **671**, L14
- Fazio, G. G., Hora, J. L., Allen, L. E., et al. 2004, *ApJS*, **154**, 10
- Ferland, G. J. 1999, *PASP*, **111**, 1524
- Foot, C. J. 2011, *Atomic Physics*, repr. (twice with corr.) edn., Oxford Master Series in Physics Atomic, Optical, and Laser Physics No. 7 (Oxford: Oxford Univ. Press)
- Gaia Collaboration, Vallenari, A., Brown, A. G. A., et al. 2023, *A&A*, **674**, A1
- Gardner, J. P., Mather, J. C., Abbott, R., et al. 2023, *PASP*, **135**, 068001
- Genzel, R. 1992, in *Saas-Fee Advanced Course 21: The Galactic Interstellar Medium*, ed. W. B. Burton, B. G. Elmegreen, R. Genzel, D. Pfenniger, & P. Bartholdi, **275–391**
- Glass, I. S. 1999, *Handbook of Infrared Astronomy*, Cambridge Observing Handbooks for Research Astronomers No. 1 (Cambridge, U.K.; New York: Cambridge University Press)
- Gordon, K. D., Clayton, G. C., Misselt, K. A., Landolt, A. U., & Wolff, M. J. 2003, *ApJ*, **594**, 279
- Graczyk, D., Soszyński, I., Poleski, R., et al. 2011, *Acta Astron.*, **61**, 103
- Greenfield, P. & Miller, T. 2016, *Astronomy and Computing*, **16**, 41
- Habart, E., Peeters, E., Berné, O., et al. 2024, *A&A*, **685**, A73
- Habart, E., Walmsley, M., Verstraete, L., et al. 2005, *Space Sci. Rev.*, **119**, 71
- Hartigan, P., Raymond, J., & Pierson, R.

- 2004, *ApJ*, **614**, L69
- Herter, T. 1994, *Exp Astron*, **3**, 255
- Hoare, M. G., Kurtz, S. E., Lizano, S., Keto, E., & Hofner, P. 2007, in *Protostars and Planets V*, ed. B. Reipurth, D. Jewitt, & K. Keil, 181
- Hocdé, V., Smolec, R., Moskalik, P., Ziółkowska, O., & Rathour, R. S. 2023, *A&A*, **671**, A157
- Hohle, M. M., Neuhäuser, R., & Schutz, B. F. 2010, *Astronomische Nachrichten*, **331**, 349
- Hollenbach, D. & McKee, C. F. 1989, *ApJ*, **342**, 306
- Hollenbach, D. J., Chernoff, D. F., & McKee, C. F. 1989, in *Infrared Spectroscopy in Astronomy*, ed. E. Böhm-Vitense, 245
- Hollenbach, D. J. & Shull, J. M. 1977, *ApJ*, **216**, 419
- Hollenbach, D. J. & Tielens, A. G. G. M. 1995, in *The Physics and Chemistry of Interstellar Molecular Clouds*, ed. G. Winnewisser & G. C. Pelz, Vol. 459, 164
- Hosokawa, T., Yorke, H. W., & Omukai, K. 2010, *ApJ*, **721**, 478
- Houck, J. R., Roellig, T. L., van Cleve, J., et al. 2004, *ApJS*, **154**, 18
- Hummer, D. G. & Storey, P. J. 1987, *MNRAS*, **224**, 801
- Hyland, A. R. & Jones, T. J. 1991, in *IAU Symposium*, Vol. 148, *The Magellanic Clouds*, ed. R. Haynes & D. Milne, 202
- Hyland, A. R., Straw, S., Jones, T. J., & Gatley, I. 1992, *MNRAS*, **257**, 391
- Ilee, J. D., Wheelwright, H. E., Oudmaijer, R. D., et al. 2013, *MNRAS*, **429**, 2960
- Indebetouw, R., Brogan, C., Chen, C.-H. R., et al. 2013, *ApJ*, **774**, 73
- Jakobsen, P., Ferruit, P., de Oliveira, C. A., et al. 2022, *A&A*, **661**, A80
- Johnson, H. L. 1955, *Annales d'Astrophysique*, **18**, 292
- Johnson, H. L. & Morgan, W. W. 1953, *ApJ*, **117**, 313
- Johnstone, D., Hollenbach, D., & Bally, J. 1998, *ApJ*, **499**, 758
- Jones, O. C., Reiter, M., Sanchez-Janssen, R., et al. 2022, *MNRAS*, **517**, 1518
- Karttunen, H., Kröger, P., Oja, H., Poutanen, M., & Donner, K. J. 2007, *Fundamental Astronomy* (Springer Science & Business Media)
- Kato, D., Nagashima, C., Nagayama, T., et al. 2007, *PASJ*, **59**, 615
- Kessler, M. F., Metcalfe, L., & Salama, A. 1992, *Space Sci. Rev.*, **61**, 45
- Kim, J., Jeong, W.-S., Pak, S., Park, W.-K., & Tamura, M. 2016, *ApJS*, **222**, 2
- Kim, S.-H., Martin, P. G., & Hendry, P. D. 1994, *ApJ*, **422**, 164
- Kirwan, A., Manara, C. F., Whelan, E. T., et al. 2023, *A&A*, **673**, A166
- Klaassen, P. D., Wilson, C. D., Keto, E. R., et al. 2011, *A&A*, **530**, A53
- Koo, B.-C., Raymond, J. C., & Kim, H.-J. 2016, *Journal of The Korean Astronomical Society*, **49**, 109
- Kramida, A., Yu. Ralchenko, Reader, J., & and NIST ASD Team. 2023, *NIST Atomic Spectra Database* (ver. 5.11), [Online]. Available: <https://physics.nist.gov/asd> [2024, February 21]. National Institute of Standards and Technology, Gaithersburg, MD.
- Krumholz, M. R., Klein, R. I., & McKee, C. F. 2012, *ApJ*, **754**, 71
- Krumholz, M. R. & McKee, C. F. 2005, *ApJ*, **630**, 250
- Kudritzki, R. P. 2002, *ApJ*, **577**, 389
- Kuiper, R., Klahr, H., Beuther, H., & Henning, T. 2010, *ApJ*, **722**, 1556
- Kurtz, S. 2005, in *IAU Symposium*, Vol. 227, *Massive Star Birth: A Crossroads of Astrophysics*, ed. R. Cesaroni, M. Felli, E. Churchwell, & M. Walmsley, 111–119
- Kurucz, R. L. 1993, *VizieR Online Data Catalog*, **6039**, VI/39
- Labrie, K. & Pritchett, C. J. 2006, *ApJS*, **166**, 188
- Lenz, D. D. & Ayres, T. R. 1992, *PASP*, **104**,

- 1104
- Lequeux, J., ed. 2005, *The Interstellar Medium*, Astronomy and Astrophysics Library (Berlin, Heidelberg: Springer Berlin Heidelberg)
- Lucy, L. B. 1995, *A&A*, **294**, 555
- Lucy, L. B. 2002, *MNRAS*, **329**, 787
- Lumsden, S. L., Wheelwright, H. E., Hoare, M. G., Oudmaijer, R. D., & Drew, J. E. 2012, *MNRAS*, **424**, 1088
- Maercker, M. & Burton, M. G. 2005, *A&A*, **438**, 663
- Mannucci, F., Cresci, G., Maiolino, R., Marconi, A., & Gnerucci, A. 2010, *MNRAS*, **408**, 2115
- Marconi, A., Testi, L., Natta, A., & Walmsley, C. M. 1998, *A&A*, **330**, 696
- Marinelli, M. & Green, J. 2024, in *WFC3 Instrument Handbook for Cycle 33 v. 17*, Vol. 17, 17
- Martin, S. C. 1997, *ApJ*, **478**, L33
- Mathew, B., Banerjee, D. P. K., Subramaniam, A., & Ashok, N. M. 2012, *ApJ*, **753**, 13
- Mathew, B., Manoj, P., Narang, M., et al. 2018, *ApJ*, **857**, 30
- Maud, L. T. 2013, *High Resolution Imaging of Massive Young Stellar Objects and a Sample of Molecular Outflow Sources*, PhD thesis
- McKee, C. F. & Ostriker, E. C. 2007, *ARA&A*, **45**, 565
- McKee, C. F. & Tan, J. C. 2003, *ApJ*, **585**, 850
- McLean, I. S. 2008, *Electronic Imaging in Astronomy: Detectors and Instrumentation*, 2nd edn., Springer Praxis Books (Berlin, Heidelberg: Praxis Pub., Chichester, UK Springer e-books)
- Meixner, M., Gordon, K. D., Indebetouw, R., et al. 2006, *AJ*, **132**, 2268
- Meixner, M., Panuzzo, P., Roman-Duval, J., et al. 2013, *AJ*, **146**, 62
- Mendigutía, I., Calvet, N., Montesinos, B., et al. 2011, *A&A*, **535**, A99
- Merrill, P. W. 1958, *Lines of the Chemical Elements in Astronomical Spectra*
- Mill, J. D., O’Neil, R. R., Price, S., et al. 1994, *Journal of Spacecraft and Rockets*, **31**, 900
- Morrison, J. E., Dicken, D., Argyriou, I., et al. 2023, *PASP*, **135**, 075004
- Murakami, H., Baba, H., Barthel, P., et al. 2007, *PASJ*, **59**, S369
- Nally, C. 2023, *Astrophysics Source Code Library*, ascl:2309.012
- Nandakumar, G., Schultheis, M., Feldmeier-Krause, A., et al. 2018, *A&A*, **609**, A109
- Nayak, O., Meixner, M., Indebetouw, R., et al. 2016, *ApJ*, **831**, 32
- Nisini, B., Bacciotti, F., Giannini, T., et al. 2005, *A&A*, **441**, 159
- Nisini, B., Giannini, T., & Lorenzetti, D. 2002, *A&A*, **393**, 1035
- Nisini, B., Navarro, M. G., Giannini, T., et al. 2024, *ApJ*, **967**, 168
- Nussbaumer, H. & Storey, P. J. 1988, *A&A*, **193**, 327
- O’Connell, B., Smith, M. D., Davis, C. J., et al. 2004, *A&A*, **419**, 975
- O’Dell, C. R. & Wen, Z. 1994, *ApJ*, **436**, 194
- O’Dell, C. R., Wen, Z., & Hu, X. 1993, *ApJ*, **410**, 696
- Offner, S. S. R. & McKee, C. F. 2011, *ApJ*, **736**, 53
- Palmer, C. & Loewen, E. 2005, *Diffraction Grating Handbook* (Newport Corporation)
- Peeters, E., Habart, E., Berné, O., et al. 2024, *A&A*, **685**, A74
- Pietrzyński, G., Graczyk, D., Gallenne, A., et al. 2019, *Nature*, **567**, 200
- Pomohaci, R., Oudmaijer, R. D., Lumsden, S. L., Hoare, M. G., & Mendigutía, I. 2017, *MNRAS*, **472**, 3624
- Porter, J. M., Drew, J. E., & Lumsden, S. L. 1998, *A&A*, **332**, 999
- Pradhan, A. K. & Nahar, S. N. 2011, *Atomic Astrophysics and Spectroscopy* (Cambridge New York: Cambridge University Press)
- Purser, S. J. D. 2017, *Ionised Jets Associated*

- With Massive Young Stellar Objects, PhD thesis
- Rauscher, B. J., Arendt, R. G., Fixen, D. J., et al. 2011, in *Infrared Sensors, Devices, and Applications; and Single Photon Imaging II*, Vol. 8155 (SPIE), [110–124](#)
- Rauscher, B. J., Boehm, N., Cagiano, S., et al. 2014, *PASP*, [126](#), [739](#)
- Ray, T. P., McCaughrean, M. J., Caratti o Garatti, A., et al. 2023, *Nature*, [622](#), [48](#)
- Reipurth, B. & Heathcote, S. 1997, in *IAU Symposium*, Vol. 182, *Herbig-Haro Flows and the Birth of Stars*, ed. B. Reipurth & C. Bertout, [3–18](#)
- Reiter, M., Nayak, O., Meixner, M., & Jones, O. 2019, *MNRAS*, [483](#), [5211](#)
- Rest, A., Pierel, J., Correnti, M., et al. 2023, *The JWST HST Alignment Tool (JHAT)*, Zenodo
- Ricci, L., Robberto, M., & Soderblom, D. R. 2008, *AJ*, [136](#), [2136](#)
- Richardson, T., Ginsburg, A., Indebetouw, R., & Robitaille, T. P. 2024, *ApJ*, [961](#), [188](#)
- Rieke, G. 2007, *ARA&A*, [45](#), [77](#)
- Rieke, G. H. 2021, *Detection of Light*, third edition edn. (Cambridge: Cambridge University Press)
- Rieke, G. H., Ressler, M. E., Morrison, J. E., et al. 2015, *PASP*, [127](#), [665](#)
- Rieke, G. H., Young, E. T., Engelbracht, C. W., et al. 2004, *ApJS*, [154](#), [25](#)
- Rieke, M. J., Kelly, D. M., Misselt, K., et al. 2023, *PASP*, [135](#), [028001](#)
- Rigby, J., Perrin, M., McElwain, M., et al. 2023a, *PASP*, [135](#), [048001](#)
- Rigby, J. R., Lightsey, P. A., Marín, M. G., et al. 2023b, *PASP*, [135](#), [048002](#)
- Rigliaco, E., Pascucci, I., Duchene, G., et al. 2015, *ApJ*, [801](#), [31](#)
- Robitaille, T. P. 2011, *A&A*, [536](#), [A79](#)
- Robitaille, T. P. 2017, *A&A*, [600](#), [A11](#)
- Robitaille, T. P., Whitney, B. A., Indebetouw, R., & Wood, K. 2007, *ApJS*, [169](#), [328](#)
- Robitaille, T. P., Whitney, B. A., Indebetouw, R., Wood, K., & Denzmore, P. 2006, *ApJS*, [167](#), [256](#)
- Rogers, C., Brandl, B., & de Marchi, G. 2024a, *arXiv e-prints*, [arXiv:2412.05668](#)
- Rogers, C., de Marchi, G., & Brandl, B. 2024b, *arXiv e-prints*, [arXiv:2412.05650](#)
- Rosenberg, M. J. F., van der Werf, P. P., & Israel, F. P. 2013, *A&A*, [550](#), [A12](#)
- Rubio, M., Barbá, R. H., Walborn, N. R., et al. 1998, *AJ*, [116](#), [1708](#)
- Rubio, M., Roth, M., & Garcia, J. 1992, *A&A*, [261](#), [L29](#)
- Ryden, B. S. & Pogge, R. W. 2021, *Interstellar and Intergalactic Medium* (Cambridge: Cambridge University Press)
- Sabbi, E., Lennon, D. J., Anderson, J., et al. 2016, *ApJS*, [222](#), [11](#)
- Saral, G., Hora, J. L., Audard, M., et al. 2017, *ApJ*, [839](#), [108](#)
- Schrödinger, E. 1926, *Phys. Rev.*, [28](#), [1049](#)
- Schulz, N. S. 2012, *The Formation and Early Evolution of Stars*, *Astronomy and Astrophysics Library* (Berlin, Heidelberg: Springer)
- Seale, J. P., Meixner, M., Sewiło, M., et al. 2014, *AJ*, [148](#), [124](#)
- Sewiło, M., Carlson, L. R., Seale, J. P., et al. 2013, *ApJ*, [778](#), [15](#)
- Shu, F. H., Adams, F. C., & Lizano, S. 1987, *ARA&A*, [25](#), [23](#)
- Shull, J. M. & Draine, B. T. 1987, in *Interstellar Processes*, ed. D. J. Hollenbach & H. A. Thronson, Jr., Vol. 134, [283](#)
- Shull, J. M. & Hollenbach, D. J. 1978, *ApJ*, [220](#), [525](#)
- Siemiginowska, A., Arnaud, K. A., & Smith, R. K., eds. 2011, *Handbook of X-ray Astronomy*, *Cambridge Observing Handbooks for Research Astronomers* (Cambridge, UK New York: Cambridge University Press)
- Sim, S. A., Drew, J. E., & Long, K. S. 2005, *MNRAS*, [363](#), [615](#)
- Simcoe, R. A., Burgasser, A. J., Schechter, P. L., et al. 2013, *PASP*, [125](#), [270](#)
- Stahler, S. W. & Palla, F. 2004, *The Formation of Stars*

- Stanke, T., McCaughrean, M. J., & Zinnecker, H. 2002, *A&A*, **392**, 239
- Storey, P. J. & Hummer, D. G. 1995, *MNRAS*, **272**, 41
- Sturm, J. A., McClure, M. K., Beck, T. L., et al. 2023, *A&A*, **679**, A138
- Tennyson, J. 2005, *Astronomical Spectroscopy: An Introduction to the Atomic and Molecular Physics of Astronomical Spectra*, Imperial College Press Advanced Physics Texts No. v. 2 (London : Hackensack, N.J: Imperial College Press ; Distributed by World Scientific Pub)
- Thatte, D. e. 2009, *NICMOS Data Handbook v. 8.0*
- Tielens, A. G. G. M. 2005, *The Physics and Chemistry of the Interstellar Medium* (Cambridge: Cambridge University Press)
- Tielens, A. G. G. M. 2008, *ARA&A*, **46**, 289
- Tielens, A. G. G. M. 2021, *Molecular Astrophysics* (Cambridge: Cambridge University Press)
- Torres-Flores, S., Barbá, R., Apellániz, J. M., et al. 2013, *A&A*, **555**, A60
- Trumpler, R. J. 1930, *PASP*, **42**, 214
- Ueta, T. & Otsuka, M. 2021, *PASP*, **133**, 093002
- Vaidya, B. 2011, *Theory of Disks and Outflows around Massive Young Stellar Objects*, PhD thesis
- van der Marel, R. P. & Kallivayalil, N. 2014, *ApJ*, **781**, 121
- van Dishoeck, E. F. 2004, *ARA&A*, **42**, 119
- van Gelder, M. L., Kaper, L., Japelj, J., et al. 2020, *A&A*, **636**, A54
- van Hoof, P. A. M. 2018, *Galaxies*, **6**, 63
- Varricatt, W. P., Davis, C. J., Ramsay, S., & Todd, S. P. 2010, *MNRAS*, **404**, 661
- Vernet, J., Dekker, H., D’Odorico, S., et al. 2011, *A&A*, **536**, A105
- Walborn, N. R., Barbá, R. H., Brandner, W., et al. 1999, *AJ*, **117**, 225
- Walborn, N. R., Barbá, R. H., & Sewiło, M. M. 2013, *AJ*, **145**, 98
- Walborn, N. R., Maíz-Apellániz, J., & Barbá, R. H. 2002, *AJ*, **124**, 1601
- Ward, J. L. 2017, *High-Resolution Studies of Massive Young Stellar Objects in the Magellanic Clouds*, PhD thesis
- Ward, J. L., Oliveira, J. M., van Loon, J. Th., & Sewiło, M. 2016, *MNRAS*, **455**, 2345
- Ward, J. L., Oliveira, J. M., van Loon, J. Th., & Sewiło, M. 2017, *MNRAS*, **464**, 1512
- Wells, M., Pel, J.-W., Glasse, A., et al. 2015, *PASP*, **127**, 646
- Welty, D. E., Federman, S. R., Gredel, R., Thorburn, J. A., & Lambert, D. L. 2006, *ApJS*, **165**, 138
- Werner, M. W., Roellig, T. L., Low, F. J., et al. 2004, *ApJS*, **154**, 1
- Wesson, R. 2016, *MNRAS*, **456**, 3774
- Westerlund, B. E. 1997, *The Magellanic Clouds*
- Whitney, B. A., Sewiło, M., Indebetouw, R., et al. 2008, *AJ*, **136**, 18
- Williams, J. P. 2021, *Introduction to the Interstellar Medium* (Cambridge: Cambridge University Press)
- Wolfire, M. G. & Cassinelli, J. P. 1987, *ApJ*, **319**, 850
- Wolniewicz, L., Simbotin, I., & Dalgarno, A. 1998, *ApJS*, **115**, 293
- Wright, E. L., Eisenhardt, P. R. M., Mainzer, A. K., et al. 2010, *AJ*, **140**, 1868
- Wright, G. S., Rieke, G. H., Glasse, A., et al. 2023, *PASP*, **135**, 048003
- Yeh, S. C. C., Seaquist, E. R., Matzner, C. D., & Pellegrini, E. W. 2015, *ApJ*, **807**, 117
- Zhang, Y. & Tan, J. C. 2011, *ApJ*, **733**, 55
- Zhang, Y. & Tan, J. C. 2018, *ApJ*, **853**, 18
- Zinnecker, H. & Yorke, H. W. 2007, *ARA&A*, **45**, 481

A Spectra

A.1 Parameters of ds9 spectral extraction regions

TABLE A.1 – Parameters of ds9 spectral extraction regions shown in Fig. 9.3.

ID	Shape	Centre R.A. DEC. [deg] ^f	Semi-major [arcsec]	Semi-minor [arcsec]	Position angle ^a [°]
YSO	circle ^b	84.6953781–69.0848468	0.276	0.276	0
YSO+ Outflow ^g	ellipse	84.6953671–69.0848622	0.354	0.411	40
Shell					
S1A	epanda ^c	84.6954146–69.0848817	0.617; 1.158	0.579; 1.234	104; 184; 160
S1B	panda ^c	84.6956429–69.0847522	1.685	1.052	201; 275; 0
S2	polygon ^d	-	-	-	-
S3	ellipse	84.6941267–69.0850415	0.401	0.633	125
H ₂					
M2 ^e	circle ^b	84.6957163–69.0846712	0.285	0.285	0
M3	ellipse	84.6955054–69.0845117	0.206	0.337	140
M4	ellipse	84.6949913–69.0844567	0.355	0.446	40
M5	ellipse	84.6948543–69.0846966	0.256	0.449	0
M6	epanda ^c	84.6954465–69.0848362	0.643; 1.070	0.524; 0.872	235; 341; 25
M7	ellipse	84.6958007–69.0849439	0.252	0.385	20
M8	ellipse	84.6963591–69.0849158	0.356	0.491	55
M9	ellipse	84.6960871–69.0847636	0.231	0.287	150
Knot					
[Fe II]	circle ^b	84.6951778–69.0849126	0.241	0.241	0
O I	circle ^b	84.6951721–69.0849331	0.271	0.271	0

NOTES. ^(a) Position angle increases counter-clockwise (N-E). ^(b) Semi-major axis = semi-minor axis = radius. ^(c) Semi-major (minor) axis for the inner and outer ellipse. For a (circular) panda, semi-major (minor) = outer (inner) radius. Column six shows the start, stop, and positions angle, respectively. ^(d) The extraction polygon is defined through the following set of six points (x_i, y_i) : (84.6946092, -69.0842573); (84.6943309, -69.0842767); (84.6943187, -69.0848793); (84.6944821, -69.0849657); (84.6948693, -69.0849182); (84.6946031, -69.0848081). ^(e) M2 corresponds to the position of point source C1. ^(f) The coordinates are given in the NIRSspec frame. See discussion in Sect. 9.3.1 for details of relative R.A. and DEC. corrections. ^(g) Denoted by M1 in Fig. 9.3 and Tab. 9.7.

A.2 S7A spectrum

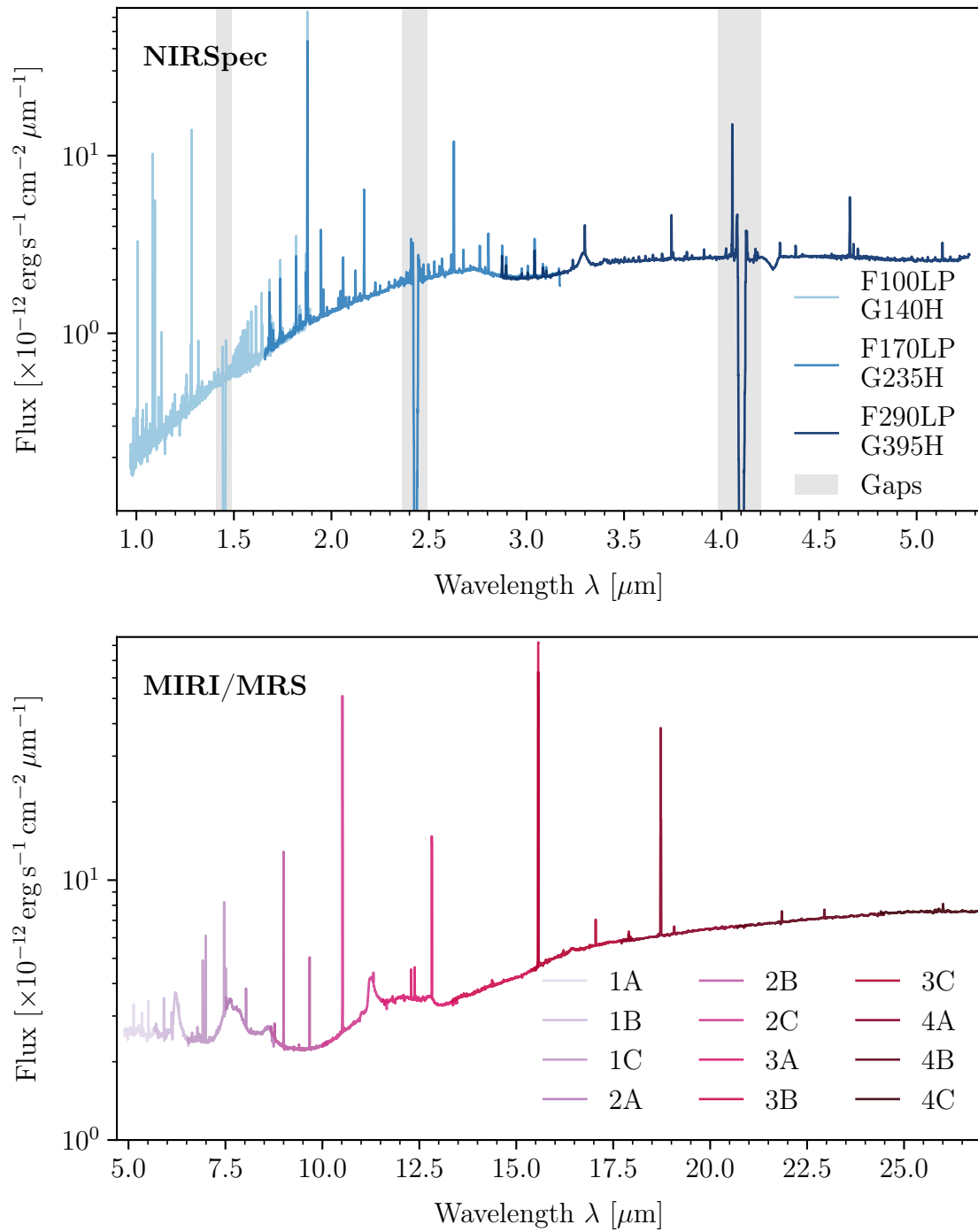


FIGURE A.1 – Observed NIRSpect (top) and MIRI/MRS (bottom) spectra of S7A spanning a wavelength range of 0.97–27 μ m. The different colours in each panel indicate the different filters/gratings of NIRSpect and IFU channels of MIRI/MRS. The details of the spectral extraction are described in Sect. 9.3.1.

A.3 YSO+Outflow Spectrum

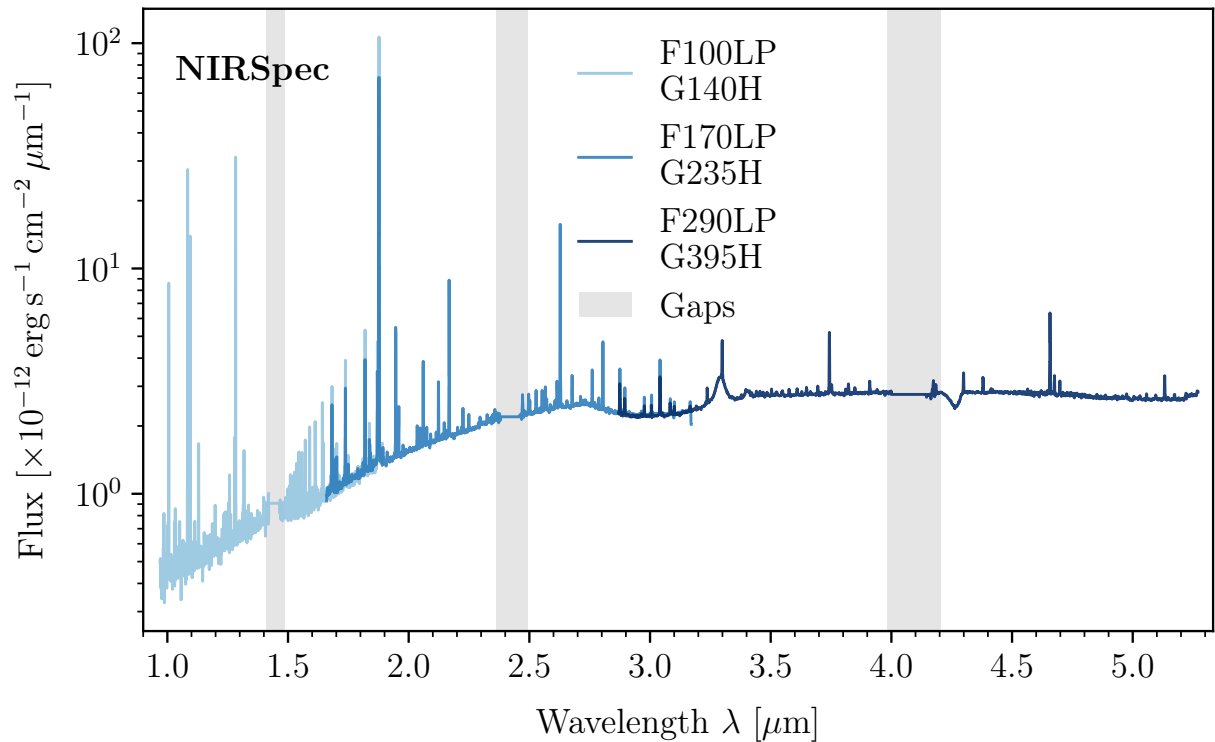


FIGURE A.2 – Observed NIRSpec spectrum extracted from the position of the YSO covering the region of the outflow (YSO+Outflow). The semi-major and minor axis of the extraction ellipse are not propagated according to equation 9.1. The size of the extraction region is chosen to cover all relevant features at the longest wavelength of the F290 filter. The NIRSpec spectrum is scaled by a factor of 0.91 to account for background. The MIRI/MRS spectra of both regions are similar as the increased PSF does not allow to distinguish the emission regions for wavelengths longer than $\gtrsim 5 \mu$ m.

A.4 Shell spectrum

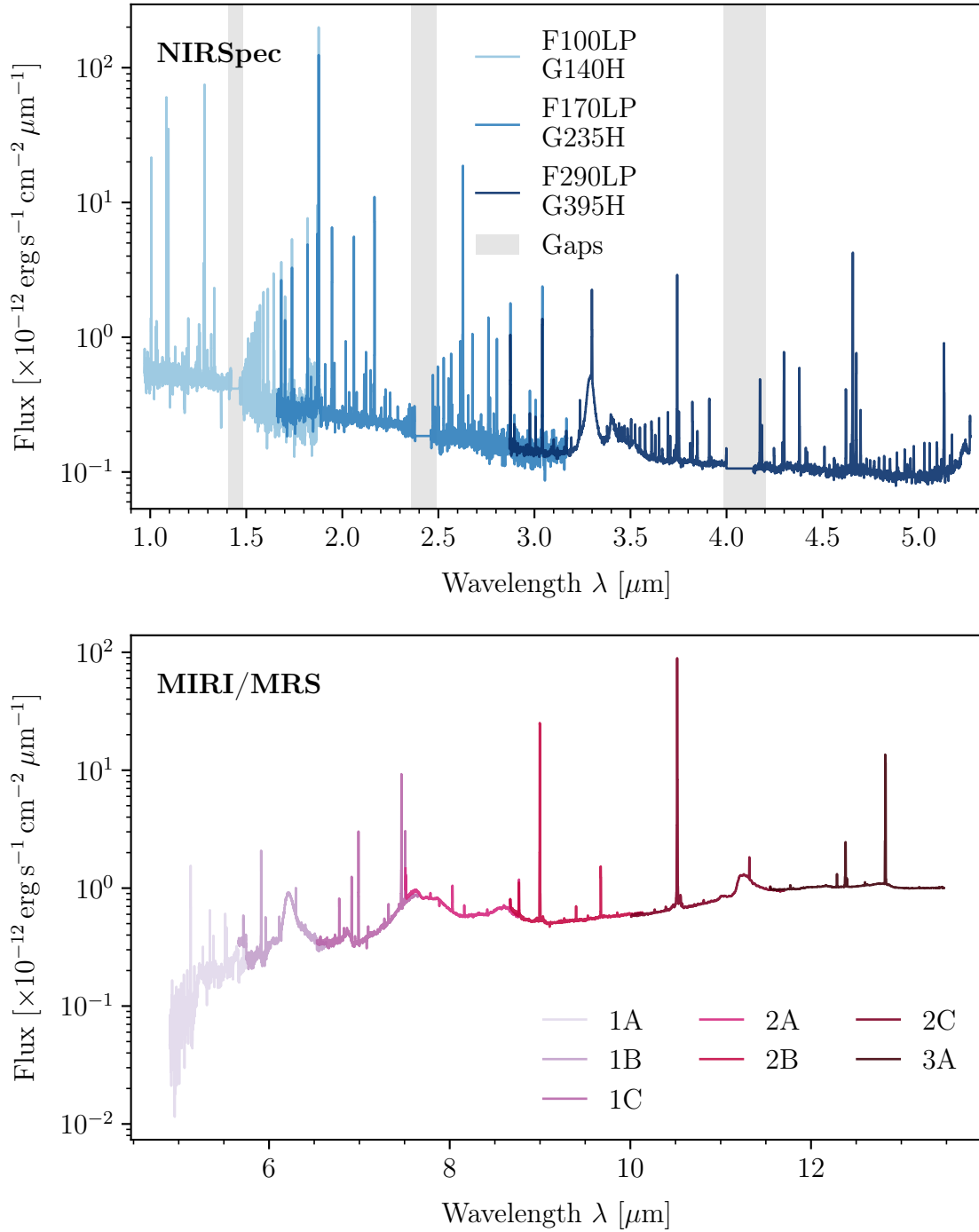


FIGURE A.3 – Partial shell spectra from extraction region S1A – the brightest part in the shell. For wavelengths longer than $\sim 13.5 \mu\text{m}$ (Ch-3B), S7A and the shell can no longer be distinguished as two separate structures due to the large PSF. The spectral extraction is non-conical. The NIRSpect and MIRI/MRS sizes of the extraction region are shown in Tab. A.1. The flux densities of NIRSpect F290 and MIRI/MRS 1A show no significant offset. No additional background-scaling of the NIRSpect data was performed.

A.5 SED of pointsource C1

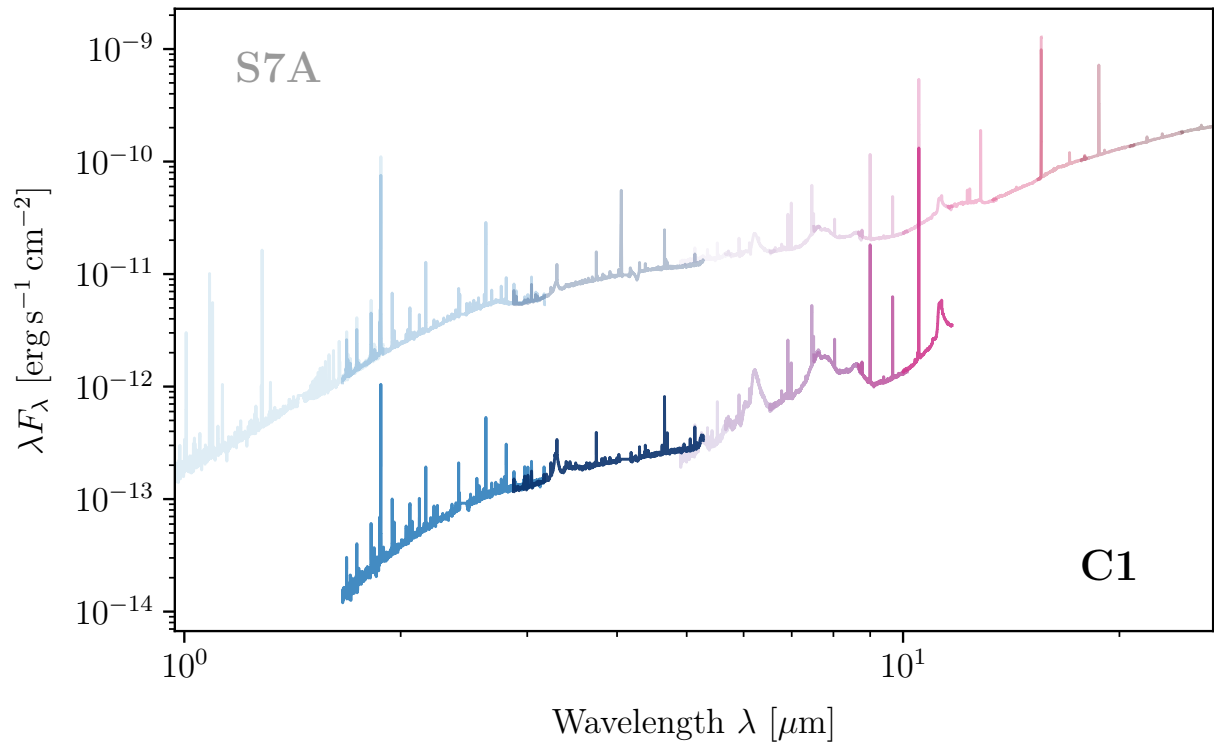


FIGURE A.4 – Observed NIRSpect and MIRI/MRS SEDs of C1 spanning a wavelength range of 1.7–11.7 μ m. For wavelengths longer than $\sim 12 \mu$ m C1 is covered by the MIRI/MRS PSF of S7A. The SED of S7A is shown for comparison. The different colours indicate the different filters/gratings of NIRSpect and IFU channels of MIRI/MRS.

B Identified emission lines

TABLE B.1 – Observed lines in the entire available wavelength range 0.97–27 μm and their identification. Lines observed in multiple NIRSpec bands are reported only once and attributed to the longer wavelength channel. For atoms and ions the third column gives their electronic configuration terms for the upper and the lower level. H_2 ro-vibrational and pure rotational lines are given in the following notation $(v', v'') \Delta J(J'')$ where $\Delta J = J' - J'' = -2$ is abbreviated as O and $\Delta J = 0, 2$ as Q, S respectively. The observed wavelength is corrected for the radial velocity of the MYSO. The last column presents the offset between observed and rest wavelengths of the emission lines in velocity space.

λ_{lab} [μm]	Species	Transition (upper – lower)	λ_{obs} [μm]	Offset [km s^{-1}]
NIRSpec F100LP/G140H				
0.98530	[C I]	$2s^2 2p^2 \ ^3P_2 - 2s^2 2p^2 \ ^1D_2$	0.98524	-17
1.00521	H I	$7 - 3 \text{ P}\delta$	1.00515	-20
1.02896	[S II]	$3s^2 3p^3 \ ^2P_{3/2}^\circ - 3s^2 3p^3 \ ^2D_{3/2}^\circ$	1.02888	-23
1.03233	[S II]	$3s^2 3p^3 \ ^2P_{3/2}^\circ - 3s^2 3p^3 \ ^2D_{5/2}^\circ$	1.03225	-24
1.03392	[S II]	$3s^2 3p^3 \ ^2P_{1/2}^\circ - 3s^2 3p^3 \ ^2D_{3/2}^\circ$	1.03387	-15
1.03733	[S II]	$3s^2 3p^3 \ ^2P_{1/2}^\circ - 3s^2 3p^3 \ ^2D_{5/2}^\circ$	1.03720	-39
1.04993 ?	Fe II ?	$3d^5 4s^2 \ ^4G_{5/2} - 3d^6(^5D)4p \ ^4F_{7/2}^\circ$	1.05038	-
1.05012 ?				$3d^5 4s^2 \ ^4G_{9/2} - 3d^6(^5D)4p \ ^4F_{7/2}^\circ$
1.08332	He I	$1s 2p \ ^3P_1^\circ - 1s 2s \ ^3S_1$	1.08328	-10
1.09160	He I	$1s 6f \ ^3F_3^\circ - 1s 3d \ ^3D_2$	1.09160	+1
1.09411	H I	$6 - 3 \text{ P}\gamma$	1.09404	-19
1.11286 ?	Fe II ?	$3d^5 4s^2 \ ^4G_{5/2} - 3d^6(^5D)4p \ ^4F_{3/2}^\circ$	1.11289	-
1.12904	O I	$2p^3(^4S)3d \ ^3D_1^\circ - 2p^3(^4S)3p \ ^3P_0^\circ$	1.12895	-24
1.13043	H_2	$3-1 \text{ S}(7)$	1.13040	-8
1.19724	He I	$1s 5d \ ^3D_2 - 1s 3p \ ^3P_1^\circ$	1.19716	-20
1.23299	H_2	$3-1 \text{ S}(1)$	1.23296	-8
1.23834	H_2	$2-0 \text{ Q}(1)$	1.23830	-10
1.25309	He I	$1s 4p \ ^3P_1^\circ - 1s 3s \ ^3S_1$	1.25301	-18
1.25702	[Fe II]	$3d^6(^5D)4s \ ^4D_{7/2} - 3d^6(^5D)4s \ ^6D_{9/2}$	1.25694	-20
1.27884	He I	$1s 5f \ ^3F_{2,3,4}^\circ - 1s 3d \ ^3D_{1,2,3}$	1.27883	-1
1.28216	H I	$5 - 3 \text{ P}\beta$	1.28208	-19
1.31068	H_2	$5-3 \text{ S}(5)$	1.31060	-18
1.31156	H_2	$4-2 \text{ S}(1)$	1.31155	-3
1.31675	O I	$2s^2 2p^3(^4S^\circ)4s \ ^3S_1^\circ - 2s^2 2p^3(^4S^\circ)3p \ ^3P_1$	1.31675	0
1.32091	[Fe II]	$3d^6(^5D)4s \ ^4D_{7/2} - 3d^6(^5D)4s \ ^6D_{7/2}$	1.32084	-16
1.48699	H_2	$2-0 \text{ O}(6)$	1.48704	+9
1.49155	H I	$27 - 4 \text{ Br}27$	1.49144	-22
1.49293	H_2	$5-3 \text{ Q}(1)$	1.49291	-6
1.49418	H I	$26 - 4 \text{ Br}26$	1.49414	-9

TABLE B.1 – *Continued.*

λ_{lab} [μm]	Species	Transition (upper – lower)	λ_{obs} [μm]	Offset [km s^{-1}]
1.49714	H I	25 – 4 Br25	1.49707	–14
1.50050	H I	24 – 4 Br24	1.50039	–22
1.50431	H I	23 – 4 Br23	1.50423	–16
1.50869	H I	22 – 4 Br22	1.50863	–11
1.50987	H ₂	4–2 O(3)	1.50977	–19
1.52647	H I	19 – 4 Br19	1.52638	–18
1.53460	H I	18 – 4 Br18	1.53445	–29
1.54431	H I	17 – 4 Br17	1.54423	–17
1.55607	H I	16 – 4 Br16	1.55598	–18
1.57050	H I	15 – 4 Br15	1.57039	–20
1.58849	H I	14 – 4 Br14	1.58841	–14
1.61137	H I	13 – 4 Br13	1.61128	–16
1.64117	H I	12 – 4 Br12	1.64108	–16
1.64400	[Fe II]	$3d^6(^5D)4s a^4D_{7/2} - 3d^7 a^4F_{9/2}$	1.64390	–17
NIRSpec F170LP/G235H				
1.68111	H I	11 – 4 Br11	1.68095	–30
1.68776	H ₂	1–0 S(9)	} 1.68772 –9	–6
1.68778	Fe II	$3d^6(^3F_1)4s c^4F_{9/2} - 3d^6(^5D)4p z^4D_{9/2}^\circ$		
1.70071	He I	$1s4d ^3D_2 - 1s3p ^3P_1^\circ$	1.70056	–27
1.73669	H I	10 – 4 Br10	1.73652	–29
1.74188	Fe II	$3d^6(^3F_1)4s c^4F_{7/2} - 3d^6(^5D)4p z^4D_{7/2}^\circ$	1.74182	–10
1.74796	H ₂	1–0 S(7)	1.74786	–17
1.81791	H I	9 – 4 Br ϵ	1.81776	–25
1.83576	H ₂	1–0 S(5)	1.83563	–22
1.84026	Fe II	$3d^6(^3F_1)4s c^4F_{7/2} - 3d^6(^5D)4p z^4F_{7/2}^\circ$	1.84017	–15
1.85282	H ₂	2–1 S(7)	1.85271	–18
1.86903	He I	$1s4f ^3F_2^\circ - 1s3d ^3D_3$	1.86892	–20
1.87561	H I	4 – 3 P α	1.87547	–24
1.89194	H ₂	1–0 S(4)	1.89185	–15
1.90946	He I	$1s4d ^1D_2 - 1s3p ^1P_1^\circ$	1.90933	–21
1.94509	H I	8 – 4 Br δ	1.94493	–24
1.95482	He I	$1s4p ^3P_{0,1,2}^\circ - 1s3d ^3D_{1,2,3}$	1.95469	–20
1.95756	H ₂	1–0 S(3)	1.95745	–17
2.03376	H ₂	1–0 S(2)	2.03363	–20
2.05869	He I	$1s2p ^1P_1^\circ - 1s2s ^1S_0$	2.05855	–20
2.06558	H ₂	3–2 S(5)	2.06540	–27
2.07348	H ₂	2–1 S(3)	2.07334	–21
2.08939	Fe II	$3d^6(^3F_1)4s c^4F_{3/2} - 3d^6(^5D)4p z^4F_{3/2}^\circ$	2.08938	–1
2.11259	He I	$1s4s ^3S_1 - 1s3p ^3P_1^\circ$	2.11251	–11

TABLE B.1 – *Continued.*

λ_{lab} [μm]	Species	Transition (upper – lower)	λ_{obs} [μm]	Offset [km s^{-1}]
2.12183	H ₂	1–0 S(1)	2.12170	–18
2.12801	H ₂	3–2 S(4)	2.12784	–25
2.15422	H ₂	2–1 S(2)	2.15408	–20
2.16612	H I	7 – 4 Br γ	2.16597	–20
2.20140	H ₂	3–2 S(3)	2.20121	–26
2.22329	H ₂	1–0 S(0)	2.22317	–16
2.24772	H ₂	2–1 S(1)	2.24759	–17
2.28704	H ₂	3–2 S(2)	2.28684	–26
2.29350	CO	2–0		
2.32270	CO	3–1		
2.34445	H ₂	4–3 S(3)	2.34443	–2
2.35560	H ₂	2–1 S(0)	2.35542	–23
2.36035	H I	27 – 5 Pf27	2.36009	–32
2.36694	H I	26 – 5 Pf26	2.36683	–14
2.37438	H I	25 – 5 Pf25	2.37420	–23
2.38282	H I	24 – 5 Pf24	2.38267	–20
2.38647	H ₂	3–2 S(1)	2.38639	–9
2.39247	H I	23 – 5 Pf23	2.39236	–13
2.40355	H I	22 – 5 Pf22	2.40350	–6
2.40659	H ₂	1–0 Q(1)	2.40652	–8
2.41344	H ₂	1–0 Q(2)	2.41334	–13
2.41639	H I	21 – 5 Pf21	2.41626	–16
2.42373	H ₂	1–0 Q(3)	2.42363	–12
2.43749	H ₂	1–0 Q(4)	2.43738	–14
2.44900	H I	19 – 5 Pf19	2.44885	–19
2.45475	H ₂	1–0 Q(5)	2.45463	–15
2.46999	H I	18 – 5 Pf18	2.46981	–21
2.47556	H ₂	1–0 Q(6)	2.47544	–14
2.49525	H I	17 – 5 Pf17	2.49507	–23
2.49995	H ₂	1–0 Q(7)	2.49985	–12
2.50148	H ₂	3–2 S(0)	2.50148	0
2.52609	H I	16 – 5 Pf16	2.52596	–16
2.52804	H ₂	1–0 Q(8)	2.52769	–42
2.54151	H ₂	4–3 S(1)	2.54135	–19
2.55099	H ₂	2–1 Q(1)	2.55088	–12
2.55851	H ₂	2–1 Q(2)	2.55841	–12
2.55985	H ₂	1–0 Q(9)	2.55976	–11
2.56433	H I	15 – 5 Pf15	2.56419	–16
2.56983	H ₂	2–1 Q(3)	2.56971	–15
2.58496	H ₂	2–1 Q(4)	2.58490	–7

TABLE B.1 – *Continued.*

λ_{lab} [μm]	Species	Transition (upper – lower)	λ_{obs} [μm]	Offset [km s^{-1}]
2.60398	H ₂	2–1 Q(5)	2.60386	–14
2.61265	H I	14 – 5 Pf14	2.61250	–17
2.61921	He I	$1s6f \ ^3F_{2,3,4} - 1s4d \ ^3D_{1,2,3}$	2.61910	–13
2.62587	H I	6 – 4 Br β	} 2.62577	–11
2.62688	H ₂	1–0 O(2)		–126
2.62692	H ₂	2–1 Q(6)		–131
2.63512	H ₂	1–0 Q(11)	2.63494	–21
2.65383	H ₂	2–1 Q(7)	2.65376	–8
2.67513	H I	13 – 5 Pf13	2.67500	–14
2.71030	H ₂	3–2 Q(1)	2.71015	–17
2.71866	H ₂	3–2 Q(2)	2.71855	–13
2.72010	H ₂	2–1 Q(9)	2.71999	–12
2.73124	H ₂	3–2 Q(3)	2.73113	–12
2.75827	H I	12 – 5 Pf12	2.75813	–15
2.76926	H ₂	3–2 Q(5)	2.76920	–7
2.78616	H ₂	2–1 O(2)	2.78610	–7
2.80250	H ₂	1–0 O(3)	2.80242	–8
NIRSpec F290LP/G395H				
2.87300	H I	11 – 5 Pf11	2.87272	–28
2.88824	H ₂	4–3 Q(1)	2.88800	–24
2.89330	O I	$2s^22p^3(^4S^\circ)4p \ ^3P_0 - 2s^22p^3(^4S^\circ)4s \ ^3S_1^\circ$	} 2.89320	–11
2.89352		$2s^22p^3(^4S^\circ)4p \ ^3P_2 - 2s^22p^3(^4S^\circ)4s \ ^3S_1^\circ$		–33
2.89359		$2s^22p^3(^4S^\circ)4p \ ^3P_1 - 2s^22p^3(^4S^\circ)4s \ ^3S_1^\circ$		–41
2.89937	H ₂	3–2 Q(9)	2.89838	–103
2.91188	H ₂	4–3 Q(3)	2.91184	–4
2.97406	H ₂	2–1 O(3)	2.97383	–23
3.00387	H ₂	1–0 O(4)	3.00362	–25
3.03920	H I	10 – 5 Pf10	3.03892	–27
3.08132	Fe II	$3d^6(^3P_1)4s \ ^4P_{5/2} - 3d^6(^5D)4p \ ^4P_{5/2}^\circ$	3.08114	–18
3.09854	O I	$2s^22p^3(^4S^\circ)4d \ ^3D^\circ - 2s^22p^3(^4S^\circ)4p \ ^3P_2$	3.09828	–21
3.16377	H ₂	3–2 O(3)	3.16352	–24
3.23499	H ₂	1–0 O(5)	3.23473	–24
3.29699	H I	9 – 5 Pf9	3.29671	–26
3.37646	H ₂	4–3 O(3)	3.37601	–40
3.39582	H ₂	3–2 O(4)	3.39495	–76
3.43787	H ₂	2–1 O(5)	3.43768	–16
3.45285	H I	27 – 6 Hu27	3.45268	–15
3.46697	H I	26 – 6 Hu26	3.46662	–31
3.48296	H I	25 – 6 Hu25	3.48254	–36

TABLE B.1 – *Continued.*

λ_{lab} [μm]	Species	Transition (upper – lower)	λ_{obs} [μm]	Offset [km s^{-1}]
3.48580	H ₂	0–0 S(17)	3.48254	–31
3.50081	H ₂	1–0 O(6)	3.50069	–18
3.50116	H I	24 – 6 Hu24	3.50069	–41
3.52203	H I	23 – 6 Hu23	3.52181	–18
3.54610	H I	22 – 6 Hu22	} 3.54611	+1
3.54759	H ₂	0–0 S(16)		–125
3.57410	H I	21 – 6 Hu21	3.57371	–33
3.60697	H I	20 – 6 Hu20	3.60672	–21
3.64592	H I	19 – 6 Hu19	3.64563	–24
3.69263	H I	18 – 6 Hu18	3.69233	–25
3.74056	H I	8 – 5 Pf γ	3.74028	–22
3.74939	H I	17 – 6 Hu17	3.74906	–26
3.81945	H I	16 – 6 Hu16	3.81906	–30
3.84611	H ₂	0–0 S(13)	3.84588	–18
3.90755	H I	15 – 6 Hu15	3.90726	–22
3.99615	H ₂	0–0 S(12)	3.99601	–10
4.02087	H I	14 – 6 Hu14	4.02044	–32
4.03772	He I	$1s5f$ $^3\text{F}_{2,3,4}^{\circ}$ – $1s4d$ $^3\text{D}_{1,2,3}$	4.03751	–16
4.04093	He I	$1s5f$ $^1\text{F}_3^{\circ}$ – $1s4d$ $^1\text{D}_2$	4.04063	–23
4.05226	H I	5 – 4 Br α	4.05205	–16
4.17079	H I	13 – 6 Hu13	4.17049	–22
4.18108	H ₂	0–0 S(11)	4.18086	–16
4.29592	He I	$1s3p$ $^3\text{P}_1^{\circ}$ – $1s3p$ $^3\text{S}_1$	4.29563	–20
4.37645	H I	12 – 6 Hu12	4.37617	–19
4.40979	H ₂	0–0 S(10)	4.40951	–19
4.41667	H ₂	1–1 S(11)	4.41633	–23
4.61802	[K III]	$3s^23p^5$ $^2\text{P}_{1/2}^{\circ}$ – $3s^23p^5$ $^2\text{P}_{3/2}^{\circ}$	4.61741	–40
4.65378	H I	7 – 5 Pf β	4.65352	–17
4.67251	H I	11 – 6 Hu ϵ	} 4.67224	–17
4.67195	[Fe II]	$3d^7$ $a^4\text{F}_{3/2}$ – $3d^6(^5\text{D})4s$ $a^6\text{D}_{1/2}$		+19
4.69461	H ₂	0–0 S(9)	4.69441	–13
4.84769	H I	25 – 7	4.84735	–21
4.95419	H ₂	1–1 S(9)	4.95382	–23
4.97088	H I	22 – 7	4.97026	–40
?	?	?	5.00102	-
?	?	?	5.00098	-
5.02609	H I	21 – 7	5.02556	–32
5.05312	H ₂	0–0 S(8)	5.05290	–13
5.09132	H I	20 – 7	5.09118	–8
5.12866	H I	10 – 6 Hu δ	5.12842	–14

TABLE B.1 – *Continued.*

λ_{lab} [μm]	Species	Transition (upper – lower)	λ_{obs} [μm]	Offset [km s^{-1}]
5.16928	H I	19 – 7	5.16894	–20
?	?	?	5.21667	–
5.23885	H ₂	2–2 S(9)	5.23928	+25
5.26368	H I	18 – 7	5.26305	–36
MIRI/MRS 1A				
4.92370	H I	23 – 7	4.92364	–5
4.95419	H ₂	1–1 S(9)	4.95401	–11
4.97088	H I	22 – 7	4.97067	–13
5.02609	H I	21 – 7	5.02586	–13
5.05312	H ₂	0–0 S(8)	5.05290	–13
5.09132	H I	20 – 7	5.09113	–11
5.12866	H I	10 – 6 H α	5.12842	–14
5.16928	H I	19 – 7	5.16900	–16
5.26368	H I	18 – 7	5.26344	–14
5.33014	H ₂	1–1 S(8)	5.33004	–6
5.34017	[Fe II]	$3d^7 a^4F_{9/2} - 3d^6(^5D)4s a^6D_{9/2}$	5.33997	–11
MIRI/MRS 1B				
5.37977	H I	17 – 7	5.37961	–9
5.51116	H ₂	0–0 S(7)	5.51110	–3
5.52519	H I	16 – 7	5.52506	–7
5.71146	H I	15 – 7	5.71121	–13
5.81092	H ₂	1–1 S(7)	5.81064	–14
5.90821	H I	9 – 6 H γ	5.90789	–17
5.95684	H I	14 – 7	5.95652	–16
5.98200	[K IV]	$3s^23p^4 ^3P_1 - 3s^23p^4 ^3P_2$	5.98225	+13
6.10856	H ₂	0–0 S(6)	6.10825	–15
6.29192	H I	13 – 7	6.29155	–17
6.50098	H I	25 – 8	6.50061	–17
MIRI/MRS Channel 1C				
6.56469	H I	24 – 8	6.56453	–7
6.77199	H I	12 – 7	6.77165	–15
6.82588	H I	21 – 8	6.82571	–7
6.90952	H ₂	0–0 S(5)	6.90918	–15
6.98527	[Ar II]	$3s^23p^5 ^2P_{1/2}^{\circ} - 3s^23p^5 ^2P_{3/2}^{\circ}$	6.98495	–14
7.09271	H I	19 – 8	7.09222	–21
7.27165	H I	18 – 8	7.27136	–12
7.28006	H ₂	1–1 S(5)	7.27963	–18

TABLE B.1 – *Continued.*

λ_{lab} [μm]	Species	Transition (upper – lower)	λ_{obs} [μm]	Offset [km s^{-1}]
7.31770	[Na III]	$2s^22p^5 \ ^2P_{1/2}^{\circ} - 2s^22p^5 \ ^2P_{3/2}^{\circ}$	7.31721	-20
7.45986	H I	6 – 5 Pf α	7.46197	+85
7.50249	H I	8 – 6 Hu β	7.50207	-17
7.50810	H I	11 – 7	} 7.50774	-17
7.50658	[Ni I]	$3d^8(^3F)4s^2 \ ^3F_3 - 3d^8(^3F)4s^2 \ ^3F_4$		-14
MIRI/MRS Channel 2A				
7.78037	H I	16 – 8	7.77999	-15
8.02505	H ₂	0–0 S(4)	8.02504	0
8.15489	H I	15 – 8	8.15486	-1
?	?	?	8.40904	-
8.66450	H I	14 – 8	8.66407	-15
MIRI/MRS Channel 2B				
8.72056	H I	23 – 9	8.72001	-19
8.76006	H I	10 – 7	8.75988	-6
8.99138	[Ar III]	$3s^23p^4 \ ^3P_1 - 3s^23p^4 \ ^3P_2$	8.99084	-18
9.39202	H I	13 – 8	9.39168	-11
9.66491	H ₂	0–0 S(3)	9.66461	-9
MIRI/MRS Channel 2C				
10.51050	[S IV]	$3s^23p \ ^2P_{3/2}^{\circ} - 3s^23p \ ^2P_{1/2}^{\circ}$	10.50989	-17
11.30750	[Ni I]	$3d^8(^3F)4s^2 \ ^3F_2 - 3d^8(^3F)4s^2 \ ^3F_3$	} 11.30809	+15
11.30870	H I	9 – 7		-16
MIRI/MRS Channel 3A				
11.76190	[Cl IV]	$3s^23p^2 \ ^3P_2 - 3s^23p^2 \ ^3P_1$	11.76177	-3
12.27861	H ₂	0–0 S(2)	12.27838	-5
12.37190	H I	7 – 6 Hu α	12.37159	-7
12.38717	H I	11 – 8	12.38682	-8
12.58708	H I	14 – 9	12.58649	-14
12.61097	H I	19 – 10	12.61062	-8
12.81355	[Ne II]	$2s^22p^5 \ ^2P_{1/2}^{\circ} - 2s^22p^5 \ ^2P_{3/2}^{\circ}$	12.81342	-3
MIRI/MRS Channel 3B				
14.18308	H I	13 – 9	14.18190	-25
14.36780	[Cl II]	$3s^23p^4 \ ^3P_1 - 3s^23p^4 \ ^3P_2$	14.36621	-33
MIRI/MRS Channel 3C				
15.55510	[Ne III]	$2s^22p^4 \ ^3P_1 - 2s^22p^4 \ ^3P_2$	15.55573	+12
?	?	?	15.75329	-

TABLE B.1 – *Continued.*

λ_{lab} [μm]	Species	Transition (upper – lower)	λ_{obs} [μm]	Offset [km s^{-1}]
16.20910	H I	10 – 8	16.20854	–10
16.88063	H I	12 – 9	16.88004	–11
17.03500	H ₂	0–0 S(1)	17.03446	–10
17.88500	[P III]	$3s^23p \ ^2P_{3/2}^{\circ} - 3s^23p \ ^2P_{1/2}^{\circ}$	17.88568	+11
17.93595	[Fe II]	$3d^7 \ a^4F_{7/2} - 3d^7 \ a^4F_{9/2}$	17.93598	0
MIRI/MRS Channel 4A				
18.71300	[S III]	$3s^23p^2 \ ^3P_2 - 3s^23p^2 \ ^3P_1$	18.71267	–5
19.06190	H I	8 – 7	19.06151	–6
MIRI/MRS Channel 4B				
21.83020	[Ar III]	$3s^23p^4 \ ^3P_0 - 3s^23p^4 \ ^3P_1$	21.83066	+6
22.33157	H I	13 – 10	} 22.33746	–40
22.34046	H I	11 – 9		+79
22.92500	[Fe III]	$3d^6 \ ^5D_4 - 3d^6 \ ^5D_3$	22.92856	+47
MIRI/MRS Channel 4C				
25.98829	[Fe II]	$3d^6(^5D)4s \ a^6D_{9/2} - 3d^6(^5D)4s \ a^6D_{7/2}$	25.98769	–7

C Continuum-subtracted Line Emission Maps

C.1 Fluorescent Fe II transitions

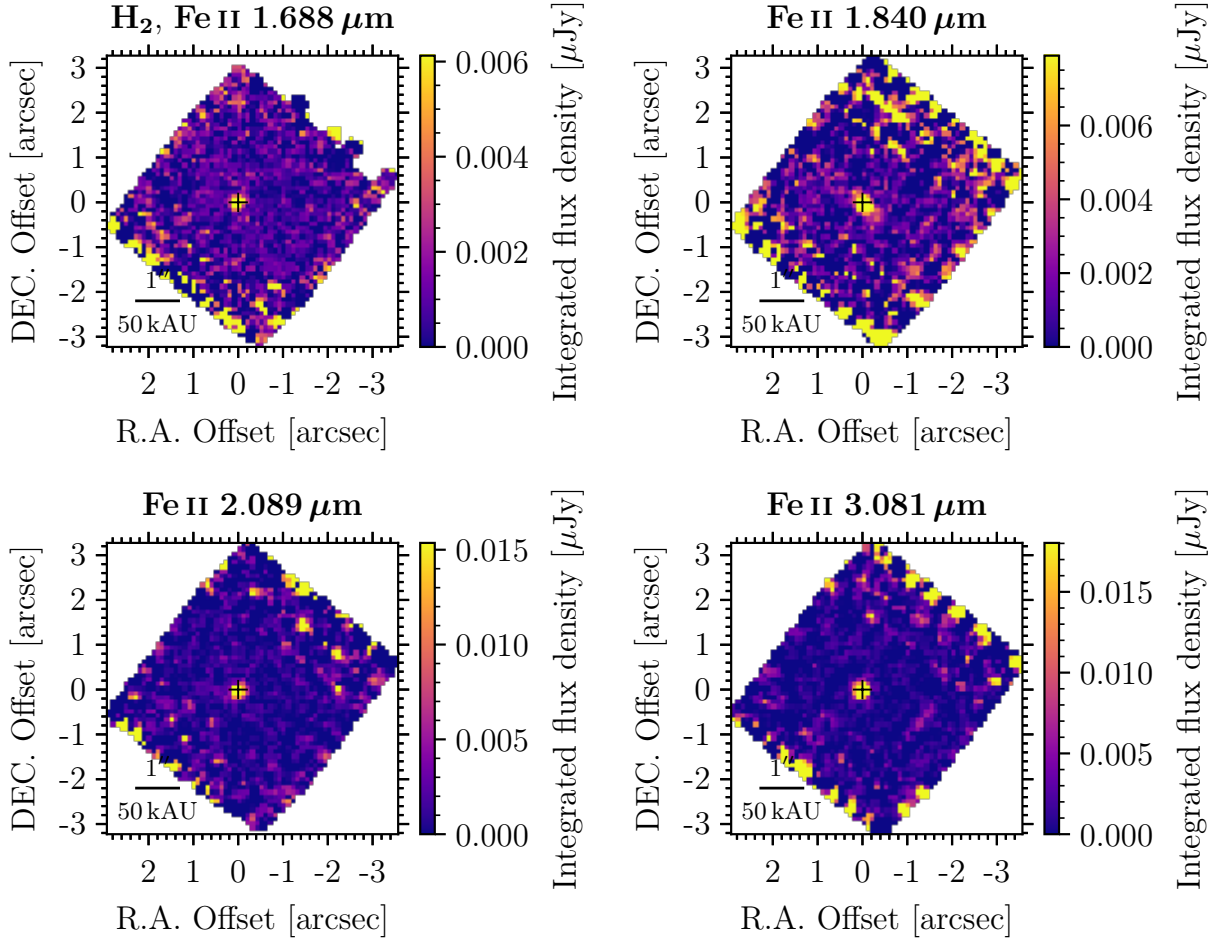


FIGURE C.1 – **Upper left:** M0 map of the H₂ 1–0S(9) and fluorescent Fe II $c^4F_{9/2} - z^4F_{9/2}^{\circ}$ transition at 1.68776 μm and 1.68778 μm , respectively. This line is probably a blend of both contributions as other Fe II transitions at 1.840 μm ($c^4F_{7/2} - z^4F_{7/2}^{\circ}$; **upper right**) and 2.089 μm ($c^4F_{3/2} - z^4F_{3/2}^{\circ}$; **lower right**) originating from the same multiplet are also observed. Similarly, the presence of the ro-vibrational line H₂ 1–0Q(11) at 2.635 μm originating from the same upper level as H₂ 1–0S(9) cannot exclude the presence of the latter transition. **Lower right:** M0 map of Fe II 3.08132 μm $c^4P_{5/2} - z^4P_{5/2}^{\circ}$.

C.2 NIR [Fe II] and O I knot-tracing lines

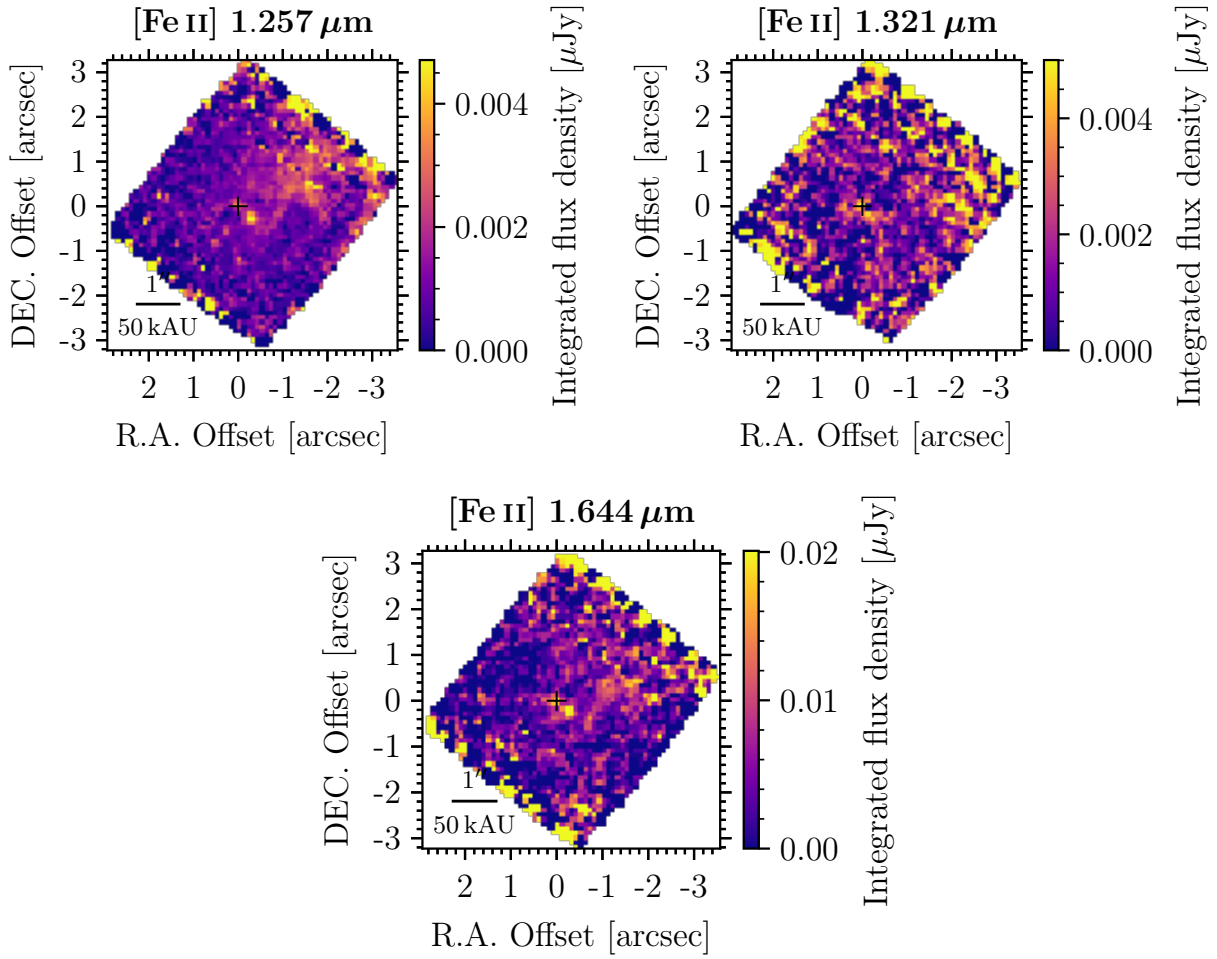


FIGURE C.2 – Moment 0 maps showing the three NIR [Fe II] knot-tracing emission lines at 1.257 μm ($a^4D_{7/2} - a^6D_{9/2}$), 1.321 μm ($a^4D_{7/2} - a^6D_{7/2}$) and 1.644 μm ($a^4D_{7/2} - a^4F_{9/2}$).

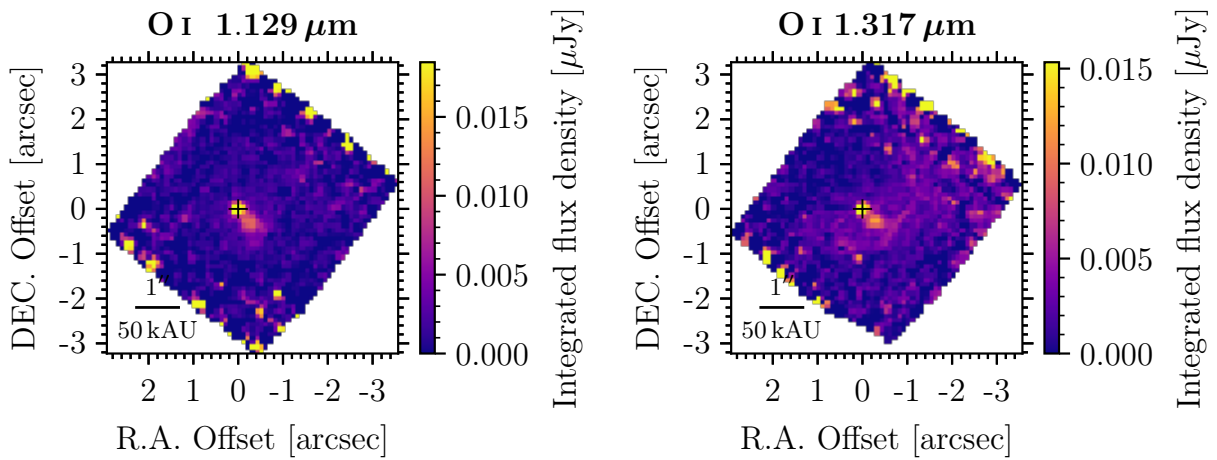


FIGURE C.3 – Moment 0 maps showing two NIR fluorescent O I knot-tracing emission lines at 1.129 μm ($^3D_1^\circ - ^3P_0^\circ$) and 1.32 μm ($^3S_1^\circ - ^3P_1$). The 2.89 μm ($^3P_J - ^3S_1^\circ$) transition discussed in the text is shown in Fig. 9.6.

C.3 Electric-dipole forbidden transitions

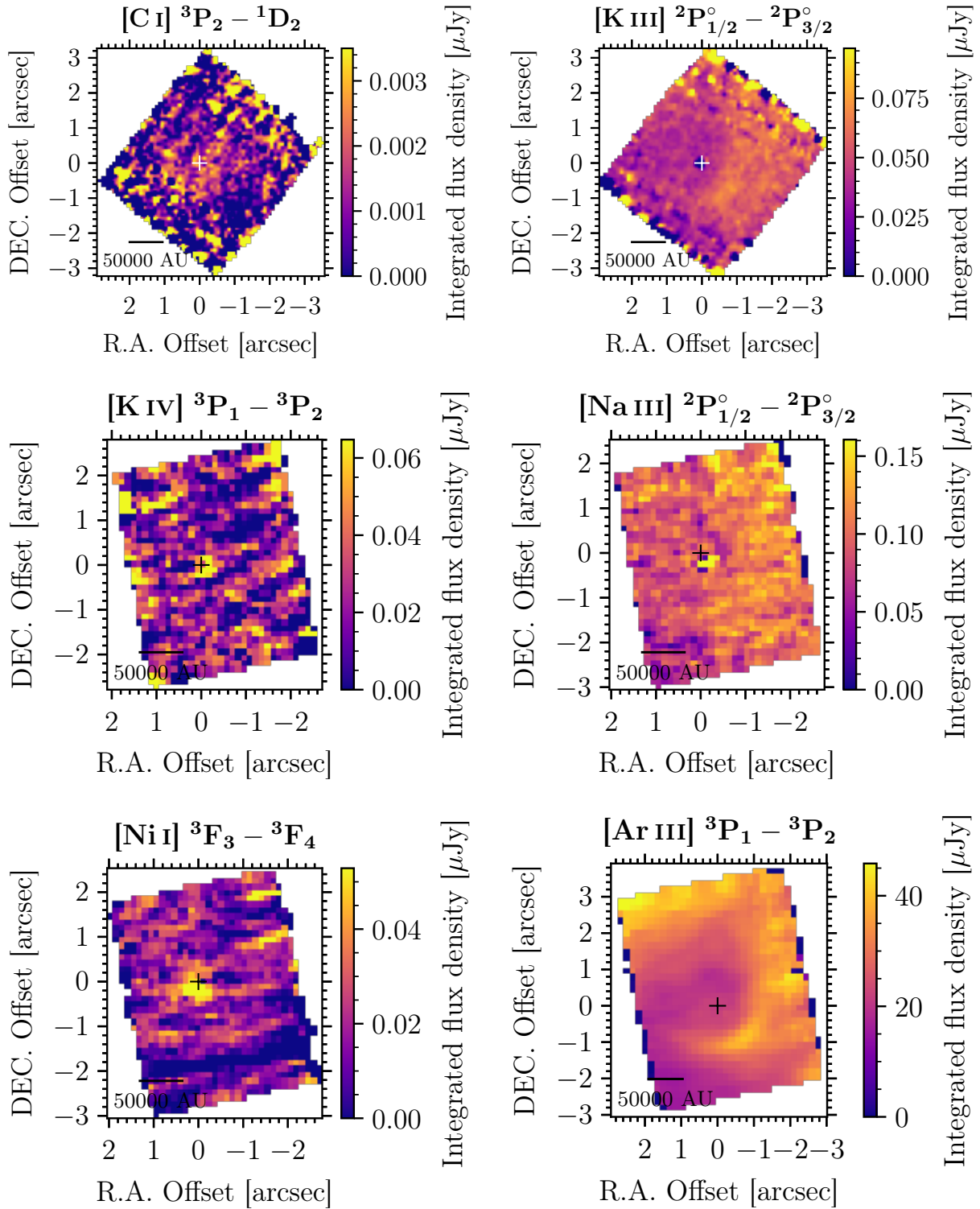


FIGURE C.4 – Moment 0 maps showing the emission regions of the observed electric-dipole forbidden transitions.

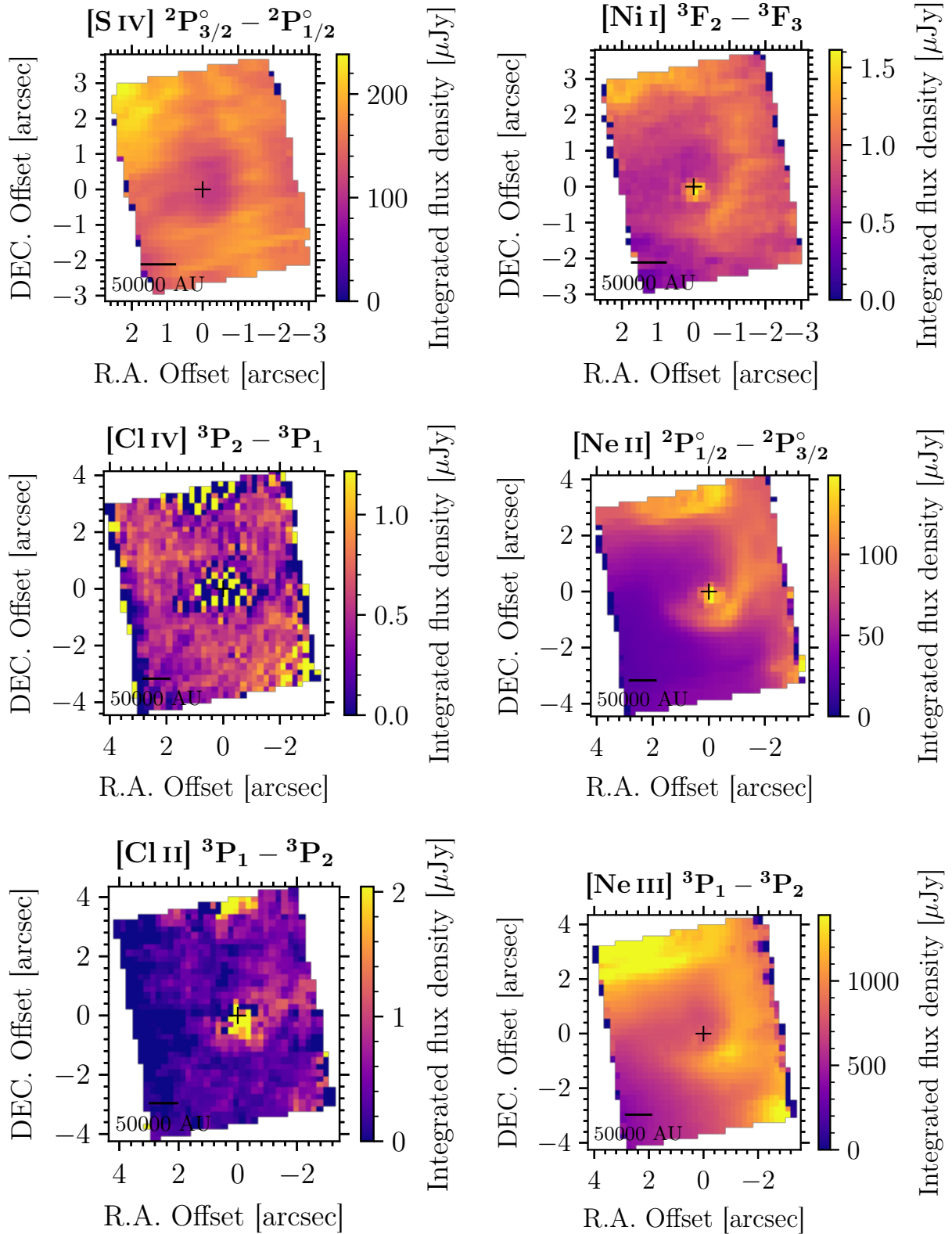


FIGURE C.4 – Moment 0 maps showing the emission regions of the observed electric-dipole forbidden transitions. The [Cl IV] transitions suffers from undersampling of the MIRI/MRS 3A PSF (for more details see [Nisini et al. 2024](#), Sect. 2.4).

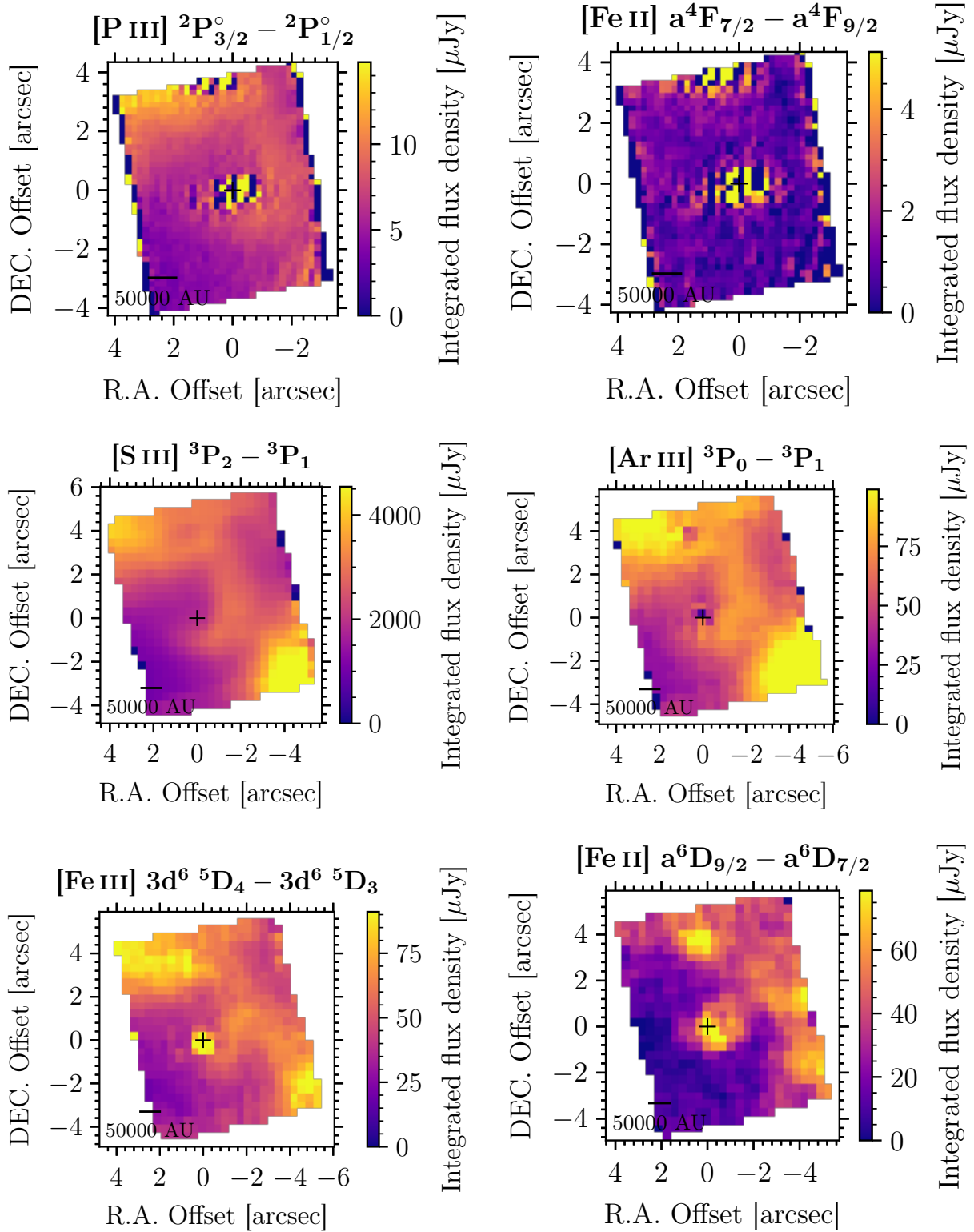


FIGURE C.4 – Moment 0 maps showing the emission regions of the observed electric-dipole forbidden transitions. The [P III] and [Fe II] transitions (first row) suffers from undersampling of the MIRI/MRS 3C PSF (for more details see [Nisini et al. 2024](#), Sect. 2.4).

C.4 Unidentified transitions

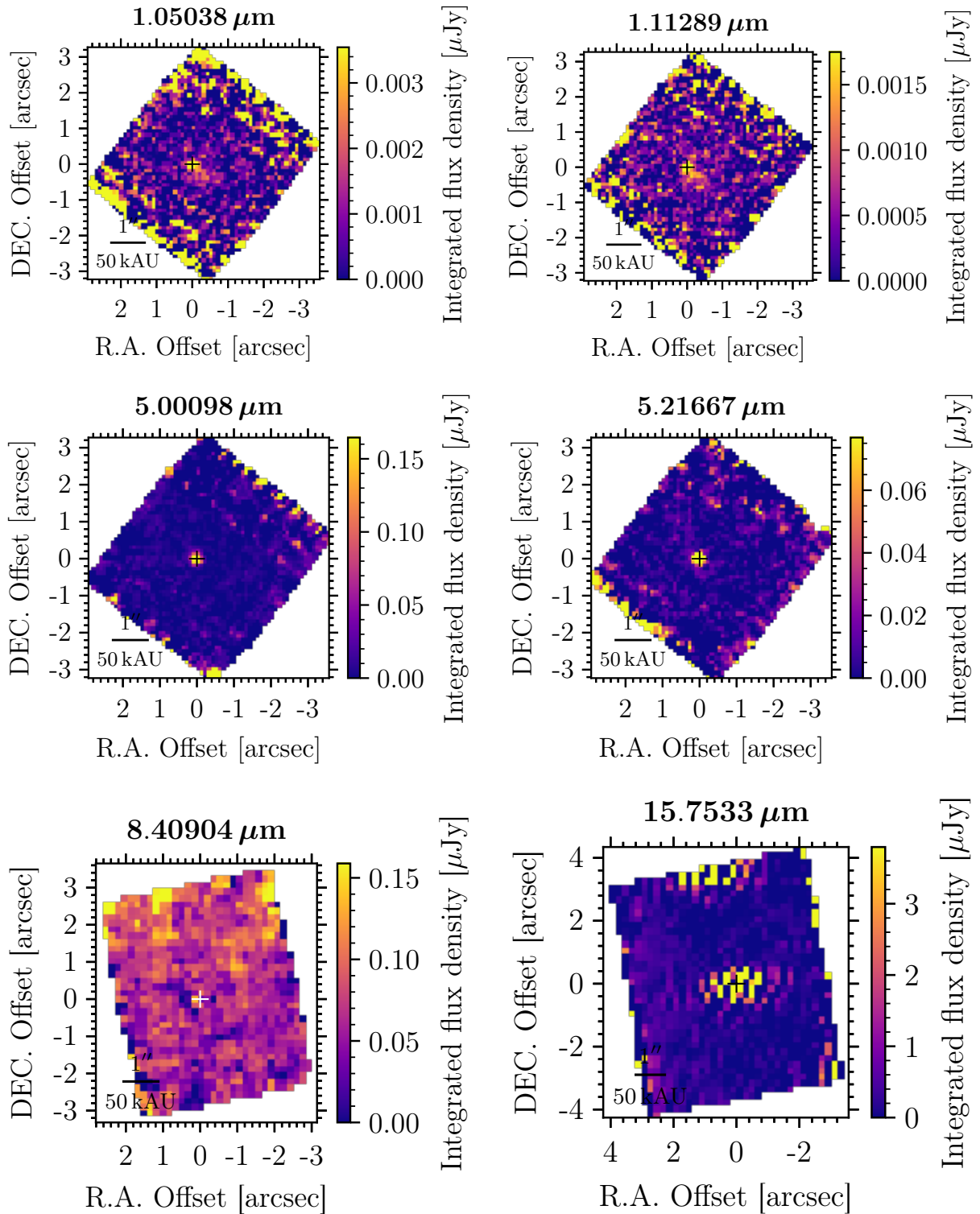


FIGURE C.5 – Moment 0 maps of yet unidentified emission lines.

D Ionisation potentials of observed atoms

TABLE D.1 – Ionisation energies for elements observed in the spectrum of S7A. The second column gives the first $E_{\text{I} \rightarrow \text{II}}$ to ionise a neutral atom, the third column the ionisation energy $E_{\text{II} \rightarrow \text{III}}$ to remove a further electron from the single-ionised ion and the fourth the energy required to obtain a +3-ion from a +2-ion (Draine 2011, appendix D). The relevant ionisation energies based on the observed lines in the spectrum are reported in black. Those of higher ionisation stages not observed are shown in gray and given for completeness. Nitrogen (N) is included as it has been previously detected in HST images of S7A (Walborn et al. 2002).

Species	$E_{\text{I} \rightarrow \text{II}}$ [eV]	$E_{\text{II} \rightarrow \text{III}}$ [eV]	$E_{\text{III} \rightarrow \text{IV}}$ [eV]
H	13.5984		
He	24.5874	54.416	
O	13.6181	35.121	54.936
N	14.5341	29.601	47.449
Ne	21.5645	40.963	63.423
Na	5.1391	47.286	71.620
Mg	7.6462	15.035	80.144
Si	8.1517	16.346	33.493
P	10.4867	19.769	30.203
S	10.3600	23.338	34.790
Cl	12.9676	23.814	39.911
Ar	15.7596	27.630	40.735
K	4.3407	31.628	45.806
Fe	7.9024	16.188	30.651
Ni	7.6398	18.169	35.187

E Line Flux Densities

E.1 Fit results

TABLE E.1 – Calculated line fluxes for the observed lines in Tab. B.1 for the region of the YSO S7A ($r_{\text{init,NIRSpec}} = 0''.2$ and scaled by 0.91 and $r_{\text{init,MIRI}} = 0''.3$; see Tab. A.1 and Sect. 9.3.1). Lines observed in multiple NIRSpec bands are reported only once and attributed to the longer wavelength channel. The transitions are abbreviated. For the full configuration see Tab. B.1. For unidentified lines, the observed instead of the vacuum wavelength is given.

λ_{lab} [μm]	Species	Transition	F [$\text{erg s}^{-1} \text{cm}^{-2}$]	δF [$\text{erg s}^{-1} \text{cm}^{-2}$]	FWHM [μm]	FWHM [km s^{-1}]	Δv [km s^{-1}]
NIRSpec F100LP/G140H							
0.98530	[C I]	$^3\text{P}_2 - ^1\text{D}_2$	8.85×10^{-17}	3.30×10^{-17}	4.14×10^{-4}	126	+19
1.00521	H I	P δ	1.75×10^{-15}	9.34×10^{-17}	4.22×10^{-4}	126	+19
1.02896	[S II]	$^2\text{P}_{3/2}^{\circ} - ^2\text{D}_{3/2}^{\circ}$	6.43×10^{-17}	1.31×10^{-17}	4.32×10^{-4}	126	+19
1.03233	[S II]	$^2\text{P}_{3/2}^{\circ} - ^2\text{D}_{5/2}^{\circ}$	9.08×10^{-17}	1.53×10^{-17}	4.34×10^{-4}	126	+19
1.03392	[S II]	$^2\text{P}_{1/2}^{\circ} - ^2\text{D}_{3/2}^{\circ}$	6.65×10^{-17}	1.73×10^{-17}	4.34×10^{-4}	126	+19
1.03733	[S II]	$^2\text{P}_{1/2}^{\circ} - ^2\text{D}_{5/2}^{\circ}$	3.09×10^{-17}	1.78×10^{-17}	4.36×10^{-4}	126	+19
1.05038	?	?	1.04×10^{-16}	2.32×10^{-17}	4.41×10^{-4}	126	+19
1.08332	He I	$^3\text{P}_1^{\circ} - ^3\text{S}_1$	6.21×10^{-15}	1.96×10^{-16}	4.56×10^{-4}	126	+9
1.09160	He I	$^3\text{F}_3^{\circ} - ^3\text{D}_2$	1.35×10^{-16}	1.54×10^{-17}	4.59×10^{-4}	126	+10
1.09411	H I	P γ	3.49×10^{-15}	1.19×10^{-16}	4.60×10^{-4}	126	+9
1.11286?	Fe II?	$b^4\text{G}_{5/2} - z^4\text{F}_{3/2}^{\circ}$	1.25×10^{-16}	1.18×10^{-17}	4.68×10^{-4}	126	+9
1.12904	O I	$^3\text{D}_1^{\circ} - ^3\text{P}_0^{\circ}$	4.68×10^{-16}	2.95×10^{-17}	4.75×10^{-4}	126	+9
1.13043	H ₂	3–1 S(7)	3.05×10^{-17}	2.94×10^{-17}	4.75×10^{-4}	126	+9
1.19724	He I	$^3\text{D}_2 - ^3\text{P}_1^{\circ}$	9.27×10^{-17}	1.60×10^{-17}	5.00×10^{-4}	125	+8
1.23299	H ₂	3–1 S(1)	6.22×10^{-17}	9.96×10^{-18}	5.15×10^{-4}	125	+8
1.23834	H ₂	2–0 Q(1)	6.30×10^{-17}	5.16×10^{-18}	5.17×10^{-4}	125	+8
1.25309	He I	$^3\text{P}_1^{\circ} - ^3\text{S}_1$	1.03×10^{-16}	9.73×10^{-18}	5.24×10^{-4}	125	+15
1.25702	[Fe II]	$a^4\text{D}_{7/2} - a^6\text{D}_{9/2}$	1.54×10^{-16}	1.13×10^{-17}	5.25×10^{-4}	125	+15
1.27884	He I	$^3\text{P}_1^{\circ} - ^3\text{S}_1$	3.58×10^{-16}	3.29×10^{-17}	5.34×10^{-4}	125	+15
1.28216	H I	P β	9.44×10^{-15}	1.82×10^{-16}	5.36×10^{-4}	125	+15
1.31068	H ₂	5–3 S(5)	4.07×10^{-17}	1.01×10^{-17}	5.48×10^{-4}	125	+15
1.31156	H ₂	4–2 S(1)	5.28×10^{-17}	1.04×10^{-17}	5.48×10^{-4}	125	+15
1.31675	O I	$^3\text{S}_1^{\circ} - ^3\text{P}_1$	3.28×10^{-16}	4.05×10^{-17}	5.50×10^{-4}	125	+15
1.32091	[Fe II]	$a^4\text{D}_{7/2} - a^6\text{D}_{7/2}$	6.50×10^{-17}	1.52×10^{-17}	5.56×10^{-4}	126	+15
1.48699	H ₂	2–0 O(6)	4.24×10^{-17}	1.40×10^{-17}	6.23×10^{-4}	125	+11
1.49155	H I	Br27	5.98×10^{-17}	1.92×10^{-17}	6.25×10^{-4}	125	+11
1.49293	H ₂	5–3 Q(1)	2.70×10^{-17}	1.26×10^{-17}	6.25×10^{-4}	125	+11
1.49418	H I	Br26	6.71×10^{-17}	1.43×10^{-17}	6.26×10^{-4}	125	+11
1.49714	H I	Br25	1.16×10^{-16}	1.90×10^{-17}	6.27×10^{-4}	125	+11
1.50050	H I	Br24	1.19×10^{-16}	2.35×10^{-17}	6.29×10^{-4}	125	+11

TABLE E.1 – *Continued.*

λ_{lab} [μm]	Species	Transition	F [$\text{erg s}^{-1} \text{cm}^{-2}$]	δF [$\text{erg s}^{-1} \text{cm}^{-2}$]	FWHM [μm]	FWHM [km s^{-1}]	Δv [km s^{-1}]
1.50431	H I	Br23	1.44×10^{-16}	3.05×10^{-17}	6.30×10^{-4}	125	+11
1.50869	H I	Br22	1.82×10^{-16}	2.12×10^{-17}	6.32×10^{-4}	125	+11
1.50987	H ₂	4–2 O(3)	8.03×10^{-17}	1.96×10^{-17}	6.33×10^{-4}	125	+11
1.52647	H I	Br19	2.39×10^{-16}	3.53×10^{-17}	6.39×10^{-4}	125	+11
1.53460	H I	Br18	3.11×10^{-16}	4.25×10^{-17}	6.42×10^{-4}	125	+15
1.54431	H I	Br17	3.50×10^{-16}	4.30×10^{-17}	6.46×10^{-4}	125	+15
1.55607	H I	Br16	3.57×10^{-16}	5.53×10^{-17}	6.51×10^{-4}	125	+15
1.57050	H I	Br15	4.64×10^{-16}	5.10×10^{-17}	6.57×10^{-4}	125	+15
1.58849	H I	Br14	5.45×10^{-16}	4.66×10^{-17}	6.65×10^{-4}	125	+15
1.61137	H I	Br13	6.53×10^{-16}	6.38×10^{-17}	6.75×10^{-4}	125	+15
1.64117	H I	Br12	8.42×10^{-16}	6.21×10^{-17}	6.90×10^{-4}	126	+12
1.64400	[Fe II]	$a^4D_{7/2} - a^4F_{9/2}$	2.96×10^{-16}	4.89×10^{-17}	6.91×10^{-4}	126	+12
1.681111	H I	Br11	1.08×10^{-15}	1.17×10^{-16}	7.00×10^{-4}	124	+12
1.68776	H ₂	1–0 S(9)	3.96×10^{-16}	2.41×10^{-17}	7.03×10^{-4}	124	+12
1.70071	He I	$^3D_2 - ^3P_1^{\circ}$	2.53×10^{-16}	2.43×10^{-17}	7.08×10^{-4}	124	+12
1.736685	H I	Br10	1.46×10^{-15}	7.18×10^{-17}	7.29×10^{-4}	125	+12
1.74188	Fe II	$c^4F_{7/2} - z^4D_{7/2}^{\circ}$	1.25×10^{-16}	2.10×10^{-17}	7.32×10^{-4}	125	+12
1.74796	H ₂	1–0 S(7)	1.13×10^{-16}	3.51×10^{-17}	7.34×10^{-4}	125	+12
1.817908	H I	Br ϵ	1.98×10^{-15}	7.68×10^{-17}	6.64×10^{-4}	109	+8
1.83576	H ₂	1–0 S(5)	2.63×10^{-16}	1.86×10^{-17}	6.70×10^{-4}	109	+8
1.840169	Fe II	$c^4F_{7/2} - z^4F_{7/2}^{\circ}$	1.60×10^{-16}	4.04×10^{-17}	6.72×10^{-4}	109	+8
1.85282	H ₂	2–1 S(7)	6.08×10^{-17}	3.32×10^{-17}	6.77×10^{-4}	109	+8
1.86903	He I	$^3F_3^{\circ} - ^3D_2$	1.27×10^{-15}	7.42×10^{-17}	6.83×10^{-4}	109	+5
1.875613	H I	P α	4.99×10^{-14}	7.50×10^{-16}	6.85×10^{-4}	109	+8
NIRSpec F170LP/G235H							
1.68111	H I	Br11	1.04×10^{-15}	1.45×10^{-16}	8.76×10^{-4}	156	+22
1.68776	H ₂	1–0 S(9)	3.60×10^{-16}	3.89×10^{-17}	8.79×10^{-4}	156	+22
1.70071	He I	$^3D_2 - ^3P_1^{\circ}$	2.61×10^{-16}	2.12×10^{-17}	8.86×10^{-4}	156	+22
1.73669	H I	Br10	1.38×10^{-15}	1.22×10^{-16}	9.05×10^{-4}	156	+23
1.74188	Fe II	$c^4F_{7/2} - z^4D_{7/2}^{\circ}$	1.43×10^{-16}	5.31×10^{-17}	9.08×10^{-4}	156	+22
1.74796	H ₂	1–0 S(7)	1.11×10^{-16}	2.54×10^{-17}	9.11×10^{-4}	156	+23
1.81791	H I	Br ϵ	2.04×10^{-15}	1.06×10^{-16}	9.47×10^{-4}	156	+22
1.83576	H ₂	1–0 S(5)	2.35×10^{-16}	1.54×10^{-17}	9.57×10^{-4}	156	+20
1.84026	Fe II	$c^4F_{7/2} - z^4F_{7/2}^{\circ}$	2.57×10^{-16}	2.92×10^{-17}	9.59×10^{-4}	156	+36
1.85282	H ₂	2–1 S(7)	8.43×10^{-17}	4.14×10^{-17}	9.65×10^{-4}	156	+19
1.86903	He I	$^3F_3^{\circ} - ^3D_2$	1.37×10^{-15}	1.23×10^{-16}	9.74×10^{-4}	156	+19
1.87561	H I	P α	5.11×10^{-14}	8.15×10^{-16}	9.77×10^{-4}	156	+19
1.89194	H ₂	1–0 S(4)	1.07×10^{-16}	2.23×10^{-17}	9.86×10^{-4}	156	+19
1.90946	He I	$^1D_2 - ^1P_1^{\circ}$	9.10×10^{-17}	2.21×10^{-17}	9.95×10^{-4}	156	+20

TABLE E.1 – *Continued.*

λ_{lab} [μm]	Species	Transition	F [$\text{erg s}^{-1} \text{cm}^{-2}$]	δF [$\text{erg s}^{-1} \text{cm}^{-2}$]	FWHM [μm]	FWHM [km s^{-1}]	Δv [km s^{-1}]
1.94509	H I	Br δ	3.37×10^{-15}	1.04×10^{-16}	1.01×10^{-3}	156	+20
1.95482	He I	$^3\text{P}_J^\circ - ^3\text{D}_J$	1.52×10^{-16}	2.76×10^{-17}	1.02×10^{-3}	156	+20
1.95756	H ₂	1–0 S(3)	5.61×10^{-16}	2.89×10^{-17}	1.02×10^{-3}	156	+20
2.03376	H ₂	1–0 S(2)	2.75×10^{-16}	2.22×10^{-17}	9.91×10^{-4}	146	+13
2.05869	He I	$^1\text{P}_1^\circ - ^1\text{S}_0$	1.57×10^{-15}	8.12×10^{-17}	1.00×10^{-3}	146	+13
2.06558	H ₂	3–2 S(5)	5.87×10^{-17}	3.56×10^{-17}	1.01×10^{-3}	146	+14
2.07348	H ₂	2–1 S(3)	1.85×10^{-16}	2.87×10^{-17}	1.01×10^{-3}	146	+13
2.08939	Fe II	$c^4\text{F}_{3/2} - z^4\text{F}_{3/2}^\circ$	1.78×10^{-16}	2.60×10^{-17}	1.02×10^{-3}	146	+14
2.11259	He I	$^3\text{S}_1 - ^3\text{P}_1^\circ$	1.36×10^{-16}	2.87×10^{-17}	1.03×10^{-3}	146	+14
2.12183	H ₂	1–0 S(1)	8.54×10^{-16}	4.49×10^{-17}	1.03×10^{-3}	146	+13
2.12801	H ₂	3–2 S(4)	5.00×10^{-17}	1.71×10^{-17}	1.04×10^{-3}	146	+13
2.15422	H ₂	2–1 S(2)	7.53×10^{-17}	1.91×10^{-17}	1.05×10^{-3}	146	+16
2.16612	H I	Br γ	5.97×10^{-15}	9.85×10^{-17}	1.05×10^{-3}	146	+16
2.20140	H ₂	3–2 S(3)	1.02×10^{-16}	2.66×10^{-17}	1.07×10^{-3}	146	+16
2.22329	H ₂	1–0 S(0)	3.47×10^{-16}	3.86×10^{-17}	1.08×10^{-3}	146	+15
2.24772	H ₂	2–1 S(1)	2.24×10^{-16}	2.48×10^{-17}	1.09×10^{-3}	146	+15
2.28704	H ₂	3–2 S(2)	9.61×10^{-17}	2.08×10^{-17}	1.11×10^{-3}	146	+16
2.29350	CO	2–0	2.70×10^{-16}	7.64×10^{-17}	1.10×10^{-3}	146	+15
2.32270	CO	3–1	3.36×10^{-16}	8.31×10^{-17}	1.21×10^{-3}	156	–4
2.34445	H ₂	4–3 S(3)	1.48×10^{-16}	4.50×10^{-17}	1.23×10^{-3}	157	–4
2.35560	H ₂	2–1 S(0)	3.21×10^{-16}	1.55×10^{-16}	1.23×10^{-3}	157	–4
2.36035	H I	Pf27	2.32×10^{-16}	5.23×10^{-17}	1.23×10^{-3}	156	–3
2.36694	H I	Pf26	2.95×10^{-16}	4.07×10^{-17}	1.24×10^{-3}	157	–4
2.37438	H I	Pf25	1.19×10^{-16}	4.61×10^{-17}	1.24×10^{-3}	157	–4
2.38282	H I	Pf24	5.18×10^{-16}	9.55×10^{-17}	1.25×10^{-3}	156	–4
2.38647	H ₂	3–2 S(1)	$<3.06 \times 10^{-16}$	-	-	-	–4
2.39247	H I	Pf23	4.33×10^{-16}	5.61×10^{-17}	1.25×10^{-3}	156	–3
2.40355	H I	Pf22	8.10×10^{-16}	1.03×10^{-16}	1.26×10^{-3}	157	–3
2.40659	H ₂	1–0 Q(1)	1.88×10^{-15}	3.08×10^{-16}	1.26×10^{-3}	156	–4
2.41344	H ₂	1–0 Q(2)	} detector gap				
2.41639	H I	Pf21					
2.42373	H ₂	1–0 Q(3)					
2.43749	H ₂	1–0 Q(4)					
2.44900	H I	Pf19					
2.45475	H ₂	1–0 Q(5)	$<3.87 \times 10^{-15}$	-	-	-	+17
2.46999	H I	Pf18	7.60×10^{-16}	1.26×10^{-16}	1.28×10^{-3}	155	+17
2.47556	H ₂	1–0 Q(6)	7.84×10^{-17}	7.48×10^{-17}	1.28×10^{-3}	155	+17
2.49525	H I	Pf17	6.77×10^{-16}	8.01×10^{-17}	1.29×10^{-3}	155	+16
2.49995	H ₂	1–0 Q(7)	2.05×10^{-16}	5.40×10^{-17}	1.29×10^{-3}	155	+17
2.50148	H ₂	3–2 S(0)	$<1.34 \times 10^{-16}$	-	-	-	+17

TABLE E.1 – *Continued.*

λ_{lab} [μm]	Species	Transition	F [$\text{erg s}^{-1} \text{cm}^{-2}$]	δF [$\text{erg s}^{-1} \text{cm}^{-2}$]	FWHM [μm]	FWHM [km s^{-1}]	Δv [km s^{-1}]
2.52609	H I	Pf16	7.77×10^{-16}	9.23×10^{-17}	1.31×10^{-3}	155	+17
2.52804	H ₂	1–0 Q(8)	2.13×10^{-16}	9.16×10^{-17}	1.31×10^{-3}	155	+17
2.54151	H ₂	4–3 S(1)	5.10×10^{-17}	1.80×10^{-17}	1.32×10^{-3}	155	+17
2.55099	H ₂	2–1 Q(1)	3.52×10^{-16}	2.78×10^{-17}	1.32×10^{-3}	155	+17
2.55851	H ₂	2–1 Q(2)	1.08×10^{-16}	3.01×10^{-17}	1.32×10^{-3}	155	+16
2.55985	H ₂	1–0 Q(9)	9.16×10^{-17}	4.30×10^{-17}	1.32×10^{-3}	155	+17
2.56433	H I	Pf15	8.73×10^{-16}	9.72×10^{-17}	1.33×10^{-3}	155	+17
2.56983	H ₂	2–1 Q(3)	2.37×10^{-16}	6.20×10^{-17}	1.33×10^{-3}	155	+16
2.58496	H ₂	2–1 Q(4)	7.85×10^{-17}	3.02×10^{-17}	1.34×10^{-3}	155	+17
2.60398	H ₂	2–1 Q(5)	1.33×10^{-16}	3.02×10^{-17}	1.35×10^{-3}	155	+17
2.61265	H I	Pf14	8.82×10^{-16}	9.32×10^{-17}	1.13×10^{-3}	130	+8
2.61921	He I	$^3F_J - ^3D_J$	2.09×10^{-16}	5.59×10^{-17}	1.14×10^{-3}	130	+9
2.62587	H I	Br β	} blend				+8
2.62688	H ₂	1–0 O(2)					+8
2.62692	H ₂	2–1 Q(6)					+8
2.63512	H ₂	1–0 Q(11)	4.86×10^{-17}	2.63×10^{-17}	1.14×10^{-3}	130	+8
2.65383	H ₂	2–1 Q(7)	1.29×10^{-16}	2.75×10^{-17}	1.15×10^{-3}	130	+8
2.67513	H I	Pf13	1.07×10^{-15}	8.62×10^{-17}	1.16×10^{-3}	130	+8
2.71030	H ₂	3–2 Q(1)	2.44×10^{-16}	3.87×10^{-17}	1.18×10^{-3}	130	+8
2.71866	H ₂	3–2 Q(2)	7.59×10^{-17}	3.17×10^{-17}	1.18×10^{-3}	130	+8
2.72010	H ₂	2–1 Q(9)	4.85×10^{-17}	3.30×10^{-17}	1.18×10^{-3}	130	+8
2.73124	H ₂	3–2 Q(3)	5.01×10^{-17}	3.97×10^{-17}	1.19×10^{-3}	130	+8
2.75827	H I	Pf12	1.30×10^{-15}	1.21×10^{-16}	1.20×10^{-3}	130	+8
2.76926	H ₂	3–2 Q(5)	8.69×10^{-17}	6.68×10^{-17}	1.19×10^{-3}	129	+4
2.78616	H ₂	2–1 O(2)	2.04×10^{-16}	4.05×10^{-17}	1.20×10^{-3}	129	+5
2.80250	H ₂	1–0 O(3)	1.76×10^{-15}	1.22×10^{-16}	1.21×10^{-3}	129	+4
2.87299	H I	Pf11	1.46×10^{-15}	9.59×10^{-17}	1.23×10^{-3}	128	+4
2.88824	H ₂	4–3 Q(1)	9.21×10^{-17}	2.09×10^{-17}	1.24×10^{-3}	128	+4
2.89330	O I	$^3P_J - ^3S_1^o$	7.33×10^{-16}	6.61×10^{-17}	1.24×10^{-3}	128	+4
2.89937	H ₂	3–2 Q(9)	5.42×10^{-17}	4.39×10^{-17}	1.24×10^{-3}	128	+4
2.91188	H ₂	4–3 Q(3)	3.97×10^{-17}	2.23×10^{-17}	1.25×10^{-3}	128	+4
2.97406	H ₂	2–1 O(3)	3.04×10^{-16}	4.78×10^{-17}	1.28×10^{-3}	128	+6
3.00387	H ₂	1–0 O(4)	4.17×10^{-16}	6.32×10^{-17}	1.29×10^{-3}	128	+6
3.03920	H I	Pf10	1.89×10^{-15}	7.46×10^{-17}	1.30×10^{-3}	128	+5
3.08114	Fe II	$c^4P_{5/2} - z^4P_{5/2}^o$	5.16×10^{-16}	5.88×10^{-17}	1.32×10^{-3}	128	+6
3.09828	O I	$^3D_3^o - ^3P_2$	3.33×10^{-16}	4.48×10^{-17}	1.33×10^{-3}	128	–14
3.16377	H ₂	3–2 O(3)	2.15×10^{-16}	5.93×10^{-17}	1.36×10^{-3}	128	–15
NIRSpec F290LP/G395H							
2.87300	H I	Pf11	1.38×10^{-15}	1.13×10^{-16}	1.46×10^{-3}	152	+21

TABLE E.1 – *Continued.*

λ_{lab} [μm]	Species	Transition	F [$\text{erg s}^{-1} \text{cm}^{-2}$]	δF [$\text{erg s}^{-1} \text{cm}^{-2}$]	FWHM [μm]	FWHM [km s^{-1}]	Δv [km s^{-1}]
2.88824	H ₂	4–3 Q(1)	8.94×10^{-17}	2.82×10^{-17}	1.46×10^{-3}	152	+21
2.89330	O I	$^3\text{P}_J - ^3\text{S}_1^\circ$	6.81×10^{-16}	4.86×10^{-17}	1.47×10^{-3}	152	+20
2.89937	H ₂	3–2 Q(9)	$<1.45 \times 10^{-16}$	-	-	-	+21
2.91188	H ₂	4–3 Q(3)	$<7.73 \times 10^{-17}$	-	-	-	+21
2.97406	H ₂	2–1 O(3)	2.67×10^{-16}	2.71×10^{-17}	1.51×10^{-3}	152	+21
3.00387	H ₂	1–0 O(4)	3.29×10^{-16}	3.78×10^{-17}	1.52×10^{-3}	152	+20
3.03920	H I	Pf10	1.75×10^{-15}	9.14×10^{-17}	1.54×10^{-3}	152	+20
3.08132	Fe II	$c^4\text{P}_{5/2} - z^4\text{P}_{5/2}^\circ$	4.96×10^{-16}	4.12×10^{-17}	1.56×10^{-3}	152	+21
3.09854	O I	$^3\text{D}_3^\circ - ^3\text{P}_2$	3.00×10^{-16}	4.38×10^{-17}	1.57×10^{-3}	152	+21
3.16377	H ₂	3–2 O(3)	1.42×10^{-16}	3.18×10^{-17}	1.61×10^{-3}	152	+22
3.23499	H ₂	1–0 O(5)	5.14×10^{-16}	5.72×10^{-17}	1.64×10^{-3}	152	+22
3.29699	H I	Pf9	2.77×10^{-15}	1.36×10^{-16}	1.67×10^{-3}	152	+22
3.37646	H ₂	4–3 O(3)	8.87×10^{-17}	4.78×10^{-17}	1.72×10^{-3}	152	+23
3.39582	H ₂	3–2 O(4)	1.96×10^{-16}	7.51×10^{-17}	1.72×10^{-3}	152	+22
3.43787	H ₂	2–1 O(5)	1.71×10^{-16}	5.98×10^{-17}	1.73×10^{-3}	151	+18
3.45285	H I	Hu27	2.56×10^{-16}	2.97×10^{-17}	1.74×10^{-3}	151	+18
3.46697	H I	Hu26	2.26×10^{-16}	3.55×10^{-17}	1.75×10^{-3}	151	+18
3.48296	H I	Hu25	1.95×10^{-16}	3.79×10^{-17}	1.76×10^{-3}	151	+19
3.48580	H ₂	0–0 S(17)	6.36×10^{-17}	2.82×10^{-17}	1.76×10^{-3}	151	+19
3.50081	H ₂	1–0 O(6)	-	-	-	-	-
3.50116	H I	Hu24	3.60×10^{-16}	3.96×10^{-17}	1.77×10^{-3}	151	+18
3.52203	H I	Hu23	2.02×10^{-16}	6.40×10^{-17}	1.78×10^{-3}	151	+19
3.54610	H I	Hu22	2.78×10^{-16}	6.34×10^{-17}	1.79×10^{-3}	151	+18
3.54759	H ₂	0–0 S(16)	-	-	-	-	-
3.57410	H I	Hu21	3.79×10^{-16}	4.93×10^{-17}	1.80×10^{-3}	151	+18
3.60697	H I	Hu20	3.79×10^{-16}	5.10×10^{-17}	1.82×10^{-3}	151	+19
3.64592	H I	Hu19	4.34×10^{-16}	5.72×10^{-17}	1.84×10^{-3}	151	+18
3.69263	H I	Hu18	4.93×10^{-16}	9.04×10^{-17}	1.74×10^{-3}	141	+18
3.74056	H I	Pf γ	4.06×10^{-15}	9.11×10^{-17}	1.76×10^{-3}	141	+19
3.74939	H I	Hu17	5.56×10^{-16}	7.12×10^{-17}	1.76×10^{-3}	141	+19
3.81945	H I	Hu16	5.46×10^{-16}	6.38×10^{-17}	1.80×10^{-3}	141	+18
3.84611	H ₂	0–0 S(13)	2.12×10^{-16}	3.87×10^{-17}	1.81×10^{-3}	141	+19
3.90755	H I	Hu15	8.42×10^{-16}	9.08×10^{-17}	1.84×10^{-3}	141	+19
3.99615	H ₂	0–0 S(12)	8.54×10^{-17}	4.09×10^{-17}	1.68×10^{-3}	126	+12
4.02087	H I	Hu14	8.05×10^{-16}	1.53×10^{-16}	1.69×10^{-3}	126	+11
4.03772	He I	$^3\text{F}_J^\circ - ^3\text{D}_J$	1.76×10^{-16}	7.82×10^{-17}	1.70×10^{-3}	126	+11
4.04093	He I	$^1\text{F}_3^\circ - ^1\text{D}_2$	$<1.75 \times 10^{-16}$	-	-	-	+11
4.05226	H I	Br α	2.66×10^{-14}	5.10×10^{-16}	1.70×10^{-3}	126	+11
4.17079	H I	Hu13	8.89×10^{-16}	1.99×10^{-16}	1.75×10^{-3}	126	+11
4.18108	H ₂	0–0 S(11)	5.69×10^{-16}	8.23×10^{-17}	1.76×10^{-3}	126	+12

TABLE E.1 – *Continued.*

λ_{lab} [μm]	Species	Transition	F [$\text{erg s}^{-1} \text{cm}^{-2}$]	δF [$\text{erg s}^{-1} \text{cm}^{-2}$]	FWHM [μm]	FWHM [km s^{-1}]	Δv [km s^{-1}]
4.29592	He I	$^3\text{P}_1^{\circ} - ^3\text{S}_1$	1.40×10^{-15}	9.70×10^{-17}	2.15×10^{-3}	150	+19
4.37645	H I	Hu12	1.11×10^{-15}	4.60×10^{-17}	2.19×10^{-3}	150	+19
4.40979	H ₂	0–0 S(10)	2.05×10^{-16}	3.92×10^{-17}	2.20×10^{-3}	150	+19
4.41667	H ₂	1–1 S(11)	1.35×10^{-16}	3.91×10^{-17}	2.21×10^{-3}	150	+19
4.61802	[K III]	$^2\text{P}_{1/2}^{\circ} - ^2\text{P}_{3/2}^{\circ}$	9.20×10^{-17}	8.30×10^{-17}	1.95×10^{-3}	126	+13
4.65378	H I	Pf β	6.79×10^{-15}	1.55×10^{-16}	1.96×10^{-3}	126	+13
4.67251	H I	Hu ϵ	} blend				+13
4.67195	[Fe II]	$a^4\text{F}_{3/2} - a^6\text{D}_{1/2}$					+13
4.69461	H ₂	0–0 S(9)	6.97×10^{-16}	4.94×10^{-17}	1.98×10^{-3}	126	+13
4.84769	H I	25–7	2.98×10^{-16}	4.81×10^{-17}	2.47×10^{-3}	152	+11
4.92370	H I	23–7	1.80×10^{-16}	8.35×10^{-17}	2.50×10^{-3}	152	+10
4.95419	H ₂	1–1 S(9)	1.31×10^{-16}	4.45×10^{-17}	2.52×10^{-3}	152	+11
4.97088	H I	22–7	4.13×10^{-16}	4.80×10^{-17}	2.53×10^{-3}	126	+10
5.00015	?	?	} blend				
5.00102	?	?					
5.02609	H I	21–7	2.30×10^{-16}	5.61×10^{-17}	2.11×10^{-3}	126	+9
5.05312	H ₂	0–0 S(8)	3.16×10^{-16}	5.28×10^{-17}	2.13×10^{-3}	126	+9
5.09132	H I	20–7	3.07×10^{-16}	4.16×10^{-17}	2.14×10^{-3}	126	+9
5.12866	H I	Hu δ	1.57×10^{-15}	8.52×10^{-17}	2.16×10^{-3}	126	+9
5.16928	H I	19–7	3.80×10^{-16}	5.26×10^{-17}	2.17×10^{-3}	126	+9
5.21667	?	?	1.40×10^{-16}	1.14×10^{-16}	2.20×10^{-3}	126	+9
5.23885	H ₂	2–2 S(9)	8.75×10^{-17}	5.04×10^{-17}	2.20×10^{-3}	126	+9
5.26368	H I	18–7	1.12×10^{-16}	6.42×10^{-17}	2.21×10^{-3}	126	+9
MIRI/MRS Channel 1A							
4.92370	H I	23–7	1.06×10^{-16}	4.95×10^{-17}	1.70×10^{-3}	103	–10
4.95419	H ₂	1–1 S(9)	-	-	-	-	-
4.97088	H I	22–7	-	-	-	-	-
5.02609	H I	21–7	9.51×10^{-17}	6.12×10^{-17}	2.01×10^{-3}	120	+15
5.05312	H ₂	0–0 S(8)	2.73×10^{-16}	3.66×10^{-17}	1.64×10^{-3}	97	0
5.09132	H I	20–7	-	-	-	-	-
5.12866	H I	Hu δ	1.07×10^{-15}	9.67×10^{-17}	1.51×10^{-3}	88	+11
5.16928	H I	19–7	1.76×10^{-16}	4.06×10^{-17}	1.74×10^{-3}	101	+18
5.26368	H I	18–7	1.86×10^{-16}	5.25×10^{-17}	2.09×10^{-3}	119	+25
5.33014	H ₂	1–1 S(8)	-	-	-	-	-
5.34017	[Fe II]	$a^4\text{F}_{9/2} - a^6\text{D}_{9/2}$	9.74×10^{-16}	6.14×10^{-17}	1.53×10^{-3}	86	+5
5.37977	H I	17–7	2.69×10^{-16}	4.84×10^{-17}	2.00×10^{-3}	111	+9
5.51116	H ₂	0–0 S(7)	1.57×10^{-15}	6.48×10^{-17}	1.35×10^{-3}	73	0
5.52519	H I	16–7	3.38×10^{-16}	3.57×10^{-17}	2.02×10^{-3}	110	+10

TABLE E.1 – *Continued.*

λ_{lab} [μm]	Species	Transition	F [$\text{erg s}^{-1} \text{cm}^{-2}$]	δF [$\text{erg s}^{-1} \text{cm}^{-2}$]	FWHM [μm]	FWHM [km s^{-1}]	Δv [km s^{-1}]
5.71146	H I	15 – 7	3.08×10^{-16}	6.14×10^{-17}	1.73×10^{-3}	90	+12
MIRI/MRS Channel 1B							
5.71146	H I	15 – 7	3.85×10^{-16}	6.87×10^{-17}	2.02×10^{-3}	106	+12
5.81092	H ₂	1–1 S(7)	$<1.44 \times 10^{-16}$	-	-	-	+12
5.90821	H I	Hu γ	2.22×10^{-15}	5.71×10^{-17}	2.09×10^{-3}	106	+12
5.95684	H I	14 – 7	4.86×10^{-16}	4.27×10^{-17}	2.11×10^{-3}	106	+12
5.98200	[K IV]	$^3\text{P}_1 - ^3\text{P}_2$	$<1.44 \times 10^{-16}$	-	-	-	+11
6.10856	H ₂	0–0 S(6)	9.59×10^{-16}	5.97×10^{-17}	1.94×10^{-3}	95	+12
6.29192	H I	13 – 7	7.02×10^{-16}	9.84×10^{-17}	1.99×10^{-3}	95	+12
6.50098	H I	25 – 8	1.13×10^{-16}	3.47×10^{-17}	2.32×10^{-3}	107	+32
6.56469	H I	24 – 8	8.11×10^{-17}	2.45×10^{-17}	2.33×10^{-3}	107	+32
MIRI/MRS Channel 1C							
6.56469	H I	24 – 8	1.15×10^{-16}	3.53×10^{-17}	2.02×10^{-3}	92	+11
6.77199	H I	12 – 7	6.58×10^{-16}	6.54×10^{-17}	2.08×10^{-3}	92	+10
6.82588	H I	21 – 8	$<1.61 \times 10^{-16}$	-	-	-	+11
6.90952	H ₂	0–0 S(5)	5.29×10^{-15}	6.82×10^{-17}	2.00×10^{-3}	86	+10
6.98527	[Ar II]	$^2\text{P}_{1/2}^{\circ} - ^2\text{P}_{3/2}^{\circ}$	7.72×10^{-15}	1.21×10^{-16}	2.02×10^{-3}	86	+10
7.09271	H I	19 – 8	1.69×10^{-16}	3.05×10^{-17}	2.05×10^{-3}	86	+10
7.27165	H I	18 – 8	2.08×10^{-16}	3.55×10^{-17}	2.18×10^{-3}	90	+11
7.28006	H ₂	1–1 S(5)	$<1.01 \times 10^{-16}$	-	-	-	+11
7.31770	[Na III]	$^2\text{P}_{1/2}^{\circ} - ^2\text{P}_{3/2}^{\circ}$	2.58×10^{-16}	7.31×10^{-17}	2.19×10^{-3}	90	+11
7.45986	H I	Pf α	1.19×10^{-14}	4.03×10^{-16}	2.23×10^{-3}	90	+11
7.50249	H I	Hu β	2.98×10^{-15}	1.50×10^{-16}	2.09×10^{-3}	84	+11
7.50658	[Ni I]	$^3\text{F}_3 - ^3\text{F}_4$	$<4.15 \times 10^{-16}$	-	-	-	+11
7.50810	H I	11 – 7	6.80×10^{-16}	9.90×10^{-17}	2.09×10^{-3}	84	+11
MIRI/MRS Channel 2A							
7.78037	H I	16 – 8	-	-	-	-	
8.02505	H ₂	0–0 S(4)	1.69×10^{-15}	5.82×10^{-16}	1.71×10^{-3}	64	–5
8.15489	H I	15 – 8	1.40×10^{-16}	3.93×10^{-17}	1.91×10^{-3}	70	–2
8.40908	?	?	1.91×10^{-17}	1.85×10^{-17}	1.45×10^{-3}	52	–3
8.66450	H I	14 – 8	1.52×10^{-16}	4.96×10^{-17}	1.75×10^{-3}	61	+10
MIRI/MRS Channel 2B							
8.72056	H I	23 – 9	1.89×10^{-16}	6.13×10^{-17}	2.91×10^{-3}	100	+13
8.76006	H I	10 – 7	1.10×10^{-15}	1.04×10^{-16}	2.92×10^{-3}	100	+13
8.99138	[Ar III]	$^3\text{P}_1 - ^3\text{P}_2$	3.68×10^{-14}	6.27×10^{-16}	3.00×10^{-3}	100	+13
9.39202	H I	13 – 8	2.97×10^{-16}	4.80×10^{-17}	3.09×10^{-3}	99	+7

TABLE E.1 – *Continued.*

λ_{lab} [μm]	Species	Transition	F [$\text{erg s}^{-1} \text{cm}^{-2}$]	δF [$\text{erg s}^{-1} \text{cm}^{-2}$]	FWHM [μm]	FWHM [km s^{-1}]	Δv [km s^{-1}]
9.66491	H ₂	0–0 S(3)	8.92×10^{-15}	2.81×10^{-16}	3.18×10^{-3}	99	+7
MIRI/MRS Channel 2C							
10.51050	[S IV]	$^2\text{P}_{3/2}^{\circ} - ^2\text{P}_{1/2}^{\circ}$	1.83×10^{-13}	2.46×10^{-15}	3.53×10^{-3}	100	+11
11.30750	[Ni I]	$^3\text{F}_2 - ^3\text{F}_3$	} blend				-24
11.30870	H I	9–7					-
MIRI/MRS Channel 3A							
11.76190	[Cl IV]	$^3\text{P}_2 - ^3\text{P}_1$	$<4.94 \times 10^{-16}$	-	-	-	+2
12.27861	H ₂	0–0 S(2)	4.94×10^{-15}	1.19×10^{-16}	4.27×10^{-3}	104	+4
12.37190	H I	Hu α	6.27×10^{-15}	1.47×10^{-16}	4.30×10^{-3}	104	+3
12.38715	H I	11–8	7.98×10^{-16}	1.76×10^{-16}	4.31×10^{-3}	104	+1
12.58708	H I	14–9	4.48×10^{-16}	1.42×10^{-16}	4.18×10^{-3}	99	+1
12.61097	H I	19–10	$<4.02 \times 10^{-16}$	-	-	-	+1
12.81355	[Ne II]	$^2\text{P}_{1/2}^{\circ} - ^2\text{P}_{3/2}^{\circ}$	6.22×10^{-14}	3.86×10^{-16}	4.26×10^{-3}	99	-2
MIRI/MRS Channel 3B							
14.18308	H I	13–9	8.99×10^{-16}	1.54×10^{-16}	4.20×10^{-3}	88	+29
14.36780	[Cl II]	$^3\text{P}_1 - ^3\text{P}_2$	3.29×10^{-16}	1.53×10^{-16}	3.84×10^{-3}	81	+19
MIRI/MRS Channel 3C							
15.55510	[Ne III]	$^3\text{P}_1 - ^3\text{P}_2$	4.70×10^{-13}	2.263×10^{-15}	7.19×10^{-3}	138	-14
15.75329	?	?	$<1.54 \times 10^{-15}$	-	-	-	-15
16.20910	H I	10–8	$<1.93 \times 10^{-15}$	-	-	-	-14
16.88063	H I	12–9	$<1.24 \times 10^{-15}$	-	-	-	+5
17.03500	H ₂	0–0 S(1)	1.02×10^{-14}	6.32×10^{-16}	7.19×10^{-3}	127	+6
17.88500	[P III]	$^2\text{P}_{3/2}^{\circ} - ^2\text{P}_{1/2}^{\circ}$	4.12×10^{-15}	2.35×10^{-16}	8.87×10^{-3}	149	-12
17.93595	[Fe II]	$a^4\text{F}_{7/2} - a^4\text{F}_{9/2}$	1.92×10^{-15}	4.32×10^{-16}	8.90×10^{-3}	149	-13
MIRI/MRS Channel 4A							
17.88500	[P III]	$^2\text{P}_{3/2}^{\circ} - ^2\text{P}_{1/2}^{\circ}$	3.32×10^{-15}	3.84×10^{-16}	8.82×10^{-3}	148	-12
17.93595	[Fe II]	$a^4\text{F}_{7/2} - a^4\text{F}_{9/2}$	$<1.27 \times 10^{-15}$	-	-	-	-13
18.71300	[S III]	$^3\text{P}_2 - ^3\text{P}_1$	3.18×10^{-13}	1.75×10^{-15}	9.22×10^{-3}	148	+4
19.06190	H I	8–7	5.38×10^{-15}	1.02×10^{-15}	9.40×10^{-3}	148	+4
MIRI/MRS Channel 4B							
21.83020	[Ar III]	$^3\text{P}_0 - ^3\text{P}_1$	8.04×10^{-15}	7.84×10^{-16}	1.02×10^{-2}	141	-19
22.33157	H I	13–10	} blend				-20
22.34046	H I	11–9					-20
22.92500	[Fe III]	$^5\text{D}_4 - ^5\text{D}_3$	6.28×10^{-15}	5.70×10^{-16}	1.08×10^{-2}	141	-20

TABLE E.1 – *Continued.*

λ_{lab} [μm]	Species	Transition	F [$\text{erg s}^{-1} \text{cm}^{-2}$]	δF [$\text{erg s}^{-1} \text{cm}^{-2}$]	FWHM [μm]	FWHM [km s^{-1}]	Δv [km s^{-1}]
MIRI/MRS Channel 4C							
25.98829	[Fe II]	$a^6\text{D}_{9/2} - a^6\text{D}_{7/2}$	7.54×10^{-15}	8.69×10^{-16}	1.34×10^{-2}	155	+5

TABLE E.2 – Observed lines showing emission in a C-shell-like structure around S7A based on the compiled M0 maps. Flux densities are calculated for the brightest part of the shell – S1A (see Tab. A.1).

λ_{lab} [μm]	Species	Transition	F [$\text{erg s}^{-1} \text{cm}^{-2}$]	δF [$\text{erg s}^{-1} \text{cm}^{-2}$]	FWHM [μm]	FWHM [km s^{-1}]	Δv [km s^{-1}]
NIRSpec F100LP/G140H							
1.00521	H I	P δ	1.16×10^{-14}	5.76×10^{-16}	4.21×10^{-4}	125	+17
1.02896	[S II]	$2^{\circ}\text{P}_{3/2} - 2^{\circ}\text{D}_{3/2}$	3.97×10^{-16}	3.23×10^{-17}	4.31×10^{-4}	125	+17
1.03233	[S II]	$2^{\circ}\text{P}_{3/2} - 2^{\circ}\text{D}_{5/2}$	4.92×10^{-16}	5.75×10^{-17}	4.32×10^{-4}	125	+17
1.03392	[S II]	$2^{\circ}\text{P}_{1/2} - 2^{\circ}\text{D}_{3/2}$	4.16×10^{-16}	5.97×10^{-17}	4.33×10^{-4}	125	+17
1.03733	[S II]	$2^{\circ}\text{P}_{1/2} - 2^{\circ}\text{D}_{5/2}$	1.48×10^{-16}	3.77×10^{-17}	4.34×10^{-4}	125	+17
1.08332	He I	$3^{\circ}\text{P}_1 - 3^{\circ}\text{S}_1$	3.73×10^{-14}	1.02×10^{-15}	4.56×10^{-4}	125	+8
1.09160	He I	$3^{\circ}\text{F}_3 - 3^{\circ}\text{D}_2$	9.64×10^{-16}	7.55×10^{-17}	4.59×10^{-4}	125	+8
1.09411	H I	P γ	2.30×10^{-14}	4.86×10^{-16}	4.60×10^{-4}	125	+8
1.19724	He I	$3^{\circ}\text{D}_2 - 3^{\circ}\text{P}_1$	5.95×10^{-16}	2.50×10^{-17}	5.03×10^{-4}	125	+22
1.25309	He I	$3^{\circ}\text{P}_1 - 3^{\circ}\text{S}_1$	5.34×10^{-16}	2.78×10^{-17}	5.03×10^{-4}	120	+15
1.27884	He I	$3^{\circ}\text{P}_1 - 3^{\circ}\text{S}_1$	2.09×10^{-15}	1.12×10^{-16}	5.13×10^{-4}	120	+15
1.28216	H I	P β	4.90×10^{-14}	3.29×10^{-16}	5.15×10^{-4}	120	+15
1.31675	O I	$3^{\circ}\text{S}_1 - 3^{\circ}\text{P}_1$	3.52×10^{-16}	4.66×10^{-17}	5.29×10^{-4}	120	+15
1.61137	H I	Br13	1.46×10^{-15}	6.55×10^{-17}	5.81×10^{-4}	107	+14
1.64117	H I	Br12	1.89×10^{-15}	7.78×10^{-17}	5.91×10^{-4}	107	+14
NIRSpec F170LP/G235H							
1.68111	H I	Br11	2.50×10^{-15}	9.11×10^{-17}	8.62×10^{-4}	153	+24
1.70071	He I	$3^{\circ}\text{D}_2 - 3^{\circ}\text{P}_1$	1.12×10^{-15}	5.17×10^{-17}	8.72×10^{-4}	153	+23
1.73669	H I	Br10	3.39×10^{-15}	9.05×10^{-17}	8.91×10^{-4}	153	+25
1.81791	H I	Br ϵ	4.93×10^{-15}	8.37×10^{-17}	9.32×10^{-4}	153	+24
1.86905	He I	$3^{\circ}\text{F}_3 - 3^{\circ}\text{D}_2$	6.07×10^{-15}	3.49×10^{-16}	8.80×10^{-4}	141	+23
1.87561	H I	P α	1.32×10^{-13}	1.03×10^{-15}	8.83×10^{-4}	141	+22
1.90946	He I	$1^{\circ}\text{D}_2 - 1^{\circ}\text{P}_1$	4.26×10^{-16}	3.16×10^{-17}	8.99×10^{-4}	141	+22
1.94509	H I	Br δ	7.30×10^{-15}	1.25×10^{-16}	9.16×10^{-4}	141	+23
1.95482	He I	$3^{\circ}\text{P}_J - 3^{\circ}\text{D}_J$	4.20×10^{-16}	1.42×10^{-17}	9.21×10^{-4}	141	+23

TABLE E.2 – *Continued.*

λ_{lab} [μm]	Species	Transition	F [$\text{erg s}^{-1} \text{cm}^{-2}$]	δF [$\text{erg s}^{-1} \text{cm}^{-2}$]	FWHM [μm]	FWHM [km s^{-1}]	Δv [km s^{-1}]
2.05869	He I	$^1\text{P}_1^\circ - ^1\text{S}_0$	6.17×10^{-15}	4.58×10^{-17}	8.95×10^{-4}	130	+19
2.11259	He I	$^3\text{S}_1 - ^3\text{P}_1^\circ$	3.32×10^{-16}	2.64×10^{-17}	9.19×10^{-4}	130	+18
2.16612	H I	Br γ	1.14×10^{-14}	1.97×10^{-16}	9.28×10^{-4}	128	+17
2.52609	H I	Pf16	6.16×10^{-16}	3.66×10^{-17}	1.09×10^{-3}	128	+14
2.56433	H I	Pf15	7.83×10^{-16}	3.74×10^{-17}	1.10×10^{-3}	128	+12
2.61265	H I	Pf14	9.08×10^{-16}	5.03×10^{-17}	1.12×10^{-3}	128	+12
2.61921	He I	$^3\text{F}_J - ^3\text{D}_J$	3.73×10^{-16}	6.19×10^{-17}	1.12×10^{-3}	128	+25
2.62587	H I	Br β	2.16×10^{-14}	1.04×10^{-15}	1.12×10^{-3}	128	+11
2.67513	H I	Pf13	1.08×10^{-15}	5.72×10^{-17}	1.15×10^{-3}	128	+12
2.75827	H I	Pf12	1.54×10^{-15}	8.53×10^{-17}	1.18×10^{-3}	128	+12
NIRSpec F290LP/G395H							
2.873	H I	Pf11	1.80×10^{-15}	5.48×10^{-17}	1.46×10^{-3}	151	+26
3.0392	H I	Pf10	2.42×10^{-15}	2.46×10^{-17}	1.54×10^{-3}	151	+25
3.29699	H I	Pf9	3.59×10^{-15}	7.37×10^{-17}	1.57×10^{-3}	142	+22
3.5741	H I	Hu21	1.87×10^{-16}	8.96×10^{-18}	1.62×10^{-3}	136	+23
3.60697	H I	Hu20	2.10×10^{-16}	7.56×10^{-18}	1.64×10^{-3}	136	+24
3.64592	H I	Hu19	2.44×10^{-16}	9.60×10^{-18}	1.66×10^{-3}	136	+23
3.69263	H I	Hu18	2.85×10^{-16}	6.94×10^{-18}	1.56×10^{-3}	126	+20
3.74056	H I	Pf γ	5.06×10^{-15}	9.50×10^{-17}	1.58×10^{-3}	126	+20
3.74939	H I	Hu17	3.25×10^{-16}	2.23×10^{-17}	1.59×10^{-3}	126	+20
3.81945	H I	Hu16	3.90×10^{-16}	1.09×10^{-17}	1.62×10^{-3}	126	+20
3.90755	H I	Hu15	4.85×10^{-16}	1.54×10^{-17}	1.66×10^{-3}	126	+20
4.02087	H I	Hu14	6.44×10^{-16}	3.06×10^{-17}	1.69×10^{-3}	125	+15
4.03773	He I	$^3\text{F}_J^\circ - ^3\text{D}_J$	4.29×10^{-16}	2.82×10^{-17}	1.70×10^{-3}	125	+15
4.04093	He I	$^1\text{F}_3^\circ - ^1\text{D}_2$	1.51×10^{-16}	2.33×10^{-17}	1.70×10^{-3}	125	+14
4.05226	H I	Br α	2.70×10^{-14}	9.25×10^{-16}	1.70×10^{-3}	125	+15
4.17079	H I	Hu13	7.61×10^{-16}	2.33×10^{-17}	1.75×10^{-3}	125	+15
4.29592	He I	$^3\text{P}_1^\circ - ^3\text{S}_1$	1.28×10^{-15}	6.71×10^{-17}	1.80×10^{-3}	125	+18
4.37645	H I	Hu12	9.88×10^{-16}	3.92×10^{-17}	1.84×10^{-3}	125	+18
4.61802	[K III]	$^2\text{P}_{1/2}^\circ - ^2\text{P}_{3/2}^\circ$	6.96×10^{-16}	4.05×10^{-17}	1.94×10^{-3}	126	+16
4.65378	H I	Pf β	8.59×10^{-15}	4.21×10^{-16}	1.96×10^{-3}	126	+16
4.67251	H I	Hu ϵ	1.33×10^{-15}	7.24×10^{-17}	1.97×10^{-3}	126	+16
5.12866	H I	Hu δ	1.87×10^{-15}	1.36×10^{-16}	2.15×10^{-3}	125	+14
MIRI/MRS Channel 1A							
5.12866	H I	Hu δ	2.02×10^{-15}	1.71×10^{-16}	1.42×10^{-3}	83	+8
MIRI/MRS Channel 1B							
5.90821	H I	Hu γ	3.78×10^{-15}	7.37×10^{-17}	1.96×10^{-3}	99	+12

TABLE E.2 – *Continued.*

λ_{lab} [μm]	Species	Transition	F [$\text{erg s}^{-1} \text{cm}^{-2}$]	δF [$\text{erg s}^{-1} \text{cm}^{-2}$]	FWHM [μm]	FWHM [km s^{-1}]	Δv [km s^{-1}]
6.29192	H I	13 – 7	8.53×10^{-16}	6.00×10^{-17}	1.96×10^{-3}	93	+11
MIRI/MRS Channel 1C							
6.77199	H I	12 – 7	1.07×10^{-15}	3.35×10^{-17}	2.13×10^{-3}	94	+12
6.98527	[Ar II]	$^2\text{P}_{1/2}^{\circ} - ^2\text{P}_{3/2}^{\circ}$	5.69×10^{-15}	9.06×10^{-17}	2.06×10^{-3}	88	+13
7.45986	H I	Pf α	1.96×10^{-14}	4.91×10^{-16}	2.14×10^{-3}	86	+12
7.50249	H I	Hu β	4.93×10^{-15}	1.29×10^{-16}	2.11×10^{-3}	84	+12
7.50658	[Ni I]	$^3\text{F}_3 - ^3\text{F}_4$	$<3.70 \times 10^{-16}$	-	-	-	+11
MIRI/MRS Channel 2A							
8.15489	H I	15 – 8	2.01×10^{-16}	5.82×10^{-17}	1.76×10^{-3}	65	-4
8.66450	H I	14 – 8	2.30×10^{-16}	8.58×10^{-17}	1.63×10^{-3}	56	+9
MIRI/MRS Channel 2B							
8.76006	H I	10 – 7	1.67×10^{-15}	1.49×10^{-16}	2.88×10^{-3}	98	+13
8.99138	[Ar III]	$^3\text{P}_1 - ^3\text{P}_2$	8.61×10^{-14}	1.41×10^{-15}	2.96×10^{-3}	98	+13
9.39202	H I	13 – 8	5.14×10^{-16}	4.35×10^{-17}	3.10×10^{-3}	98	+9
MIRI/MRS Channel 2C							
10.51050	[S IV]	$^2\text{P}_{3/2}^{\circ} - ^2\text{P}_{1/2}^{\circ}$	3.39×10^{-13}	5.78×10^{-15}	3.52×10^{-3}	100	+8
11.30750	[Ni I]	$^3\text{F}_2 - ^3\text{F}_3$	} blend ?				
11.30870	H I	9 – 7					
MIRI/MRS Channel 3A							
12.3719	H I	Hu α	7.72×10^{-15}	1.24×10^{-16}	4.19×10^{-3}	101	+3
12.38715	H I	11 – 8	9.06×10^{-16}	1.26×10^{-16}	4.20×10^{-3}	101	+5
12.58708	H I	14 – 9	3.71×10^{-16}	6.08×10^{-17}	3.97×10^{-3}	94	+2
12.81355	[Ne II]	$^2\text{P}_{1/2}^{\circ} - ^2\text{P}_{3/2}^{\circ}$	6.48×10^{-14}	3.53×10^{-16}	4.04×10^{-3}	94	+2

E.2 ALFA fitted spectra

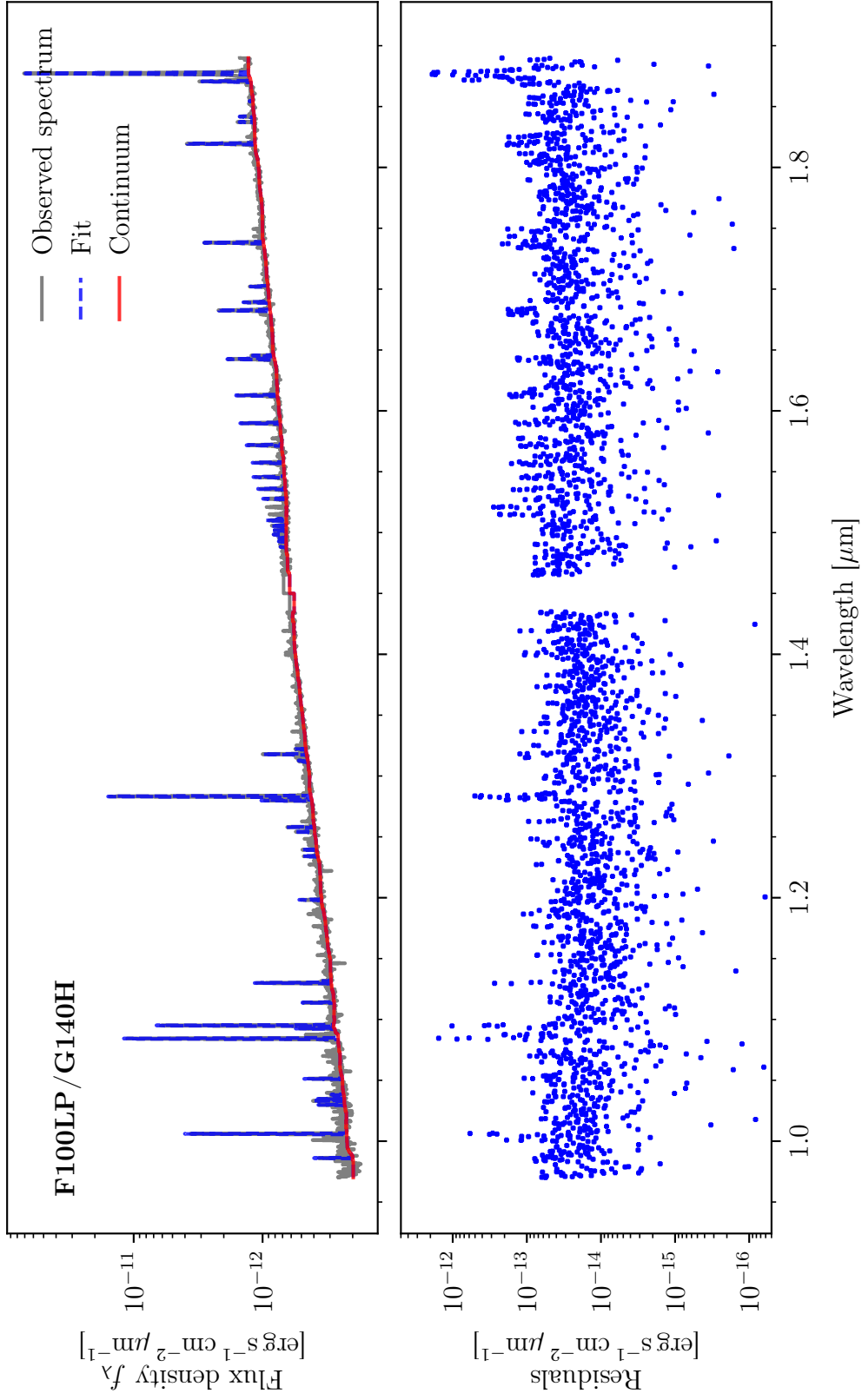


FIGURE E.1 – ALFA fits to the spectrum extracted at the position of YSO. The residuals are calculated by subtracting the best fit from the continuum-subtracted spectrum.

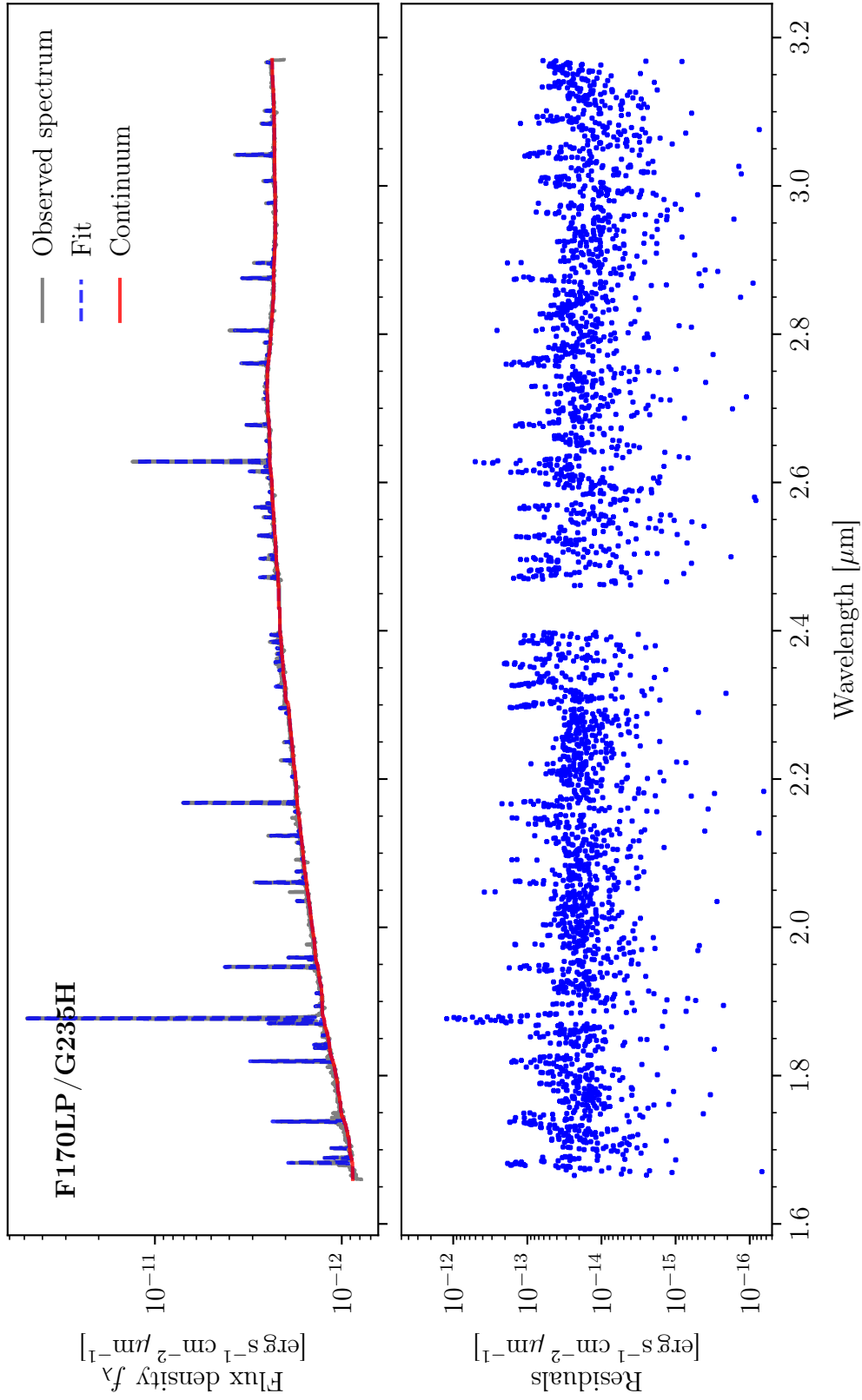


FIGURE E.1 – *Continued.*

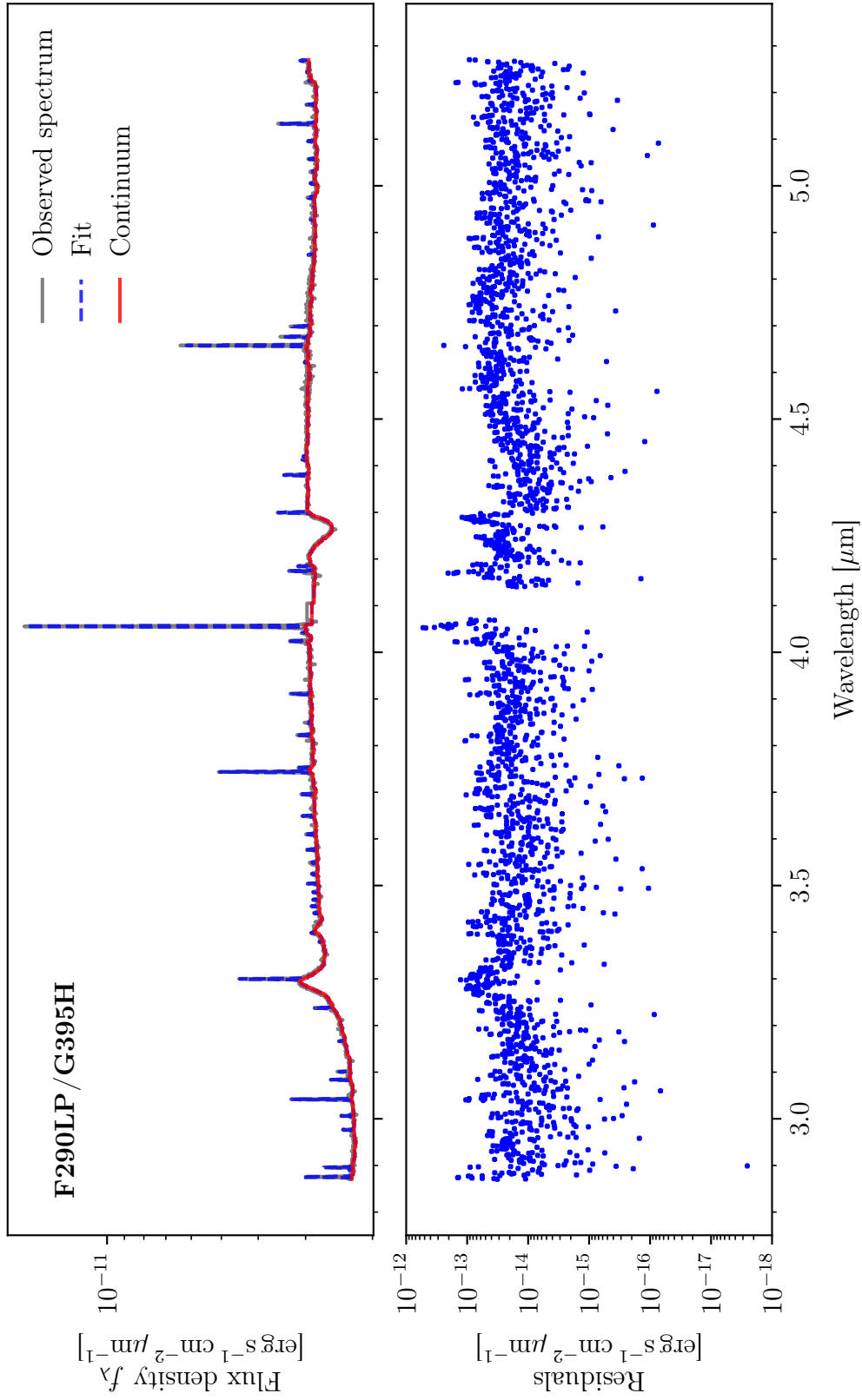


FIGURE E.1 – *Continued.*

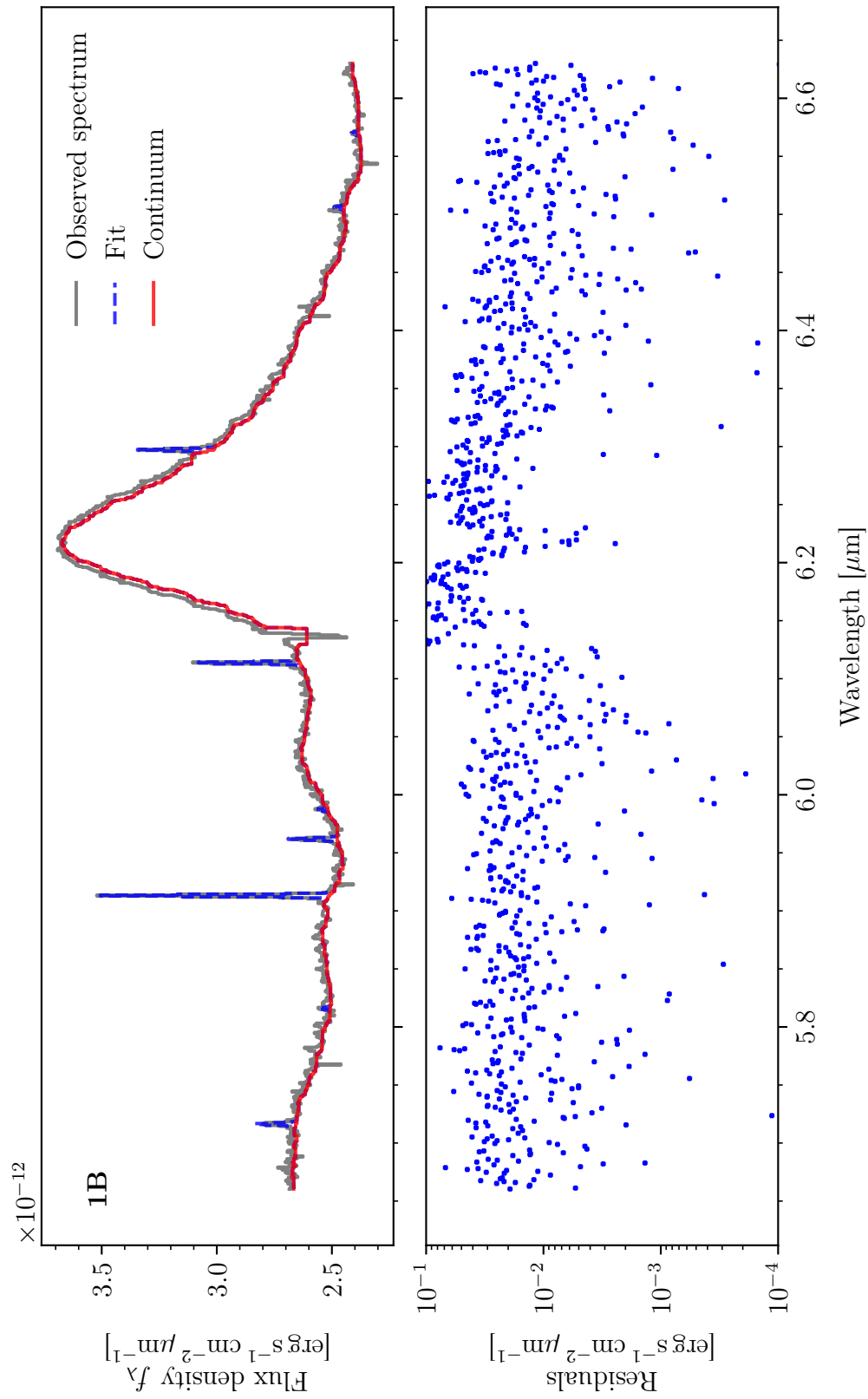


FIGURE E.1 - *Continued.*

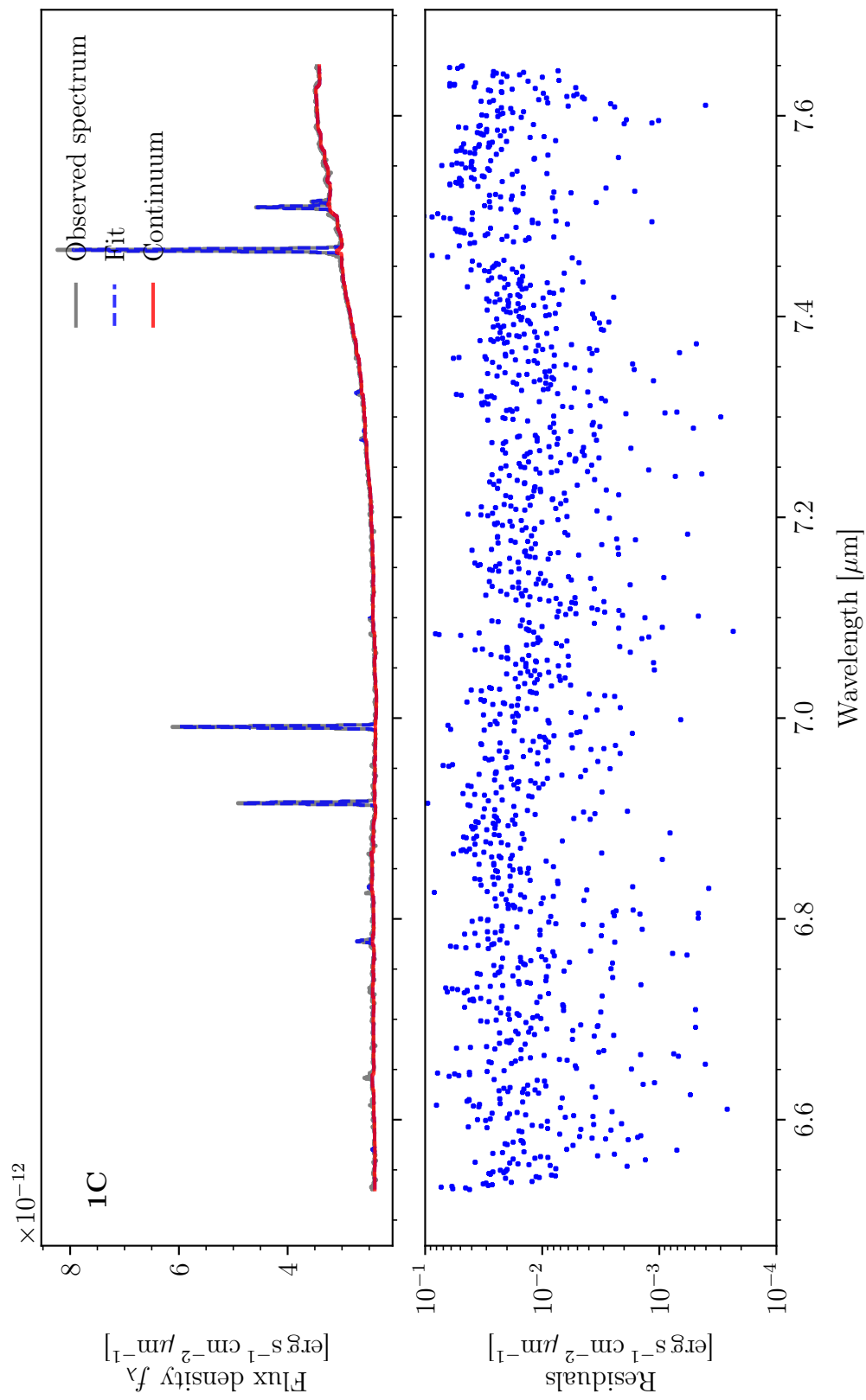


FIGURE E.1 – *Continued.*

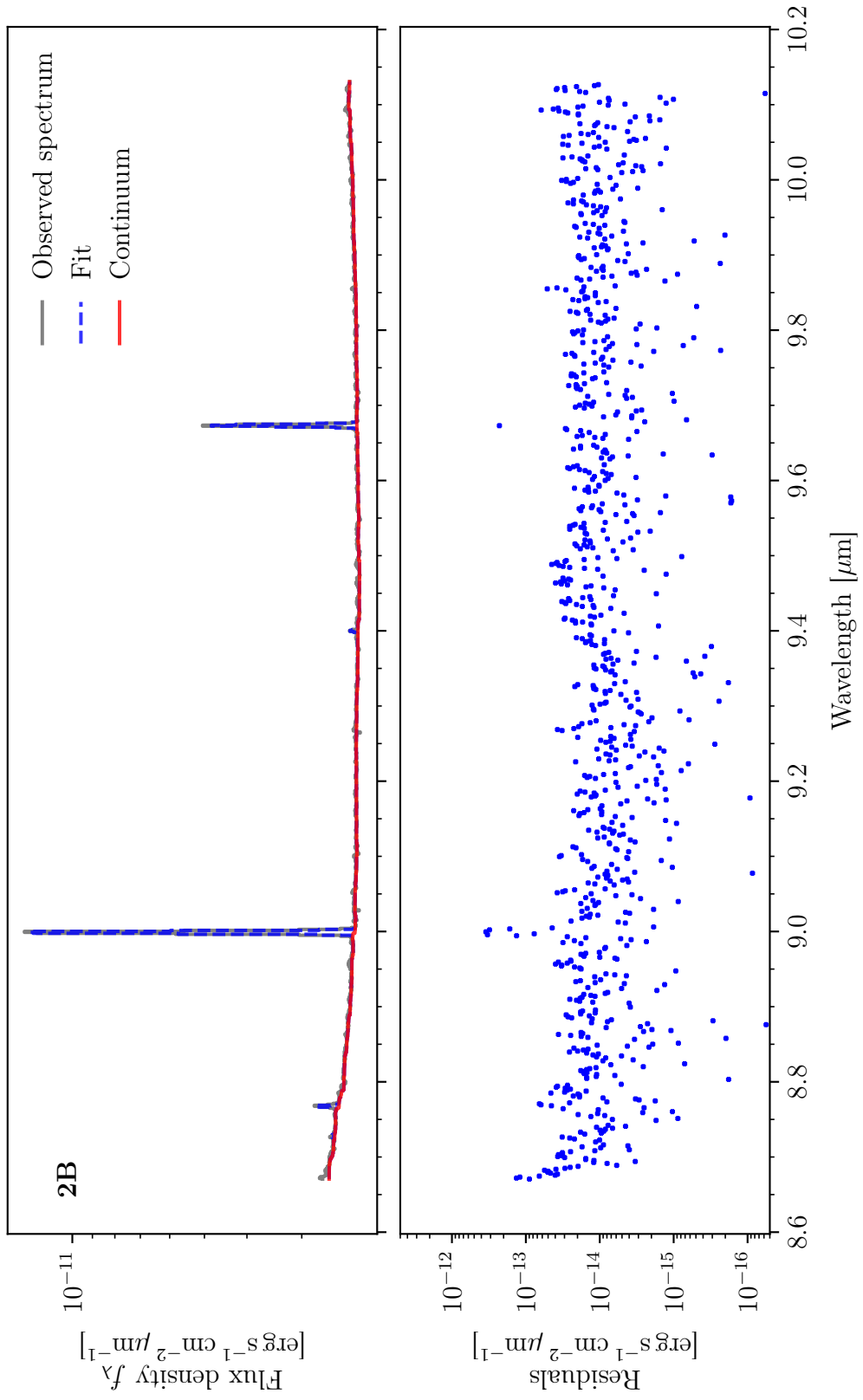


FIGURE E.1 – Continued.

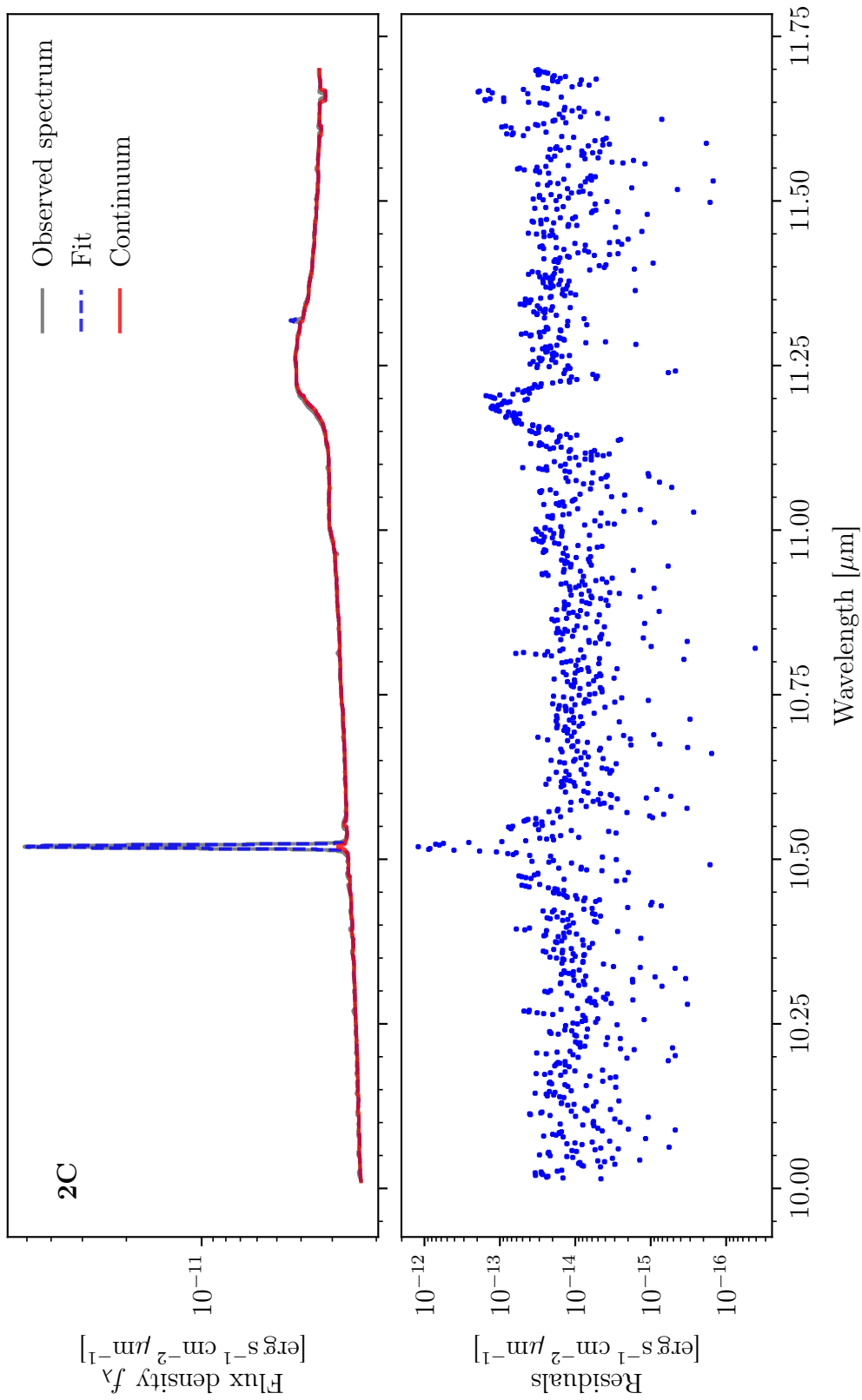


FIGURE E.1 – *Continued.*

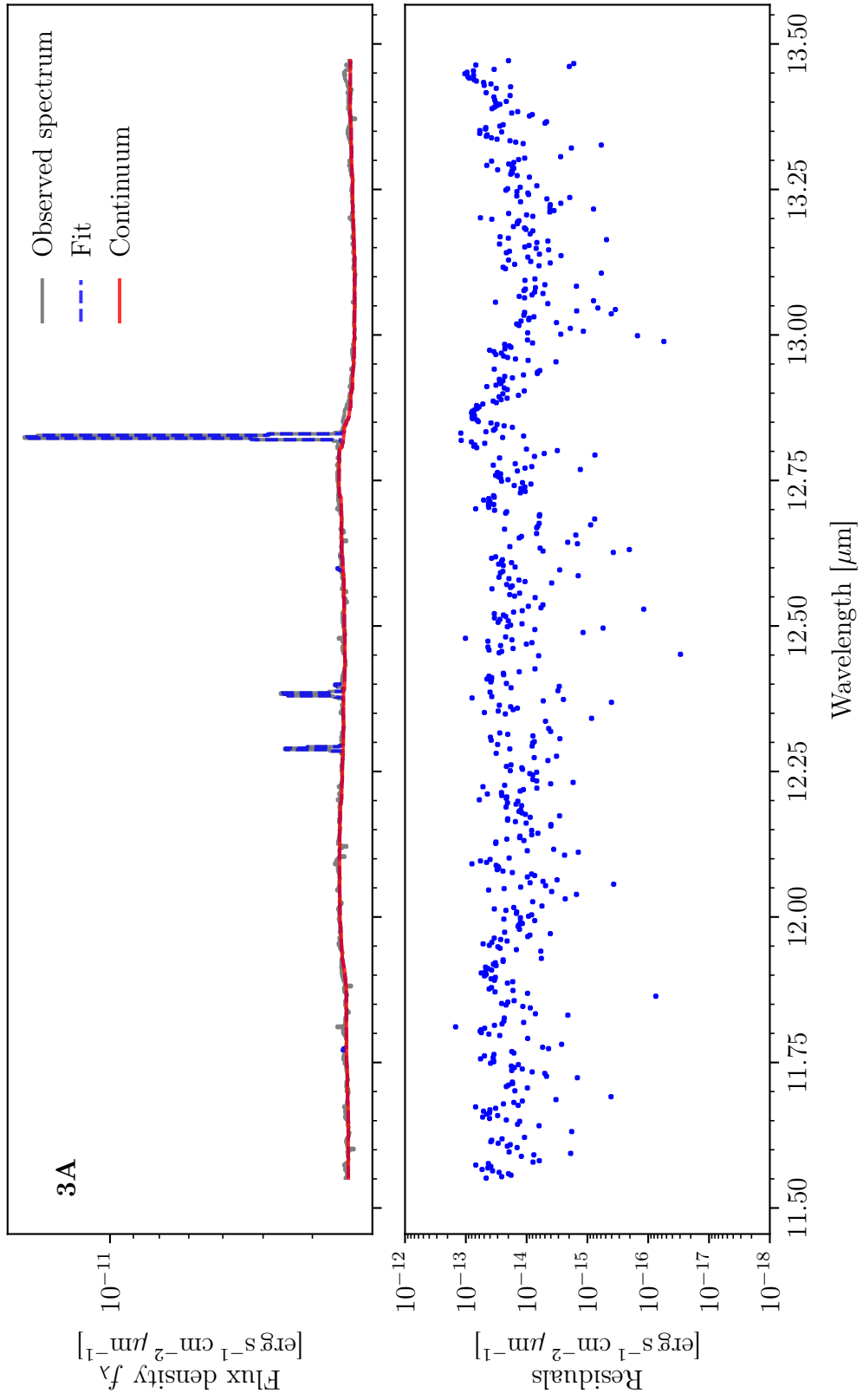


FIGURE E.1 – *Continued.*

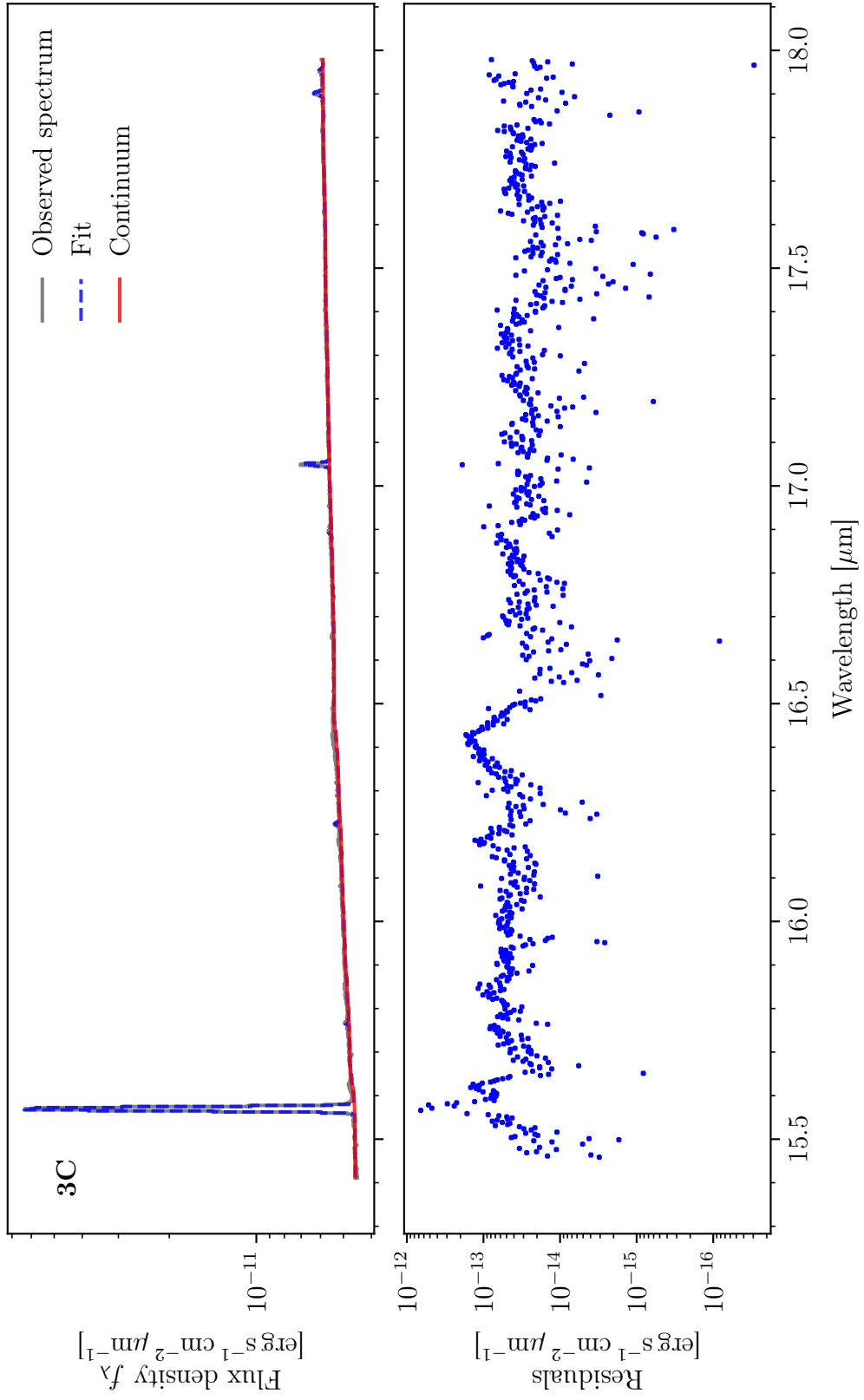


FIGURE E.1 – *Continued.*

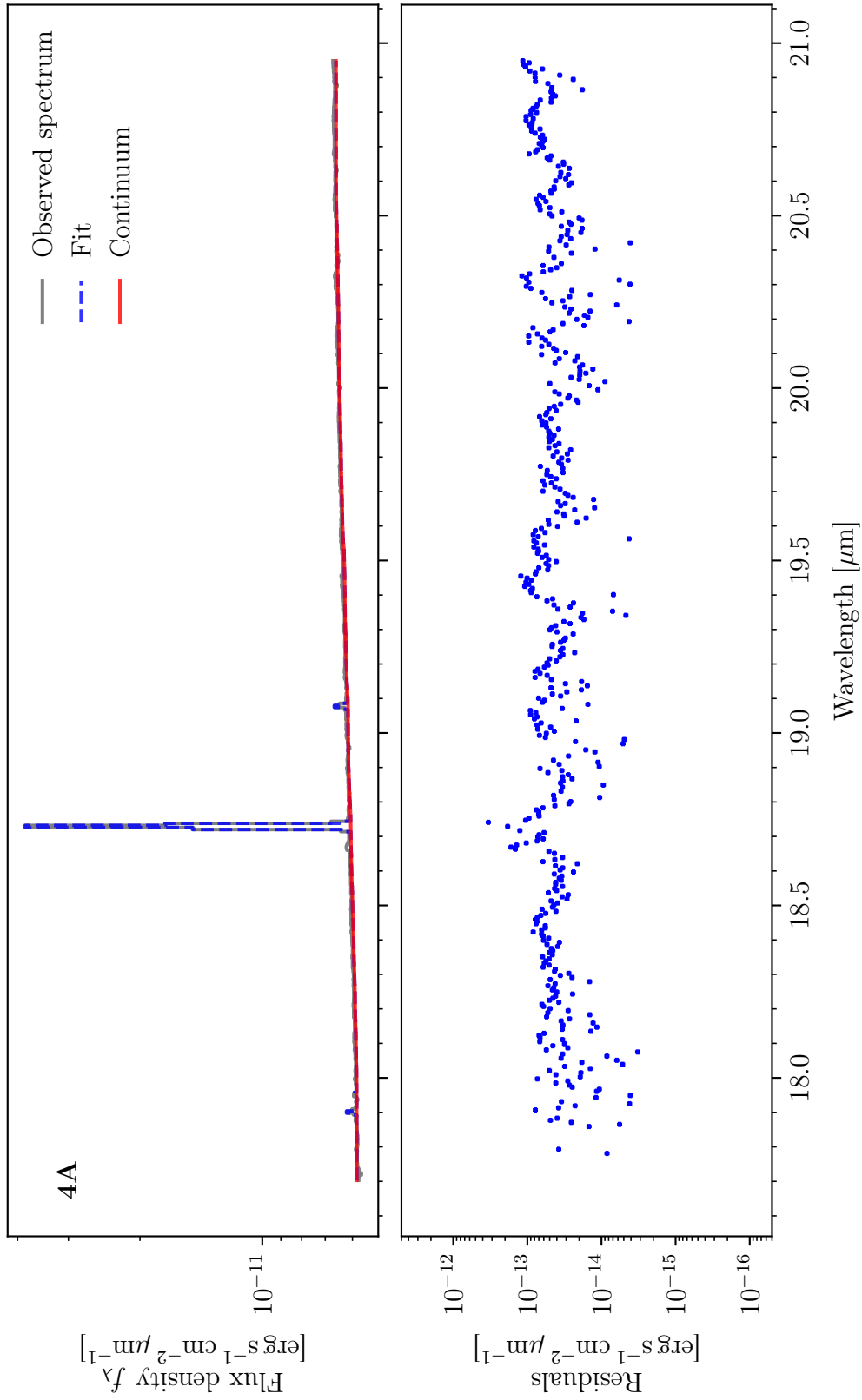


FIGURE E.1 – *Continued.*

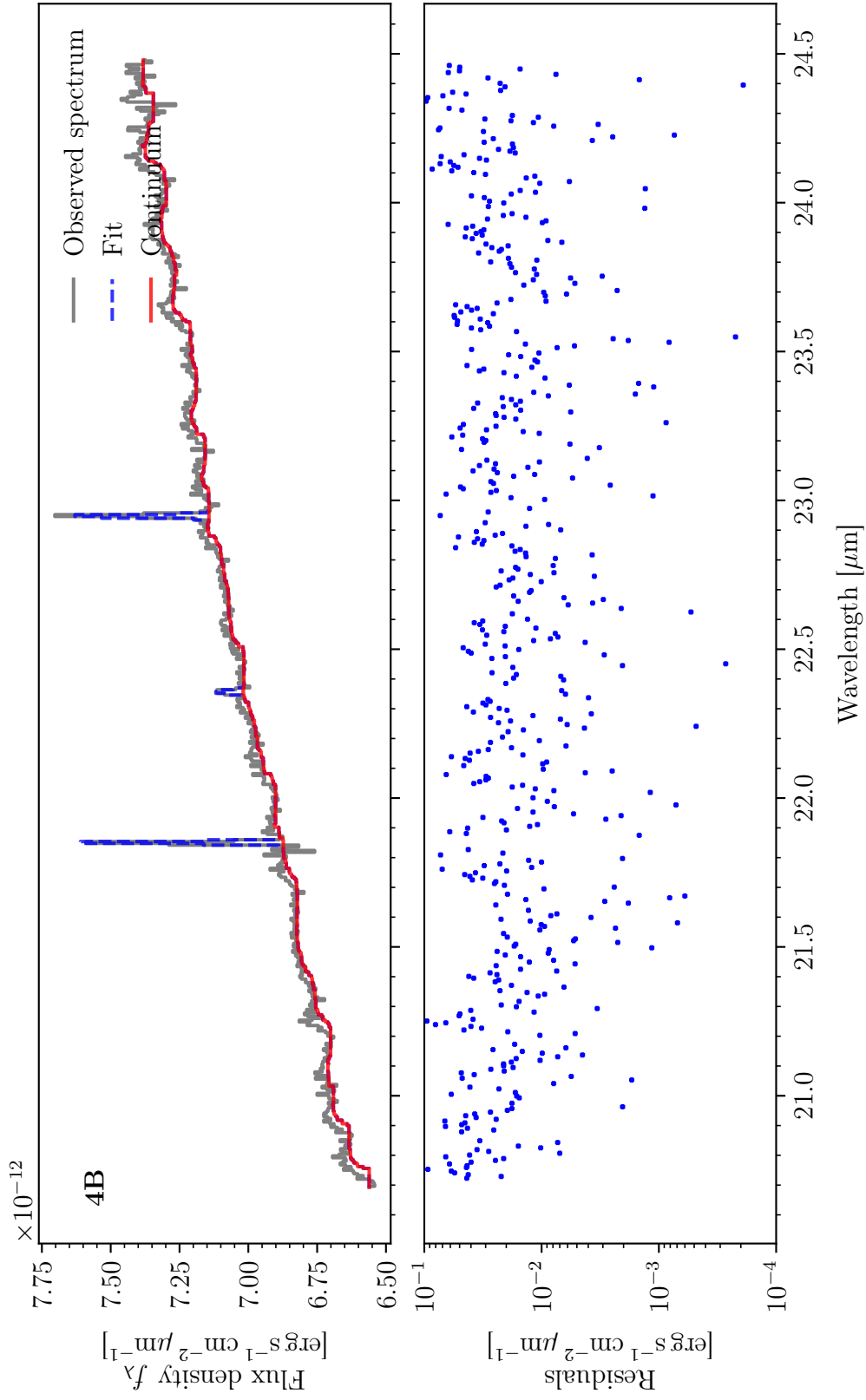


FIGURE E.1 – *Continued.*

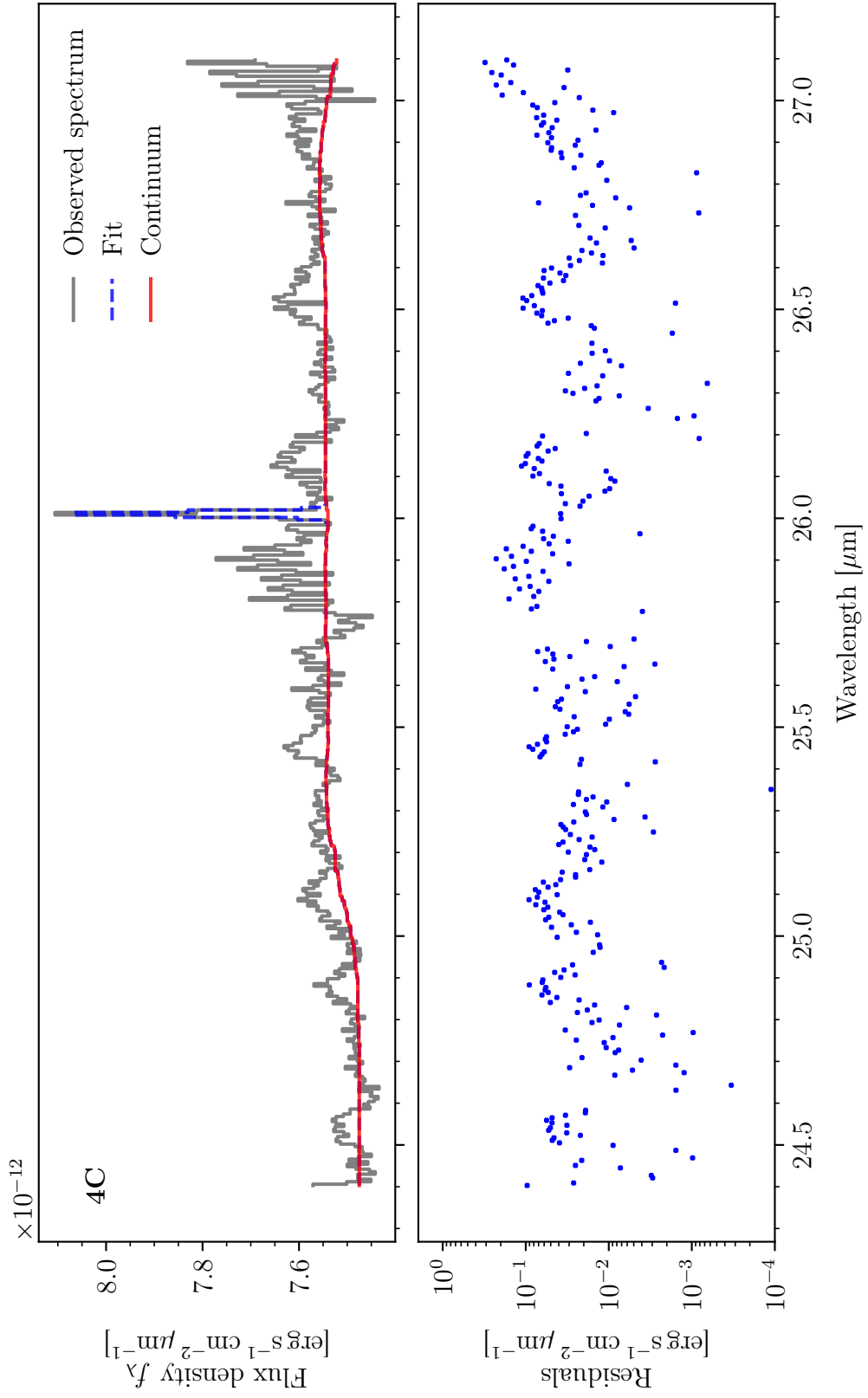


FIGURE E.1 – *Continued.*